

# Tortuosity and microstructure effects in porous media: classical theories, empirical data and modern methods

Holzer, L. <sup>\*1</sup>, Marmet, P. <sup>1</sup>, Fingerle, M. <sup>2</sup>, Wiegmann, A. <sup>2</sup>, Neumann, M. <sup>3</sup>, Schmidt, V. <sup>3</sup>

<sup>1</sup> ZHAW Winterthur, School of Engineering, Institute of Computational Physics,  
Wildbachstrasse 21, CH-8400 Winterthur, Switzerland

<sup>2</sup> Math2Market GmbH, Richard-Wagner-Strasse 1, D-67655 Kaiserslautern, Germany

<sup>3</sup> Ulm University, Institute of Stochastics, Helmholtzstrasse 18, D-89069 Ulm, Germany

\* Corresponding author

## Abstract

Tortuosity is an important morphological characteristic, which describes the limiting effects of the pore structure on the transport properties of porous media. In this paper, the relevant aspects of tortuosity and associated transport in porous media are reviewed thoroughly.

The classical theories related to tortuosity and associated equations for the prediction of effective transport properties are summarized separately for flow, conduction and diffusion. These theories evolved over a long period, and their evolution is tightly linked with the progress of relevant methodologies such as tomography and 3D image analysis. As a result of this long history, many different definitions and nomenclatures can be found in literature, which is the source of severe confusion and frequent misconception. In order to clarify the discussion on this topic, a new classification scheme and a systematic nomenclature for the different tortuosity types are proposed in this paper. Three main classes of tortuosity are distinguished: a) direct geometric, b) indirect physics-based and c) mixed (geometric and physics-based) tortuosities.

An extensive review of empirical data focusing on tortuosity-porosity relationships reveals a systematic pattern associated with the different tortuosity types. For example, the values of direct geometric as well as mixed tortuosities are systematically lower than those from indirect physics-based tortuosities. Systematic differences can be observed even within single tortuosity classes. For example, when comparing direct geometric tortuosities, the values for medial axis tortuosity are systematically larger than those for geodesic tortuosity. Hence, a scientific treatment of tortuosity always has to provide a clear definition of the tortuosity type under consideration, which is tightly related to the underlying method of computation.

The review of methods for characterization of porous media, in general, and computation of tortuosity, in specific, includes the following disciplines: 3D imaging, image processing (qualitative and quantitative), numerical transport simulation, stochastic geometry and virtual materials testing. Particular emphasis is put on the different methods of computation, which are specific for the different types of tortuosity. An extensive list of available software packages with their modular options is also provided.

Finally, mathematical and empirical expressions for microstructure-property relationships are discussed for a) conduction and diffusion and b) flow/permeability. The evolution of these expressions is intimately related to the methodological improvements in tomography, image analysis, numerical transport simulation, stochastic geometry and virtual materials testing. This evolution led to a better understanding of the different tortuosity types and of their impact on transport

properties. However, the methodological progress also resulted in the perception of additional relevant characteristics such as the constrictivity and, in case of viscous flow, the hydraulic radius. Hence, new mathematical expressions for microstructure-property relationships make use of modern methods that enable to characterize these morphological characteristics in a specific way (i.e. specific computation of tortuosity type, constrictivity and/or hydraulic radius). Compared to classical equations (e.g., the Carman-Kozeny equation or Archie's law), the new expressions provide a higher prediction power of effective properties, in particular for porous and composite materials with complex microstructures.

## 1. Introduction

Tortuosity ( $\tau$ ) is widely recognized as a key concept for transport in porous media, which describes the impact of pore structure (at all scales) on effective transport properties. Tortuosity is a dimensionless parameter that depends on the windedness of transport pathways. The increase of path lengths due to tortuous pore morphology can contribute significantly to the transport resistance. This concept was introduced almost 100 years ago by Kozeny in 1927 [190]. Since then, tortuosity has been widely applied in various research disciplines, such as chemical engineering, geoscience, materials science and life science. Uncountable studies dealing with tortuosity have been performed, using different methodologies (physical theory, laboratory experiments, numerical simulations, 3D imaging and image processing) and combinations thereof. It is beyond the scope of this article to present a detailed review of all these studies. For this purpose we refer to excellent review articles on tortuosity in specific (e.g. by Clennell [55], Ghanbarian et al. [109], Shen and Chen [304], Tjaden et al. [329]) and on transport in porous media in general (e.g. [3,18,27,74,130,131,289,333,351]).

In order to explain the focus of this paper, it must be emphasized that until now there exists no unifying theory for the tortuosity concept. Therefore, the discussion of tortuosity bears considerable potential for confusion. Many different definitions of tortuosity have been presented, depending either on the characterization method (direct geometric 3D analysis by tomography and image processing vs. indirect calculation from effective properties) and/or on the underlying transport mechanism (flow, diffusion and conduction). Confusion is amplified by the fact that many different tortuosity-terms are in use (see Table 1). Unfortunately, in many cases there exists no clear definition for these terms and moreover, a globally accepted classification scheme as well as a systematic nomenclature for the different tortuosity types are missing.

Table 1: List of tortuosity ( $\tau$ ) terms from literature

- geometric $\tau$	- fudge factor $\tau$
- geodesic $\tau$	- retardation factor $\tau$
- medial axis $\tau$	- streamline $\tau$
- percolation path $\tau$	- volume averaged $\tau$
- fast marching method (FMM) $\tau$	- area averaged $\tau$
- distance propagating method (DPM) $\tau$	- path-length $\tau$
- pore centroid $\tau$	- random walk $\tau$
- path tracking method (PTM) $\tau$	- relative $\tau$
- pore throat $\tau$	- formation $\tau$
- (bulk) diffusional $\tau$	- fractal $\tau$
- Knudsen $\tau$	- (in)active phase $\tau$
- electric $\tau$	- total electrode $\tau$
- ionic $\tau$	- characteristic $\tau$
- thermal $\tau$	- experimental $\tau$
- hydraulic $\tau$	- impedance (EIS) $\tau$
- flux-based/physics-based $\tau$	- crack $\tau$
- indirect or inverse $\tau$	- three phase boundary (TPB) $\tau$
- direct $\tau$	- $\tau$ factor ( $T$ )
- kinematic $\tau$	- $\tau$ tensor

As will be discussed in this article, the different tortuosity terms have distinct meanings and can therefore not be used interchangeably. However, the meaning of a specific tortuosity term is often strongly related to the methodology by which tortuosity is determined. Therefore, the topic of tortuosity must be discussed in context with the corresponding methodologies (i.e. 3D imaging and image analysis, transport simulation or laboratory experiments) and their continuing development.

Initially, the basic theories on tortuosity (e.g., Carman-Kozeny equations) were developed at a time when direct measurement of tortuosity by means of tomography and 3D image analysis was not possible. Therefore tortuosity was determined indirectly - usually from effective transport properties that were measured experimentally. This led to a certain gap between theoretical descriptions, which are based on considerations of path lengths in simplified geometric models (e.g. in bundles of tubes or in packed spheres), and empirical investigations, which derive tortuosity values indirectly from bulk effective properties. Hence, different definitions for tortuosity evolved over time, depending on the basic approach (theory vs. experiment vs. modeling), depending also on the field of research, on an associated 'school of thinking' (e.g. petro-physics vs. electrochemistry), and also largely on the availability of certain characterization techniques (e.g. pore scale modeling or 3D analysis by tomography and image processing).

Over the last two decades significant progress was achieved in high-resolution tomography as well as in stochastic modeling and numerical simulation of 3D image data representing the morphology of microstructures. These methodological improvements open new possibilities for studying microstructure-property relationships, in general, as well as for measuring tortuosity directly from the microstructure by means of 3D analysis and transport simulation, in particular. Due to the availability of new methods, it is now possible to compare different tortuosity concepts and establish correlations between the different tortuosity types. These new possibilities are the basis for the present review article, which is structured as follows:

In Chapter 2, the classical theories and concepts of tortuosity (starting with Carman-Kozeny equations), as well as the underlying definitions for the most important tortuosity types are presented in a chronological (historical) order. At the end of Chapter 2, a classification-scheme is introduced together with a systematic tortuosity-nomenclature. Three main categories are distinguished: direct geometric tortuosities, indirect physics-based tortuosities and mixed (geometric and physics-based) tortuosities. This classification may help to avoid confusion in future debates.

In Chapter 3, empirical data from literature is collected and compared. The collection includes more than 2000 data-points (i.e. tortuosity-porosity-couples) from 70 studies in various fields such as geology, battery and fuel cell research. Thereby, empirical approaches are considered as well as investigations that are based on computational modeling and simulation. The collection of literature data represents the basis for an empirical description, which shows how tortuosity varies for different types of materials and microstructures. Furthermore, in many of these studies different types of tortuosity are measured for the same materials. These datasets enable to define a relative order among the different tortuosity types. More precisely, it turns out that for a given material, the values of certain types of tortuosity tend to be systematically lower than

the values of other tortuosity types. This comparison of different tortuosity types results in a surprisingly clear and consistent pattern.

In Chapter 4, modern methods for microstructure characterization and associated calculation approaches for tortuosity are reviewed. Chapter 4 is structured according to the workflow, which is typical for this kind of microstructure characterization. First, an overview of modern tomography methods is presented with a special emphasis on recent innovations and on current trends. Subsequently, calculation approaches by image analysis and by transport simulation are discussed for all three tortuosity categories: direct geometric, indirect physics-based and mixed (geometric and physics-based) tortuosities. In addition, an extensive list with available software packages for image processing, which include codes for the computation of specific tortuosity types, is presented. Finally, modern methods of stochastic geometry used for virtual materials testing are discussed in context with their applications in Digital Materials Design and Digital Rock Physics, which are all strongly associated with the investigation of tortuosity.

In Chapter 5, it is discussed how the recent progress in tomography, 3D image analysis, microstructure modeling and virtual materials testing can be used for a thorough understanding of microstructure-property relationships. Based on modern 3D characterization techniques, the effects from tortuous pathways can now be distinguished from other microstructure effects, such as the limitations arising from narrow bottlenecks and from the friction at pore walls. New morphological descriptors were introduced for the bottleneck effect (i.e. constrictivity), for the wall friction effect (i.e. hydraulic radius) and also for the path length effect (i.e. tortuosity). As a consequence, new formulas describing the complex relationships between microstructure and effective transport properties have been established recently. The evolution of morphological descriptors and associated formulas describing the micro-macro relationships are reviewed in this chapter. For porous media with random microstructures, these new formulas have a higher prediction power compared to traditional equations from the literature, such as e.g. the Carman-Kozeny equation for viscous flow.

Finally, a summary and conclusions are presented in Chapter 6.

## 2. Review of theories and a classification of tortuosity types

In this chapter, the classical concepts and theories of tortuosity are reviewed. The concept of tortuosity typically started with the Carman-Kozeny equations and then evolved and diverged from there. Although tortuosity is related to porous media transport, it must be emphasized that the purpose of this chapter is not to give a review on transport equations and associated transport simulations. For such topics we refer to dedicated books (e.g. Bird et al [27]).

For a given porous medium, tortuosity ( $\tau$ ) is basically defined as the ratio of effective path length ( $L_{eff}$ ) over direct path length ( $L_0$ ) through the considered porous medium (see e.g. [47,84,113,190]), i.e.

$$\text{Eq. 1} \quad \tau = \frac{L_{eff}}{L_0}$$

The direct path length ( $L_0$ ) is equal to the sample dimension in transport direction. For theoretical treatment one simply has to find a suitable definition of the effective path length ( $L_{eff}$ ), and for practical application one simply has to find a suitable method to measure the effective path length ( $L_{eff}$ ). Unfortunately, definition and measurement of  $L_{eff}$  are not as simple as it appears at a first glance, which explains the emergence of numerous different approaches and concepts over the last 100 years. In this chapter, we therefore describe the most important types of tortuosity (i.e. hydraulic, conductive, diffusive and geometric tortuosities) in separate subsections. For each tortuosity type, we present the evolution of emerging definitions and concepts in a chronological (historical) order.

## 2.1 Hydraulic tortuosity

### 2.1.1 Classical Carman-Kozeny theory

For porous media, the volumetric flow ( $Q$ ) induced by a pressure gradient ( $\Delta P/L_0$ ) can be described by Darcy's law from 1856 [65]

$$\text{Eq. 2} \quad Q = v_s A = - \frac{\kappa A}{\mu} \frac{\Delta P}{L_0},$$

with superficial velocity ( $v_s$ ), cross-section area ( $A$ ), dynamic viscosity ( $\mu$ ) and permeability ( $\kappa$ ). All resistive effects of the microstructure are implicitly and indistinguishably contained within the permeability ( $\kappa$ ). 'In early times', when 3D methods were not yet available, flow and its relationship to the underlying microstructure were modeled based on a simplified geometrical model consisting of a bundle of parallel tubes (i.e. equivalent channel model, see Kozeny (1927) [190]).

Capillary flow in a straight tube can be described with the Hagen-Poiseuille equation

$$\text{Eq. 3} \quad v_c = - \frac{r^2}{8 \mu} \frac{\Delta P}{L_0},$$

with capillary velocity ( $v_c$ , also called interstitial velocity) and tube radius ( $r$ ). The comparison of Eqs. 2 and 3 reveals that permeability ( $\kappa$ ) in tube models scales with  $r^2/8$ . For models where capillary tubes are not straight, the effective length of the capillary flow path ( $L_{eff}$ ) is larger than the direct length ( $L_0$ ), which leads to a reduction of the effective pressure gradient. In order to correct this effect, Kozeny introduced the notion of hydraulic tortuosity, which he defined as the ratio of the effective hydraulic path length over the direct length (i.e.  $\tau_{hydr} = L_{eff\_hydr}/L_0$ ). This leads to

$$\text{Eq. 4} \quad v_c = - \frac{r^2}{8 \mu} \frac{\Delta P}{L_{eff\_hydr}} = - \frac{r^2}{8 \mu \tau_{hydr}} \frac{\Delta P}{L_0}.$$

In order to adapt Poiseuille's description of a single tube for equivalent tubes (as analogy for porous media), it is necessary to consider also the impact of pore volume fraction on superficial velocity and associated volume flow. According to Dupuit's

relation, superficial velocity ( $v_s$  in Eq. 2 for porous media flow) is equal to the capillary velocity ( $v_c$  in Eq. 4 for tube flow) multiplied by porosity (i.e.  $v_s = v_c \varepsilon$ ). In analogy to Darcy's law, the equation for volume flow in the capillary tubes model thus becomes

$$\text{Eq. 5} \quad Q = v_s A = - \frac{r^2 \varepsilon A}{8 \mu T_{hydr}} \frac{\Delta P}{L_0}.$$

The distinct notation of tortuosity factor ( $T$ ) in Eq. 5 originates from a later extension of Dupuit's relation by Carman [47], which is discussed below in context with Eq. 14.

Permeability strongly depends on the effective hydraulic radius ( $r_{hydr}$ ), which represents a tube equivalent radius that is characteristic for the overall viscous drag. Kozeny also introduced the hydraulic radius as the ratio of area open to flow (in a 2D cross-section perpendicular to flow) over the perimeter of this area exposed to flow. For a given volume of porous media, the hydraulic radius can also be defined as the ratio of the pipes volume open to flow over the corresponding surface area of these pipes. For a single straight tube, the hydraulic radius is thus half of the tube radius ( $r_{hydr\_tube} = \pi r^2 L / 2 \pi r L = r/2$ ). In a more generalized description for porous media, the volume-to-surface ratio is rewritten as the ratio of porosity over specific surface area (per volume) ( $r_{hydr\_K} = \varepsilon / S_V = r/2$ , with subscript K for Kozeny). For non-circular tubes, Kozeny additionally introduced a shape correction factor ( $c_K$ ). This leads to the well-known semi-empirical Kozeny equation [190]

$$\text{Eq. 6} \quad Q = v_s A = - \frac{r_{hydr\_K}^2}{c_K} \frac{\varepsilon}{T_{hydr}} \frac{A \Delta P}{\mu L_0} = - \frac{\varepsilon^3 A}{c_K S_V^2 T_{hydr} \mu} \frac{\Delta P}{L_0}.$$

For the specific case of circular tubes, the Kozeny factor  $c_K$  is equal to 2. For non-circular tube cross-sections, shape correction factors in the range from 1.5 to 2.6 were specified based on experimental data.

Combining Eq. 6 with Eq. 2, we obtain an expression for permeability in terms of porosity, Kozeny factor, specific surface area (per volume) and hydraulic tortuosity. This expression, also called Kozeny equation in the literature, reads as

$$\text{Eq. 7} \quad \kappa = \frac{\varepsilon^3}{c_K S_V^2 T_{hydr}}.$$

In 1937, Carman [47] presented some important modifications of Kozeny's equations, in order to describe permeability in granular materials (instead of a bundle of parallel tubes). For this purpose he considered a simplified geometrical model of packed spheres. Specific surface area per total volume ( $S_V$ ) is replaced by surface area per solid volume ( $a_V$ ), which then requires the solid volume fraction ( $1-\varepsilon$ ) as a correction term. For mono-sized spheres, the surface area per solid volume ( $a_V$ ) can be written as a function of the particle diameter ( $a_V = 6/D_p$ ). For non-spherical particles, the hydraulic radius needs to be corrected with a shape factor ( $c_C$ , with subscript C for Carman). With this correction, one obtains

$$\text{Eq. 8} \quad r_{hydr\_C} = \frac{c_C \varepsilon}{a_V (1-\varepsilon)} = \frac{c_C D_p \varepsilon}{6 (1-\varepsilon)}.$$

Permeability of a packed spheres model (as analogy for granular materials) is thus described with the Carman-Kozeny equation

$$\text{Eq. 9} \quad \kappa = \frac{c_c^2 \varepsilon^3}{2 a_v^2 (1-\varepsilon)^2 T_{hydr}} = \frac{c_c^2 D_p^2 \varepsilon^3}{72 (1-\varepsilon)^2 T_{hydr}}.$$

Thereby the Kozeny factor ( $c_k$ ) for tube shapes becomes obsolete and can be replaced with a constant value of 2. The Carman factor ( $c_c$ ) for correction of non-spherical particle shapes was determined experimentally for grain-sorted powders, whereby values in the range from 0.28 (for mica) to 1 (for spherical particles) were obtained.

Carman [47] pointed out that the comparison of Eq. 2 (Darcy, porous media) with Eq. 3 (Hagen-Poiseuille, tube flow) requires a careful consideration of the involved velocities. In principle, velocity can be defined as the ratio of path length over characteristic residence time ( $t$ ) during which a particle is travelling from inlet to outlet. Three different velocities must be distinguished in this context, which was later also discussed by Epstein in 1989 [84]:

a) The capillary velocity ( $v_c$ ) used in Eq. 3 for tubes is also called intrinsic or interstitial velocity for porous media. The notion of capillary velocity is based on a microscopic consideration of particles travelling through porous media (or through a single tube). Their capillary velocity can be described as the ratio of the effective tortuous path length, denoted by  $L_{eff\_hydr}$ , over the residence time ( $t$ ), i.e.

$$\text{Eq. 10} \quad v_c = \frac{L_{eff\_hydr}}{t}$$

Thereby,  $L_{eff\_hydr}$  is interpreted as a mean length, which is characteristic for a large number of particle pathways. Subsequently, homogenized 'mean' properties of locally defined quantities are denoted with angle brackets, i.e.  $\langle x \rangle$  denotes the homogenized mean of  $x$ . For complex porous media, it was not possible for a rather long time to measure the mean length of hydraulic transport pathways or streamlines ( $L_{eff\_hydr}$ ). However, a simpler approach to determine the mean capillary velocity  $\langle v_c \rangle$  without measuring  $L_{eff\_hydr}$  was later presented by Duda et al. [73] and Matyka and Koza [220], who used  $\langle v_c \rangle$  for calculating a volume averaged tortuosity based on pore scale modeling (see the discussion in context with Eq. 20).

b) The interstitial axial velocity ( $v_x$ ) is based on a macroscopic observation of flow in porous media, where only the direct path length ( $L_0$ ), i.e. the sample length between inlet and outlet planes is known. The residence time ( $t$ ) is the same as for the microscopic observation related to capillary velocity. Then,  $v_x$  is given by the ratio of direct path length over residence time, i.e.

$$\text{Eq. 11} \quad v_x = \frac{L_0}{t}.$$

Capillary velocity ( $v_c$ ) and interstitial axial velocity ( $v_x$ ) are equivalent only for the case of a single, straight tube, where  $L_{eff\_hydr} = L_0$ .

c) Finally, in a porous media, the macroscopic superficial velocity ( $v_s$ ) in Darcy's law (Eq. 2) can be deduced from the ratio of volume flow over cross-section area (i.e.  $v_s = Q/A$ ). According to Dupuit's relation, the macroscopic superficial velocity in porous media ( $v_s$ ) can also be obtained from the interstitial axial velocity ( $v_x$ , e.g. in a single tube or in porous media consisting of tubes) with correction of the volume effect using porosity ( $\varepsilon$ ). In this way one obtains

$$\text{Eq. 12:} \quad v_s = \frac{Q}{A} = v_x \varepsilon = \frac{L_0}{t} \varepsilon .$$

The careful distinction of three different flow velocities leads to two main conclusions:

First, from the ratio of Eq. 10 over Eq. 11, Carman obtained two equivalent definitions of hydraulic tortuosity, - first as ratio of mean path lengths and second as ratio of mean velocities, i.e.

$$\text{Eq. 13} \quad \tau_{hydr} = \frac{\langle L_{eff.hydr} \rangle}{L_0} = \frac{\langle v_c \rangle}{\langle v_x \rangle}$$

For a long time, conventional definitions of tortuosity focused on the ratio of path lengths. However, with the rise of numerical simulations the consideration of mean velocity components has gained importance as an equivalent definition for tortuosity (see Eq. 20).

Second, by combining Eqs 10 - 13, Carman also obtained

$$\text{Eq. 14} \quad v_s = v_c \varepsilon \frac{1}{\tau_{hydr}},$$

as an extension of Dupuit's relation. Substituted in Eq. 5, tortuosity was thus introduced for a second time in context of flow equations (i.e. first, for the correction of pressure gradient by Kozeny and second, for the correction of velocity by Carman). As a consequence, the meaning of the tortuosity factor ( $T$ ) in Eqs. 5-9 has to be redefined as hydraulic tortuosity by a power of 2 (see [47,55,84]), i.e.,

$$\text{Eq. 15} \quad T_{hydr} = \left( \frac{L_{eff.hydr}}{L_0} \right)^2 = \tau_{hydr}^2.$$

### 2.1.2 From classical Carman-Kozeny theory to modern characterization of microstructure effects

#### a) Limitations of the Carman-Kozeny approach

The Carman-Kozeny equations describe two main transport limitations arising from the microstructure. First, viscous drag induced by wall friction is captured with the hydraulic radius ( $r_{hydr}$ ). Second, non-viscous effects are attributed to reduced pore volume fraction and/or to increased length of transport pathways. These non-viscous effects are described with dimensionless microstructure descriptors for porosity ( $\varepsilon$ ) and hydraulic tortuosity ( $\tau_{hydr}$ ). Variations of tortuous path lengths affect both, superficial velocity and effective pressure gradient, and thus, tortuosity appears with a power of 2 in the Carman-Kozeny equations.

The Carman-Kozeny equations were introduced at a time when tomography and 3D image analysis were not yet available and therefore hydraulic radius and tortuosity could not be measured directly from the microstructure. As a loophole to this problem, Carman considered a simplified geometrical model consisting of mono-sized spheres as an analogy for the complex pore structure in granular media. For this simplified model the hydraulic radius can be described with easily accessible geometric descriptors ( $\varepsilon$ ,  $S_V$ ,  $a_V$ ,  $D_p$ ), as summarized in previous sections. However, the determination of hydraulic tortuosity remained a major problem. Based on geometric analysis of streamlines in a packed bed of spheres, Carman proposed to use a constant value of  $\sqrt{2}$  for  $\tau_{hydr}$ .

Experimental validations confirmed that the Carman-Kozeny equations are capable to predict permeability and flow reasonably well for simple granular media consisting of mono-sized spheres. For non-spherical particles, Carman introduced a shape correction factor ( $c_c$ ), which has to be fitted for different particle shapes and size distributions separately. It turns out that the uncertainties of permeability predictions with the Carman-Kozeny equations increase with geometric complexity of the granular material (e.g. for non-spherical particles, for wide particle size distributions and for anisotropic particle packing and grain orientation). In the meanwhile, numerous studies have shown that the semi-empirical Carman-Kozeny approach is highly uncertain for materials with complex microstructures (see e.g. [149,153,244,246]). Despite these uncertainties, the Carman-Kozeny equations are still widely used for the study of granular materials such as battery electrodes (materials science) and sandstones (geoscience). As will be discussed in Chapter 5, new equations using new morphological descriptors from 3D analysis have been presented in literature, which provide reliable predictions of flow and permeability also for porous media (granular and non-granular) with complex microstructures.

#### b) Controversy about realistic values for hydraulic tortuosity

Much effort was expended in order to visualize the streamlines and to estimate the associated streamline tortuosity. Already in 1956, Carman [48] was able to visualize streamlines by injecting dye into dense packed glass spheres. With this experiment he demonstrated that on average the streamlines diverge from the direction of macroscopic flow by an angle of about  $45^\circ$ . Based on these observations Carman concluded that the hydraulic streamline tortuosity ( $\tau_{hydr\_streamline}$ ) in porous granular media must be approximately  $\sqrt{2}$ . Thus, in early theoretical work, hydraulic tortuosity was often replaced by a constant value of  $\sqrt{2}$ .

Contrariwise, in experimental work, tortuosity is usually calculated indirectly from relative properties at macroscopic scale. A relative property is defined as ratio of the effective property (e.g. effective electrical conductivity ( $\sigma_{eff}$ ) of a porous medium saturated with electrolyte) over the intrinsic property of the transporting medium (e.g. intrinsic conductivity of the pure electrolyte ( $\sigma_0$ )), which results in  $\sigma_{rel} = \sigma_{eff}/\sigma_0$ . A simple relationship between microstructure and the macroscopic relative property is then often assumed, according to which, for example, the relative conductivity ( $\sigma_{rel}$ ) depends only on porosity ( $\varepsilon$ ) and electrical tortuosity (i.e.  $\sigma_{rel} = \varepsilon / \tau_{ele}^2$ ). Hence, when relative conductivity is known from experiment or simulation, the indirect electrical tortuosity can then be calculated easily ( $\tau_{indir\_ele} = \sqrt{\varepsilon/\sigma_{rel}}$ ). By assuming the same simple

relationship for relative diffusivity, the indirect diffusional tortuosity can be determined in the same way, i.e. by  $\tau_{indir\_diff} = \sqrt{(\varepsilon/D_{rel})}$ .

For flow and permeability, the micro-macro relationship is more complex since it involves additional microstructure descriptors for the viscous effects (i.e.  $r_{hydr}$ ). For example, the Carman-Kozeny formulations could be used for calculation of indirect hydraulic tortuosity (i.e. by combining and reformulating Eqs. 6, 7, 9, 15). The resulting expression for indirect hydraulic tortuosity then reads as follows

$$\text{Eq. 16} \quad \tau_{indir\_hydr} = \sqrt{\frac{r_{hydr}^2 \varepsilon}{\kappa}} = \sqrt{\frac{\varepsilon^3}{C_K S_V^2 \kappa}}.$$

However, this equation is rarely used because the involved descriptors are more difficult to determine. For simplicity, the indirect 'hydraulic' tortuosity is thus often calculated with the same simple approach as described above for relative conductivity or relative diffusivity. As a consequence, the computed values that are reported in literature for indirect tortuosities are usually much higher than  $\sqrt{2}$ , and sometimes even up to 20 [25,171,285,286].

In Chapter 3 we present an extensive collection of empirical data from literature, which is the basis for a systematic comparison of different tortuosity types. This collection of literature data illustrates a clear mismatch between the relatively high values ( $\gg 2$ ) for indirect tortuosities versus relatively low values in the range of  $\sqrt{2}$  for streamline-tortuosities, as predicted by Carman [48]. A possible explanation for this mismatch is given below in section 2.1.2 d.

### c) New methods for characterization of volume averaged hydraulic tortuosity

Over the last two decades considerable progress was achieved in tomography, 3D image processing and pore scale modeling. This allows for a computation of the 3D geometry of streamlines based on simulated flow fields and the associated effective path lengths can be described statistically (see e.g. [185–187,189,219]). However, in order to extract a physically relevant mean value for the effective path length ( $L_{eff}$ ), the question arises how the single streamlines have to be counted in the statistical analysis? Bear [18] and Clennell [55] argued that hydraulic streamline tortuosity should be calculated by weighting the streamlines with the corresponding fluid fluxes, i.e.,

$$\text{Eq. 17} \quad L_{eff\_weighted} = \frac{\sum_i L_i w_i}{\sum_i w_i}$$

where  $w_i$  represents a weighting factor for the flux represented by streamline  $i$ . In the meanwhile, several weighting approaches were presented in literature (see e.g. [185–187,189,219,238]). For a detailed discussion we refer to Duda [73], who concluded that these different weighting approaches lead to inconsistent results. In particular, circular Eddy-currents may impose a significant source of error. Last but not least, statistical analysis of streamline geometry is computationally expensive.

A much easier method to compute hydraulic tortuosity was then presented by Matyka and Koza[220] and Duda et al. [73], based on earlier work from Koponen et al. [187]. Instead of focusing on the challenging analysis and weighting of streamlines, their

method is based simply on the integration of local vector components from the 3D velocity field:

$$\text{Eq. 18} \quad \tau_{mixed\_hydr\_vav} = \frac{\langle v_c \rangle}{\langle v_x \rangle} = \frac{\int_V v_c(r) d^3r}{\int_V v_x(r) d^3r}$$

$$\approx \frac{\sum_{k=1}^n \frac{1}{n} \sqrt{v_x(k)^2 + v_y(k)^2 + v_z(k)^2}}{\sum_{k=1}^n \frac{1}{n} v_x(k)} = \frac{\sum_{k=1}^n \sqrt{v_x(k)^2 + v_y(k)^2 + v_z(k)^2}}{\sum_{k=1}^n v_x(k)},$$

where n is the number of discrete control volumes with equal volume (e.g. voxels from tomography and from the simulated flow field, respectively).

It must be emphasized, that this definition of hydraulic tortuosity is compatible with an alternative definition from Carman (see Eq. 13), who described tortuosity also as the ratio of capillary velocity ( $v_c$ ) over interstitial axial velocity ( $v_x$ ). According to Matyka and Koza [220],  $\langle v_c \rangle$  is the 'average magnitude of the intrinsic velocity over the entire pore volume' (i.e. mean capillary velocity) and  $\langle v_x \rangle$  represents the 'volumetric average of the velocity component parallel to the macroscopic flow direction' (i.e. the mean interstitial axial velocity). The mean values are obtained by integration of local properties (i.e. vectors components) at each point r in a discretized (mesh- or voxel-based) velocity field, which is obtained from numerical simulation of flow.

Compared to streamline-analyses, this method has several important advantages: a) neither streamline extraction nor weighting of streamlines are necessary, b) problems with eddy currents are solved in an elegant way, c) implementation is relatively easy and computation is relatively cheap and d) this method not only holds for fluid flow, but also for other transport processes such as diffusion and electrical conduction.

In literature, this type of tortuosity is called area (2D) or volume (3D) averaged tortuosity. For 2D-cases it was introduced by Koponen, 1996 [187]. For 3D-cases it was first applied in 2011 by Matyka and Koza [220], Duda et al. [73] and Ghassemi and Pak [110]. Since then it is increasingly used for characterization of all kinds of porous media (see e.g. [97,162,167,235,281–283,303]).

Throughout the present article, the volume averaged as well as the streamline tortuosities are denoted as 'mixed' tortuosities (i.e.  $\tau_{mixed\_hydr\_vav}$ ,  $\tau_{mixed\_hydr\_streamline}$ ). The term 'mixed' emphasizes the fact that this category incorporates 'mixed' information. First, it includes geometric information from 3D analysis of simulated flow fields. Second, it also includes physics-based information from simulation of a specific transport process (i.e. flow, diffusion or conduction). Thereby, the mixed information is neither determined directly from microstructure nor indirectly from effective or relative properties. (Note: A new tortuosity-classification with direct, indirect and mixed tortuosities is introduced in Chapter 2.5, see Fig. 3).

d) New microstructure descriptors for bottleneck effect and constrictivity

As mentioned in section 2.1.2 b, the values measured for mixed tortuosities (i.e.

$\tau_{mixed\_hydr\_vav}$ ,  $\tau_{mixed\_hydr\_streamline}$ ) are roughly compatible with Carman's estimation of hydraulic tortuosity (ca.  $\sqrt{2}$ ). In contrast, the relatively high values for indirect

tortuosities ( $\tau_{indir\_hydr}$  or  $\tau_{indir\_ele}$ ) indicate that the corresponding effective path lengths are overestimated. Obviously, by computing tortuosity indirectly using effective properties, other limiting effects in addition to path lengths are attributed to the indirect tortuosity, which explains the relatively high values. In particular the limitations arising from narrow bottlenecks are not addressed separately. The omission of the bottleneck effect is also a major shortcoming of the Carman-Kozeny theory. In fact, it was shown by Petersen [259] in 1958 that the retarding impact of varying cross-sections for flow in a straight tube can be described with a so-called constrictivity factor ( $\beta_{Petersen}$ ), which he defined as the ratio of cross-section areas at open ( $A_{max}$ ) and at constricted locations ( $A_{min}$ ), i.e.,

$$\text{Eq. 19} \quad \beta_{Petersen} = \frac{A_{max}}{A_{min}} = \frac{r_{max}^2}{r_{min}^2},$$

where  $r_{min}$  and  $r_{max}$  denote the radii of the disk-shaped cross-sections  $A_{min}$  and  $A_{max}$ , respectively. For the simple case of a constricted pipe, the bottleneck effect and the associated microstructure descriptors ( $\beta$ ,  $r_{min}$ ,  $r_{max}$ ) are visualized at the bottom of Fig. 23. In recent years, it became more and more accepted that the bottleneck effect (i.e. constrictivity) is an important retarding effect for transport in porous media, which needs to be considered separately from and/or in addition to the path lengths effect (i.e. 'true' tortuosity) (see e.g. [20–22,30,141,142,312,349]). However, until recently there were no methods available to quantify constrictivity ( $\beta$ ) from complex microstructures. A suitable method was then introduced by Holzer et al. [142] in 2013, which was later formalized in the framework of stochastic geometry [240]. Thereby, the average sizes of bulges and bottlenecks are obtained from two different size distribution curves, see Münch and Holzer [233]: a) continuous pore size distribution (*cPSD*), for which there is a one-to-one relationship with the granulometry function [218], is used to characterize the size of bulges, and b) a geometrically defined mercury intrusion pore size distribution (*MIP-PSD*, also called porosimetry curve) is used to characterize the size distribution of bottlenecks. The mean radii corresponding to the volumetric 50% quantiles (i.e.  $r_{50}$ ) of these two pore size distributions are considered as mean effective sizes for bulges ( $r_{50\_cPSD} = r_{max}$ ) and bottlenecks ( $r_{50\_MIP\_PSD} = r_{min}$ ), respectively. Constrictivity ( $\beta$ ) is then defined as the ratio of the squared effective bottleneck radius ( $r_{min}$ ) over the squared effective bulge radius ( $r_{max}$ ), which is the inverse of Petersen's definition of constrictivity, i.e.,

$$\text{Eq. 20} \quad \beta = \frac{A_{min}}{A_{max}} = \frac{r_{min}^2}{r_{max}^2} = \frac{1}{\beta_{Petersen}}.$$

It is important to note that  $r_{min}$  and  $r_{max}$  do not describe minimum and maximum radii of a pore structure, but they represent mean values of two different size distribution curves capturing the sizes of either narrow bottlenecks (*MIP-PSD*,  $r_{min}$ ) or wide bulges (*cPSD*,  $r_{max}$ ). For further reading about constrictivity we refer to [141,240,312].

The fact that constrictivity, still today, is often not included in the traditional transport equations explains the relatively high values that are typically obtained when calculating indirect tortuosity from effective transport properties, e.g. with Eq. 16 [142,312]. In Sections 2.1.2b+c, a striking discrepancy between mixed tortuosities (with characteristic values in the range of  $\sqrt{2}$ ) and indirect tortuosity (with values typically  $>2$ ) was

described. This discrepancy can mainly be attributed to the exclusion of constrictivity (bottleneck effect) from the calculation of indirect tortuosity, which is well documented by Wiedenmann et al. [349]. Indirect tortuosities that are derived from relative or effective properties (e.g. permeability, conductivity) are thus often also interpreted as fudge factors (or structure factors), because they represent an overall resistive effect of the microstructure, which is not or only partly related to the lengths of transport pathways (see e.g. Clennell [55]).

In summary, based on improved methods for 3D image analysis over the last two decades, new descriptors for microstructure characteristics have become available. These innovations include new types of tortuosities (direct-geometric and mixed types) and new approaches for measuring characteristic length, hydraulic radius, bottleneck size and constrictivity. Based on these new descriptors also new expressions for the quantitative relationship between microstructure and effective properties (permeability, conductivity, diffusivity) could be formulated. In contrast to the Carman-Kozeny equations, these new expressions have a high prediction power also for materials with complex microstructures. The mathematical description of micro-macro relationships for transport in porous media and how these equations evolved over time is reviewed in Chapter 5 (see Figs. 22, 23).

## 2.2 Electrical tortuosity

The concept of electrical tortuosity ( $\tau_{ele}$ ) was developed since ca. 1940 (see Archie [8]) in parallel to the hydraulic tortuosity concept. The electrical tortuosity describes resistive effects of the microstructure, which limit the effective electrical conductivity ( $\sigma_{eff}$ ) and, equivalently, increase the effective electrical resistance ( $R_{eff}$ ) in porous media saturated with electrolyte. Thereby, Ohm's law can be used to describe the electrical flux ( $J_{ele}$ ) in a saturated porous media, i.e.,

$$\text{Eq. 21} \quad J_{ele} = \frac{1}{R_{eff}} \frac{\Delta U}{L_0} = \sigma_{eff} \frac{\Delta U}{L_0},$$

with the potential gradient ( $\Delta U/L_0$ ) as driving force. The resistive formation factor ( $F_R$ ) was then defined as the ratio of effective electrical resistance of the porous media ( $R_{eff}$ ) over the intrinsic resistance of the electrolyte ( $R_0$ ):

$$\text{Eq. 22} \quad F_R = \frac{R_{eff}}{R_0} = \frac{\sigma_0}{\sigma_{eff}} = \frac{1}{\sigma_{rel}} = \frac{1}{M}.$$

The inverse of the formation factor is the relative conductivity ( $\sigma_{rel}$ ), which is also called microstructure ( $M$ )-factor. The difference between effective and intrinsic properties is due to the mentioned resistive effects of the underlying microstructure. According to Archie's law [8], which reads as

$$\text{Eq. 23} \quad F_R = \frac{1}{\varepsilon^m},$$

the formation factor can also be described as a power law of porosity ( $\varepsilon$ ) with a so-called empirical cementation exponent ( $m$ ).

Archie's law is widely used in geo- and soil-science. However, it has limited validity because it relates effective transport properties and associated formation factor to a single microstructure characteristic (i.e. porosity) and it ignores all other morphological effects. In an alternative approach by Wyllie and Rose, 1950 [357] the formation factor was described with an additional microstructure characteristic, namely the so-called structural factor ( $X_{ele}$ ), defined by

$$\text{Eq. 24} \quad F_R = \frac{X_{ele}}{\varepsilon} = \frac{\tau_{ele}^2}{\varepsilon}.$$

In analogy with Carman's formulation for flow, the structural factor ( $X_{ele}$ ) was also considered as an equivalent of the (electrical) tortuosity factor ( $T_{ele} = \tau_{ele}^2$ ). This relationship is nowadays more commonly formulated as

$$\text{Eq. 24b} \quad \sigma_{eff} = \frac{\sigma_0 \varepsilon}{\tau_{ele}^2}.$$

Hence, the electrical tortuosity ( $\tau_{indir\_ele}$ ) can be obtained indirectly by plugging experimental results for the formation factor (or relative conductivity) and porosity into Eq. 24, which leads to

$$\text{Eq. 25} \quad \tau_{indir\_ele} = \sqrt{F_R \varepsilon} = \sqrt{\frac{\varepsilon}{\sigma_{rel}}}.$$

This kind of indirect tortuosity (sometimes also called formation tortuosity) is nowadays very prominent, because it can be obtained easily from numerical simulations of electric conduction, e.g. with commercial software like GeoDict from Math2Market [350] or with open source software such as TauFactor from Imperial College London [59]. It must be emphasized that the determination of this indirect electrical tortuosity does not consider any geometric information. It is therefore by no means a measure for the true length of transport pathways. Whenever the tortuosity is afterwards used to determine effective conductivities, this is a good way to define tortuosity, though.

Katsube et al. [171] performed an extensive investigation on shales that were saturated with electrolyte. The measured values of  $F_R$  were in the range from 140 to  $> 17'000$  and porosities were in the range from  $<0.01$  to 0.1. Hence, the corresponding indirect electrical tortuosities took values in the range from 3.4 to 12. Katsube et al. [171] interpreted these values for  $\tau_{indir\_ele}$  as unrealistically high based on geometric considerations. This interpretation is in accordance with Carman's 45° argument for the streamlines and associated estimation of  $\sqrt{2}$  for streamline tortuosity. Katsube et al. concluded that the empirical results for the indirect electrical tortuosities are unrealistically high because other important microstructure effects (in addition to  $\varepsilon$ ,  $\tau$ ) are not yet included in Eqs. 24 and 25. Owen [250] and Dullien [74] argued that the influence from narrow bottlenecks needs to be considered as an additional resistive effect. The formation factor was thus redefined by adding constrictivity ( $\beta$ ) from Eq. 20 (see also [30]), which results in

$$\text{Eq. 26} \quad F_R = \frac{\tau_{ele}^2}{\varepsilon \beta}.$$

It must be emphasized that the method for direct measurement of constrictivity from porous media was only introduced in 2013 (Holzer et al. [142]). Because of a lack of suitable methods, constrictivity was thus not considered - until recently - as a separate microstructure characteristic in the calculation of indirect electrical tortuosity. As a consequence, unrealistically high values ( $> 3$ ) are often reported in literature for the indirect electrical tortuosity. These high tortuosity values must be interpreted as mixed information that includes resistive effects not only from tortuous path lengths but also from narrow bottlenecks.

Nevertheless, nowadays it is more and more accepted that the bottleneck effect and constrictivity should be considered separately from the path length effect. Hence, indirect tortuosity is now sometimes also calculated based on a separate treatment of constrictivity (see e.g. He et al. [124]), i.e.,

$$\text{Eq. 27} \quad \tau_{indir\_ele\_II} = \sqrt{\frac{\varepsilon \beta}{\sigma_{rel}}}.$$

Today, the recent progress in numerical simulation and 3D image processing opens new possibilities for the computation of other (mixed) types of electrical tortuosity. In analogy to the hydraulic tortuosity discussed above, also the electrical tortuosity can be extracted from simulated 3D fields of electrical flux. This approach provides either streamline ( $\tau_{mixed\_ele\_Streamline}$ ) or volume averaged tortuosities ( $\tau_{mixed\_ele\_Vav}$ ) (see Matyka and Koza [220] and Duda et al. [73]). Furthermore, it should be noted, that electrical conduction and associated electrical tortuosity are not limited to porous media saturated with electrolyte. The same principles can be used to describe electrical conduction of solid phases and associated electrical tortuosity (e.g. electrical conduction in cermet electrodes of solid oxide fuel cells).

### 2.3 Diffusional tortuosity

This section mainly deals with tortuosity in context with molecular diffusion (also called bulk diffusion), which is the dominant process in systems where chemical interactions between particles (ions, molecules) are negligible. Typically this is the case for electrolytes with a high level of dilution and/or with an ideal, inert tracer. Also gas transport at low pressure in macro- and mesoporous media is often dominated by molecular diffusion. Contrariwise, in systems where advection or surface effects (adsorption or dispersion) are important, molecular diffusion may not be the dominant transport process anymore.

The Knudsen number ( $K_n$ ) is used to distinguish between different diffusion regimes in porous media.  $K_n$  is defined by the ratio of mean free path length ( $\lambda$ ) over the characteristic length ( $L_c$ ), i.e.,

$$\text{Eq. 28} \quad K_n = \frac{\lambda}{L_c}.$$

The mean free path length ( $\lambda$ ) depends on pressure, temperature and on the effective cross-sectional area of the gas species. Typically it is in the range of 30 to 200 nm. For example, for air at room temperature and ambient pressure  $\lambda$  is 68 nm [159]. The

characteristic length ( $L_c$ ) is an ill-defined property, but it is usually considered as being equivalent to the characteristic pore radius. Hence, for gas transport in nanoporous media with  $r_{50} < 10$  nm, the Knudsen number is much larger than 1. In this case, we say that we are in the Knudsen diffusion regime, which is controlled by molecule-wall collisions [265]. For gas transport in macro-porous media,  $K_n$  is  $< 1$ , meaning that we are in the regime of bulk molecular diffusion, which is controlled by molecule-molecule collisions. For all liquid electrolytes,  $\lambda$  is very small (nm or smaller) so that diffusion in porous media is usually controlled by bulk diffusion. For Knudsen numbers close to 1, both transport phenomena must be considered. Bosanquet's approximation [265] or the Dusty Gas Model [337] are then often used to model transport in this mixed-regime.

### 2.3.1 Bulk diffusion

For molecular or bulk diffusion ( $K_n < 1$ ), Fick's first law can be used to describe diffusional flux ( $J_D$ ), which is driven by a concentration gradient ( $\Delta c/L_0$ ). The flux in porous media directly scales with diffusivity ( $D_{eff}$ ), which is an effective property of the system under consideration (see e.g. Satterfield and Sherwood [287]). More precisely,

$$\text{Eq. 29} \quad J_D = -D_{eff} \frac{\Delta c}{L_0}.$$

The effective diffusivity ( $D_{eff}$ ) of a porous medium depends on the intrinsic diffusivity ( $D_0$ ) of pure electrolyte or pure gas, respectively, and on the resistive effects from the microstructure. The transport limitations from obstacles in the microstructure are quantitatively expressed by the relative diffusivity ( $D_{rel}$ , also called microstructure factor or  $M$ -factor), which is a dimensionless characteristic, i.e.,

$$\text{Eq. 30} \quad D_{eff} = D_0 M = D_0 D_{rel}.$$

Initially, all resistive effects from the underlying microstructure were attributed to the diffusional tortuosity factor ( $D_{rel} = 1/T_{diff}$ , with  $T_{diff} = \tau_{diff}^2$ ), see [287]. Still today some authors prefer this definition of tortuosity, which can then be considered as a global transport resistance (e.g. Elwinger et al, [82]). However, it was recognized very early that diffusion depends on different microstructure effects, which are associated with path length variations as well as with pore volume variations. Hence,  $D_{rel}$  was then defined in an analogous way as the relative electrical conductivity, including porosity in addition to tortuosity (in analogy to  $\sigma_{rel}$  in Eqs. 22 and 25, see [63,84,357]), i.e.,

$$\text{Eq. 31} \quad D_{rel} = \frac{\varepsilon}{\tau_{diff}^2}.$$

This leads to the frequently used indirect diffusional tortuosity defined by

$$\text{Eq. 32} \quad \tau_{indir\_diff} = \sqrt{\frac{\varepsilon}{D_{rel}}}.$$

Note that the mathematical treatment for numerical simulation of bulk diffusion (Fick's law) and electrical conduction (Ohm's law) is identical. In both approaches the Laplace equation is solved. For completion, it is mentioned here that this analogy also applies to Fourier's law of heat conduction ( $Q_{thermal} = -\lambda_{eff} (\Delta T/L_0)$ ; with  $Q_{thermal}$  = thermal flux,  $\lambda_{eff}$  = effective heat conduction). It follows that the impact of pore structure on the effective

properties of all three processes (bulk diffusion, electric and thermal conduction) must be identical. In fact, it was reported from several experimental studies that the same values are obtained for indirect electrical and diffusional tortuosities when the same porous media was analyzed [106,183,356].

Furthermore, in a similar way as discussed previously for the indirect electrical tortuosity, also unrealistically high values for indirect diffusional tortuosity were often reported in empirical studies of diffusion. These high values must be attributed again to the fact that the bottleneck effect is not treated as a separate resistive effect. Following van Brakel and Hertjes [30] and in analogy to the electrical tortuosity, this can be improved by introducing constrictivity ( $\beta$ ) to the equation for relative diffusion, i.e.,

$$\text{Eq. 33} \quad D_{rel} = \frac{\varepsilon \beta}{\tau_{diff}^2}.$$

Nevertheless, still today the indirect diffusional tortuosity is often calculated based on Eq. 32, without considering constrictivity separately. We conclude, that diffusional tortuosity for systems with  $Kn < 1$  (bulk diffusion described with Fick's law) is in principle identical with electrical tortuosity (described by Ohmic conduction), and therefore the limiting effects of pore structures are the same (as discussed by Clennell [55]).

Furthermore, also in analogy to electrical conduction, more sophisticated tortuosity types can be determined nowadays based on numerical simulation of diffusional flux and 3D image processing. The resulting streamline- and volume averaged tortuosities ( $\tau_{mixed\_diff\_Streamline}$ ,  $\tau_{mixed\_diff\_Vav}$ ) represent more rigorous measures of the diffusive path lengths, since they do not mix with a hidden bottleneck effect, as it is usually the case for indirect tortuosity ( $\tau_{indir\_diff}$ ).

In context with diffusion, random walk methods can be used to simulate Brownian motion of particles. From the random walk simulation, a statistical measure for the displacement of moving particles (i.e. the mean square displacement, MSD) can be extracted. The MSD is proportional to the product of time and intrinsic diffusivity ( $MSD = f(D_0 t)$ ). In porous media, the particle diffusion is hindered by the obstacles of the pore wall. This limiting effect is quantitatively captured by the random walk tortuosity ( $\tau_{mixed\_diff\_Rwalk}$ ), which is defined as the ratio of MSD in free space over MSD in the porous medium.

In principle, the movements in each direction sum together and therefore, the MSD can be decomposed into the Axial Square Displacements (ASD). The axial tortuosities in x-, y-, and z-directions ( $\tau_{x/y/z\_mixed\_diff\_Rwalk}$ ) can then be calculated from the corresponding ASDs. Pytrax is a simple and efficient random walk implementation for calculating the directional tortuosity from 2D and 3D images (see Tranter et al. [334]).

### 2.3.2 Knudsen diffusion

In nanoporous materials with  $Kn \gg 1$  (i.e. in the Knudsen regime), gas diffusion is controlled by collisions with the pore walls. Numerically, this process can be simulated with the random walk method (see e.g. Babovsky, 1986 [12]). For each particle the corresponding diffusivity can be calculated from displacement length and travel time.

For simulations that are based on a large number of particles and sufficiently long travelling time these calculations result in a homogenized effective Knudsen diffusivity ( $D_{eff\_Kn}$ ). The relative Knudsen diffusivity ( $D_{rel\_Kn}$ ) is then again defined as the ratio of effective over intrinsic Knudsen diffusivity, i.e.,

$$\text{Eq. 34} \quad D_{rel\_Kn} = \frac{D_{eff\_Kn}}{D_{0\_Kn}} = \frac{\varepsilon}{\tau_{Kn}^2}.$$

Similar as the relative diffusivity in the bulk diffusion regime, also the relative Knudsen diffusivity is a dimensionless property, which describes the resistive impact of pore microstructure against transport. The corresponding indirect Knudsen tortuosity ( $\tau_{indir\_Kn}$ ) is obtained by

$$\text{Eq. 35} \quad \tau_{indir\_Kn} = \sqrt{\frac{\varepsilon}{D_{rel\_Kn}}}.$$

Note that such computed values for relative Knudsen diffusivity ( $D_{rel\_Kn}$ ) and for the indirect Knudsen tortuosity ( $\tau_{indir\_Kn}$ ) strongly depend on the intrinsic Knudsen diffusivity ( $D_{0\_Kn}$ , sometimes also called apparent diffusivity ( $D_a$ )).  $D_{0\_Kn}$  itself can be computed using characteristic length ( $L_c$ ) and thermal velocity ( $v_{th} = k_b T/m$ ), i.e.,

$$\text{Eq. 36} \quad D_{0\_Kn} = \frac{1}{3} L_c v_{th}.$$

The characteristic length ( $L_c$ ) is a rather ill defined property, which is somehow related to pore size distribution and to the average pore size, respectively. The uncertainty associated with  $L_c$  propagates into the relative Knudsen diffusivity and into the associated Knudsen tortuosity ( $\tau_{indir\_Kn}$ ), which is critically discussed by Zalc et al. [365].

Unfortunately, to the best of our knowledge, there is currently no method available for a more direct analysis of Knudsen tortuosity based on effective path lengths ( $L_{eff}/L_0$ ), as it is the case for bulk molecular diffusion, for electric conduction and also for viscous flow (see the discussion of mixed-streamline and -volume averaged tortuosities). Knudsen tortuosity is thus generally determined indirectly and therefore it is difficult to understand Knudsen tortuosity as a resistance that is related to distinct morphological features of the pore structure and to the corresponding length of transport pathways.

In literature, the interpretation of Knudsen tortuosity in context with gas diffusion in nanoporous media is highly controversial. For example, Ferguson et al. [92] used different methods (Random walk, FVM) for modeling transport at continuum scale and in the Knudsen regime, which enabled to compute both tortuosities (i.e. for bulk diffusion and for Knudsen diffusion). Also Gao et al. [103] compared different modeling approaches (Knudsen, Dusty Gas and Oscillator models) that were used to characterize diffusivity and tortuosity in nanoporous media. Gao et al. emphasizes that the resulting tortuosity is highly dependent on the definition of the characteristic pore size (i.e. characteristic length) and on other experimental parameters (chemical species, temperature, pressure). Therefore, Gao et al. [103] suggested using the coordination number (i.e. average number of vertices that are connected to the nodes) instead of the Knudsen tortuosity in order to describe the impact of nanoscale microstructure on diffusive transport. This approach leads to more stable results and the physical and

geometric interpretations of the coordination number are clearer than the indirect Knudsen tortuosity.

### 2.3.3 Limitations to the concept of diffusional tortuosity

In nanoporous materials, transport mechanisms very often consist of a superposition of several processes such as bulk molecular diffusion, Knudsen diffusion, viscous flow, adsorption and surface diffusion (see the examples in [103,124]). For such cases with a mixed transport mechanism it seems no longer possible to maintain the initial tortuosity concept as proposed by Kozeny and Carman, which is based either on the ratio of path lengths ( $L_{eff}/L_0$ ) or on the ratio of velocity components ( $\langle v_c \rangle / \langle v_x \rangle$ ), see Eq. 13. It is obvious that the indirect tortuosity, which is then usually applied also for mixed transport mechanisms, has limited value in explaining distinct (geometric) microstructure effects. Also in this case the indirect tortuosity must be rather understood as a fudge factor that describes the bulk resistive effects from microstructure, and should not be interpreted as a measure for effective path lengths.

In very fine-grained, nanoporous media the molecular radii of gas species and the thickness of the surface adsorption layer can be in a similar range as the pore radii. In this case, variations of molecular radii and thickness of adsorption layers can become equally important for effective transport as the pore size and pore structure. Tortuosity in such systems is nowadays often determined with dedicated methods of numerical modeling (e.g. molecular dynamics [124]) or experimental characterization (e.g. NMR [82]), but the link with the initial geometrical tortuosity concept (i.e. with path lengths) is often not clear, since other physical effects (e.g. adsorption) may become dominant for diffusion.

## 2.4 Direct geometric tortuosity

Geometric tortuosity includes a whole group of tortuosity types, which entirely depend on the pore morphology, and which are therefore determined directly from 3D images representing the pore microstructure. The steadily increasing importance of geometric tortuosity types is triggered by the recent progress in the fields of tomography and 3D image analysis, which is summarized in Chapter 4. Many different approaches to measure geometric path lengths and associated geometric tortuosities can be found in literature. The following section describes the most prominent examples.

It must be emphasized that geometric tortuosities do not take into account any information regarding the transport mechanisms. This is in contrast, for example, to streamline and volume averaged tortuosities, which are based on simulations of conduction, diffusion or flow. This is also in contrast to indirect tortuosities, which are extracted from effective properties that are related to specific transport mechanisms.

### 2.4.1 Skeleton and medial axis tortuosity

The medial axis tortuosity ( $\tau_{dir\_medial\_axis}$ ) can be considered as a prototype for the family of geometric tortuosities. Therefore in literature it is often just called 'geometric tortuosity' without further specification (see e.g. Stenzel et al. [312]). The computation of medial axis tortuosity is based on several rather complex image-processing steps, which are illustrated in Fig. 1: The raw data from tomography is first segmented into its

constituent phases. The example in Fig. 1a shows a fuel cell anode with the phases nickel, Gd-doped ceria and pores [136]. For each phase a medial axis skeleton (MAS, see Chapter 5 of Soille [310] for details) is then produced (Figs. 1b and 1c). The shortest pathways through the MAS network, which connect couples of inlet and outlet points, are found e.g. with the help of the Dijkstra algorithm. For propagation algorithms on graphs to determine shortest path lengths, the reader is referred to Jeulin et al. [161]. The voxel-based skeleton is then transformed into a 3D graph, *i.e.*, into a network representation consisting of vertices (nodes) and edges (branches) between them. A small portion of a 3D graph is shown in Fig. 1d. Note that further information can be attached to edges and vertices in form of additional characteristics of the local microstructure (e.g. local pore size and bottleneck size of each segment, coordinates and coordination nr of each node etc.). The analysis of the 3D graph is computationally cheap. It reveals a distribution of medial axis tortuosities for each space direction (Fig. 1e). Based on graph analysis, tortuosity information of each pathway can be combined with local pore characteristics, such as the paths orientation. The example from Keller et al. [178,179] in Fig. 1f shows a stereographic projection of pore path orientations in an anisotropic clay rock. The path orientation information is combined with the medial axis tortuosities of each path. Tortuosity values are indicated with a color code. In this example, the pathways parallel to the bedding plane (*yz*-direction) have lower medial axis tortuosities (2.7, dark blue) compared to the pathways perpendicular to the bedding plane (*x*-direction: up to 13, yellow), which of course has a strong impact on the anisotropy of the macroscopic permeability.

Reproducibility of medial axis tortuosity among different research groups may be a challenge, since there exist many different methods for skeleton extraction from 3D voxel data (see Soille [310] for a detailed description of different skeletonization algorithms). Throughout the present paper, we use the following nomenclature: If the skeleton is not a medial axis representation, then we speak of  $\tau_{dir\_skeleton}$  instead of  $\tau_{dir\_medial\_axis}$ . The procedure for generation of a medial axis skeleton (MAS) can be found e.g. in Lindquist et al. [206]. MAS generation is typically based on an iterative erosion process called topological thinning. The resulting skeleton consists of lines or curves with a thickness of one voxel. These curves are always located in the center of the pore bodies. As previously mentioned, the shortest pathways between couples of inlet and outlet points can then be algorithmically computed, e.g., by means of the Dijkstra algorithm [69]. It turns out that for complex pore structures a robust skeletonization procedure is challenging.

Efforts have been made to develop algorithms for an accelerated computation of shortest pathways. Besides the propagation algorithm in Jeulin et al. [161] mentioned above, TESAR (Tree-structure Extraction algorithm delivering Skeletons that are Accurate and Robust) was introduced by Sato et al. [284]. Thereby the distance field used in the Dijkstra algorithm is modified, such that the shortest pathways in a pore network can be found in a fast and reliable way. This algorithm thus also reveals a medial axis skeleton (MAS). It was later implemented in commercial software, such as Avizo Fire (thermofischer.com), which was used by many authors as a basis for graph analysis in order to compute medial axis tortuosity (see e.g. [60,102,136,178,179,312]; examples are shown in Fig. 1). Keller et al. [178] also presented a detailed description of the transformation steps from a voxel-based skeleton, via a 3D graph to a vector-based

list of segments and nodes (assigned with local pore characteristics, such as effective lengths, orientation, pore size and bottleneck size).

Open source software solutions for skeletonization and extraction of medial axes are available e.g. as Matlab code (Tort3D described by Al-Raoush and Madhoun [5]) or in ImageJ/Fiji (see <https://imagej.net/Skeletonize3D> and [imagej.net/AnalyzeSkeleton](https://imagej.net/AnalyzeSkeleton)).

Furthermore, Thiedemann et al. [325] also presented methodological details that can be used for an extension of medial axis tortuosity towards weighting of pathways for their fluxes. This approach is based on a detailed analysis of the 3D graph including various local structural characteristics (see also Jungnickel [168] for a general reference to graph theory). Thereby the bottleneck size, which limits the flux of a specific pathway, is used for weighting the segments and local path lengths, which in turn affects the overall statistics of effective path lengths and the associated medial axis tortuosity. The weighting with bottleneck size can be understood intuitively as an analogue of the previously discussed weighting of streamlines by flux. A similar approach was recently also described by Nemati et al. [238].

In summary, the computation of medial axis tortuosity is based on various complex image-processing steps (e.g. skeleton extraction, 3D graph analysis). Therefore, its implementation is complex and its computation may be time consuming. A major disadvantage is the fact that skeleton extraction can be done in many different ways, which may lead to different results for the same type of geometric tortuosity. Moreover, it becomes difficult to interpret the extracted skeletons as transport networks in case of high porosities. Nevertheless, based on fundamental graph theory, this approach allows combining tortuosity with other local characteristics (bottleneck size, pore path orientation, connectivity), which are important for understanding the influence of microstructure on effective transport properties.

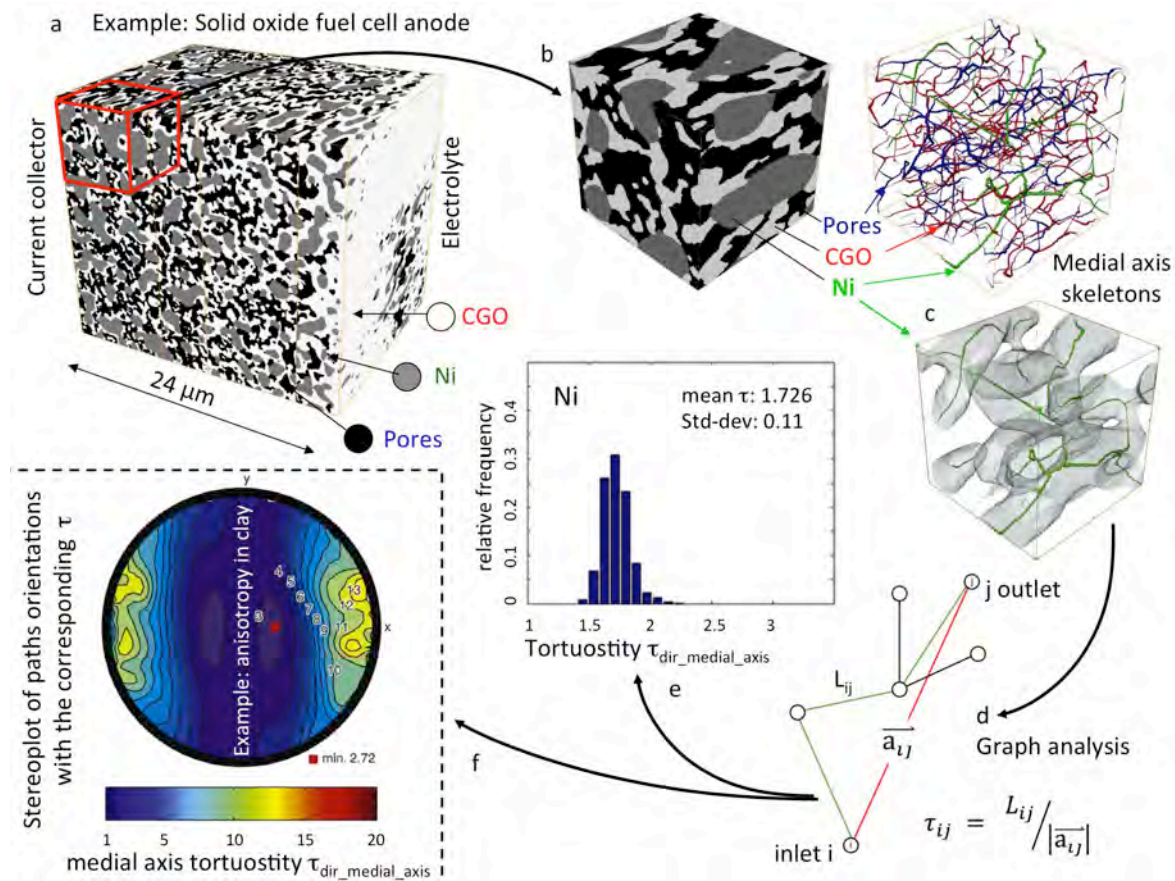


Fig. 1: Illustration of image processing steps, which are the basis for computation of medial axis tortuosity ( $\tau_{dir\_medial\_axis}$ ): a) FIB-SEM tomography and phase segmentation of a cermet anode for solid oxide fuel cells (SOFC) with pores (black), nickel (gray) and Gd-doped ceria (CGO, white) from Holzer et al. [136], b) zoom-in of a, c) medial axis skeletons (MAS) of each phase, d) schematic illustration of a graph consisting of branches/edges and nodes/vertices (e.g. used for analyzing path lengths), e) graph analysis, i.e. statistical analysis of paths lengths and associated medial axis tortuosities (mean  $\tau$ ) for the nickel phase in the main transport-direction (z) and f) stereoplot showing anisotropic distribution of tortuosities in a clay rock (d + f from Keller et al.[178,179]).

#### 2.4.2 Path tracking method (PTM) tortuosity

The path tracking method (PTM) was introduced by Sobieski et al. [307–309]. It allows for a fast computation of a geometric tortuosity that is very similar to the skeleton approach discussed in the previous section. However, the PTM algorithm is only applicable for microstructures consisting of packed spheres. It identifies tetragonal structures formed by four neighboring spheres. These tetragons represent an approximation of the interstitial pore space. The algorithm then finds the shortest pathways through the material by connecting gravity centers in the base triangles of neighboring tetragons. The resulting pathways from PTM are similar to the shortest pathways in a network skeleton. Despite this similarity, it must be emphasized that the pathways used for PTM differ in general from the medial axis representation.

In [309], a comparison of the PTM tortuosity ( $\tau_{dir\_PTM}$ ) with the hydraulic volume averaged tortuosity ( $\tau_{mixed\_hydr\_Vav}$ ) is presented, which shows almost identical results. However, whereas the geometric PTM approach is fast and easy, the hydraulic volume averaged tortuosity (based on e.g. LBM simulations) is computationally expensive and time consuming. Hence, PTM is a fast method for measuring geometric tortuosity in 3D models of packed spheres or particles.

### 2.4.3 Geodesic tortuosity

The concept of geodesic tortuosity relies on the geodesic metric in image data introduced by Lantuéjoul [200] and is used, *e.g.*, in [114,213,312] to compute the corresponding geodesic tortuosity. The geodesic tortuosity is based on a statistical analysis of shortest path lengths ( $L_{eff}$ ) from inlet- to outlet-planes divided by the sample length ( $L_0$ ). For this purpose, the shortest path lengths are defined in terms of geodesic distances within the set of those voxels that represent the transporting phase (see *e.g.* Stenzel et al [312]). Fig. 2 illustrates the difference between geodesic (red) and medial axis (green) tortuosity. For the medial axis tortuosity there is only one starting point per pore body in the inlet plane, whereas for the geodesic tortuosity all voxels of the transporting phase in the inlet plane are taken as starting points. With increasing distance the numerous pathways starting from different seed points concentrate on a few geodesic tracks. In both cases (*i.e.* geodesic and medial axis tortuosities) the shortest pathways can be calculated using the Dijkstra algorithm [69,327]. However, whereas in the case of medial axis tortuosity the shortest pathways are restricted to the centerlines, for the case of geodesic tortuosity all voxels of the transporting phase are interpreted as vertices of a graph, which are connected to their neighboring voxels (26-neighborhood). Thus, in average, the geodesic pathways are shorter than the medial axis pathways. Note that — due to discretization errors on the voxel grid — single geodesic pathways might be longer than the corresponding paths along the skeleton. In [312] the following relationship

$$\text{Eq. 37:} \quad \tau_{dir\_geodesic} = 0.76 \tau_{dir\_median\_axis}$$

has been empirically derived by linear regression, using 43 virtual microstructures generated by a specific type of a 3D stochastic microstructure model. The coefficient of determination  $R^2$  quantifying the goodness of fit for linear regression was equal to 0.81. Note that  $R^2$  is between 0 and 1, where 1 indicates a perfect fit.

A mathematical formalization of geodesic tortuosity in the framework of random sets, a key object in stochastic geometry and mathematical morphology for microstructure characterization [53,218], was recently provided by Neumann et al. [240,243], while a slightly modified version of geodesic tortuosity was presented by Barman et al. [11].

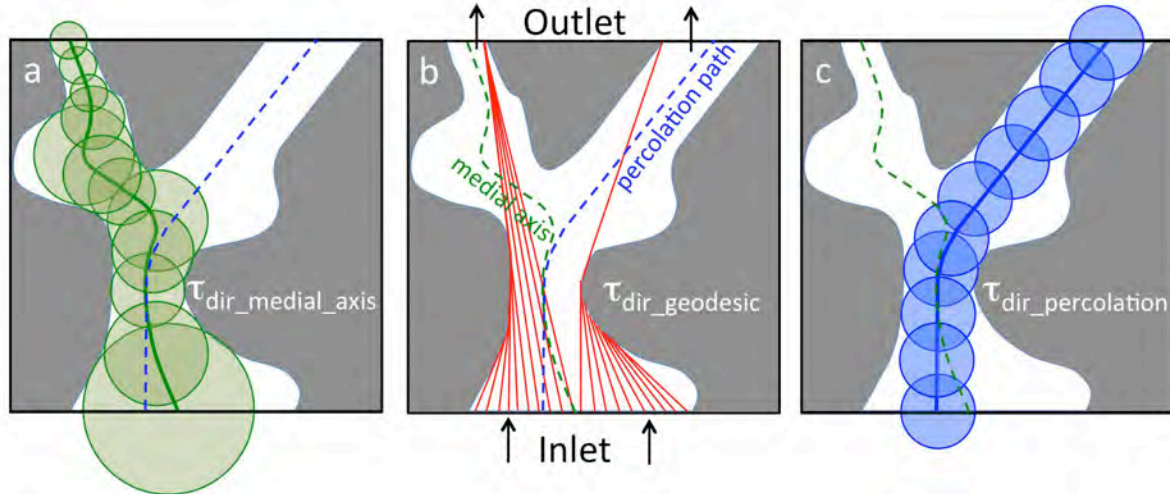


Fig. 2: Schematic illustration of geometric pore pathways used to measure path lengths for a) medial axis tortuosity, b) geodesic tortuosity and c) percolation path tortuosity. (Note: Pathways from medial axis and percolation methods are indicated as dotted lines with green and blue colors, respectively, as guides to the eye)

#### 2.4.4 Fast marching method (FMM) tortuosity

The fast marching method (FMM) tortuosity is very similar to the geodesic tortuosity, in the sense that it also considers geodesic distances within the voxel space of a given phase. The FMM algorithm is based on the simulation of a propagating front from inlet-to-outlet-plane, which is described e.g. by Vicente et al. [338]. In particular, FMM solves the following Eikonal equation (see Sethian et al. [296–299])

$$\text{Eq. 38} \quad \|\nabla T(x)\| F(x) = 1, (F(x) > 0)$$

on the voxel grid, where  $T(x)$  is the arrival time at location  $x$  and  $F(x)$  is the speed of the front. For each voxel the minimum arrival time is computed and by taking into account the speed of the front, this results in a distance map representing the shortest path lengths ( $L_{FMM}$ ). For each pixel in the outlet plane, the corresponding FMM tortuosity can be calculated by dividing  $L_{FMM}$  through the sample length ( $L_0$ ).

Jørgensen et al., 2011 [165,166] describes the FMM method in context with microstructure analysis of SOFC electrodes. Thereby, FMM is also used to extract additional (local) information of the transporting phase network, such as the distribution of interface distances, distribution of characteristic path diameters and identification of dead end pores. A further application of FMM was presented by Taiwo et al. [317] for battery electrodes. A recipe for the implementation of FMM can be found in Appendix E (supplementary info) of Hamann et al [121].

In summary, the FMM tortuosity is very similar to the geodesic tortuosity, in the sense that it also finds the shortest (geodesic) pathways within the voxel space representing the transporting phase. In addition it is computationally cheap and relatively fast.

#### 2.4.5 Percolation path tortuosity

Percolation path tortuosity is based on an algorithm that finds the pathway(s) with the least constricting bottleneck(s) (i.e. with the largest minimum bottleneck size). Hence, this algorithm allows the largest possible sphere(s) to travel from inlet- to outlet-plane and, at the same time, it finds the shortest path through the network for this sphere. Tortuosity is then defined as ratio of percolation path length over direct length ( $\tau_{dir\_percolation} = L_{percolation}/L_0$ ). This method is, for example, implemented in the GeoDict Software ([www.math2market.com](http://www.math2market.com)). Thereby it is possible not only to calculate the percolation path for a single largest sphere but also for a defined number (n) of largest spheres. Hence, it enables us to find the  $n$  least constricting pathways and it calculates the corresponding mean tortuosity.

As shown in Fig. 2c, the blue sphere (with radius corresponding to the least constricting bottleneck) can not pass through the narrow bottlenecks of the direct pathway (left) and hence it has to take a deviation (right pathway). Percolation tortuosity is thus often larger than medial axis tortuosity, which takes more direct pathways through narrow bottlenecks.

The percolation pathways capture the maximum possible opening, which can be intuitively associated with a pathway of high flux. In contrast, the pathways for medial axis and geodesic tortuosities capture their shortest pathways regardless of the bottleneck radius, and therefore medial axis and geodesic tortuosities do not represent characteristics that can be related to pathways of high flux. Considering percolation path tortuosity for varying radii reveals interesting insights on porous microstructures going beyond the information gained by geodesic tortuosity. This is demonstrated using an example of paper-based materials in [218,241].

#### 2.4.6 Pore centroid tortuosity

For the pore centroid method (see e.g. [60,166]), the 3D image volume is processed as a stack of 2D images. In each 2D section the position of the center of mass is determined for the transporting phase (e.g. pores). These centers are then tracked in transporting direction perpendicular to the 2D images, which results in one single tortuous centroid path. The centroid tortuosity is then calculated as the ratio of the effective centroid path length ( $L_{eff}$ ) over the sample thickness ( $L_0$ ). The pore centroid method is a quick and simple method, which is, e.g., implemented in the Avizo Software ([www.thermofischer.com](http://www.thermofischer.com)). For increasing volume fractions, the mass center approaches the image center and thus, pore centroid tortuosity goes to one. One can think of simple examples for microstructures with low values of centroid tortuosity, where the actual transportation paths are highly tortuous. Hence, the relevance of the centroid tortuosity in context with microstructure - property relationships is highly uncertain.

Finally, further approaches for the extraction of geometric tortuosity from 3D images can be found in literature. They are usually based on distance propagation and/or shortest path algorithms (see examples in [49,51,302]).

#### 2.5 Tortuosity types: Classification scheme and nomenclature

### Tortuosity classification scheme

Method of determination	indirect	Input: effective properties Experimental: Simulation:	indirect <b>physics-based</b> $\tau$ $\tau_{indiv\_diff} = \sqrt{\epsilon D_0 / D_{eff}}$
	mixed	 <b>mixed</b> $\tau$ <b>geometric 3D analysis</b> of volume fields from num. transport simulation ( <b>physics-based</b> )	
	direct	<b>direct geometric</b> $\tau$ 3D analysis of microstructure	Specific transport process: flow, diffusion, conduction
		<b>geometric</b> <b>mixed</b> <b>physics-based</b>	<b>Type of definition</b>

### Tortuosity nomenclature

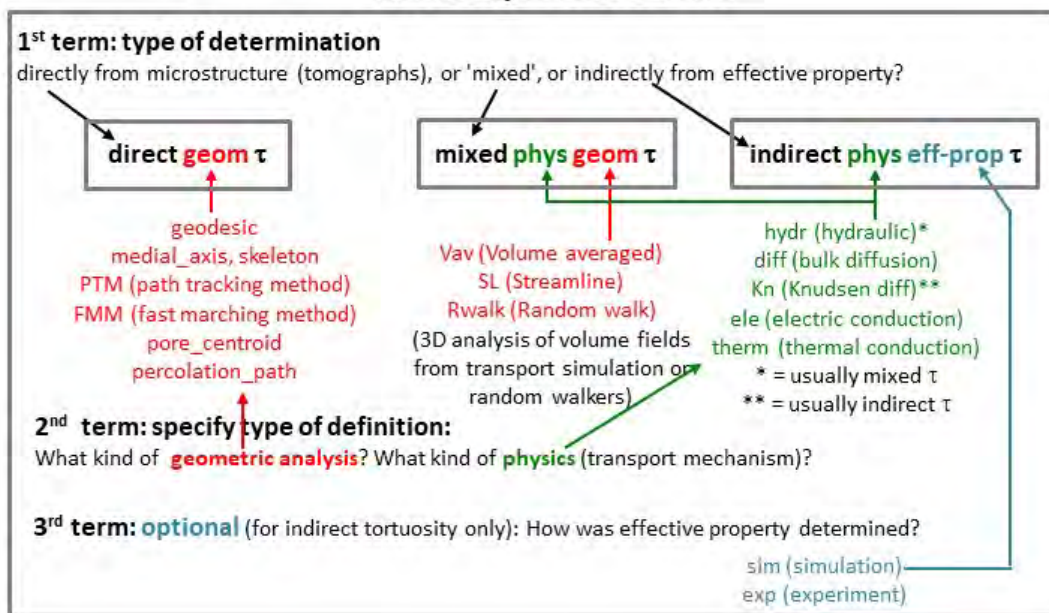


Fig. 3: Tortuosity classification scheme (top) and tortuosity nomenclature (bottom). Three main classes of tortuosity can be identified based on the method of determination: direct  $\tau$ , mixed  $\tau$  and indirect  $\tau$ . For precise tortuosity nomenclature, additional information on the type of definition (geometric, physics-based) and on the effective property characterization method (for indirect  $\tau$ ) is added in the second and third terms. The classification scheme and nomenclature should help avoiding confusion in the discussion on tortuosity.

#### 2.5.1 Classification scheme

The above-presented review reveals a multitude of different tortuosity types, which is a source of confusion in the discussion of the topic. For clarification, we propose to use a rough classification scheme and we introduce a detailed nomenclature, as shown in Fig. 3.

The classification (Fig. 3, top) is based on two main criteria: Method of determination and type of definition. The method of determination is in most cases either based on a direct geometric analysis of the microstructure using tomography and 3D image analysis (called direct  $\tau$ ). Alternatively, tortuosity can be deduced indirectly from effective transport properties (called indirect  $\tau$ ). The indirect tortuosity is also based on a certain assumption of the relationship between tortuosity and effective transport property (e.g. Eq. 32 for diffusion). The concept of definition is in most cases either based on the assumption that tortuosity and associated path lengths ( $L_{eff}$ ) are geometric properties of the microstructure (called geometric  $\tau$ ) or, alternatively, the definition emphasizes that tortuosity is a function of the transport process under investigation, such as viscous flow, diffusion or electric conduction (called physics-based  $\tau$ ).

It turns out that the method of determination and the concept of definition are generally linked with each other in a specific way, which leads to a reduction to three main categories of tortuosity. The first category consists of direct, geometric tortuosity types. The second category consists of indirect, physics-based tortuosity types. And the third category consists of mixed types, including streamline and volume averaged tortuosities (i.e.  $\tau_{mixed\_phys\_streamline}$ ,  $\tau_{mixed\_phys\_Vav}$ ). The definition of mixed types emphasizes both, the dependency on the transport process (i.e. physics-based) as well as the geometric aspect of path lengths and associated tortuosity. Characterization of mixed types is challenging, because the required information cannot be obtained directly from 3D image analysis of the microstructure. First, it requires some numerical 3D simulation to compute a transport-specific volume field of velocities or fluxes. In a second step, 3D image analysis is then used to extract the lengths of streamlines or the volume-averaged ratio of vector components from these volume fields (see Section 2.1.2c).

### 2.5.2 Nomenclature

Based on our classification scheme we introduce a new tortuosity nomenclature (Fig. 3, bottom). Thereby, three main categories of direct, mixed and indirect determination are distinguished. The nomenclature then contains additional information on the type of definition.

#### Category I: direct geometric tortuosities ( $\tau_{dir\_geom}$ )

The name includes a first term (dir), which emphasizes direct 3D analysis of the microstructure, e.g. from tomography data. The second term (geom) specifies the geometric method. The following examples of direct geometric tortuosities were discussed previously in this section:

- $\tau_{dir\_medial\_axis}$  and  $\tau_{dir\_skeleton}$
- $\tau_{dir\_PTM}$  (path tracking method)
- $\tau_{dir\_percolation}$
- $\tau_{dir\_geodesic}$
- $\tau_{dir\_FMM}$  (fast marching method)
- $\tau_{dir\_pore\_centroid}$

Note: In a recent review by Fu et al. (2020) [98] different names are used for geometric tortuosities.  $\tau_{dir\_geodesic}$  is termed 'direct shortest path searching method' (DSPSM) and  $\tau_{dir\_skeleton}$  is termed 'skeleton shortest path searching method' (SSPSM).

Category II: mixed tortuosities ( $\tau_{mixed\_phys\_streamline}$ ,  $\tau_{mixed\_phys\_Vav}$ ,  $\tau_{mixed\_diff\_Rwalk}$ )

The first term (mixed) defines the category. Mixed tortuosities are neither calculated directly from a morphological analysis of the pore structure, nor are they determined indirectly from effective properties. Typically, mixed tortuosities are obtained by a multi-step process, which starts with a specific simulation of transport, and which is then complemented with an additional postprocessing step of the simulation output. This simulation output can be, for example, a velocity field from simulation of flow, conduction or diffusion. The output can also consist of a large number of random walkers, which are obtained by simulation of diffusion.

The second term (physics-based) thus contains information about the specific transport process under consideration. This can be either viscous flow (hydr), bulk diffusion (diff), electric or thermal conduction (ele, therm). The third term then describes the geometric method, which is either based on the analysis of streamlines or volume-averaged vector components (i.e., ratio of velocity vector components) or lengths of random walkers:

- $\tau_{mixed\_hydr\_streamline}$
- $\tau_{mixed\_diff\_streamline}$
- $\tau_{mixed\_ele\_streamline}$
- $\tau_{mixed\_therm\_streamline}$
- $\tau_{mixed\_hydr\_Vav}$
- $\tau_{mixed\_diff\_Vav}$
- $\tau_{mixed\_ele\_Vav}$
- $\tau_{mixed\_therm\_Vav}$
- $\tau_{mixed\_diff\_Rwalk}$

Note: In literature, tortuosities belonging to categories II (mixed) and III (indirect) are often not distinguished and all of them are called 'flux-based' or 'physical' (see e.g. Tjaden et al. [329] and Fu et al. [98]). Usually the flux-based hydraulic tortuosities are calculated from streamlines or velocity fields (i.e. they belong to the category II: mixed tortuosities), whereas the flux-based electrical and diffusive tortuosities are typically calculated from the corresponding effective properties (i.e. they belong to category III: indirect tortuosity).

Category III: indirect physics-based tortuosities ( $\tau_{indir\_phys\_sim/exp}$ )

The first term (indirect) defines the category. The second term (physics-based) contains information about the specific transport process under consideration. The physical nature of transport is either electrical conduction (ele), thermal conduction (therm), bulk diffusion (diff), Knudsen diffusion (Kn) or hydraulic flow (hydr):

- |   |  |
|---|--|
| - $\tau_{indir\_ele \dots \_sim \text{ or } \dots \_exp}$ | $\tau_{indir\_ele} = \sqrt{(\varepsilon/\sigma_{rel})}$ or $= \sqrt{(1/\sigma_{rel})}$ or $= \sqrt{(\varepsilon\beta/\sigma_{rel})}$ |
| - $\tau_{indir\_therm}$                                   | $\tau_{indir\_therm} = \sqrt{(\varepsilon/K_{rel})}$ or $= \sqrt{(1/K_{rel})}$ or $= \sqrt{(\varepsilon\beta/K_{rel})}$              |
| - $\tau_{indir\_diff}$                                    | $\tau_{indir\_diff} = \sqrt{(\varepsilon/D_{rel})}$ or $= \sqrt{(1/D_{rel})}$ or $= \sqrt{(\varepsilon\beta/D_{rel})}$               |
| - $\tau_{indir\_Kn}$                                      | $\tau_{indir\_Kn} = \sqrt{(1/D_{Kn\_rel})}$ (see Eq. 35)   |
| - $\tau_{indir\_hydr}$                                    | $\tau_{indir\_hydr} = \sqrt{(r_h^2 \varepsilon/\kappa)}$ (see Eq. 16)  |

The value of the effective property used as input for indirect tortuosity may be different if it is determined by simulation or with an experimental approach (see e.g. the discussion of apparent tortuosity-discrepancy for Li ion batteries by Usselgio-Viretta et al. [336]).

Therefore, we recommend adding a third term that describes the nature of effective property input ('sim' for simulation or 'exp' for experimental).

It is well documented that the indirect tortuosity is dependent on the method by which the underlying effective property is determined. Examples for experimental characterization approaches are diffusion cells, tracer diffusion experiments, measurements of electrical resistance and formation factor, electrochemical experiments (EIS), flow-cell experiments for gases or liquids. It is clear that the measured transport properties may strongly depend on experimental parameters, which then also affects the indirect tortuosity. In a similar way, methodological details of transport simulation will influence the resulting effective properties and associated indirect tortuosity. These aspects can not be captured by nomenclature and should therefore be described separately.

Furthermore, values obtained for indirect tortuosity are also heavily dependent on the underlying mathematical expression, which describes the relationship between the effective property (input) and tortuosity (output). In most cases, this relation is of the same type as Eqs. 25 and 32 (e.g.  $\tau_{indir\_ele} = \sqrt{(\varepsilon/\sigma_{rel})}$ ). However, different relationships can be found in literature, either without consideration of porosity ( $\tau_{indir\_ele\_inclPore} = \sqrt{(1/\sigma_{rel})}$ ), where inclPore means that the pore volume effect is included in this indirect tortuosity calculation) or with separate consideration of constrictivity in addition to porosity (see Eq. 27:  $\tau_{indir\_ele\_exBN} = \sqrt{(\varepsilon\beta/\sigma_{rel})}$ , where exBN means that the bottleneck effect is excluded from this indirect tortuosity calculation). Hence, for electrical conduction, details of the indirect tortuosity calculation can be expressed as follows:

$$\begin{array}{ll}
 - \tau_{indir\_ele} & = \sqrt{(\varepsilon/\sigma_{rel})} & \text{(standard case: Eq. 25)} \\
 - \tau_{indir\_ele\_inclPore} & = \sqrt{(1/\sigma_{rel})} \\
 - \tau_{indir\_ele\_exBN} & = \sqrt{(\varepsilon\beta/\sigma_{rel})}
 \end{array}$$

The cases for thermal conduction and diffusion can be treated analogously. In any case, it is recommended that if the indirect tortuosity for diffusion and conduction is not derived with the standard expression (Eqs. 25 and 32) this should be emphasized explicitly and the corresponding mathematical expression should be declared. Finally, it must be emphasized that the indirect tortuosity for flow is rarely used, because it requires knowledge of the hydraulic radius (see Eq. 16).

Hence, the indirect tortuosity can be determined in many different ways, which makes comparisons difficult. To avoid confusion, 'indirect tortuosity' always calls for some detailed specifications (in addition to nomenclature) regarding a) the underlying method used to determine the effective property by experiment or simulation, and b) the underlying equation, which relates indirect tortuosity with effective property and which is used to calculate the indirect tortuosity. Without these specifications, 'indirect tortuosity' is an ill-defined characteristic.

### 3. Review of empirical data from literature: tortuosity-porosity ( $\tau$ - $\varepsilon$ )-relationships

Table 2 represents a list of data sets with tortuosity-porosity ( $\tau$ - $\varepsilon$ ) couples collected from literature. Each line in this table represents a set of data points for a specific

material type, which is characterized with a specific tortuosity type. More than 2200 data points were collected semi-automatically from literature (using the webplotdigitizer [276]) in order to investigate specific  $\tau$ - $\varepsilon$  patterns for certain types of materials and microstructures.

$\tau$ - $\varepsilon$  relationships are collected for 7 types of porous materials:

- a) Solid oxide fuel cell (SOFC) electrodes and sintered ceramics,
- b) Gas diffusion layers (GDL) of polymer electrolyte membrane fuel cells (PEM-FC) and other fibrous materials (e.g. paper),
- c) Battery electrodes, mostly from Li-ion batteries (LIB),
- d) Geological materials (sandstones, clays, soils),
- e) 2D-models of granular materials (packed circles, ellipses, squares or rectangles)
- f) 3D-models of granular materials (packed spheres and ellipsoids, mono-sized and poly-dispersed), and experimental model materials (e.g. glass beads)
- g) 3D models of networked pore structures (from stochastic simulation) and foams.

In our comparison of empirical data, we also consider the used tortuosity types as a criterion for discrimination. The data is thus also used to compare the different tortuosity types according to our classification scheme (see Fig. 3) with the main categories: I) direct geometric  $\tau$ , II) mixed  $\tau$  and III) indirect physics-based  $\tau$ .

Table 2

List with empirical tortuosity-porosity ( $\tau$ - $\varepsilon$ )-data from literature

Table 2 is based on 2204 tortuosity-porosity ( $\tau$ - $\varepsilon$ ) data points, which are collected from 69 references in the literature. The corresponding source file for table 2, which contains additional detailed information, can be downloaded from the electronic appendix ('Appendix\_electronic\_1-Table\_2.xls'). It must be emphasized that 'porosity' in this table always means the effective porosity, where this information is available. The effective porosity represents the fraction of pore space, which forms a contiguous network and which excludes trapped pores. In subsequent figures derived from this table the effective porosity is plotted (not total porosity).

**SOFC electrodes and porous ceramics** (e.g. separation membrane for SOEC, ceramic catalyst support etc.)

Legend: Nr of dataset) Reference [Ref Nr],  $\tau$  type, ( $\tau$  method) material

- 1) Grew et al. [117],  $\tau_{indir\_diff}$ , (from sim with Laplace solver, Fick's diff) Ni-YSZ anode
- 2) Grew et al. [119],  $\tau_{indir\_diff}$ , (from sim with Laplace solver, Fick's diff) Ni-YSZ anode
- 3) Iwai et al. [156],  $\tau_{indir\_diff}$ , (from sim with random walk, bulk diff) Ni-YSZ anode
- 4) Kishimoto et al. [181],  $\tau_{indir\_diff}$ , (from sim with LBM, bulk diff) Ni-YSZ anode
- 5) Cooper et al. [61],  $\tau_{indir\_diff}$ , (sim with CFD-FVM, Avizo, random walk, 'StarCCM+') LSCF
- 6) Cooper et al. [59], comparison of various  $\tau$ -types specified below, LSCF cathode
- 6a)  $\tau_{dir\_pore\_centroid}$ , (image analysis / Avizo Fire, voxel based)
- 6b)  $\tau_{dir\_diff\_sim}$ , (simulation of thermal cond., 'StarCCM+' / Laplace s., Fourier's law, mesh based)
- 6c)  $\tau_{dir\_diff\_sim}$ , (sim. of bulk diffusion, 'AvizoXlab' / Laplace solver, Fick's law, voxel based)
- 6d)  $\tau_{dir\_diff\_sim}$ , (sim. of bulk diffusion, 'TauFactor' / Laplace solver, Fick's law, voxel based)
- 6e)  $\tau_{dir\_diff\_sim}$ , (simulation of bulk diffusion, (in-house) / random walk, voxel based)
- 7) Wilson et al. [352],  $\tau_{indir\_diff}$ , (from simulation with Laplace solver, Fick's diff) Ni-YSZ anode
- 8) Tjaden et al. [331], comparison of tortuosity types, porous YSZ support layer:
- 8a)  $\tau_{dir\_FMM}$ , (image analysis / in-house (Matlab) / FIB-SEM)

- 8b)  $\tau_{dir\_FMM}$ , (image analysis / in-house (Matlab) / X-ray nano CT)
- 8c)  $\tau_{indir\_therm}$ , (sim. of thermal cond., 'StarCCM+' / Laplace, Fourier, mesh based / FIB-SEM)
- 8d)  $\tau_{indir\_therm}$ , (sim. of thermal cond., 'StarCCM+' / Laplace, Fourier, mesh based / XnCT)
- 8e)  $\tau_{indir\_diff}$ , (diffusion cell experiment / Gas diffusion at 30°C and 100°C / Fick's law)
- 9) Joos et al. [164],  $\tau_{indir\_diff}$ , (from simulation with Laplace solver) LSCF cathode
- 10) Laurencin et al. [202],  $\tau_{indir\_diff}$ , (from sim with Laplace solver) Ni-YSZ anode
- 11) Holzer et al. [136],  $\tau_{dir\_median\_axis}$ , (Avizo skeletonization / Matlab) Ni-YSZ anode
- 12a) Pecho et al. [255],  $\tau_{dir\_geodesic}$ , (Image analysis, in-house) Ni-YSZ anode
- 12b) Pecho et al. [255], supplementary material
- 13) Holzer et al. [142],  $\tau_{dir\_geodesic}$ , (Image analysis, in-house) Ni-YSZ anode
- 14a) Wiedenmann et al. [349],  $\tau_{dir\_median\_axis}$ , (Avizo / Matlab) sintered mineral Olivine / Wollast.
- 14b) Wiedenmann et al. [349],  $\tau_{indir\_ele\_exp}$ , (from experiment with EIS cell) Olivine / Wollastonite
- 15) Zheng et al. [374],  $\tau_{indir\_diff}$ , (from sim with Laplace solver) stochastic model for anode
- 16) Lichtner et al. [205],  $\tau_{indir\_diff}$ , (from sim with Laplace solver, GeoDict) LSM-YSZ cathode
- 17) Almar et al. [7],  $\tau_{indir\_diff}$ , (from sim with Laplace solver) LSCF and BSCF cathodes
- 18) Endler et al. [83],  $\tau_{indir\_diff}$ , (from sim with Laplace solver) LSCF cathode
- 19) Holzer et al. [141], 2 tortuosity types, porous Zr-oxide used as Diaphragm in pH sensor:
- 19a)  $\tau_{dir\_geodesic}$ , (image analysis / in-house)
- 19b)  $\tau_{indir\_ele}$ , (simulation of electrical conduction, GeoDict / Laplace solver / Ohm's law)
- 20) Haj et al. [120],  $\tau_{dir\_geodesic}$ , (Image analysis, in-house) sintered Ni
- 21a) Kishimoto et al. [182],  $\tau_{indir\_diff}$ , (Laplace solver, Fick's diff) pores in CGO anode
- 21b) Kishimoto et al. [182],  $\tau_{indir\_ele}$ , (Laplace solver, Ohm's law) solid phase in CGO anode
- 22a) Shanti et al. [300],  $\tau_{indir\_diff}$ , (from sim with Laplace solver, gas diff), sintered alumina
- 22b) Shanti et al. [300],  $\tau_{dir\_skeleton}$ , (Amira skeletonization / shortest path analysis), alumina

### PEM FC (GDL) and fibrous materials

Legend: Nr of dataset) Reference [Ref Nr],  $\tau$  type, ( $\tau$  method) material

- 23) Yu et al. [363],  $\tau_{indir\_diff\_exp}$ , (from diffusion experiment) Pt electrode
- 24) Sarkar and Bhattacharyya [283],  $\tau_{mixed\_hydr\_Vav}$ , (from LBM-sim, Navier-Stokes) GDL through-plane dir.
- 25a) Garcia-Salaberry et al. [105],  $\tau_{indir\_diff}$ , (from LBM-sim) GDL through-plane, var. thicknesses
- 25b) Garcia-Salaberry et al. [105],  $\tau_{indir\_diff}$ , (from LBM-sim) GDL in-plane, various thicknesses
- 26) Froning et al. [97],  $\tau_{mixed\_hydr\_Vav}$ , (from LBM-sim, NS gas flow) GDL in-plane direction
- 27a) Flückiger et al. [94],  $\tau_{indir\_diff\_exp}$ , (from experiment) GDL dry, no Filler
- 27b) Flückiger et al. [94],  $\tau_{indir\_diff\_exp}$ , (from experiment) GDL dry, with Filler
- 28) Froning, et al. [96],  $\tau_{mixed\_hydr\_Vav}$ , (from LBM, NS) PEM GDL real/virtual, w/o Filler
- 29) Holzer et al. [140], 2 tortuosity types, PEM GDL dry IP and TP, compression series:
- 29a)  $\tau_{dir\_geodesic}$ , (image analysis, in-house) var. thickness from in-situ  $\mu$ -CT compression exp.
- 29b)  $\tau_{indir\_ele}$ , (simulation of electrical conduction, GeoDict / Laplace solver / Ohm's law)
- 30) Holzer et al. [139], 2 tortuosity types, PEM GDL wet IP and TP,  $\mu$ -CT imbibition exp.:
- 30a)  $\tau_{dir\_geodesic}$ , (image analysis / in-house, from dynamic XCT-imbibition experiment)
- 30b)  $\tau_{indir\_ele}$ , (simulation of electrical conduction, GeoDict / Laplace solver / Ohm's law)
- 31) Huang et al. [148],  $\tau_{dir\_FMM}$ , (from image analysis) fibrous cloths

### Battery electrodes

Legend: Nr of dataset) Reference [Ref Nr],  $\tau$  type, ( $\tau$  method) material

- 32) Cooper et al. [60], LI-Battery (LiFePO<sub>4</sub>)
- 32a)  $\tau_{dir\_pore\_centroid}$ , (image analysis / Avizo Fire, voxel based)
- 32b)  $\tau_{indir\_therm}$ , (sim. of thermal cond., 'StarCCM+' / Laplace solver Fourier's law, mesh based)
- 33) Tariq et al. [323],  $\tau_{indir\_diff}$ , (Star-CCM+, CD adapco, FVM) LIB (graphite)
- 34) Shearing et al. [301],  $\tau_{indir\_diff}$ , (Star-CCM+, CD adapco, FVM) LIB (LMO)
- 35) Taiwo et al. [317],  $\tau_{dir\_FMM}$ , (image analysis, in-house SW) LIB (LCO, LMO, graphite)

- 36) Almar et al. [6],  $\tau_{indir\_diff}$ , (GeoDict, Laplace solver) LIB  
 37) Shearing et al. [302],  $\tau_{indir\_diff}$ , (TauFactor, Laplace solver) LIB (graphite)  
 38) Hutzenlaub et al. [151],  $\tau_{indir\_diff}$ , (GeoDict, Laplace solver) LIB  
 39) Ebner et al. [76],  $\tau_{indir\_diff}$ , (BruggemannEstimator, Laplace) LIB (LCO, LMO, graphite)  
 40) Hamann et al. [121],  $\tau_{dir\_FMM}$ , (image analysis, Mablabs, Fiji) LLCZN garnet electrolyte  
 41) Landesfeind et al. [196],  $\tau_{indir\_ele\_exp}$ , (EIS experiment) LIB (3-6% binder)  
 42a) Landesfeind et al. [195],  $\tau_{indir\_ele\_exp}$ , (EIS experiment) LIB (NMC, NCA, graphite)  
 42b) Landesfeind et al. [195],  $\tau_{indir\_ele}$ , (Laplace solver, in-house) LIB (NMC, NCA, graphite)  
 43) various authors, cit in Landesfeind et al. [197],  $\tau_{indir\_ele}$ , LIB

### Earth Science + Geo-engineering (rocks: sandstones, clays / soils / mortar)

Legend: Nr of dataset) Reference [Ref Nr],  $\tau$  type, ( $\tau$  method) material

- 44) Berg [20],  $\tau_{dir\_skeleton}$  (flux-weighted, e-Core network model) Fontainebleau sandstone  
 45) Provis et al. [270],  $\tau_{indir\_diff}$ , (Random walk sim., in-house ) Alkali activated fly ash mortar  
 46a) Klinkenberg [183], cited in 47) Ziarani [376]  $\tau_{indir\_ele}$ , (sim. Laplace solver) soil  
 46b) Klinkenberg [183],[376]  $\tau_{indir\_ele}$ , (Laplace) unconsolidated sand and glass beads  
 46c) Klinkenberg [183],[376]  $\tau_{indir\_ele}$ , (Laplace) sandstones and limestones  
 48) Keller et al. [178],  $\tau_{dir\_median\_axis}$ , (Avizo skeletonization/Matlab) Opalinus Clay  
 49) Berg [21],  $\tau_{dir\_skeleton}$  (flux-wieghted, e-Core network model) Bentheimer sandstone  
 50) Keller et al. [158],  $\tau_{dir\_median\_axis}$ , (Avizo skeletonization/Matlab) Opalinus Clay  
 51) various authors cited in Kristensen et al. [191],  $\tau_{indir\_diff\_exp}$ , (experiments) soils  
 52) Boving et al. (cited in 51) [191],  $\tau_{indir\_diff\_exp}$ , (tracer diffusion experiments) soils  
 53) Nemati [238],  $\tau_{dir\_skeleton}$  (flux-weighted, Pore network model) Berea sandstone

### Granular porous media I: 2D models (circles, ellipsoids, squares, rectangles)

Legend: Nr of dataset) Reference [Ref Nr],  $\tau$  type, ( $\tau$  method) material

- 54a) Saomoto and Katagiri [281],  $\tau_{mixed\_hydr\_Streamline}$ , (Comsol NS+image analysis) 2D monosized  
 54b) Saomoto and Katagiri [281],  $\tau_{mixed\_ele\_Streamline}$ , (Comsol Laplace+image analysis) 2D monosized  
 55) Saomoto et al. [282], mixed tortuosity types, monosized 2D ellipsoids, aspect ratios 1- 5  
 55a)  $\tau_{mixed\_hydr\_Streamline}$ , (sim. of flow with Comsol/Image Analysis (IA) of 2D velocity field)  
 55b)  $\tau_{mixed\_ele\_Streamline}$ , (simulation of el. conduction with Comsol / IA of 2D velocity field)  
 55c)  $\tau_{mixed\_hydr\_Vav}$ , (simulation of flow with Comsol / IA of 2D velocity field)  
 55d)  $\tau_{mixed\_ele\_Vav}$ , (simulation of el. conduction with Comsol / IA of 2D velocity field)  
 56) Nabovati et al. [235],  $\tau_{mixed\_hydr\_Vav}$ , (LBM, Navier Stokes) 2D squares and rectangles  
 57) Ghassemi and Pak [110],  $\tau_{mixed\_diff\_Vav}$ , (LBM) 2D spheres polydispersed

### Granular porous media II: 3D models (packed spheres, ellipsoids, sands) and model materials (glass beads, sand)

Legend: Nr of dataset) Reference [Ref Nr],  $\tau$  type, ( $\tau$  method) material

- 39) Ebner et al. [76],  $\tau_{indir\_diff}$ , (BruggemannEstim/Laplace) Battery sphere packing model  
 58) Gommès et al. [114],  $\tau_{dir\_geodesic}$ , (Matlab, in-house) Battery Poisson sphere model  
 59) Chung et al. [54],  $\tau_{indir\_diff}$ , (Batt3D/Laplace) Battery models packed beds with ESyS  
 60) Sobieski [307],  $\tau_{dir\_PTM}$  (in-house, virtual 3D with DEM) polydispersed sphere packing  
 61a) Sheikh and Pak [303],  $\tau_{mixed\_diff\_Vav}$  (LBM C++, IA) 3D polydispersed sphere packing  
 61b) Sheikh and Pak [303],  $\tau_{indir\_diff}$  (LBM C++) polydispersed sphere packing with DEM  
 62) Pawlowski et al. [253],  $\tau_{mixed\_hydr\_SL}$  (OpenF./VGSMAX/ImageVis3D) chromatography  
 63) Al-Roush and Madhoun [5],  $\tau_{dir\_median\_axis}$  (Tort3D/Matlab) Silica Sand polydisperse  
 64a) Hormann et al. [145],  $\tau_{dir\_geodesic}$  (Fiji, in-house), Silica monoliths/chromatography  
 64b) Hormann et al. [145],  $\tau_{dir\_median\_axis}$  (Fiji, skeletonize3D/analyzeSkeleton) Silica monoliths  
 46) Klinkenberg [183], in Ziarani [303,376],  $\tau_{indir\_ele\_exp}$ , unconsolidated sand

65) Johnson et al. [163],  $\tau_{indir\_diff}$  (TauFactor) packed agar/cellulose for chromatography

### Models of networked structures with continuous phases (stochastic model) and foams

Legend: Nr of dataset) Reference [Ref Nr],  $\tau$  type, ( $\tau$  method) material

66a) Stenzel et al. [312],  $\tau_{dir\_geodesic}$  (in-house) SSGM stochastic spatial graph model

66b) Stenzel et al. [312],  $\tau_{indir\_ele}$  (GeoDict, Laplace solver) SSGM graph model, continuous phase

67) Gaiselmann et al. [102],  $\tau_{dir\_median\_axis}$ , (Avizo skel/Matlab) SSGM graph model

68) Knackstedt et al. [184],  $\tau_{dir\_diff}$  (Laplace, bulk diffusion) PU open cell foams

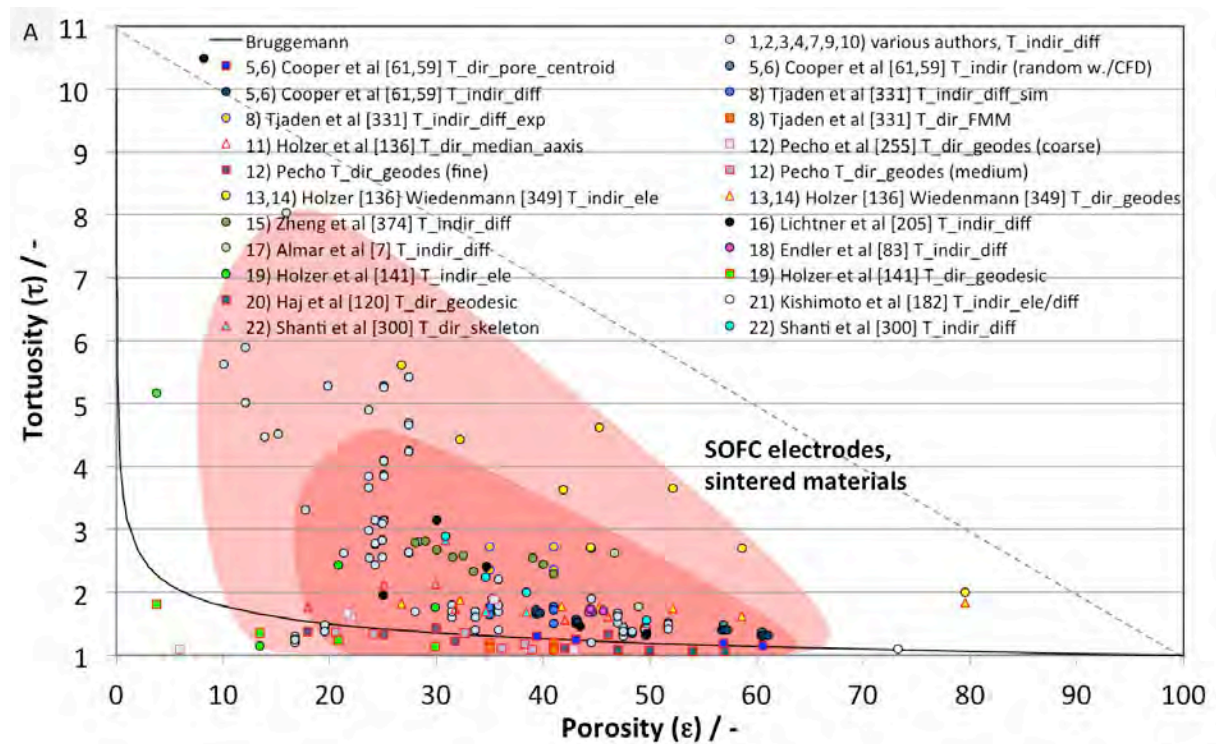
69) Vicente et al. [338],  $\tau_{dir\_FMM}$  (in-house image analysis) Metal open cell foams

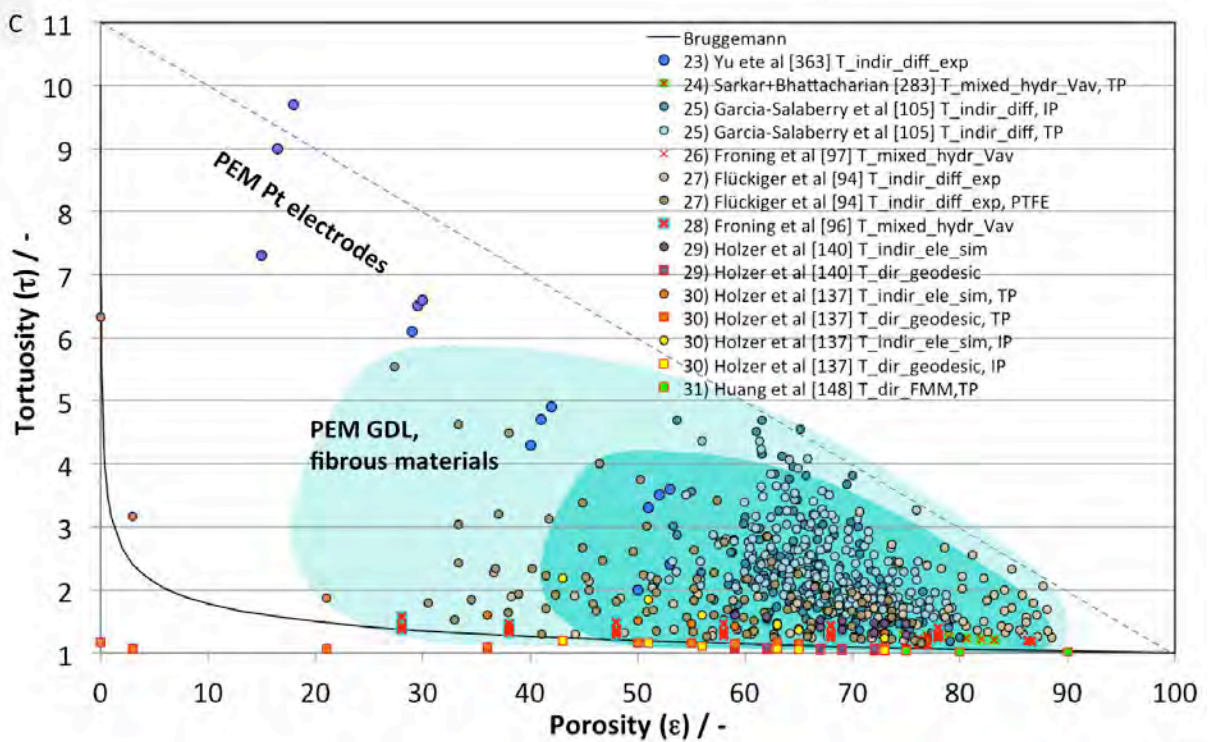
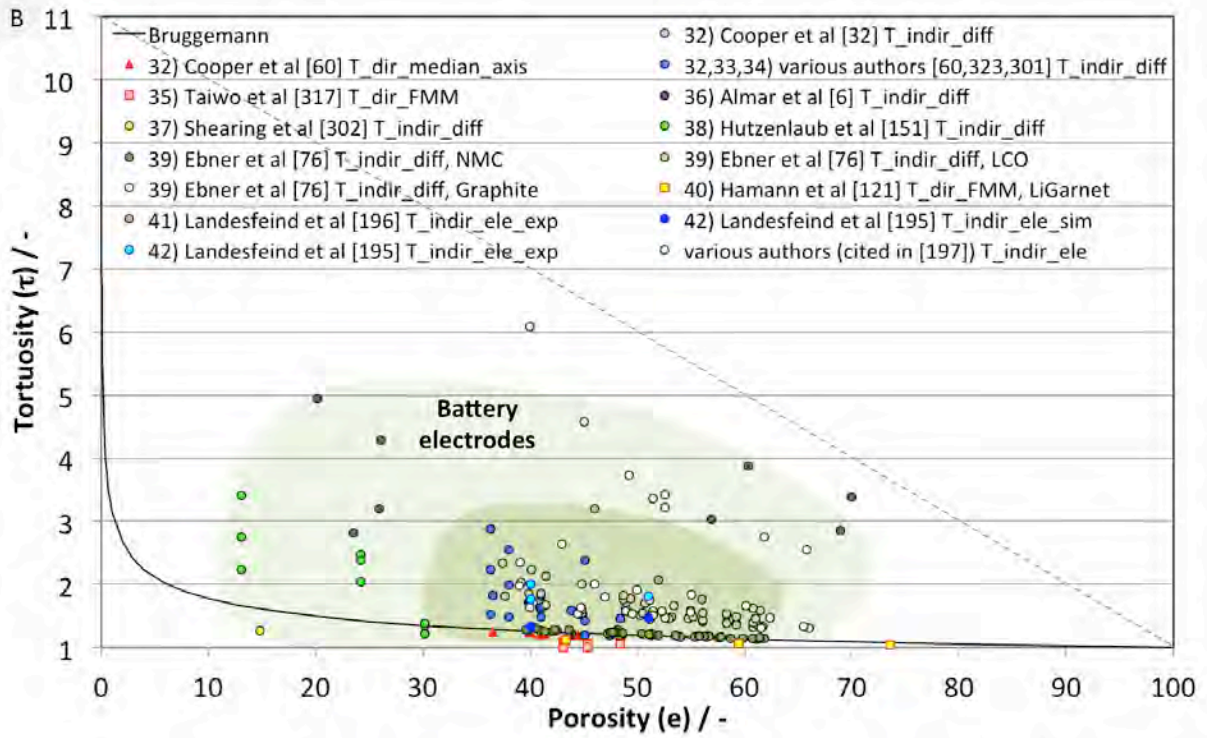
22a) Shanti et al. [300],  $\tau_{dir\_median\_axis}$  (Image analysis) Alumina packed spheres polydispersed

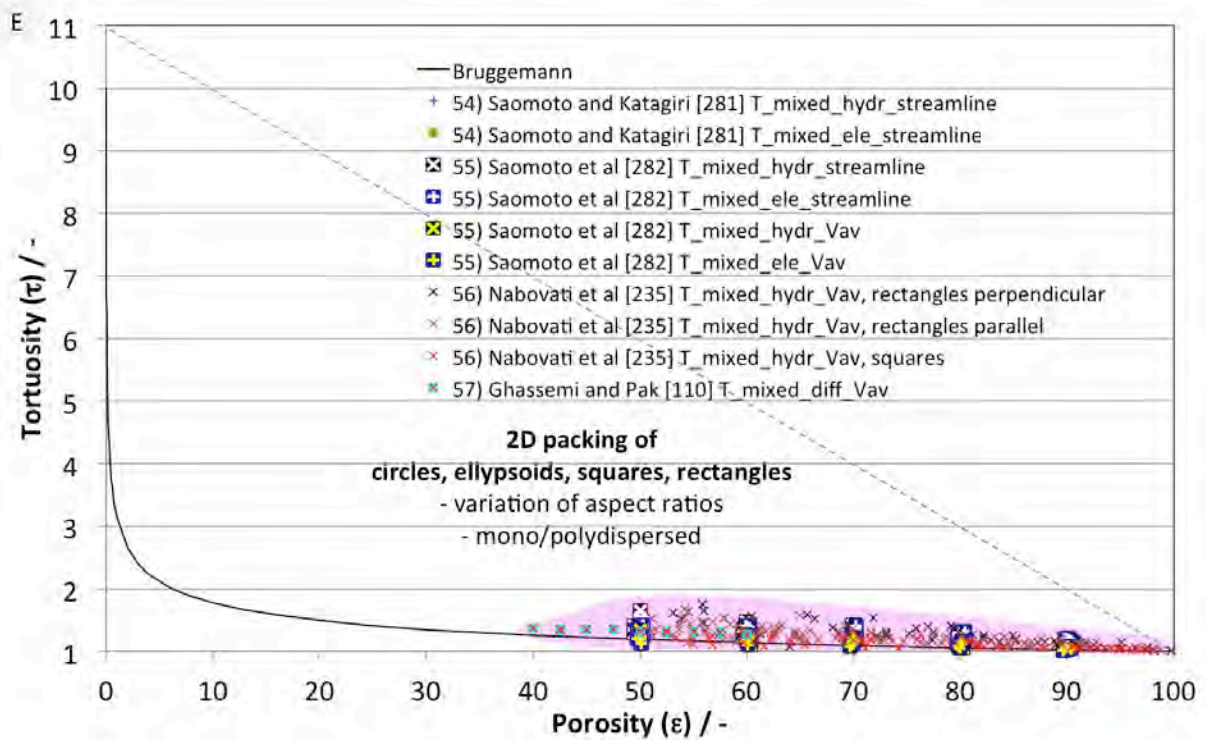
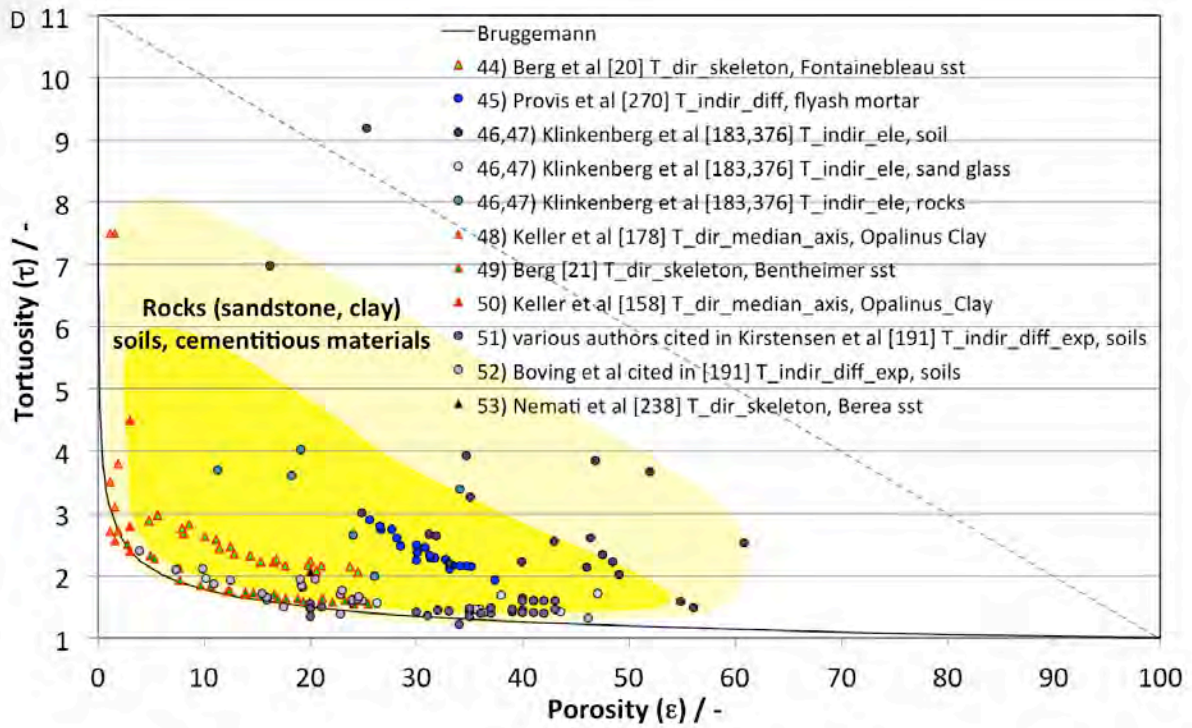
22b) Shanti et al. [300],  $\tau_{indir\_diff}$  (Laplace, bulk diffusion) Alumina packed spheres polydispersed

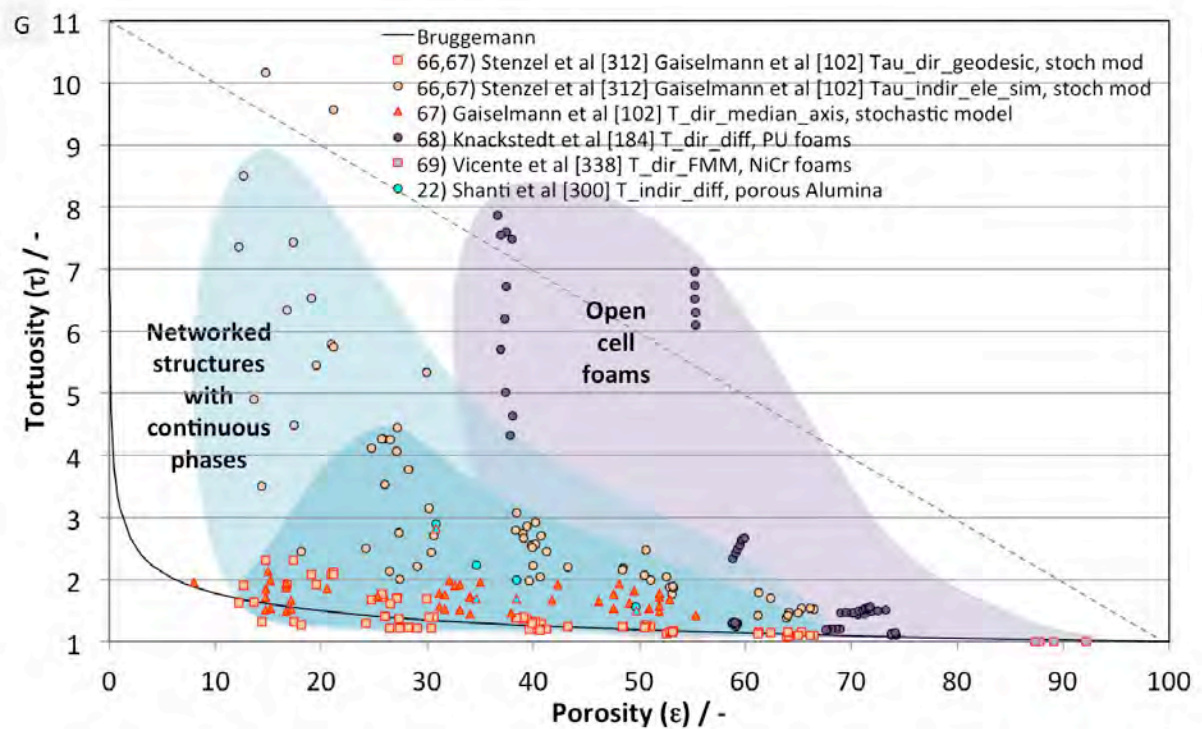
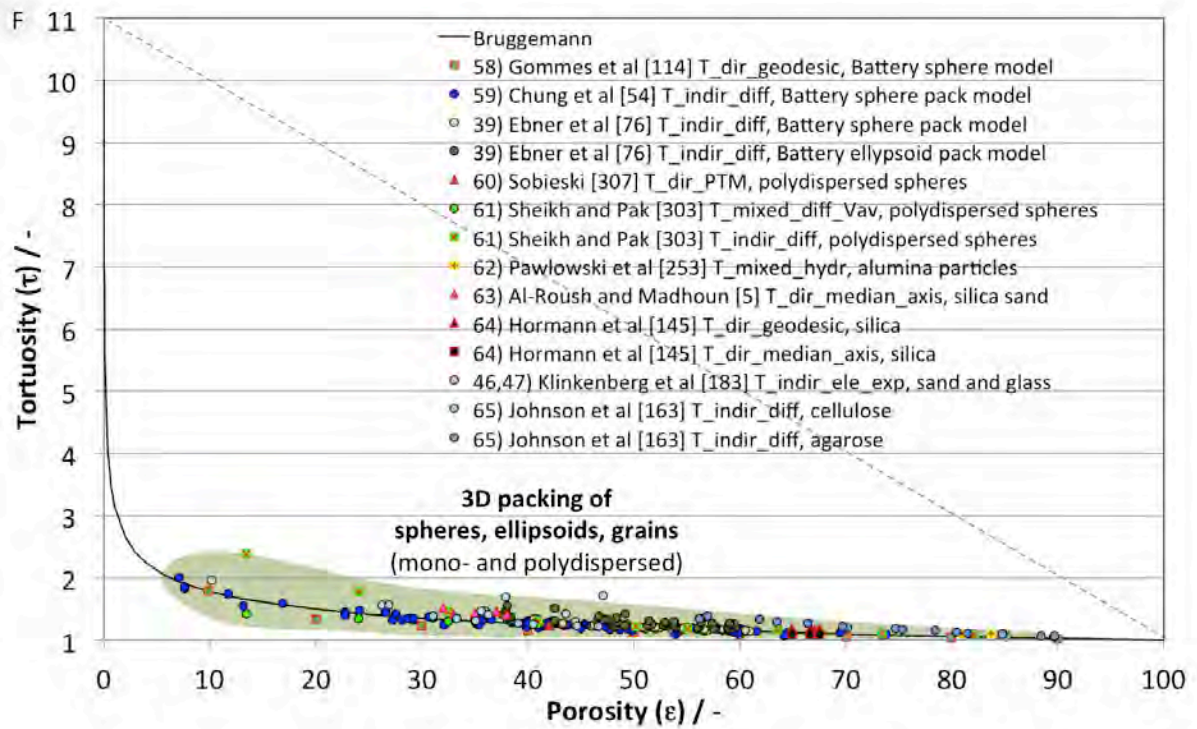
### 3.1 Empirical data for different materials and microstructure types

The empirical data cover a large variety of materials with a wide range of porosities and with different complexities of the microstructures. It includes for example simple structures consisting of mono-sized spheres, but also more complex structures of packed fibers, foams and composite materials (e.g. SOFC electrodes). When plotting empirical tortuosity-porosity ( $\tau$ - $\epsilon$ ) data for specific material types, this usually results in a relatively large scatter, so that no specific  $\tau$ - $\epsilon$  relationship can be attributed to the specific material types. This finding indicates that even within a single material type the structural variety is large. Nevertheless, as shown in Fig. 4A-H, for each material type a characteristic field (i.e. a more or less dense cloud of data points) can be observed in the  $\tau$ - $\epsilon$  plots.









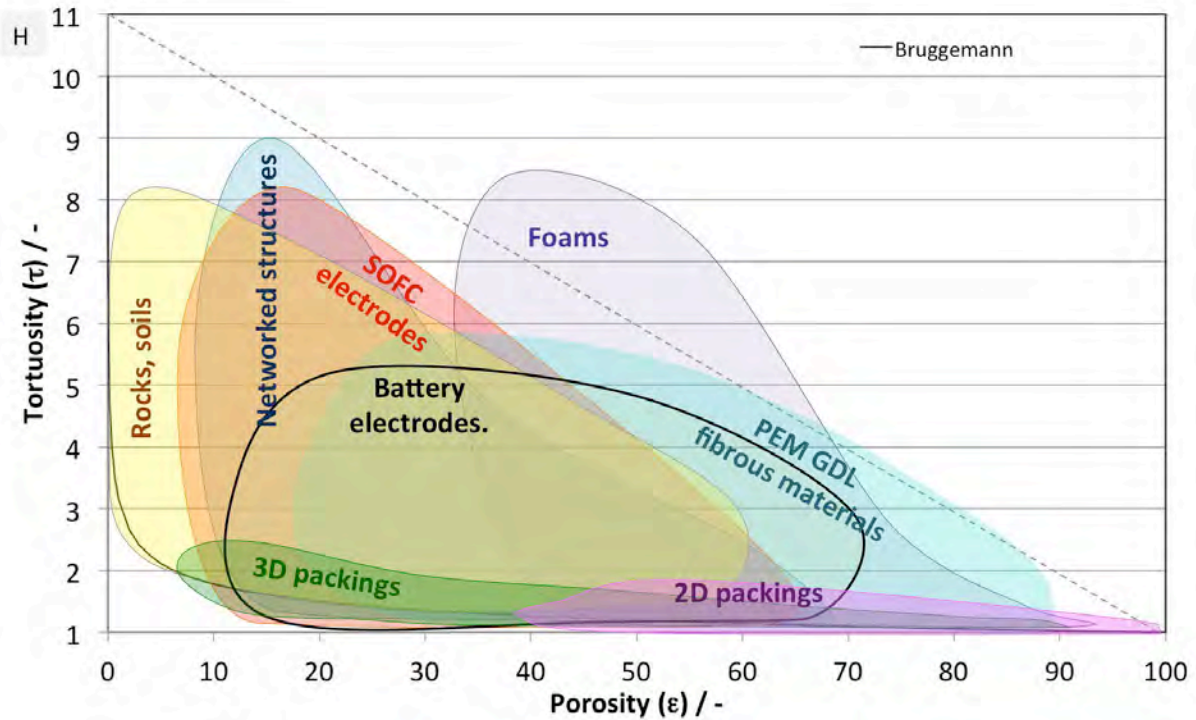


Fig. 4: Plots of tortuosity vs. effective porosity for different materials and microstructures, as presented in Table 2. For each material a characteristic fields is indicated with a specific color. Fig. 4H gives an overview of characteristic fields for all different material types. The underlying source file with detailed information from 69 references can be downloaded from the electronic appendix ('Appendix\_electronic\_1-Table\_2.xls').

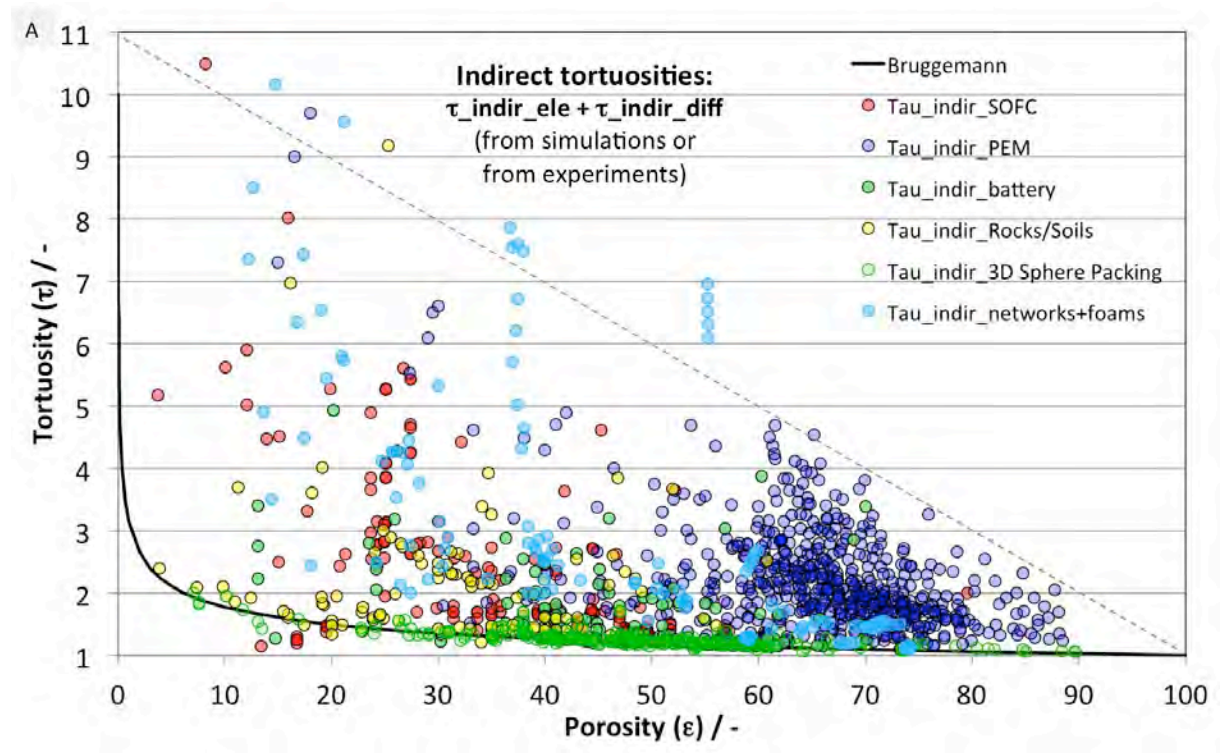
Fig. 4H illustrates that the characteristic fields of the different material types tend to have a strong overlap. Hence, it seems that  $\tau$ - $\epsilon$  relationships are not really suitable to capture the strong differences between the involved types of materials and structures. Nevertheless, for simple microstructures, such as packed spheres and ellipsoids, the scatter of characteristic fields is relatively small (see Figs. 4E and 4F). For these rather simple microstructures, the corresponding data points are located in a narrow band close to and often slightly above the Bruggemann trend line (i.e.  $T = \tau^2 = 1/\epsilon^{0.5}$ ). It must be emphasized that the plots in Fig. 4 do not distinguish between different types of tortuosity, which may be one reason for the observed scatter of  $\tau$ - $\epsilon$  datapoints.

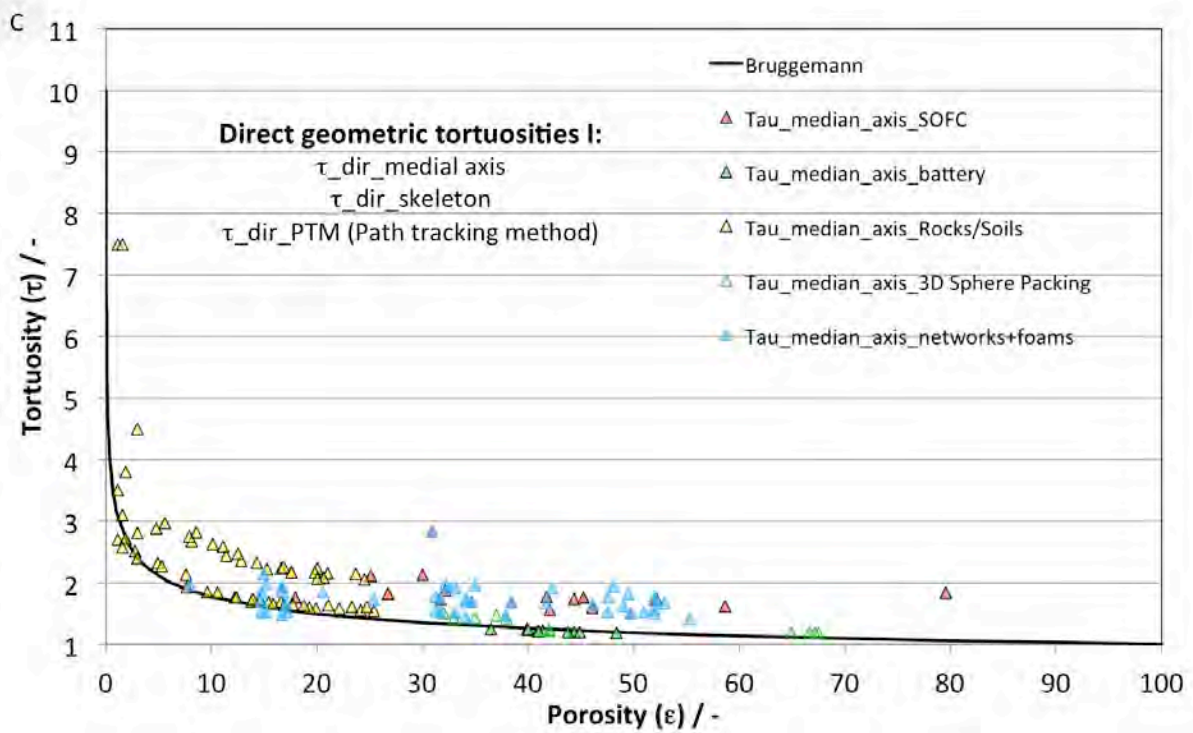
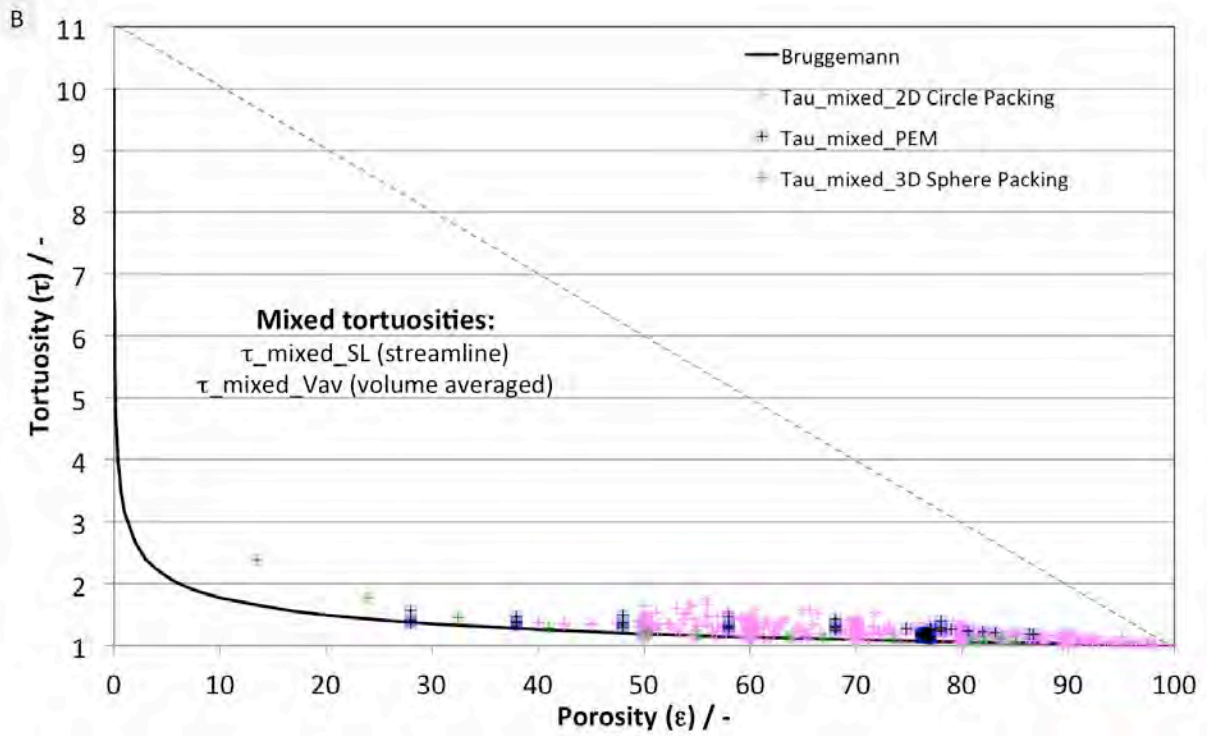
### 3.2 Empirical data for different tortuosity types

The same empirical data from Table 2 can be plotted separately for each tortuosity type (instead of each materials type). The results in Fig. 5 illustrate that the indirect tortuosities (Fig. 5A) scatter over a much larger range than the mixed (Fig. 5B) and geometric (Fig. 5C, D) tortuosity types. In Fig. 5E geometric and mixed tortuosities are plotted together (but with a different scale on the y-axis compared to Fig. 5A-D). The characteristic field in red, representing geodesic and FMM tortuosities, shows the lowest values. Geodesic and FMM tortuosities are often slightly below the Bruggemann trend line and only rarely they take values larger than 2. In contrast, the Bruggemann trend line typically defines the lower bound for mixed tortuosities (green characteristic field) and for those geometric tortuosities, which are derived from a skeleton (medial axis and

PTM, blue characteristic field). For porosities below 0.3 the medial axis/PTM tortuosities often also reach values greater than 2. It must be mentioned here that for mixed tortuosities, the empirical data at low porosities is missing, but it is expected that the values increase with decreasing porosity, also for the mixed tortuosity types.

The empirical results indicate that the large scatter observed for most materials and microstructure types can be mainly attributed to data points containing indirect tortuosity types. A surprising insight is the fact that the different tortuosity types give a more characteristic pattern than the different material types. The latter are discussed in the previous section. This indicates that in general the value of tortuosity is more strongly influenced by the type of tortuosity than by the type of material or microstructure. This finding strongly emphasizes the necessity of clearly defining (and choosing carefully) the type of tortuosity, which is used for the characterization of porous media.





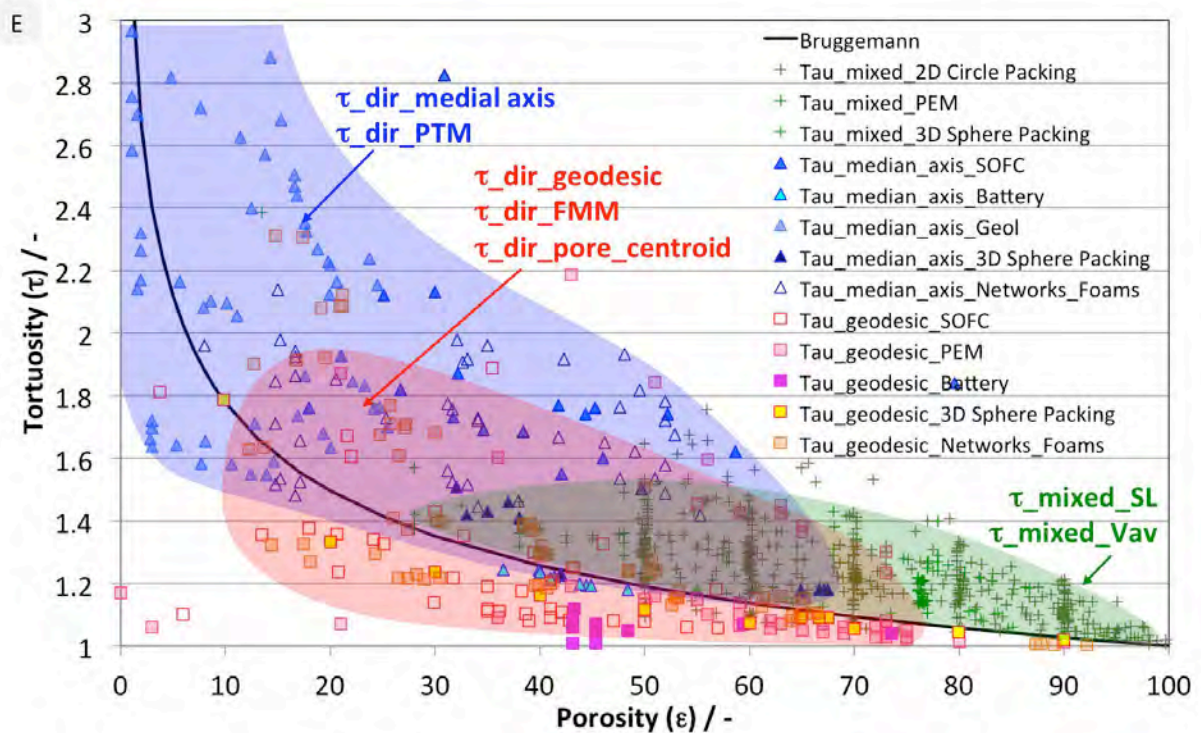
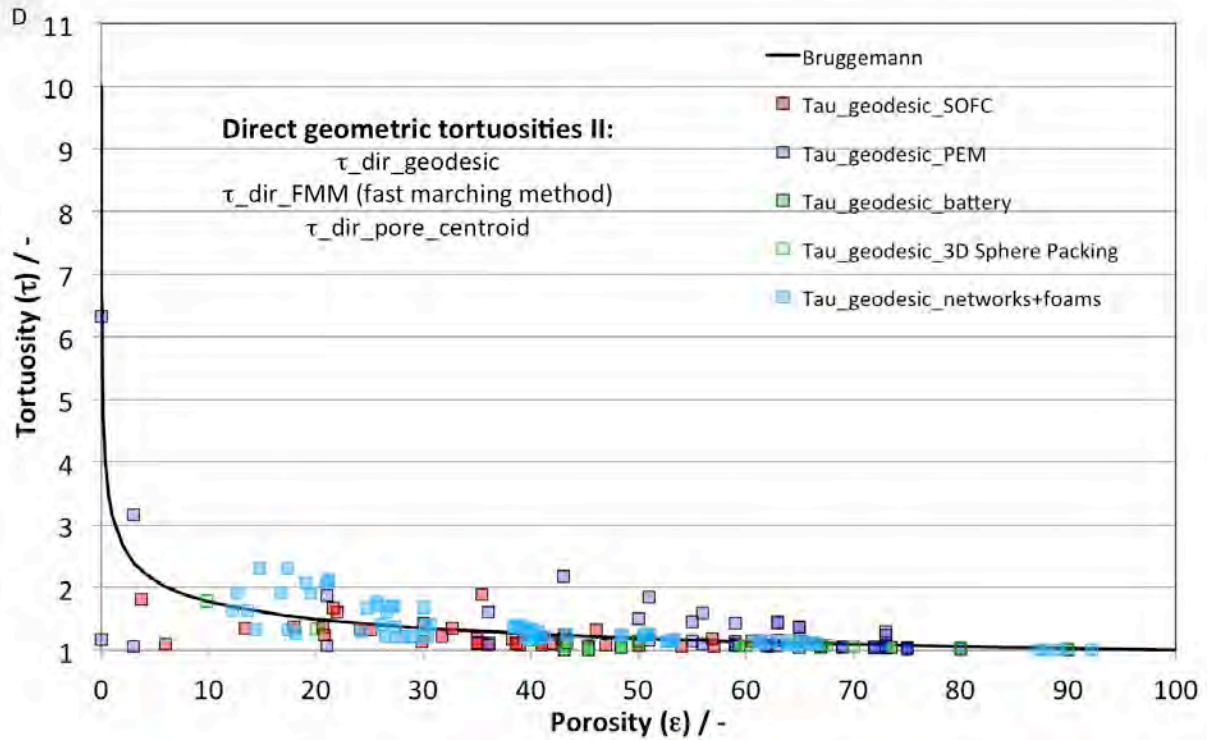


Fig. 5: Plots of tortuosity vs. effective porosity for different tortuosity types. Fig. 5 is based on the same data source as Fig. 4, which is presented in Table 2. Note that in Fig. 5E the y-axis has a different scale compared to Figs. 5A-D. Characteristic fields for different (direct and mixed) tortuosity types are indicated with a specific color in Fig. 5E.

### 3.3 Direct comparison of tortuosity types based on selected data sets

In this section, we focus on the comparison of different tortuosity types. The comparison is based on selected data sets from literature, where the same samples (i.e. the same materials and microstructures) are characterized with different tortuosities. For each example, we refer to the corresponding Nr of data set(s) in Table 2.

Example 1:  $\tau_{indir\_diff}$  VERSUS  $\tau_{dir\_pore\_centroid}$  from SOFC and battery electrodes

$$\text{Eq. 39} \quad \tau_{dir\_pore\_centroid} = 0.5 \ln \tau_{diff\_indir} + 1$$

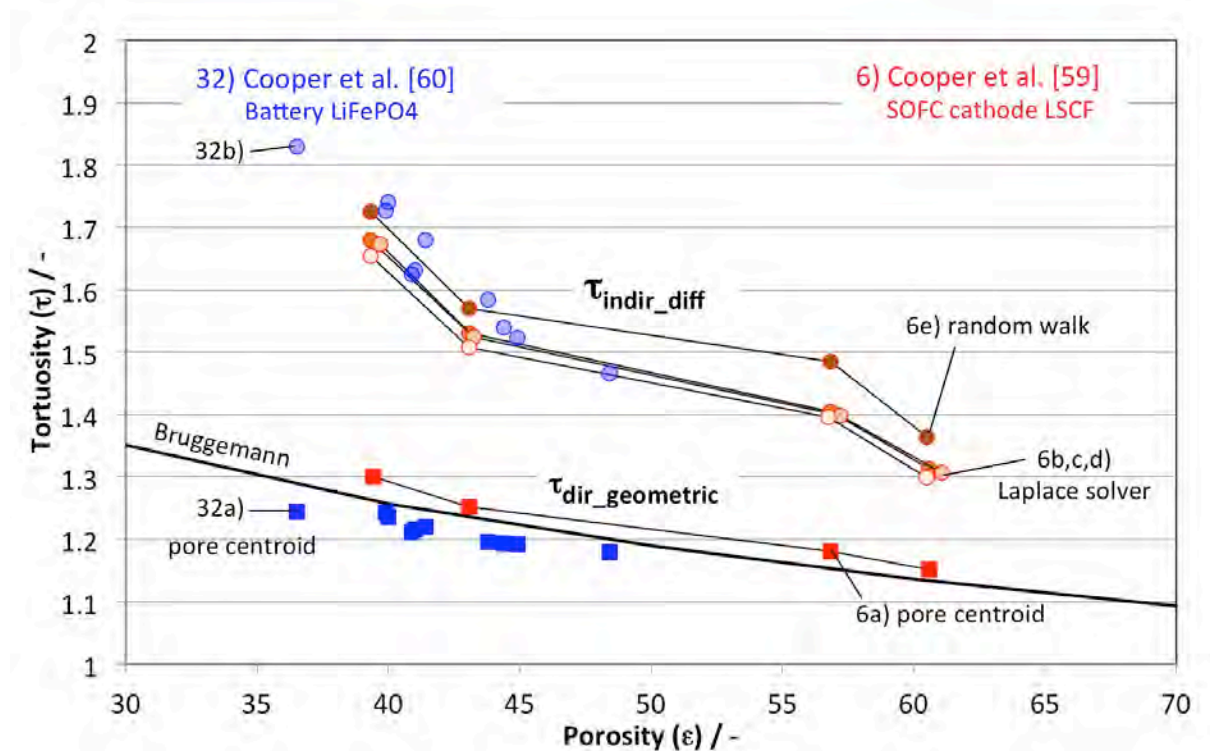


Fig. 6: Comparison of indirect (circles) vs. direct geometric tortuosities (squares) for SOFC cathodes (red symbols indicating values from Cooper et al. [61]) and for battery electrodes (blue symbols indicating values from Cooper et al. [60]). Both materials show the same pattern, where the values for indirect tortuosity ( $\tau_{indir\_diff\_sim}$ ) are consistently higher than those for geometric tortuosity ( $\tau_{dir\_pore\_centroid}$ ). The values for geometric tortuosity are very close to the Bruggemann trend line.

Cooper et al. [61] (Data-set Nr 6a-e) used 5 different methods to extract tortuosity from an SOFC cathode material (LSCF). The data set includes four indirect tortuosities that were determined with different simulation approaches (6b:  $\tau_{indir\_therm}$  StarCCM+, mesh-based, 6c:  $\tau_{indir\_diff}$ , AvizoXlab, voxel-based, 6d:  $\tau_{indir\_diff}$ , TauFactor, voxel-based, 6e:  $\tau_{indir\_diff}$ , random walk algorithm, voxel-based). All four approaches give very similar results for the indirect tortuosities. In comparison, the direct geometric tortuosity (6a:  $\tau_{dir\_pore\_centroid}$ ) for the same sample is significantly lower (see Fig. 6, red symbols).

Cooper et al. [60] (Data-set Nr 32a-b, see Fig. 6, blue symbols) also presented a comparison of direct geometric tortuosities (32a:  $\tau_{dir\_pore\_centroid}$ ) with indirect diffusional tortuosities (32b:  $\tau_{indir\_therm}$ ) for a Li-ion battery electrode ( $\text{LiFePO}_4$ ). The overall pattern and even the specific tortuosity-porosity values are very similar when comparing the battery electrode (blue) with the SOFC electrode (red). For both materials the values for indirect tortuosity ( $\tau_{indir\_diff/therm}$ ) are consistently higher than those for geometric tortuosity ( $\tau_{dir\_pore\_centroid}$ ). From this data, Cooper et al. [61] deduced the following relationship:

Example 2:  $\tau_{indir\_ele\_exp}$  VS  $\tau_{dir\_median\_axis}$  from porous ceramic membranes

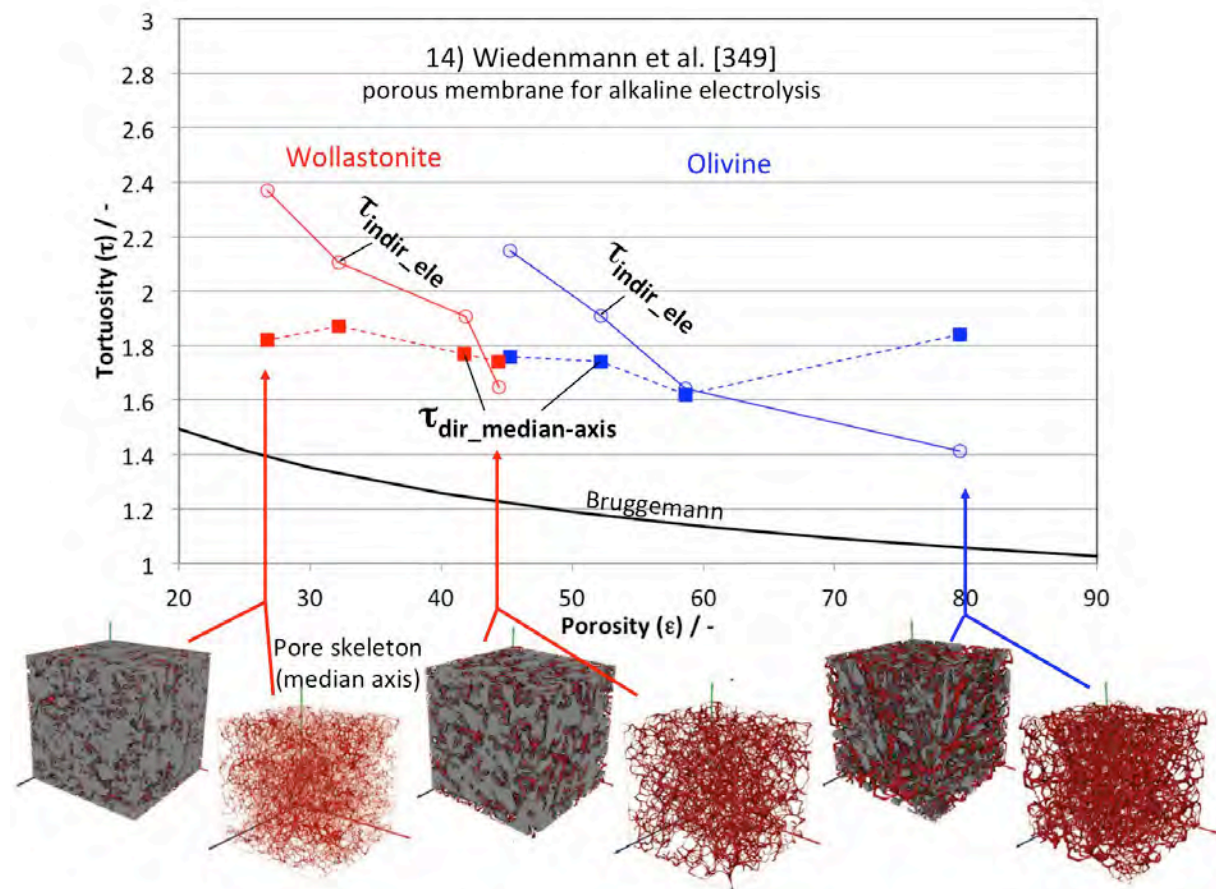


Fig. 7: Comparison of indirect ( $\tau_{indir\_ele\_exp}$ ) vs. direct geometric tortuosities ( $\tau_{dir\_medial\_axis}$ ) for porous membranes consisting of wollastonite (red) and olivine (blue) from Wiedenmann et al. [349]. The geometric tortuosities (filled squares) vary in a narrow range (1.6-1.8), whereas the indirect tortuosities (open circles) show significant variation. The variation of effective properties and associated indirect tortuosities is attributed to variations of the size of characteristic bottlenecks and corresponding constrictivities.

Wiedenmann et al. [349] (Dataset Nr. 14 in Table 2) presented a comparison of direct medial axis tortuosity (14a:  $\tau_{dir\_medial\_axis}$ ) vs. indirect, electrical tortuosities (14b:  $\tau_{indir\_ele}$ , from EIS experiments) for two different separation membranes in alkaline electrolysis

cells, consisting of sintered olivine and wollastonite. As shown in Fig. 7 the microstructures vary from fine grained and dense ( $\varepsilon = 0.27$ ) to coarse-grained and open porous ( $\varepsilon = 0.80$ ). Despite the large variation of porosity, the values for medial axis tortuosity (filled squares) are all in a very narrow range (1.62-1.84). The 3D visualizations in Fig. 7 [349] document nicely, that the basic geometry of all pore networks remains very similar for all samples, except for the coarseness, which increases with porosity (i.e. scaling). The obtained values for geometric tortuosity thus vary in a narrow range (1.73+/-0.11).

In contrast, the indirect tortuosities (open circles) increase significantly with decreasing porosity from 1.4 to 2.2 for olivine and from 1.6 to 2.4 for wollastonite. Wiedenmann et al. [349] and Holzer et al. [142] documented that the effective properties in these samples scale with constrictivity (i.e. bottlenecks), but not with geometric tortuosity. Therefore they concluded, that the variation of indirect tortuosities in this example rather represents the resistive effects arising from variations in the size of characteristic bottlenecks, rather than effects from path length variations.

### Example 3: $\tau_{indir\_ele/therm\_sim}$ versus $\tau_{indir\_diff\_exp}$ versus $\tau_{dir\_geodesic/FMM}$ from porous Zr-oxide and PEM GDL

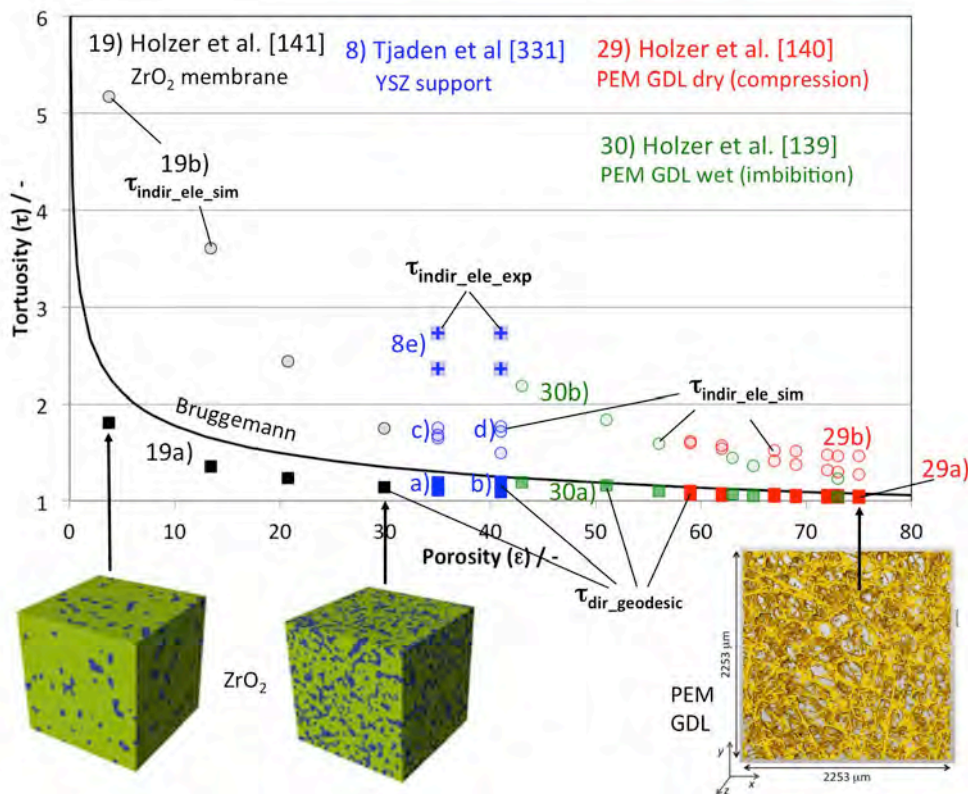


Fig. 8: Comparison of indirect ( $\tau_{indir\_ele\_exp/sim}$ ) vs. direct geometric tortuosities ( $\tau_{dir\_geodesic}$ ,  $\tau_{dir\_FMM}$ ) for various porous materials from Holzer et al. [141] (dataset 19, black symbols), Tjaden et al. [331] (dataset 8, blue symbols), and Holzer et al. [139,140] (datasets 29,30, red symbols). The direct geometric tortuosities (closed symbols) vary only in a narrow range below the Bruggemann trend line. In contrast, for the same samples, the indirect tortuosities (open symbols) show much higher values.

Fig. 8 represents a comparison of direct geometric tortuosities (geodesic/FMM) with indirect tortuosities (diffusive/electric/thermal - from simulation and experiment) based on data from Holzer et al. [141] (dataset 19), Tjaden et al. [331] (dataset 8) and Holzer et al. [139,140] (datasets 29,30). As shown in Fig. 8, all four studies document that the values for geometric tortuosities ( $\tau_{dir\_geodesic}$  and  $\tau_{dir\_FMM}$ , closed squares) are systematically lower than the results for indirect tortuosity (open circles and crosses). The samples of the three studies cover a wide range of effective porosities from 4 to 76 vol-%. In addition, the microstructures in sintered ceramics (Zr-oxide, YSZ) are very different from those in fibrous PEM GDL. Despite this obvious microstructural variation, all samples show a consistent pattern. The direct geometric tortuosities (geodesic/FMM) vary hardly and are always below the Bruggemann trend line. Only for very low porosities ( $\varepsilon < 0.2$ ) the geodesic tortuosities start to increase moderately. Apparently the geodesic path lengths are not very sensitive to variation of the pore volume fraction. In contrast the indirect tortuosities (open symbols and crosses) are always significantly higher than the Bruggemann trend line and they also show much stronger variation. For each series of material/microstructure a trend of increasing indirect tortuosities is observed when lowering the porosity.

Example 4:  $\tau_{indir\_ele\_sim}$  VERSUS  $\tau_{dir\_medial\_axis}$  VERSUS  $\tau_{dir\_geodesic}$  from stochastic 3D structures

Gaiselmann et al. [102] and Stenzel et al. [312] performed in-depth investigations on the relationship between microstructure characteristics and effective transport properties based on virtual 3D structures generated by stochastic modeling. The so-called stochastic spatial graph model (SSGM) provides 3D structures with a connected transporting phase even at low volume fractions. A large number of microstructures covering a wide range of microstructure characteristics (i.e. volume fractions, phase size distributions, constrictivity and path lengths) were created and analyzed. Three different tortuosities (medial axis, geodesic and indirect tortuosities) can be compared based on data-sets Nr. 66 and Nr. 67 from [312] and [102]. It should be noted, that in these studies electric conduction in the solid phase was investigated. However, the effect of microstructure (e.g. tortuosity) on transport in solid phases is basically the same as in the pore phase.

The results in Fig. 9 document that the indirect tortuosities ( $\tau_{indir\_ele\_sim}$ ) are consistently higher than the direct geometric tortuosities. It also reveals slight differences between direct medial axis and direct geodesic tortuosities. The medial axis tortuosity ( $\tau_{dir\_medial\_axis}$ , red symbols, Nr 67) is slightly higher than the Bruggemann trend line. In contrast the geodesic tortuosity ( $\tau_{dir\_geodesic}$ , black, Nr 66b) is usually below the Bruggemann trend line. However, for small volume fractions of the transporting phase (i.e.  $\varepsilon < 0.2$ ), both tortuosities show similar values.

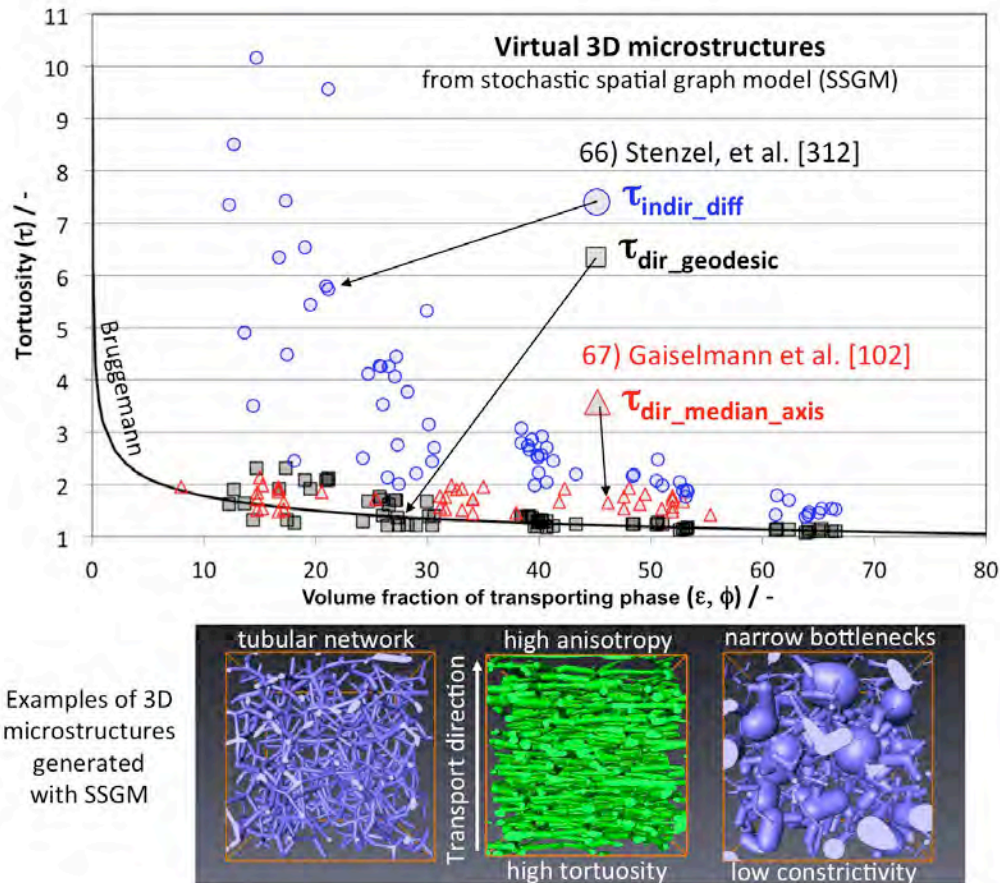


Fig. 9: Comparison of indirect ( $\tau_{indir\_ele\_sim}$ ) vs. direct geometric tortuosities ( $\tau_{dir\_geodesic}$ ,  $\tau_{dir\_medial\_axis}$ ) for virtual 3D structures created with a spatial stochastic graph model (SSGM) from Gaiselmann et al. [102] (dataset 67) and Stenzel et al. [312] (dataset 66). The direct geometric tortuosities (black squares, red triangles) vary in a narrow range, which is close to the Bruggemann trend line. For the same samples, the indirect tortuosities (blue open circles) show much higher values and a stronger variation.

#### Example 5: $\tau_{dir\_medial\_axis}$ versus $\tau_{dir\_geodesic}$ from SOFC anodes and silica monoliths

The relationship between geodesic and medial axis tortuosities is also investigated by Holzer et al. [136] (dataset 11) and Pecho et al. [255] (dataset 12) for SOFC anodes and by Hormann et al. [145] (dataset 64) for silica monoliths. Fig. 10 clearly shows that geodesic tortuosities (squares) are systematically lower than the medial axis tortuosities (triangles), even though they are measured for the same samples. Furthermore, the Bruggemann trend line can be roughly considered as the boundary between the characteristic fields for these two geometric tortuosity types. These findings are compatible with the results from Gaiselmann et al. [102] and Stenzel et al. [312] in Example 4 (Fig. 9).

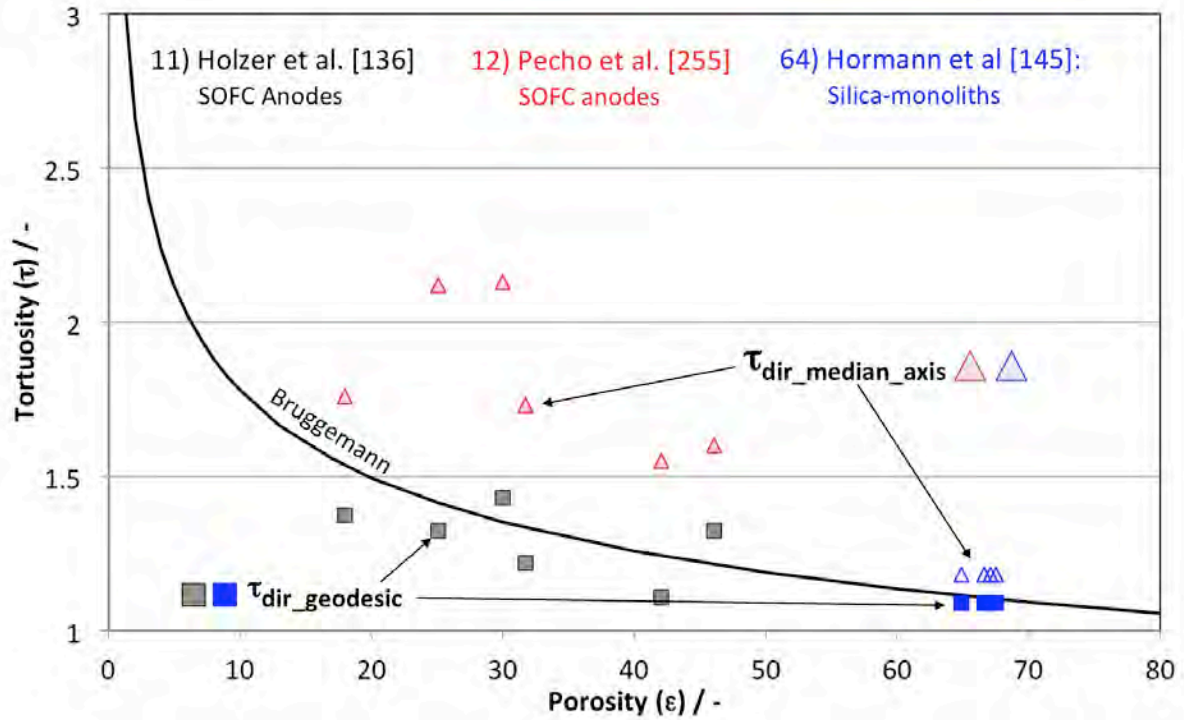


Fig. 10: Comparison of geodesic ( $\tau_{dir\_geodesic}$ ) vs. medial axis tortuosities ( $\tau_{dir\_medial\_axis}$ ) for SOFC anodes (Holzer et al. [136] and Pecho et al. [255]) and for silica monoliths (Hormann et al. [145]). The geodesic tortuosity ( $\tau_{dir\_geodesic}$ ) typically shows values close to or below the Bruggemann trend line. In contrast, the medial axis tortuosities ( $\tau_{dir\_medial\_axis}$ ) show consistently higher values.

Example 6:  $\tau_{mixed\_ele/hydr\_streamline}$  versus  $\tau_{mixed\_ele/hydr\_Vav}$  (mixed tortuosity types) for simulated particle packing (2D and 3D)

This example uses datasets with mixed tortuosity types, including the streamline tortuosity ( $\tau_{mixed\_phys\_streamline}$ ) and the volume-averaged tortuosity ( $\tau_{mixed\_phys\_Vav}$ ) for flow, conduction and diffusion.

Saomoto et al. [282] (dataset 55) simulated hydraulic flow and electrical conduction in simple 2D structures consisting of mono-sized circles and/or ellipsoids. Both mixed tortuosities (i.e. streamline and area-averaged) are extracted from the electric and hydraulic flow fields and their values are plotted in Fig. 11. Surprisingly the results for both mixed tortuosity types are almost identical. For example the electric streamline tortuosity (red square with crosses) is nearly identical to the electric volume-averaged tortuosity (blue square with crosses) (i.e.  $\tau_{mixed\_ele\_streamline} \cong \tau_{mixed\_ele\_Vav}$ ). The same holds for hydraulic tortuosities (i.e.  $\tau_{mixed\_hydr\_streamline} \cong \tau_{mixed\_hydr\_Vav}$ ). However, a significant difference is observed between electric and hydraulic tortuosities. The characteristic field for mixed electric tortuosities (i.e.  $\tau_{mixed\_ele\_streamline}$ ,  $\tau_{mixed\_ele\_Vav}$ ), which is highlighted in red color, is lower than the characteristic field for mixed hydraulic tortuosities (i.e.  $\tau_{mixed\_hydr\_streamline}$ ,  $\tau_{mixed\_hydr\_Vav}$ ), which is highlighted in blue. The boundary between these characteristic fields is roughly identical with the Bruggemann trend line.

Sheikh and Pak [303] (dataset 61, green crosses) reported diffusive volume-averaged tortuosities ( $\tau_{mixed\_diff\_Vav}$ ) from 3D poly-dispersed spheres, which are close to the values of mixed electric tortuosities in Saomoto et al. [282], but lower than the mixed hydraulic tortuosities in [282]. This finding is compatible with the general expectation that diffusive and electrical tortuosities are almost identical to each other and that the hydraulic tortuosities are generally somewhat higher, see e.g. Clennell [55].

Finally, results of volume averaged hydraulic tortuosities ( $\tau_{mixed\_hydr\_Vav}$ ) for gas diffusion layers (GDL) in PEM fuel cells are presented by Froning et al. [96] (dataset 28, crosses highlighted in yellow). Note that the microstructures of fibrous GDL considered by Froning et al. [96] are significantly different from those of poly-dispersed sphere packing in Sheikh and Pack [303]. Nevertheless, the characteristic values of  $\tau_{mixed\_hydr\_Vav}$  for these two materials (GDL in [96] and packed spheres in [303]) are rather similar. This shows again that the tortuosity values are usually more strongly depending on the type of tortuosity and less strongly on the type of material and/or microstructure.

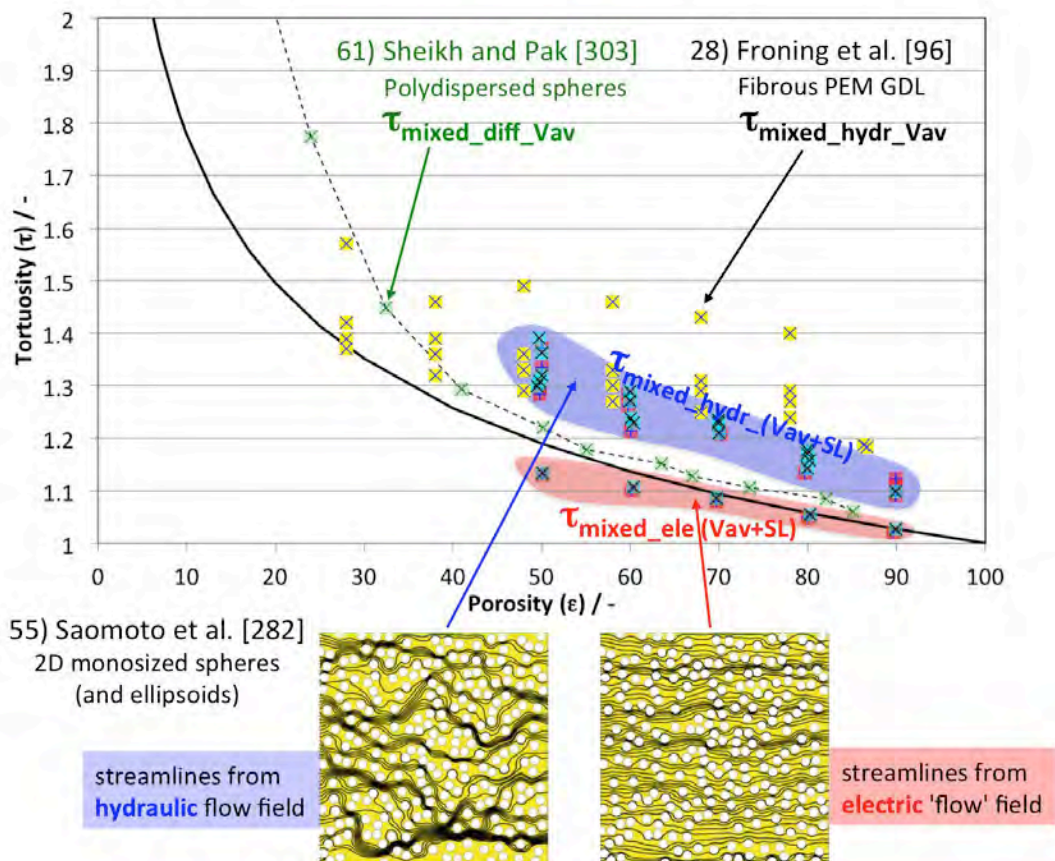


Fig. 11: Comparison of different mixed tortuosities ( $\tau_{mixed\_ele/diff/hydr\_streamline}$ ,  $\tau_{mixed\_ele/diff/hydr\_Vav}$ ). In principle, the datasets for mono-sized spheres/ellipsoids from Saomoto et al. [282] (dataset 55, 2D) and Sheikh and Pak [303] (dataset 61, 3D) show hardly a difference between streamline and volume averaged tortuosities. However, a systematic difference is caused by the underlying transport mechanism, in the sense that mixed hydraulic tortuosities (characteristic field in blue, and yellow crosses) are higher than the corresponding mixed electric tortuosities (characteristic field in red).

Overall, this example shows that the values of mixed tortuosities are relatively low. Values larger than 2 are rarely observed and can only be expected for structures with either low porosities ( $\varepsilon < 0.2$ ) or with strong anisotropy effects. Similar as observed previously for the various geometric tortuosities, also the mixed tortuosities show a relatively small scatter and the values are usually in the range between 1 and 2 (i.e. compatible with Carman's estimation of  $\sqrt{2}$ ). This is in remarkable contrast to the indirect tortuosities (not analyzed in this example), which scatter over a much larger range and often take values much larger than 2.

### 3.4 Relative order of tortuosity types

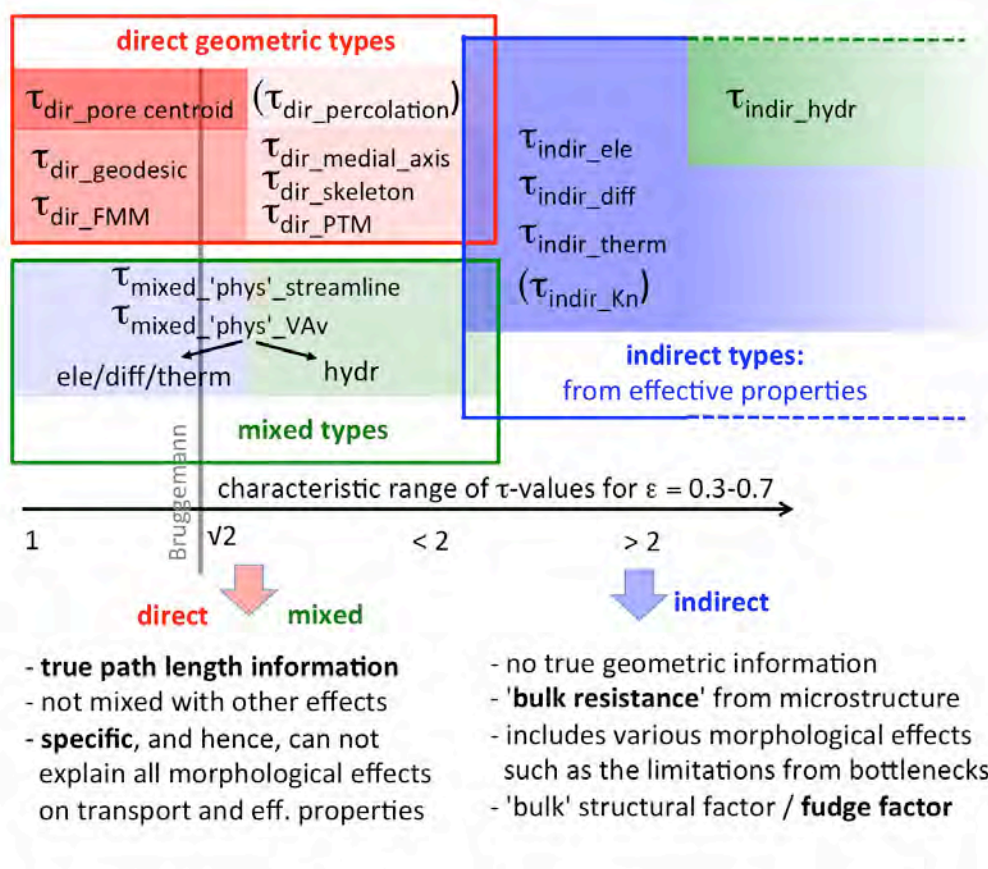


Fig. 12: The review of tortuosity-porosity data from literature reveals a universal pattern that is characterized by a consistent relative order among the different tortuosity types. This pattern is observed for many different materials and microstructures. Geometric and mixed tortuosity types typically show relatively low values close to the Bruggemann trend line. In contrast, the indirect tortuosities show higher values with a larger variability.

The empirical data from literature reveals a consistent pattern among the tortuosity types, in the sense that certain tortuosity types give consistently higher values than others. This relative order of tortuosity types, which is schematically illustrated in Fig. 12, is valid for a wide range of materials with very different microstructures.

Basically, the indirect tortuosities scatter over a much wider range than the direct geometric and the mixed tortuosity types. The direct and mixed types rarely take values greater than 2, whereas for the indirect tortuosities much larger values are measured, - sometimes even higher than 20.

For the geometric tortuosities, two subgroups can be distinguished. For medial axis and path tracking method (PTM) tortuosities, the Bruggemann trend line represents the lower bound. In contrast, geodesic and fast marching method (FMM) tortuosities typically show values that are equal or even lower than the Bruggemann trend line.

The values of mixed tortuosity types (streamline and volume averaged tortuosities) roughly overlap with the values for the direct geometric tortuosities (i.e., usually the mixed tortuosities are also close to the Bruggemann trend line (see e.g. Fu et al. [98])). In principle, the mixed streamline tortuosities are identical with the mixed volume-averaged tortuosities, provided that the same transport mechanism is considered (see e.g. Saomoto et al. [282]). However, the mixed electrical, diffusional or thermal tortuosities are consistently lower than the mixed hydraulic tortuosities. The Bruggemann trend line separates the two characteristic fields for mixed electrical/diffusional and for mixed hydraulic tortuosities (see Fig. 11).

Interpretations of different tortuosity categories:

a) The direct and mixed tortuosities are based on geometric analyses and therefore they can be considered as true measures for the path lengths through the porous medium under investigation. Consequently, in order to predict the impact of microstructure on effective transport properties, it is not sufficient to merely consider the geometric or mixed tortuosities, since other morphological effects (e.g. bottlenecks/constrictivity) in addition to path length variation also have an influence on the effective transport properties.

b) The indirect tortuosities are derived from effective (or relative) properties that are known from experiment or simulation. The indirect tortuosities can thus be considered as a measure for the bulk microstructure resistance against transport. The large values and the large variability observed for indirect tortuosities are due to the fact that they capture all different kinds of microstructure limitations, including resistive effects from narrow bottlenecks. Indirect tortuosities are thus not a realistic measure for the length of transport paths, since they tend to overestimate the effect of pure path lengths significantly.

### 3.5 Tortuosity - porosity relationships in literature

Numerous mathematical expressions describing tortuosity - porosity ( $\tau$ - $\varepsilon$ ) relationships can be found in literature. The different  $\tau$ - $\varepsilon$  relationships are reviewed by Shen and

Chen [304], Ghanbarian [109], Tjaden et al. [329] and Idris et al. [154]. Table 3 represents a selection of these  $\tau - \varepsilon$  relationships.

Note that very different mathematical expressions are proposed - usually logarithmic and power-law functions. As shown in Fig. 13, the resulting  $\tau - \varepsilon$  curves diverge greatly from each other. This chaotic picture is in contrast to the empirical data, which shows a clear pattern among different tortuosity types (as summarized in Fig. 12). Moreover, the empirical data typically results in characteristic  $\tau - \varepsilon$  fields (as shown in Figs. 5 for the different tortuosity types), but usually it does not result in clearly defined  $\tau - \varepsilon$  curves.

The large scatter in Fig. 13A for the mathematical expressions illustrates that there is no consensus how tortuosity varies with porosity. In fact, this finding questions the underlying assumption that variations of tortuosity and porosity are strictly related, so that the  $\tau - \varepsilon$  relationship could be described with one universal mathematical formula.

The behavior of microstructure characteristics can be investigated in a more general way, when 3D image analysis is applied to a large number of 3D microstructure models. Results from such studies are shown in Figs. 13B-E (taken from Neumann et al. [243] and Stenzel et al. [313]). These data sets indicate that the microstructure characteristics ( $\varepsilon$ ,  $\beta$ ,  $\tau_{dir\_geodesic}$ ) can vary in a large range within the theoretically possible constellations, except for high porosities, where tortuosity asymptotically tends to 1 (see Fig. 13D). For small porosities the variation of geodesic tortuosity is particularly large, but even at very high porosities ( $\varepsilon > 0.8$ ) there is still significant variation in the tortuosity values (Fig. 13D). A similar behavior is expected for all the other geometric and mixed tortuosities. These examples thus indicate that there exists no clear correlation between tortuosity and porosity, which could be described with a universal mathematical  $\tau - \varepsilon$  expression.

Nevertheless, mathematical expressions for tortuosity - porosity ( $\tau - \varepsilon$ ) relationships have their justification in context with specific cases of controlled microstructure variation. Such a case was described by Archie [8], who presented experimental data for porous sediments saturated with an electrolyte. For the special case, where all samples originate from the same sedimentary unit, the experimental results show a correlation between electric resistance and porosity. Archie's law (see Eq. 23:  $F_R = \varepsilon^m = 1/\sigma_{rel}$ ) describes this correlation using a so-called cementation factor ( $m$ ) as exponent. Wyllie and Rose [357] redefined the relationship between electric resistance (formation factor,  $F_R$ , respectively) and porosity by introducing the so-called structural factor (Eq. 24:  $F_R = X_{ele}/\varepsilon = 1/\sigma_{rel}$ ). Thereby,  $X_{ele}$  can be interpreted as being equivalent with Carman's tortuosity factor ( $X_{ele} = T = \tau_{ele}^2$ ). This leads to the widely used to compute indirect tortuosity by Eq. 25 (i.e.  $\tau_{indir\_ele}^2 = \varepsilon/\sigma_{rel}$ ). Thereby, indirect tortuosity can be considered as some kind of proportionality between porosity and effective properties (resistance or conductivity). For the special case where effective properties ( $F_R$ ,  $\sigma_{rel}$ ) correlate with porosity, it follows that there must be also a strict correlation with indirect tortuosity, such that Archie's law can be reformulated as follows:

Eq. 40 (Archie's law) 
$$\tau_{indir\_ele}^2 = \varepsilon^{1-m}$$

Table 3: Mathematical tortuosity - porosity ( $\tau$ - $\varepsilon$ ) relationships from literature. It must be emphasized that in most references the tortuosity type is not defined clearly. Information on ' $\tau$  type' is thus often interpreted from the context of a given paper, where possible. 'Material type' describes the microstructure for which the  $\tau$ - $\varepsilon$  relationship was derived. Note that depending on the authors, the left hand side of the equation is sometimes written as tortuosity ( $\tau$ ) and sometimes as tortuosity factor ( $\tau^2$ )

Nr	$\tau$ type	$\tau^2$ (or $\tau$ !) = $f(\varepsilon)$	material type or microstructure type	x = ..	Reference(s)
1	geom. model	$\tau_{geometric} = \frac{1}{2} \left[ 1 + \frac{1}{2} \sqrt{1 - \varepsilon} + \frac{\sqrt{(1 - \sqrt{1 - \varepsilon})^2 + (1 - \varepsilon)/4}}{1 - \sqrt{1 - \varepsilon}} \right]$	geometric 2D model of square particles		Yu and Li [362]
3, 2	geom. model	$\tau_{geometric} = 1.23 \frac{(1 - \varepsilon)^{4/3}}{x^2 \varepsilon}$	packed particles --> packed spheres -->	0.75 1	Lanfrey et al. [198]
4	geom. model	$\tau_{geometric} = \left( \frac{19}{18} \right)^{\ln(\varepsilon)/\ln(8/9)}$	Pore fractal model		Li and Yu [203]
5, 6, 7	hydr.	$\tau_{hydr}^2 = 1 - x \ln(\varepsilon)$	spheres + fibres --> plates + flakes --> high aspect ratio particles -->	0.5 1 3	Pech and Renaud, cited in Comiti and Renaud [58]
8	hydr.	$\tau_{hydr}^2 = \varepsilon^{-x}$	binary mixture of spheres	0.4	Mota et al. [229]
9	hydr.	$\tau_{hydr}^2 = \frac{\varepsilon}{1 - (1 - \varepsilon)^{2/3}}$	isotropic granular material		Du Plessis et al. [264]
10 11	hydr.	$\tau_{hydr}^2 = \sqrt{\frac{2\varepsilon}{3[1 - x(1 - \varepsilon)^{2/3}]} + \frac{1}{3}}$	monosized spheres: cubic packing --> tetrahedral packing>	1.209 1.108	Ahmadi [4]
12	hydr.	$\tau_{mix\_hyd\_Vav} = 1 + 0.8(1 - \varepsilon)$	mono-sized solid rectangles in 2D		Koponen et al. [187]
13	electr.	$\tau_{ele}^2 = 1 + 0.5(1 - \varepsilon)$ $\tau_{ele}^2 = \frac{(3 - \varepsilon)}{2}$	dilute suspension of spheres		Maxwell, 1873 [221]
14, 15	electr.	$\tau_{ele}^2 = \varepsilon^{1-x}$	cementation exponent for rocks -> and for sediments ->	1.1 2	Archie, 1942 [8]
16	electr.	$\tau_{ele}^2 = \varepsilon^{1-x}$ , identical with Bruggemann (see Nr 27)	packing of poly-dispersed spheres	1.5	Archie, 1942 [8]
17, 18, 19, 20, 21, 22	electr.	$\tau_{ele}^2 = 1 - x \ln(\varepsilon)$	spherical particles -> monosized spheres -> cubic particles --> cylinders --> overlapping spheres monosized spheres -->	0.41 0.49 0.63 1.00 0.5 0.5	Pech and Renaud, cited in Comiti and Renaud [58]

23	diff.	$\tau_{diff}^2 = \varepsilon^{-x}$	mono-sized spheres	0.4	Mota et al. [229], Delgado [66]
24	diff.	$\tau_{diff}^2 = \frac{\varepsilon}{1 - (1 - \varepsilon)^{1/3}}$	catalyst		Beeckman [19]
25	diff.	$\tau_{diff}^2 = \varepsilon + x(1 - \varepsilon)$	sand, silt, sediments	2	Iversen and Jørgensen [155]
26	non spec.	$\tau^2 = 2 - \varepsilon$			Petersen [259]
27	diff	$\tau_{diff}^2 = \varepsilon^{-1/2} = \varepsilon^{1-x}$ <b>for spheres identical with Archie</b> (see Nr 16)	polydisperse granular media: <b>spheres --&gt;</b> cylinders -->	<b>1.5</b> 2	<b>Bruggemann</b> 1935 [32] see also Tjaden et al. [330]
28	electr.	$\tau_{diff}^2 = x_1 \varepsilon^{1-x_2}$	battery electrodes and separators	x <sub>1</sub> : 0.1-2.6; x <sub>2</sub> : 1.27-5.2	Thorat 2009 [326], cited in Tjaden et al. [329]
29	electr.	$\tau_{ele}^2 = \varepsilon^{-x}$	battery electrode	0.5-2	Ebner et al. [76]
30	diff	$\tau_{diff}^2 = \varepsilon^{-1/3}$	monodisperse granular media		van Brakel and Heertjes [30]
31	hydr	$\tau_{diff}^2 = 1 - \ln(\varepsilon)$	overlapping cylinders		Tomadakis and Sotirchos [332]
32	diff	$\tau_{diff}^2 = 1 - \frac{\ln(\varepsilon)}{2}$	overlapping spheres		Weissberg [345]
33	diff	$\tau_{diff} = 1 - x \ln(\varepsilon)$	Clays dry and hygroscopic	0.357 0.503	Sun et al. [315]
34	hydr	$\tau_{hydr}^2 = \left(\frac{2 - \varepsilon}{\varepsilon}\right)^2$	cation exchange resin		Mackie [214]
35	diff	$\tau_{diff} = [1 - x(1 - \varepsilon)^{-1}]$	granular media with: spheres --> cubes --> large parallelepipeds small parallelepipeds	0.6 0.73 1.07 1.21	Pisani [261]
36	hydr	$\tau_{mixed\_hydr\_vav}^2 = x_1 - x_2 \ln(\varepsilon^2)$	monosized spheres	x <sub>1</sub> : 1.1842 x <sub>2</sub> : 0.6579	Jin et al. [162]
37	hydr	$\tau_{mixed\_hydr\_vav}^2 = x_1 - x_2 \ln(\varepsilon^2)$	monosized spheres	x <sub>1</sub> : 0.9463 x <sub>2</sub> : 0.7173	Duda et al. [73], cited in Jin et al. [162]
38	hydr	$\tau_{mixed\_hydr\_vav} = x_1(1 - \varepsilon) + x_2$	monosized spheres	x <sub>1</sub> : 0.8002 x <sub>2</sub> : 1.0454	Jin et al. [162]
39	hydr	$\tau_{mixed\_hydr\_vav} = x_1(1 - \varepsilon) + x_2$	monosized spheres	x <sub>1</sub> : 0.9119 x <sub>2</sub> : 0.9340	Duda et al. [73], cited in Jin et al. [162]
40	hydr	$\tau_{mixed\_hydr\_vav} = x_1 - x_2 \ln(\varepsilon)$	monosized spheres	x <sub>1</sub> : 1.1133 x <sub>2</sub> : 0.4845	Jin et al. [162]
41	hydr	$\tau_{mixed\_hydr\_vav} = x_1 - x_2 \ln(\varepsilon)$	monosized spheres	x <sub>1</sub> : 1.0104 x <sub>2</sub> : 0.5541	Duda et al. [73], cited in Jin et al. [162]
42	hydr	$\tau_{mixed\_hydr\_vav} = 1 - x_1 \ln(\varepsilon)$	2D monosized spheres / cubes	0.5/0.541	Saomoto and Katagiri [281]
43	ele	$\tau_{mixed\_ele\_vav} = 1 - x_1 \ln(\varepsilon)$	2D monosized spheres / cubes	0.2/0.19	Saomoto and Katagiri [281]

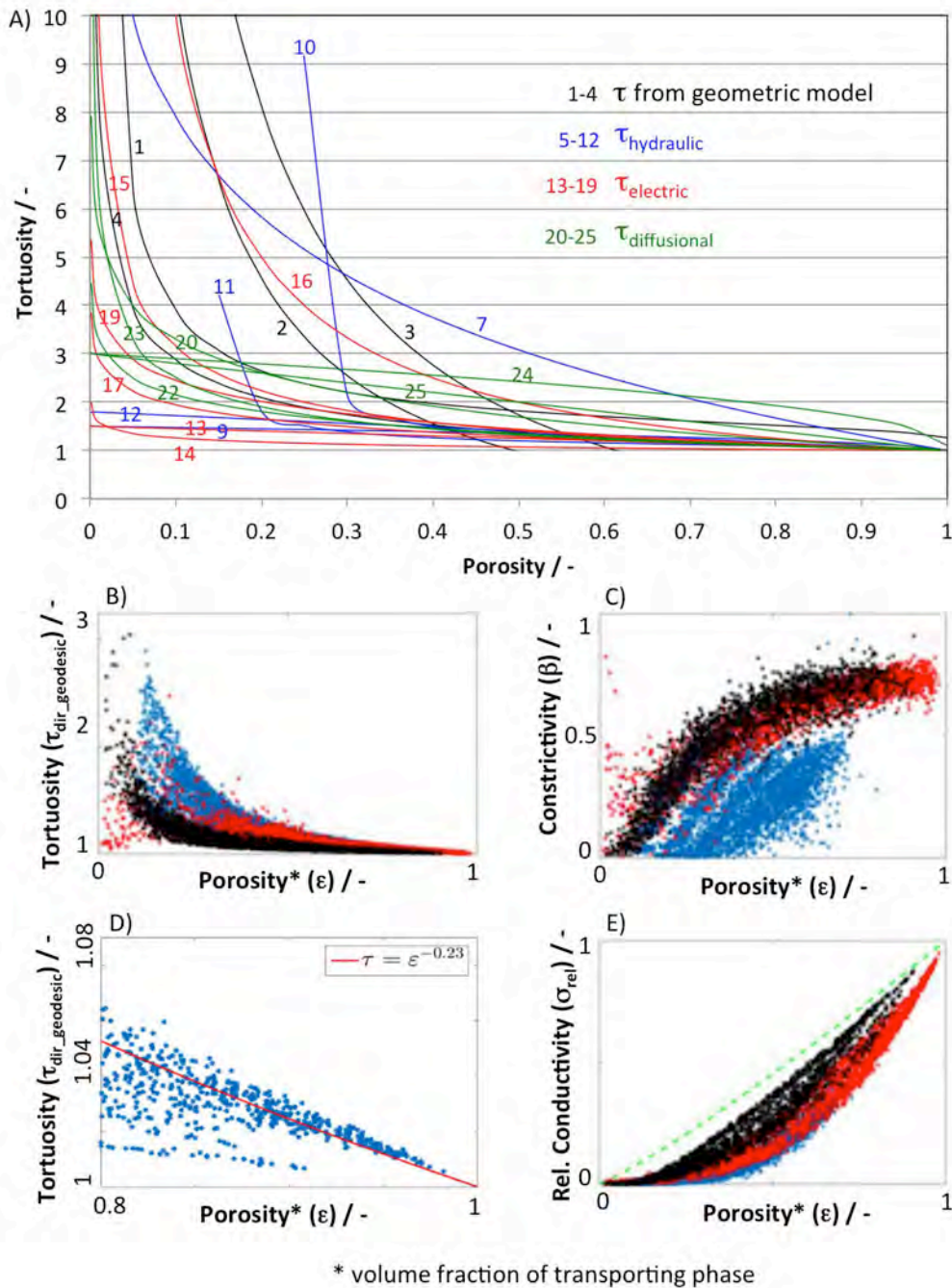


Fig. 13A: Mathematical tortuosity - porosity ( $\tau$ - $\epsilon$ ) relationships from literature. The numbers refer to the equations given in Table 3. Colors indicate which type of tortuosity is considered.

Figs. 13 B to E: Plots of tortuosity ( $\tau_{\text{dir\_geodesic}}$ ), constrictivity ( $\beta$ ), and relative electric conductivity ( $\sigma_{\text{rel}}$ ) versus porosity ( $\epsilon$ , on the x-axis). Red, blue and black data points represent three distinct types of 3D microstructures, which are generated with different stochastic models. More than 2000 different 3D structures are investigated, which cover a wide range of microstructure characteristics (Figs. 13B,C,E are taken from Neumann et al. [243] and Fig. 13D from Stenzel et al. [313]).

It must be emphasized that Archie's cementation factor ( $m > 1$ ) is a fit parameter, which is valid only for a special case of microstructure variation. The cementation factor takes a specific value for a series of rocks, which all have undergone the same diagenetic process. The common history of these sediments in the same geo-environment led to a characteristic variation of the microstructure, so that sizes of pores and bottlenecks, pore connectivity and transport path lengths vary in a characteristic way with porosity. Hence, in this case the correlation of microstructure with porosity is controlled by the diagenetic conditions and by the associated cementation process. Due to this controlled correlation, it is possible to find a suitable mathematical expression for the  $\tau - \varepsilon$  relationship of rocks in a single sedimentary unit. Thereby the indirect tortuosity represents the lumped sum of all microstructure effects. With respect to Archie's law, it must be realized that the fitting of the cementation factor ( $m$ ) has to be repeated if the rocks originate from a different sedimentary unit, because then these rocks were exposed to different diagenetic conditions, and therefore they are characterized by different  $\tau - \varepsilon$  relationships.

Such special cases are also known from materials engineering, when microstructure variations are performed in a controlled way. An example is described by Holzer et al. [141], where sintering temperatures are changed systematically, but all the other parameters (e.g. composition and sinter time) for the fabrication of porous ceramic membranes are kept constant. This results in a systematic variation of microstructure characteristics ( $\tau_{dir\_geodesic}$ ,  $\beta$ ) and effective properties ( $\sigma_{eff}$ ,  $\sigma_{rel}$ ) with porosity ( $\varepsilon$ ). Hence, for such controlled microstructure variation a suitable mathematical expression can be found for the observed  $\tau - \varepsilon$  relationship. However, this mathematical expression may no longer be valid, when one of the other fabrication parameters (e.g. composition or sinter time) is changed.

The Bruggemann equation is a special case of Archie's  $\tau - \varepsilon$  relationship (see Eq. 40), where the 'cementation factor' ( $m$ ) is fitted for a special microstructure type. For example, it was found that  $m = 1.5$  for packed spheres (and  $m=2$  for cylindrical particles), which leads to

$$\text{Eq. 41} \quad \tau_{indir\_ele}^2 = \varepsilon^{-0.5} .$$

In battery research, a modified version of the Bruggemann equation, given by

$$\text{Eq. 42} \quad \tau_{indir\_ele}^2 = \gamma \varepsilon^{1-\alpha}$$

is nowadays often used (see Thorat et al. [326]), where  $\gamma$  is an additional fit parameter. Various authors [10,42,72,77,174,326,364] presented experimental and numerical fits of Eq. 42 (e.g. Nrs 27-30 in Table 3) for different battery electrodes, which was critically reviewed by Tjaden et al. [329]. Thereby it is well illustrated that the variations of  $\gamma$  (0.1 - 2.6) and  $\alpha$  (1.27 - 5.2) are very large and the resulting  $\tau - \varepsilon$  curves differ significantly from each other, depending on the type of battery material. In addition, Tjaden et al. [329] also report examples from literature, which show that for many battery materials the Bruggemann equation and its modifications are simply not applicable. Tjaden et al. [329] thus concluded that tortuosity-porosity relationships such as the Bruggemann equation are only applicable to microstructures 'which are similar to the microstructure used to derive the respective relationship' (i.e. for special cases).

These selected examples related to Archie's and Bruggemann's equations illustrate that  $\tau - \varepsilon$  relationships should not be mistaken as universal laws. In general, when varying materials microstructures are considered, the different microstructure characteristics ( $\varepsilon, \beta, \tau, r_h, r_{min}, r_{max}$ ) can vary independently from each other, - at least to some degree. Therefore, empirical data shows a more or less wide scatter for the characteristic fields of different material types (Fig. 4) and different tortuosity types (Fig. 5), which is also true for other morphological characteristics (e.g. constrictivity) and effective properties (Fig. 13B-E).

Hence, we conclude that mathematical formulas for tortuosity-porosity relationships are valid only if they are specified:

- a) for a specific type of tortuosity (see the classification scheme and nomenclature in Fig. 3). Thereby, the scatter of data points is generally much smaller for direct geometric and mixed tortuosity types (Fig. 5B-E), compared to the indirect tortuosities (Fig. 5A).
- b) for a specific material type, which fulfills a systematic microstructure variation (e.g. rocks from the same sedimentary unit, which all had similar conditions during sedimentation and diagenesis). Furthermore, for simple microstructures such as packed spheres it is more probable that microstructure variation (i.e. densification) results in a systematic correlation between tortuosity and porosity (Fig. 4E,F), compared to more complex microstructures (e.g. SOFC electrodes, fibrous materials, foams), which tend to show a larger scatter (Figs. 4G,H) of  $\tau - \varepsilon$  couples.

From the results reviewed so far in this survey, we conclude that the tortuosity concept and its perception are highly controversial. First theories and concepts on tortuosity were introduced at a time when suitable methods for 3D microstructure analysis were not yet available. The basic theories and concepts were thus introduced based on simplified geometrical models such as parallel tubes (Kozeny [190], Scheidegger [289]) or mono-sized spheres (Carman [47]). On the other hand, in experimental studies, tortuosity still nowadays is often derived indirectly from effective properties. These indirect tortuosities can be considered as description of bulk resistance from microstructure, which does not contain any specific geometric information. In the last two decades new methods became available, which enable us to characterize tortuosity directly from the 3D microstructure. In particular, a multitude of direct geometric and mixed tortuosity types can nowadays be determined.

Despite the progress in characterization, there still exist many controversies and confusions about tortuosity, which mainly come from the fact that it is often not clearly distinguished between the different tortuosity types. As a first step to face this problem, we propose to use a clear terminology. For this purpose, a new classification scheme and a new tortuosity-nomenclature have been introduced in Chapter 2 (see e.g. Fig. 3). As a second step, systematic differences between the various tortuosity types need to be identified and understood. Obviously, to a large degree, these differences are caused to a large degree by the underlying methodological approaches and associated different levels of geometric information. In the next chapter, we thus focus on a thorough description of the different methodologies and calculation approaches for tortuosity.

## 4. Methodologies, workflows and calculation approaches

In our description of the methods for characterization of tortuosity we follow step by step the general workflow, which is illustrated in Fig. 14. The modern methods for tortuosity characterization focus on the collection and quantitative analysis of 3D information. Thereby, 3D imaging and image processing represents a prerequisite for measuring direct geometric tortuosities (i.e.  $\tau_{dir\_geom}$ ). Furthermore, 3D microstructure models (real or virtual) can be used as input for numerical transport simulations, from which effective transport properties and indirect tortuosity can be derived ( $\tau_{indir\_phys\_sim}$ ). As a third option, the 3D volume fields representing the local flux from numerical transport simulations can be used as basis for the computation of mixed type tortuosities ( $\tau_{mixed\_phys\_streamline}$ ,  $\tau_{mixed\_phys\_Vav}$ ).

For the indirect tortuosity, there also exists an alternative way of determination without using 3D information. This alternative approach is based on experimental measurement of effective transport properties ( $\tau_{indir\_phys\_exp}$ ). Nevertheless, modern methods for 3D characterization are clearly the key to a better understanding of tortuosity and associated path length effects.

### 4.1 3D imaging / tomography

#### 4.1.1 Overview and introduction to 3D imaging methods

In the following sections, we consider four main categories of tomography techniques that are relevant for pore-scale characterization of 3D microstructures:

- a) X-ray tomography:  $\mu$ -CT, nano-CT (CT = computed tomography), transmission and scanning X-ray microscopy (TXM, SXM),
- b) serial sectioning methods: focused ion beam (FIB), plasma (P)FIB, broad ion beam (BIB), pulsed laser, mechanical sectioning (Ultra-Microtom) and mechanical polishing,
- c) scanning transmission electron tomography (3D STEM), electron tomography (ET) and
- d) Atom probe tomography (APT).

At the beginning of a microstructure investigation there is always the question which tomography method should be chosen. To answer this question, first order criteria are the range of resolution and the size of the image window, which can be obtained with the different methods. A suitable tomography method must be capable to resolve the smallest relevant features of the investigated microstructure. At the same time, the 3D image window should also be large enough to capture the largest objects of interest in a representative way. The minimum size of a 3D image window with statistical relevance is called representative elementary volume (REV). For the determination of REV sizes see e.g. [70,169]. The requirements of high resolution (small voxels) and at the same time large, sufficiently large (i.e. representative) image window sizes are contradictory constraints, which must be addressed when choosing a suitable tomography method for materials characterization. Finding a good compromise for conflicting imaging parameters (i.e. resolution vs. REV) is a challenge, which requires a sound knowledge of the limitations and possibilities of the available tomography methods.

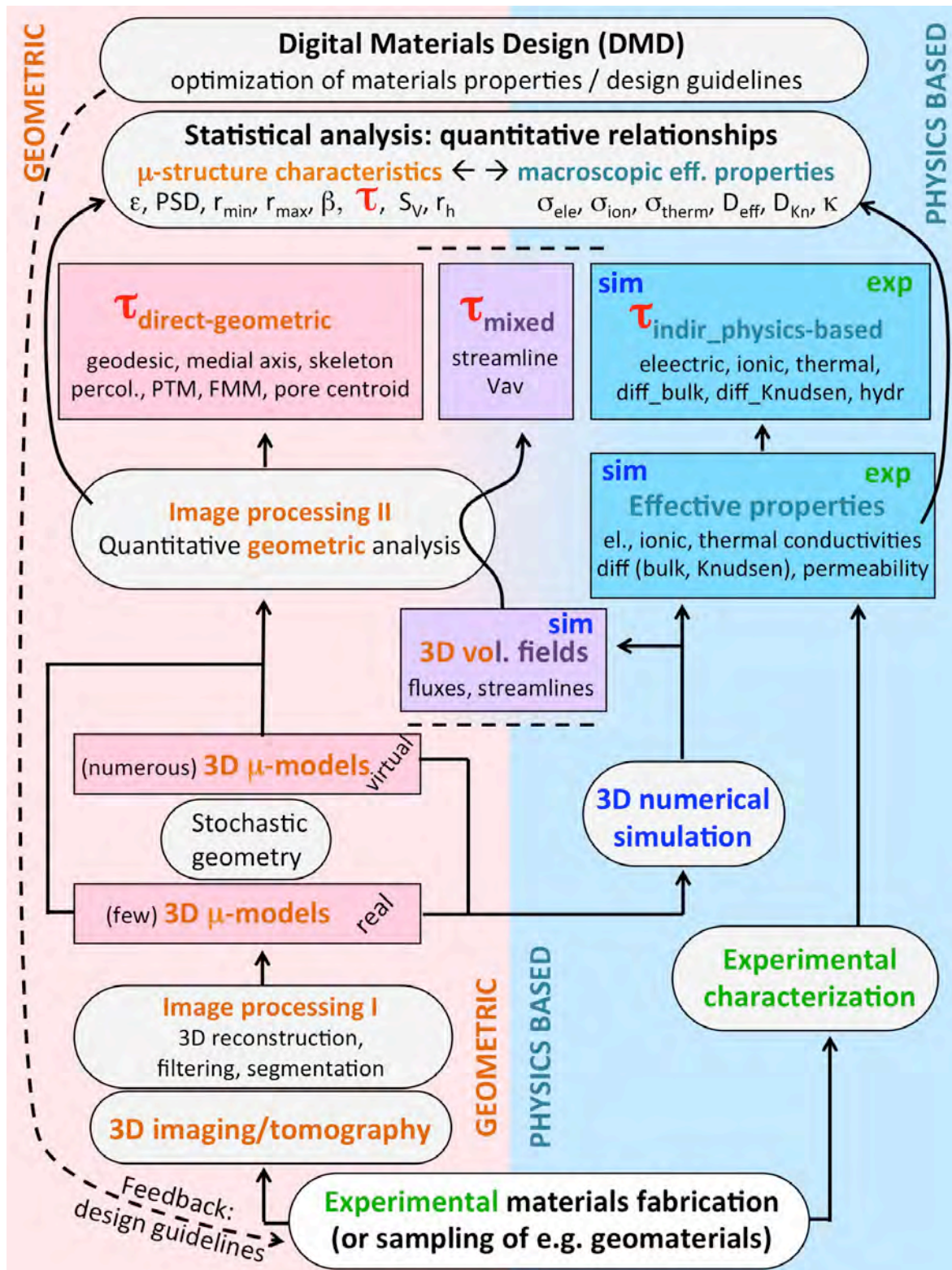


Fig. 14: Schematic illustration of methodologies and workflows for measuring direct geometric, indirect physics-based and mixed tortuosities. Round boxes represent methods and processes, which are discussed in Chapter 4. Rectangular boxes represent either data that is used as input for - or results that are obtained as output from the mentioned processes. Two boxes on top indicate the broader scientific context of tortuosity, which aims to establish quantitative micro-macro relationships and/or to perform digital materials design (see Chapter 5).

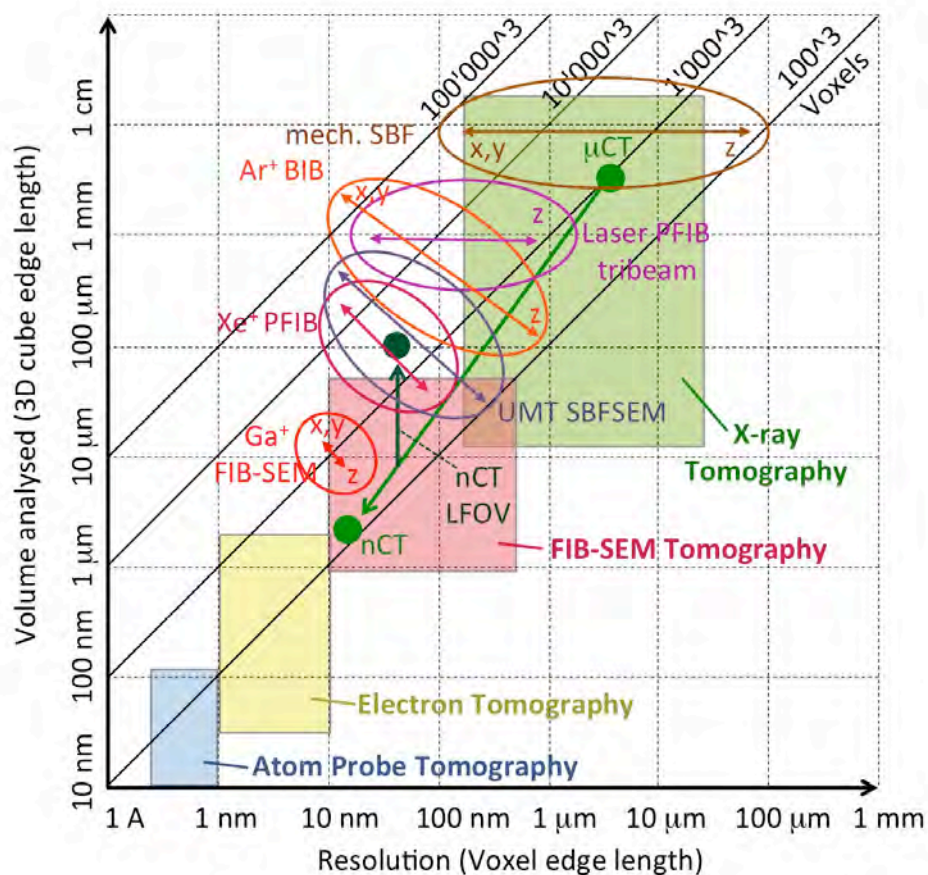


Fig. 15: Graphical representation of important tomography methods characterized by their typical voxel resolutions (x-axis) and size of analyzed volume (y-axis). Each diagonal line represents a specific size of data cube (i.e. constant number of voxels), if the 3D image window is isometric. The colored rectangles indicate characteristic performance fields for traditional tomography methods, which are redrawn from Uchic et al. [335]. The green arrows indicate recent evolution from  $\mu$ -CT to nano-CT and to large-field-of-view (LFOV) nano-CT. Ellipsoids represent the performance of serial sectioning methods. The elliptical shape of performance fields results from the fact that the serial sectioning methods tend to provide anisometric data cubes, because they reveal different properties in x,y- vs. z-directions.

Legend: nCT=nano CT,  $\mu$ CT=micro CT, LFOV=large-field-of-view, PFIB=plasma FIB, UMT SBFSEM=ultra micro-tomography serial block face SEM, BIB=broad ion beam, mech. SBF= mechanical serial block face sectioning.

Fig. 15 illustrates the range of resolutions and image window sizes that can be achieved with X-ray tomography, FIB-SEM tomography, electron tomography and atom probe tomography. Thereby the colored rectangles represent the performance fields that were typically achieved 10-15 years ago (taken from Uchic et al. [335]). At that time the different tomography methods occupied distinct performance fields (regarding resolution and image window size) with almost no overlap.

In the meanwhile, the resolution power of X-ray tomography has tremendously improved. The evolution from  $\mu$ CT to nanoCT is indicated with a green arrow in Fig. 15. For FIB-SEM tomography, the evolution went in the opposite direction. Nowadays the improvement of ion milling efficiency enables to capture much larger image windows. The evolution towards larger image windows also took place due to the introduction of new serial sectioning methods with higher milling rates (e.g. with plasma FIB and pulsed laser), whose performances are indicated with ellipses in Fig. 15.

In summary, the performance fields of X-ray CT, FIB-SEM tomography and other serial sectioning methods nowadays show a considerable overlap. However, it must be emphasized that the performance of a tomography method does not only depend on resolution and image window size. In particular, contrast and detection modes, acquisition time, but also the required sample properties (e.g. stability under imaging conditions, required sample size and sample preparation) must be considered when choosing a suitable tomography method.

#### 4.1.2 X-ray computed tomography

The resolution of X-ray tomography (XCT) has tremendously improved over the last 10 years from  $\mu$ m-range down to the 10-nm-range. XCT is now capable to resolve the microstructure of almost any material in engineering science (e.g. energy materials used in batteries and fuel cells [24,35,44,64,125–127,193,224,228,231,236,318,321–323,355], concrete and asphalt [31,262], polymer composites [104], 3D-printing [263]) as well as materials from geo- [37,38,56,71,152,208,256,371] and life sciences [274]. However, it must be emphasized that the progress is not restricted to the resolution power alone. Note that 10 to 15 years ago, XCT mainly was a static 3D methodology with micrometer resolution ( $\mu$ -CT), which typically provided attenuation contrast. In the meanwhile the high-end version of X-ray tomography provides spatial resolutions down to 10 nm (nano-CT). It can be used as a 4D methodology with fast acquisition times in the sub-second range and it provides multi-mode detection capabilities (i.e. attenuation, phase, diffraction and chemical contrasts). When speaking about X-ray tomography, we have thus to consider a very versatile group of 3D and 4D imaging methodologies, which continue to make fast progress in various directions, as discussed in a recent paper by Yan et al. [361]. For detailed information we also refer to the excellent review and overview articles by Cocco et al. [57], Maire and Withers [217], Pietsch and Wood [260], Brisard et al. [31], Rawson et al. [274] and Zeiss [366].

The following aspects of XCT are important:

a) Basic principles of XCT: In order to understand the trends in X-ray tomography one has to consider the underlying principles at first. Fig. 16 shows a schematic illustration of a modern CT-system. The sample is placed between the X-ray source and the detector. The X-rays penetrate the rotating sample so that a multitude of 2D projections are detected under different angles. Algorithms for 3D-reconstruction, e.g. so-called filtered back projection algorithms, are then used to reveal the internal 3D microstructure from the numerous 2D-projections. In absorption/attenuation tomography, the beam - sample interaction and associated beam intensity ( $I$ ) after travelling through the sample is described by the Beer-Lambert equation

Eq. 43: 
$$I = I_0 e^{-\int \mu(s) ds},$$

where  $I_0$  is the initial beam intensity,  $\mu$  is the local attenuation coefficient and  $s$  is the beam path vector. Thereby, the attenuation coefficient ( $\mu$ ) is a function of electron density and atomic number ( $Z$ ). Local variations of this attenuation coefficient are directly related to the materials microstructure, which can be reconstructed in 3D, e.g. by means of filtered back projection.

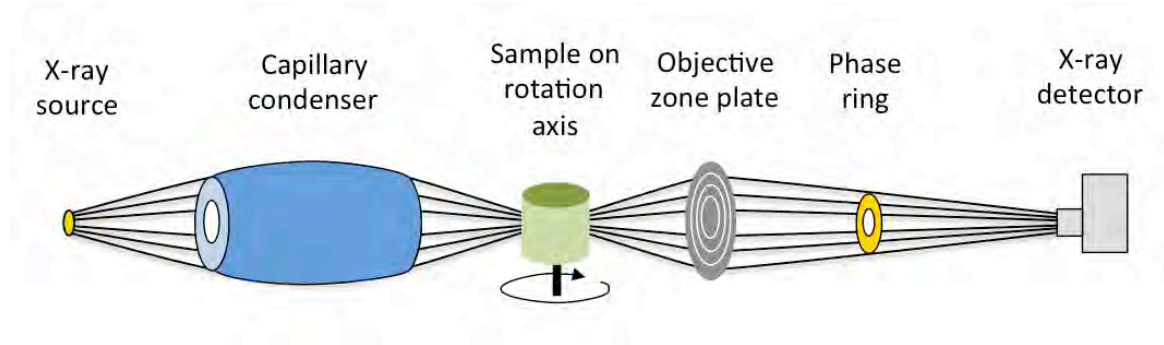


Fig. 16: Schematic illustration of a modern, laboratory based X-ray tomography system, redrawn from Zeiss [366].

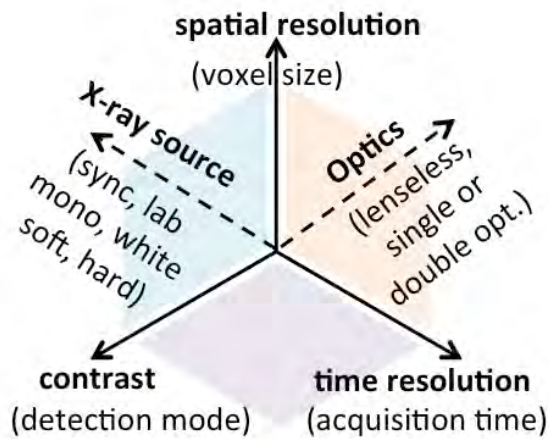


Fig. 17: Schematic illustration of imaging parameters, which need to be considered, when optimizing image acquisition with X-ray computed tomography (XCT) and/or X-ray microscopy (XM).

As indicated in Fig. 17, spatial resolution is only one of the performance relevant characteristics. Other important performance characteristics are for example time resolution/acquisition time and contrast/detection modes. The type of the X-ray source and the optical system also has a strong impact on the performance. Tremendous progress was achieved in all these technological fields. However, there also exists a multitude of interdependencies between the characteristics and parameters mentioned above. For example, faster acquisition usually leads to higher noise and therefore also to weaker contrast and lower effective spatial resolution. In the following, we briefly discuss the most important performance parameters and associated interdependencies.

b) Attenuation and phase contrasts: The interaction of X-rays with the material depends on the complex refractive index ( $n$ ) with a real part ( $1-\delta$ ) and an imaginary part ( $\beta_{x-ray}$ ), i.e.,

$$\text{Eq. 44} \quad n = (1 - \delta) + i\beta_{x-ray}$$

The attenuation coefficient ( $\mu$ ) itself depends on the imaginary part ( $\beta_{x-ray}$ ) of the complex refractive index and on the wavelength ( $\lambda$ ), where

$$\text{Eq. 45} \quad \mu = 4 \pi \beta_{x-ray} / \lambda$$

In materials with a high imaginary part ( $\beta_{x-ray}$ ), the X-rays amplitude is damped, which leads to a lower intensity (i.e. stronger absorption). The attenuation strongly decreases with the beam energy  $E$ . More precisely, it holds that  $\beta_{x-ray} = 1/E^4$ . Soft X-rays thus provide a better attenuation contrast and also a higher resolution can be achieved. However, stronger absorption at lower beam energy limits the size of samples that can be transmitted and at the same time increases the problem of beam damage with soft X-rays. The contrast between different material constituents can also be improved significantly by using dual-energy X-ray tomography (see e.g. Gondzio et al. [115]).

Phase contrast (PC) imaging is an interesting alternative for materials with a weak attenuation contrast. Local variations of the real part of the refractive index ( $1-\delta$ , see Eq. 44) induce changes of the wavelengths, which lead to beam deflections. These refractive beam-material interactions can be indirectly detected as a phase shift ( $\phi$ ). The 3D reconstruction of local  $\delta$ -values reveals the materials phase contrast, which, in opposite to the attenuation contrast, increases with beam energy ( $\Delta\delta/\Delta\beta_{x-ray} = E^2$ ). For materials with weak absorption contrast (e.g. graphite vs. lithium in battery electrodes), phase contrast imaging with hard X-rays usually gives better results.

There are different methods for phase contrast imaging (propagation PC, grating-based PC, Zernike PC). These contrast modes require more complex optics, coherent beam source and more sophisticated 3D reconstructions. However, nowadays even lab-based tomography systems offer the option of phase contrast imaging. For further explanations on attenuation and phase contrast as well as on the principles of 3D reconstruction we refer to Pietsch and Wood [260] and the references therein.

c) Spatial resolution and magnification: In principle, X-ray microscopy offers three types of magnifications, which are based on X-ray optics, light optics or geometric set-up.

c1) X-ray optics work with reflection, diffraction or refraction (see e.g.: [www.x-ray-optics.de](http://www.x-ray-optics.de)). Recent progress in nanofabrication has boosted the technology for X-ray optics (e.g. Fresnel Zone Plates FZP), which now enables voxel resolutions down to 10 nm. A major drawback of X-ray optics is the fact that it generally reduces the beam flux and therefore leads to longer acquisition times. This can be partially compensated by using brilliant synchrotron sources with a high beam flux.

c2) Conventional light optics can be introduced in detection systems that consist of a scintillator and a CCD or CMOS camera. The scintillator converts the X-rays into visible light, which can then be magnified with optical lenses similar to conventional light microscopes. In contrast to X-ray optics, the light optics is highly efficient and fast. However, the diffraction limit of visible light constrains the resolution to little less than  $1\ \mu\text{m}$ .

c3) In systems with divergent, cone-shaped beams, the image can be geometrically magnified by adjusting the relative positions of source, object and detector. The resolution in lens-less systems with purely geometric magnification is typically limited to the  $\mu\text{m}$ -range.

In modern X-ray tomography systems these three magnifying methods are combined, so that a high magnification can be achieved together with a relatively high efficiency and a relatively fast acquisition time (see e.g. [366]). The evolution of 'best' spatial resolution in X-ray tomography over the last 50 years is illustrated in Fig. 18 a) (adapted from Maire and Withers [217]). This figure shows that it is now possible to reach voxel resolutions in the  $10\ \text{nm}$ -range by soft X-ray tomography at synchrotron beam lines equipped with Fresnel Zone Plate optics. The resolution power for hard X-rays is weaker. However, soft X-ray tomography suffers from the limited sample thickness, especially for materials with strong absorption (e.g. metals, heavy elements, high density).

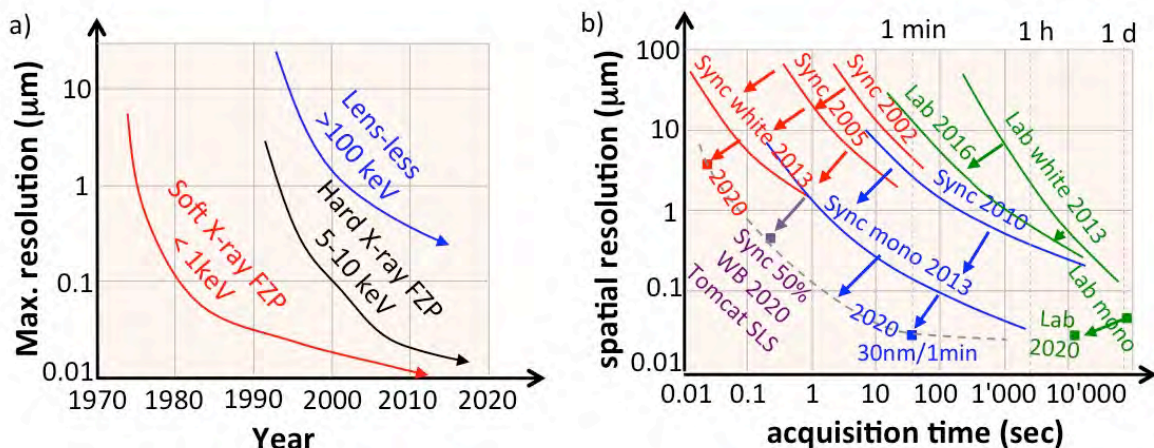


Fig. 18: Improvement of the spatial resolution in X-ray tomography. a) Evolution of best resolution over the last 50 years for lens-less systems (blue), for hard X-ray tomography with Fresnel Zone Plate (FZP) (black) and for soft X-ray tomography with FZP (red). b) Evolution of X-ray tomography, illustrating the link between spatial and temporal resolutions. Red: Synchrotron, white beam / Blue: Synchrotron, monochromatic / Green: Laboratory systems. The violet point marks the current high-end performance with sub-second and sub- $\mu\text{m}$  resolutions achieved at synchrotron with 50% white + 50% monochromatic light (pers. communication, F. Büchi, PSI, Swiss Light Source SLS, 2020). The curves in a) and b) are redrawn from Maire and Withers [217] and updated with current trends presented in the literature. For recent progress in nano CT see Yan et al. [361].

d) Time resolution vs. spatial resolution: In general, a fast acquisition time comes at the expense of increased noise. Synchrotron beams with a high brilliance can reduce the noise and are thus particularly well suited for fast X-ray imaging. Nowadays, 4D imaging at 20 to 50 Hz has become possible with white beam synchrotron tomography (see e.g. Maire et al. [216]). As shown in Fig. 18b, time resolution and spatial resolution are constraining each other. Both of them also strongly depend on various other aspects such as the facility type (synchrotron vs. laboratory systems), beam energy and beam intensity (monochromatic vs. white vs. mixed beams). Also the attenuation contrast of the material under investigation and the size of the sample represent constraining factors.

The best time resolution can be achieved with the white beam (WB) of synchrotron sources due to the relatively high beam flux, however with certain limitations in magnification. Monochromatic beams are better suited to exploit the power of magnifying systems such as FZP, which opens new capabilities for nano-CT [361]. Even lab-based systems with X-ray optics are nowadays capable of providing 50 nm resolutions. However, lab-based systems exhibit a relatively long acquisition time, which is typically several hours per 3D image. A good compromise between short acquisition time, high spatial resolution and reasonable signal to noise ratio can be reached by mixing monochromatic and white beams (e.g. 50% WB). In this way, sub-second tomography with sub- $\mu\text{m}$  resolution has become possible, as reported by Büchi (pers. comm., 2020) for the Swiss Light Source (SLS) (violet data point in Fig. 18 b). For white beam synchrotron tomography, 30 nm spatial resolutions at 1 minute acquisition time is reported as current state of the art (Yan et al. [361]).

Many parameters must be considered when optimizing temporal vs. spatial resolutions. The acquisition time can be estimated based on the required number of projections ( $N$ ), which increases with the image window size and associated number of pixels ( $q$ ) in horizontal direction, i.e.,

$$\text{Eq. 46:} \quad N = q \pi / 2$$

For example, for  $q=1024$  pixels, the required number of 2D projections ( $N$ ) is equal to 1570. With a total rotation of  $180^\circ$  this results in 8.7 projections per  $1^\circ$ . For these settings, 3D imaging at 1 Hz requires an acquisition time of 0.64 ms for a single 2D projection. By pushing the limits of fast tomography towards 100 Hz, new technological solutions needed to be developed such as fast signal processing (e.g. read out and storage of up to 100 GB per second, see Mokso et al. [226]), highly efficient optics and detector systems (Bührer et al. [35]), more brilliant sources, intelligent 3D reconstruction strategies (e.g. based on a smaller number of projections or segmentation oriented reconstructions using a priori knowledge about the phases, see [34,46,129,173]). Last but not least, fast data acquisition also calls for dedicated software that enables efficient analysis of the huge 4D image data volumes (e.g. digital image and volume correlation DIC/DVC or 4D particle tracking, see [36,158,211]). In all these fields, fast progress and innovation is currently ongoing.

e) Experimental 4D tomography: Fast X-ray tomography opens new possibilities for in-situ and in-operando studies of dynamic processes at pore-scale and even below. For lab based X-ray tomography, the possibilities of high speed 3D imaging are reviewed in a

recent article by Zwanenburg et al. [379]. With synchrotron-tomography, ultrafast 3D imaging can now be performed at 20 Hz and even faster (Maire et al. [216]). In-situ mechanical testing is one prominent example for the application of fast 4D tomography. Nano-mechanical devices for compression, tension and indentation tests, which are specially designed for dynamic tomography investigations, are nowadays commercially available. Also the preparation of small samples (e.g. pillars with sizes in the range of mm down to a few  $\mu\text{m}$ ) suitable for nano-mechanical testing is now relatively straightforward due to the availability of focused ion beam (e.g. Xe<sup>+</sup> plasma FIB) and laser technologies. In-situ tomography during mechanical testing is thus evolving rapidly, for example in the field of alloys [375] and batteries [64].

Fast tomography is also used in high temperature studies. Villanova et al. [339] reported the 4D-evolution of microstructures and nucleation of nano-droplets upon sintering of alloys at 700°C.

So-called in-operando studies enable capturing dynamic processes under real life conditions. In-operando studies of electrochemical cells (batteries, fuel cells) are very challenging, because they usually require some in-house development of dedicated experimental equipment, including miniaturization of the cells and of the electrochemical test setup. A tomography system with an efficient optical microscope was designed at the Swiss Light Source (SLS). It was recently used for in-operando studies of water clusters and two-phase flow in PEM fuel cells at temporal and spatial resolutions of <1-10 Hz and <1-10  $\mu\text{m}$ , respectively [35,81,236,358].

In battery research, synchrotron based in-operando studies have been used to reveal the 4D microstructure evolution upon degradation and/or (de-)lithiation [93,116,294].

With laboratory-based systems the acquisition time is generally longer and rather suitable for the characterization of relatively slow processes in time-lapse mode.

Nevertheless, two-phase flow in geological samples was characterized with lab-based tomography at temporal and spatial resolutions of less than 1 min and 15  $\mu\text{m}$ , respectively (Bultreys et al. [38]). The lack of attenuation contrast in two-phase flow can be approached with time-resolved phase contrast imaging as reported by Ohser et al. [247]. 4D tomography is thus applicable for dynamic studies in various fields of materials and engineering sciences and also in geology [245,258,370] as well as in life sciences [274]. The exciting possibilities of modern high-end X-ray tomography open new possibilities for the investigation of tortuosity effects. The exploitation of these opportunities requires dedicated and efficient solutions in image processing, which will be discussed below in Sections 4.2-4.4.

#### 4.1.3 FIB-SEM tomography and serial sectioning

Commercial dual beam machines combining focused ion beam (FIB) with a scanning electron microscope (SEM) became available around the year 2000. Initially FIB-SEM was used mainly for failure analysis in semiconductor industries. However, very soon it was recognized that FIB-SEM has a great potential for high-resolution 3D imaging by serial sectioning. First FIB-SEM tomography work was based on in-house developments of a machine controlled procedure for serial sectioning (Holzer et al., 2004 [135]).

Already in 2004, voxel resolutions of 6x7x16 nm could be reached based on the fully automated serial sectioning procedure with integrated drift correction. With a voxel resolution of ca. 10 nm, FIB-SEM tomography opened new possibilities to perform microstructure investigations at the sub- $\mu\text{m}$  scale. FIB-SEM tomography thus became the method of choice for 3D investigations of fine-grained porous media

[141,142,178,179,233] at the time when nano CT was not yet available. Nowadays, 3D acquisition by 'slice and view' is possible with any commercial FIB-SEM machine. Examples for applications cover the fields of geological materials (sandstone, shale, coal) [176–179,204,280], zeolite [13], graphite [143,237], polymers [237], thin films used as optical layers [249], catalysts [354], paper [11] and biomaterials [225]. FIB-SEM tomography is also very important for microstructure investigations of energy materials such as fuel cells [136,156,170,223,254,255,305,340,341,352,367] and batteries [6,87,207,210,342,377].

FIB-SEM serial sectioning can be used in combination with different detector systems such as EDS (energy dispersive spectroscopy) for mapping element concentrations and EBSD (electron backscattered diffraction) for mapping grain orientations and crystallographic information (see e.g. Uchic et al. [335]). With these analytical detection modes, FIB-SEM tomography became particularly important for the study of metals, alloys and corrosion science [157,188,192,306], but also for battery materials [99,100,271]. Furthermore, the combination of FIB-SEM tomography with a cryo-transfer system enables the study of delicate, water-containing samples such as cement suspensions, swelling clay and biomaterials [134,137,138,378]. Reviews on FIB-SEM tomography and related serial sectioning techniques are given by Holzer and Cantoni [133], Cantoni and Holzer [43], Monteiro and Paciornik [227] and Echlin et al. [78].

As indicated in Fig. 15, FIB-SEM tomography initially occupied a niche among other 3D imaging techniques due to its high resolution of ca. 10 nm. It is only in the last few years that resolutions of less than 100nm can also be reached with X-ray nano-CT. The main limitations of FIB-SEM tomography come from the milling capabilities. With a conventional Ga FIB source, high milling precision that allows slicing in the range of 10 nm is only possible with relatively low beam currents of ca. 1 nA or less. The corresponding low milling rates lead to relatively long acquisition times of ca. 10 to 24 hours for a stack of 500 to 1000 images. Low milling rates also lead to relatively small sizes of the 3D image window with edge lengths that are typically equal to only a few  $\mu\text{m}$  to tens of  $\mu\text{m}$ . The milling rates can be increased by using higher ion beam currents, but this comes at the expense of larger beam spot sizes and lower milling precision. Fortunately, over the last years, the milling capabilities of FIB-sources improved significantly [17,39,372] and also new and more efficient serial sectioning techniques were introduced such as Plasma FIB and broad ion beam (BIB) [78,79]. Hence, as indicated in Fig. 15, the various serial sectioning techniques for 3D image acquisition nowadays cover a wide range of voxel resolutions from ca. 5 nm to several  $\mu\text{m}$  and a wide range of image window sizes with edge lengths from  $\mu\text{m}$  to mm.

#### a) Basic principle of serial sectioning with a Ga<sup>+</sup> FIB-SEM dual beam machine

The FIB-SEM geometry for serial sectioning is illustrated in Fig. 19. In a first step, a cube representing the region of interest is exposed with a high beam current for rapid ion milling. The x-y imaging plane, also called 'block-face', is then polished with a lower ion beam current. Subsequently, an SE- or BSE-image is acquired by scanning the block face with the electron beam. A stack of 2D images (i.e. a 3D image volume) is then produced in a fully automated serial sectioning procedure, which consists of two alternating steps: 1) Thin layers of e.g. 10 nm thickness are sequentially removed with the ion beam and 2) SEM images (with pixel resolution of e.g. 10 nm) are acquired from the freshly exposed surfaces. In this procedure, fiducial markers are used for automated correction

of mechanical, magnetic and electronic drifts. Ideally the milling step size in z-direction is similar to the pixel resolution of the SEM images (x-y), which results in isometric voxels.

In most cases a large number of ca. 1000 or more images would be ideal in order to acquire a representative 3D image volume. The acquisition time for a single slice and view cycle includes the following components: a) FIB milling time, which depends on the beam current (milling rate), on the size of the imaging plane (x-y) and on the thickness of the milled layer (z). b) SEM imaging time, which depends on the number of pixels (i.e. area of block-face and resolution) and on the dwell time. Thereby, fast scanning negatively affects the signal-to-noise ratio. c) Time for drift correction(s) with fiducial markers. d) Time for beam stabilization after switching from electron to ion beam and back.

The total acquisition time thus depends on various parameters such as the size of the 3D image window, the ion beam current, the electron scan rate, the detector efficiency. Also contrast (or noise) and sputter rates that are characteristic for the material under investigation have an influence on the acquisition time. Depending on the chosen parameters for serial sectioning, the total acquisition time can thus vary significantly. Typically, in a relatively fast setup with small cubes of a few  $\mu\text{m}$  edge lengths, an entire slice and view cycle takes ca. 30 sec. For a stack with 1000 images this results in a total acquisition time of 8 hours and 20 min. The acquisition time can easily increase by a factor of 3 to 4, e.g. for larger cubes (tens of  $\mu\text{m}$ ), for more precise ion milling and/or slower electron scanning (higher signal-to-noise ratio). Often the number of images in the stack is then reduced to only a few 100 images in order to shorten the total acquisition time. This leads to 3D image volumes with non-isometric dimensions (e.g.  $20 \times 20 \times 5 \mu\text{m}$ ).

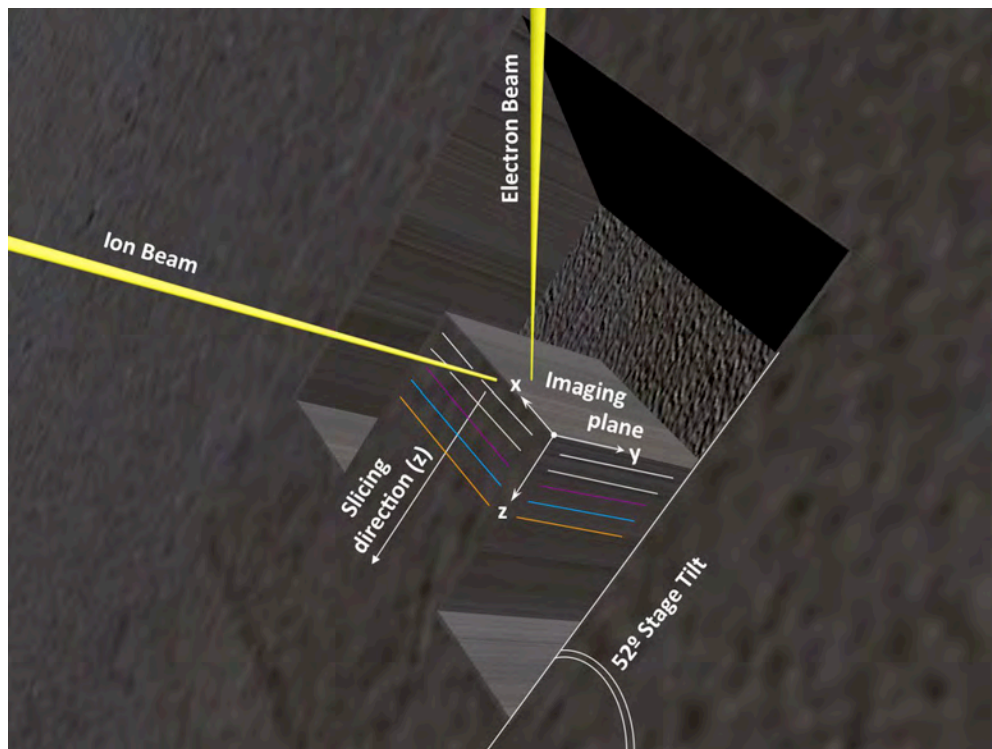


Fig. 19: Illustration of serial sectioning with a FIB-SEM dual beam system (taken from Holzer et al. [135])

## b) Trends in serial sectioning I: Improvement of milling capabilities

Over the last years the milling capabilities for serial sectioning have considerably improved due to the appearance of new ion sources and new milling techniques (for details see e.g. Bassim et al. [17] and Echlin et al. [78]):

- Conventional FIB: The liquid metal ion source (LMIS) is the basis for conventional Ga FIB. With beam currents with an order of magnitude between pA and 100 nA, the sputter rates of Ga FIB machines are relatively low, - especially for organic matter and ceramics. In the meanwhile, LMIS works with many different metals (Ga, Al, In, Au, Bi) and alloys. Nevertheless, the milling capabilities of LMIS are still rather limiting. Some improvements of the sputter rates could be achieved with a new 'rocking milling procedure'.

- Plasma (P)FIB: Magnetically enhanced inductively coupled plasma FIB sources are capable of significantly higher sputter rates. In addition, at beam currents above 10 to 50 nA, the Xe PFIB provides a much smaller beam diameter than conventional Ga FIB (at similar beam currents). The PFIB thus opens new possibilities for large area serial sectioning, whereby the edge length of the image window can reach dimensions in an order of magnitude of 100  $\mu\text{m}$ . Compared to Ga-FIB, the milling with Xe PFIB is ca. 60 times faster, but at the same time PFIB is capable to reveal small slicing thicknesses (and voxel resolutions) of ca. 10 nm. In addition, Xe PFIB produces less beam damage (i.e. the amorphous surface layer is relatively thin) and it is therefore better suited for 3D EBSD compared to conventional FIB. Applications of large area serial sectioning with Xe PFIB are discussed by Burnett et al. [39] and Zhang et al. [372,373].

- Broad Ion Beam: The hollow anode discharge (HAD) Ar source represents the basis for broad ion beam (BIB) machines, which can be used for sequential milling and polishing of large areas up to the  $\text{mm}^2$ -range. For in-plane milling and polishing with a broad ion beam, a metal blend is used with a high milling resistance (e.g. W). HAD Ar ion sources reveal high beam currents up to the  $\mu\text{A}$ -range at low beam energies ( $\leq 5$  kV). Milling at low kV induces relatively low beam damage, which makes BIB particularly suitable for 3D EBSD. Generally the z-resolution (thickness of removed layer) for BIB serial sectioning is in the 100 nm to  $\mu\text{m}$  range, but recently more precise BIB-serial sectioning with z-distances as thin as 10 nm were reported [111,353].

- Pulsed laser and combined tri-beam systems: Laser-based systems combined with various microscopy platforms (light microscopy, SEM, FIB-SEM) have been available for many years. Due to limited resolution of the laser, these systems were rather used in the past for targeted feature extraction and micromachining. Thereby, the milling precision of traditional pulsed laser-systems was not suitable for serial sectioning applications. However, modern femtosecond pulsed lasers nowadays provide much higher milling precision and, at the same time, they cause less beam damage. Recently, a femtosecond laser was integrated into a dual beam PFIB-SEM, which results in a tri-beam system. This device enables precise serial sectioning of large areas in the  $\text{mm}^2$  range. With the tri-beam system, the PFIB can be used for fine polishing after efficient milling with the laser. Typically the step size of laser milling in z-direction is 0.5 to 1.5  $\mu\text{m}$  [79,272,273].

For comparison, the typical performances of the discussed serial sectioning techniques are shown in Table 4. This table also includes ultra-micro tomography serial block face SEM (UMT SBFSEM) [67], which uses a diamond knife for mechanical sectioning. Furthermore also robotic serial sectioning by mechanical polishing [277] is also included for comparison.

Most serial sectioning techniques have a certain tendency towards anisometric voxel resolution. The pixel resolution of the SEM images (i.e. in the x-y plane) is typically in the range of 10 nm. Even large areas up to the mm<sup>2</sup> range that are produced for example with BIB, laser-PFIB tri-beam or ultra-micro tomography can be efficiently scanned at high resolution by using a stitching approach for the SEM imaging. In contrast, for these serial sectioning methods the step size in z-direction is typically limited to ca. 1 μm, which is 20 to 100 times larger than the SEM pixel resolution (see the column aspect ratio, resolution in Table 4).

The dimensions of the 3D image windows (i.e. CEL, cube edge lengths of analyzed volumes) also tend to be anisometric. For example with PFIB and BIB, the total thickness of the image stack (z-direction) that can be acquired at high slicing resolution within reasonable acquisition time is often 10 to 50 times smaller than the size of the 2D image window in x-y directions (see Table 4, column aspect ratio, CEL). These anisometric properties of serial sectioning are also visualized in Fig. 15 by elongated ellipses. The long axes of the ellipses indicate different dimensions of voxels and image windows in x-y- (top left part of ellipses) compared to z-directions (bottom right part of ellipses). Large area serial sectioning is thus particularly well suited for an analysis of anisometric samples such as the thin layers of SOFC electrodes (see e.g. Mahbub et al. [215]).

Table 4: Comparison of serial sectioning techniques and associated characteristic properties. For most serial sectioning techniques, the resolutions tend to be different for the x-y imaging plane and for the sectioning direction (z). Furthermore, the number of acquired images (slices) is usually relatively small due to long acquisition times. This results in anisometric data cubes with aspect ratios different from 1. (CEL = cube edge lengths of a 3D image window). Note that the properties (e.g. resolution, number of pixels) are estimations of characteristic values. In reality these values can vary significantly, depending on the chosen acquisition parameters.

Sectioning method	Imaging method	2D imaging plane (x,y)			Slicing direction (z)			Aspect ratios (x,y)/z	
		Resolution x,y nm	Nr of Pixels x,y -	CEL x,y μm	Resolution z nm	Nr of slices z -	CEL z μm	Resolution -	CEL -
Ga FIB-SEM	SEM	10	1000	10	10	500	5	1	2
Xe PFIB	SEM	20	10'000	200	50	1'000	50	0.4	4
Ar BIB	SEM	50	100'000	5'000	1'000	100	100	0.05	50
Laser tribeam	SEM	10	100'000	1'000	1'000	1'000	1'000	0.01	1
UMT SBFSEM	SEM, TEM, tSEM	10	50'000	500	500	100	50	0.02	10
mech. polishing	Light micr.	500	20'000	10'000	100'000	100	10'000	0.005	1

CEL = Cube Edge Length

### c) Trends in serial sectioning II: Imaging capabilities and detection modes:

A significant advantage of destructive serial sectioning compared to X-ray tomography comes from the fact that the exposed surfaces (block-faces) can be probed with many different imaging and surface characterization techniques. Thereby, SEM based serial

sectioning benefits considerably from the progress in low-voltage SE- and BSE-imaging, which provide high contrast at high resolution. This progress is mainly due to the innovative improvement of in-lens detectors [43]. In addition, fast spectral and elemental mappings with silicon drift EDS detectors open up new possibilities in 3D chemical mapping. Furthermore, new EBSD cameras enable grain orientation mappings with significantly shorter acquisition time, higher spatial resolution and larger image window size. As discussed by Echlin et al. [78], there is a clear trend in serial sectioning tomography towards larger size of the image windows (e.g. with PFIB, Laser-tribeam or BIB). Another important trend is the evolution towards simultaneous acquisition of multiple signals, which is also called multi-modal tomography (i.e. serial sectioning with simultaneous acquisition of EDX or EBSD together with SE, BSE and even with SIMS), see e.g. the 3D FIB EBSD image data considered in [99,100].

#### 4.1.4 Electron tomography

Transmission electron microscopy (TEM) enables for microstructure analysis at the nano-scale and even with atomic resolutions. Due to the invention of aberration corrected lenses, probe sizes as small as 0.05 nm can be reached with TEM [86]. In electron tomography (ET) numerous TEM projections are acquired in a tilt series at different angles, from which the corresponding 3D structure can be reconstructed. Current trends in nano-tomography (ET and X-CT) were recently reviewed by Yan et al. [361].

Distinct ET methods have been developed separately for physical and biological sciences in order to overcome the specific sample-based limitations [85]. In materials science, ET is particularly important for the study of functional materials such as nano-porous materials for chemical engineering, nanoparticle agglomerations or nanostructured catalysts in fuel cells [147,311].

A major strength of ET is obviously its high resolution-power. However, a relatively short mean free path length of electrons puts strong limitations to the maximum sample thickness, which is ca. 100 nm for mid Z-materials at 200 keV. In nano-tomography mode, ET is typically performed with a resolution of ca. 0.5 nm. The maximum sample and image window sizes are then typically not more than 100-300 nm. In atomic scale tomography mode, ET is performed with <0.1 nm resolution. The corresponding image window size is then typically not more than 10-20 nm.

Moreover, a particular strength of ET is the ability to detect different signals from the same sample. Thereby one has to distinguish between full field transmission (TEM) and scanning transmission modes (STEM). Full field imaging allows for faster acquisition and low dose imaging of delicate samples. High Z-contrast is achieved in STEM with dark field (HAADF) and bright field (BF) modes. STEM also enables spectroscopic tomography, whereby chemical maps are collected with EDS (energy dispersive spectroscopy) or EELS (electron energy loss spectroscopy). In addition, new detection modes are currently evolving, which provide interesting information about the spatial distribution of magnetic and electric fields, strain, grain orientation and/or crystallographic defects (see e.g. [361]).

Current improvements aim to push the limits of ET in various directions: a) The acquisition time is typically in the range of several hours, due to time consuming tilt by tilt tracking of objects. In future, automated repositioning can shorten the acquisition time considerably. b) The precision of the 3D reconstructions is limited due to a relatively small tilt range (missing wedge problem) and due to a relatively low number of projections. New algorithms based on machine learning are capable to reveal much better 3D reconstructions, despite these limitations. c) New sample holders and stages, as well as improved sample fabrication procedures with automated FIB (producing cylindrical instead of lamellar samples) will contribute to better data acquisition and more reliable 3D reconstructions. d) Important improvements can also be expected with respect to the detectors, which are capable to capture different signals (as mentioned above) with higher sensitivity, better signal-to-noise ratio and faster acquisition time.

#### 4.1.5 Atom probe tomography

Atom probe tomography (APT) is capable to perform 3D analysis at the atomic scale (around 0.1-0.3 nm resolution in depth and 0.3-0.5 nm laterally). Electrochemical polishing and focused ion beam (FIB) methods are used for sample preparation in the form of a very sharp tip. A very high electrostatic field (in an order of magnitude of 10 V/nm) is induced at the sharp tip, which is slightly below the point of atom evaporation. Laser or HV pulsing is then superimposed, in order to evaporate single atoms from the tip surface by a field effect (near 100% ionization). The atoms or ions are collected very efficiently with a position sensitive detector (PSD). The detector allows measuring simultaneously the mass of the ions (more precisely: the mass-over-charge ratio) by time of flight and at the same time to reconstruct the original position of the atom on the tip surface. The atoms are progressively removed from the tip so that a 3D image of the material can be reconstructed at the atomic scale.

APT has been successfully applied in materials science for many years, in particular for metals, alloys and semiconductors (e.g. for the study of interfaces and inter-diffusion phenomena). A review on APT investigations of aluminum alloys was recently given by Ceguerra and Marceau, 2019 [50]. Technical advancements such as the introduction of pulsed laser-assisted field evaporation also enable atom probe analysis of oxides, which extends the field of APT applications to geological materials and metal corrosion (see e.g. Eder et al. [80]).

Air- and temperature-sensitive samples require transfer systems between FIB and atom probe under both vacuum and cryogenic conditions [75,222]. Such a cryo-transfer system was recently used to study corrosion of nuclear glass. The sample consisted of a nano-porous gel filled with liquid electrolyte. It was shown for the first time that APT is capable to describe the 3D distribution of chemical concentrations at solid-liquid interfaces with (near) atomic resolution (Perea et al. [257]). The size of the 3D image window was 20x20x20 nm<sup>3</sup>. APT thus enables one to detect variations in the chemical composition of the electrolyte and to combine this chemical information with structural information of tortuous pathways in the nano-porous network.

#### 4.1.6 Correlative tomography

For the investigation of complex microstructures, the application of a single microscopy method with a fixed resolution and/or with a single detection mode is sometimes not

suitable for a representative characterization. For example, in materials with a wide pore size distribution, nano-tomography may be capable to capture small pores and bottlenecks, but the image window is then often too small for capturing the larger pores in a representative way. Alternatively, low-resolution tomography that provides a larger and representative image window may not be capable to resolve the smaller pores and bottlenecks. Fortunately, the contradictory requirements of a high resolution and a large representative volume can be satisfied with the help of correlative tomography, which makes use of two or more tomography methods with different resolutions and image window sizes. Furthermore, in multi-phase materials, correlative tomography can also be used to capture multimodal information. The combined detection of Z-contrast, chemical- and crystallographic information can then be used as a basis for reliable interpretation, segmentation and phase identification.

The power of correlative microscopy for advanced microstructure characterization has been recognized for many years. Thereby, complementary microscopy methods with different resolutions and detection modes are applied for the same regions of interest (RoI). Image registration is then used to combine the information of the spatially overlapping data sets [122,252]. Initially correlative microscopy was mainly based on the combination of 2D microscopy methods such as light and fluorescence microscopy, AFM, SEM, (S)TEM, (S)XTM (e.g. [88,112]). However, very soon correlative imaging approaches were also combining 2D microscopy with tomography (see e.g. Caplan et al. [45]). Nowadays, due to the progress in 3D imaging and 3D image processing, the number of studies applying correlative tomography is rapidly increasing. Correlative tomography enables characterizing the full complexity of disordered microstructures by combining multi-modal, multi-scale and multi-dimensional information acquired with multiple 3D techniques from the same region of interest (or from overlapping RoIs). A full review of correlative tomography is beyond the scope of this article. Overviews of correlative tomography are given by Burnett and Withers [40,41] for materials science applications, as well as by Bradley and Withers et al. [29] for biomaterials.

In correlative tomography various combinations of 3D techniques are possible. Typically non-destructive methods at lower resolution such as X-ray CT or confocal laser scanning microscopy are used in a first step. Subsequently, destructive 3D methods (e.g. 3D FIB-SEM, APT, ET) in combination with site-specific sampling techniques (e.g. with laser and with FIB lift-out techniques) are used for zoom-in characterization at higher resolutions. To illustrate the evolution of correlative tomography we briefly present some literature examples from the last 10 years, which are also summarized in table 'Correlative Tomography'.

In Caplan et al. [45], the correlation of various 3D and 2D methods are discussed in context with a thorough characterization of biomaterials. Tariq et al. [321] used multi-scale tomography (XCT and FIB-SEM) for the characterization of hierarchical pore structures in ceramics. The cumulative pore size distributions (PSD) obtained with multi-scale tomography are different from those obtained with mercury intrusion porosimetry (MIP). The example illustrates that it is difficult to quantify hierarchical pore structures based on information from different methods (experimental vs. imaging) and different length scales. New up-scaling approaches are needed for integration of multi-scale information in hierarchical pore networks. Shearing et al. [301] investigated the microstructure of Lithium Ion Battery electrodes with XCT at different length scales. It was possible to obtain consistent results for porosity, tortuosity and surface area with different CT scans. Apparently, with the chosen

resolutions and sizes of data volumes, it was possible with different tomography methods to capture the relevant features in a representative way. Burnett et al. [40] used correlative microscopy for the study of metal corrosion, combining multi-scale tomography with 2D maps from EBSD and EDS. This approach enabled to distinguish between pitting and inter-granular corrosion phenomena. Bradley and Withers [29] used correlative tomography for characterization of biological materials with hierarchical microstructures and anisotropic mechanical properties. Saif et al. [280] applied multi-scale tomography in combination with various 2D methods (MAPS, high resolution SEM, stitching of multiple SEM images) for characterization of oil shale pyrolysis. The multi-scale and multi-modal information enabled a thorough characterization of the heterogeneous clay microstructures, including accurate identification of porosity, organic matter and mineralogical composition. Kwiatowski da Silva et al. [194] used correlative TEM (ET) and atom probe tomography (APT) in combination with multi-scale modeling for characterization of Fe-Mn steels. This approach provides unique insight on the mechanism of Mn segregation to edge dislocations. Fam et al. [89] used different tomography methods (nano-CT, FIB-SEM, ET) at high resolutions (1 - 15 nm) for characterization of hierarchical structures in nano-porous gold catalysts. The results for porosity and pore size vary depending on the method, even though the resolutions were not very different. Most probably this puzzling picture arises from different contrast modes, which have a strong impact on the phase segmentations and associated quantitative analyses. Keller and Holzer [175] and Keller et al. [180] used XCT, FIB-SEM and ET for a thorough characterization of pores in Opalinus clay. A concept for image-based up-scaling from micro- to meso-scale porosity and associated permeability is presented. This approach is also capable of capturing the anisotropic transport properties of clays across lengths scales from nm to mm. In a recent study on PEM Fuel cells, Meyer et al. [224] combined multi-scale XCT with high resolution 2D imaging by He-FIB and TEM. The different methods give complementary information, which is important for accurate identification of relevant features in the heterogeneous multi-layer assembly, such as Pt nanoparticles in the micro-porous catalyst layer (MPL) and meso-pores in the gas diffusion layer (GDL).

Table 5: Examples of correlative tomography studies from the last 10 years, illustrating the methodological evolution and trends

1st Author	Caplan et al	Tariq et al	Shearing et al	Burnett et al	Bradley+Withers	Saif et al	Kwiatowski et al	Fam et al	Keller et al	Meyer et al
Year	2011	2011	2012	2015	2016	2017	2017	2018	2018,2013	2019
Reference	[45]	[321]	[301]	[40]	[29]	[280]	[194]	[89]	[175,180]	[224]
Material	biomat	ceramics	LIB	metal	biomat	oil shale	Fe-Mn-steels	Au catalyst	(Opalinus) Clay	PEM Fuel cell
		hierarch. pores	electrodes	corrosion		pyrolysis		hierarch. pores		
1st 3D method	ET	sync XCT	XCT	XCT	XCT	XCT	APT	ptych. sync XCT	sync XCT	XCT
Voxel size	(x nm) <sup>3</sup>	1400	600	3800	wide range	5000	0.1	13	440	372
Volume	(x μm) <sup>3</sup>	1500	220	4000	of lengths	10000	0.1	10	440	700
2nd 3D method	CLSM	FIB-SEM	XCT	XCT	scales	XCT	ET	FIB-SEM	FIB-SEM	XCT
Voxel size	(x nm) <sup>3</sup>	43	65	800	including	800	0.1	13	15	63
Volume	(x μm) <sup>3</sup>	20	45	400	time lapse	1000	0.1	10x12x3	4.5	May-65
3rd 3D method	FRET		sync XCT	FIB-SEM		FIB-SEM		ET	STEM	
Voxel size	(x nm) <sup>3</sup>		15	8x10x50		14x18x10		1.3	0.5-1	
Volume	(x μm) <sup>3</sup>		7	< 100		28x20x6		3x3x0.3	0.1-0.3	
4th 3D method	FIB-SEM									
1st 2D method	LM			FIB-SEM EBSD		HR SEM	STEM		STEM EDX	He-FIB
Pixel size	(x nm) <sup>2</sup>			50			0.05		1	0.5-60
Image window	(x μm) <sup>2</sup>			15			< 0.1		0.1	0.15-100
2nd 2D method	(S)TEM			STEM EDS		SEM EDS				TEM
Pixel size	(x nm) <sup>2</sup>			50						0.05-0.2
Image window	(x μm) <sup>2</sup>			15						0.08-0.3
3rd 2D method	AM					MAPS				
4th 2D method	SEM									
Bulk experimental		MIP	XRD							

The characteristic resolutions and image window sizes of the 3D datasets in the above mentioned correlative tomography studies are plotted in Fig. 20. This Figure illustrates that data volumes produced in current correlative tomography studies are usually smaller than  $1'000^3$  voxels. The use of relatively small data volumes in correlative tomography is in contrast to the general trend of 'non-correlative' tomography (i.e. using only one single tomography method), whereby the limits are pushed towards larger image windows and larger data volumes (e.g.  $10'000^3$  voxels). This comparison points to a certain potential for future development of correlative tomography towards larger image windows, which is particularly helpful for the characterization of materials with complex, heterogeneous microstructures.

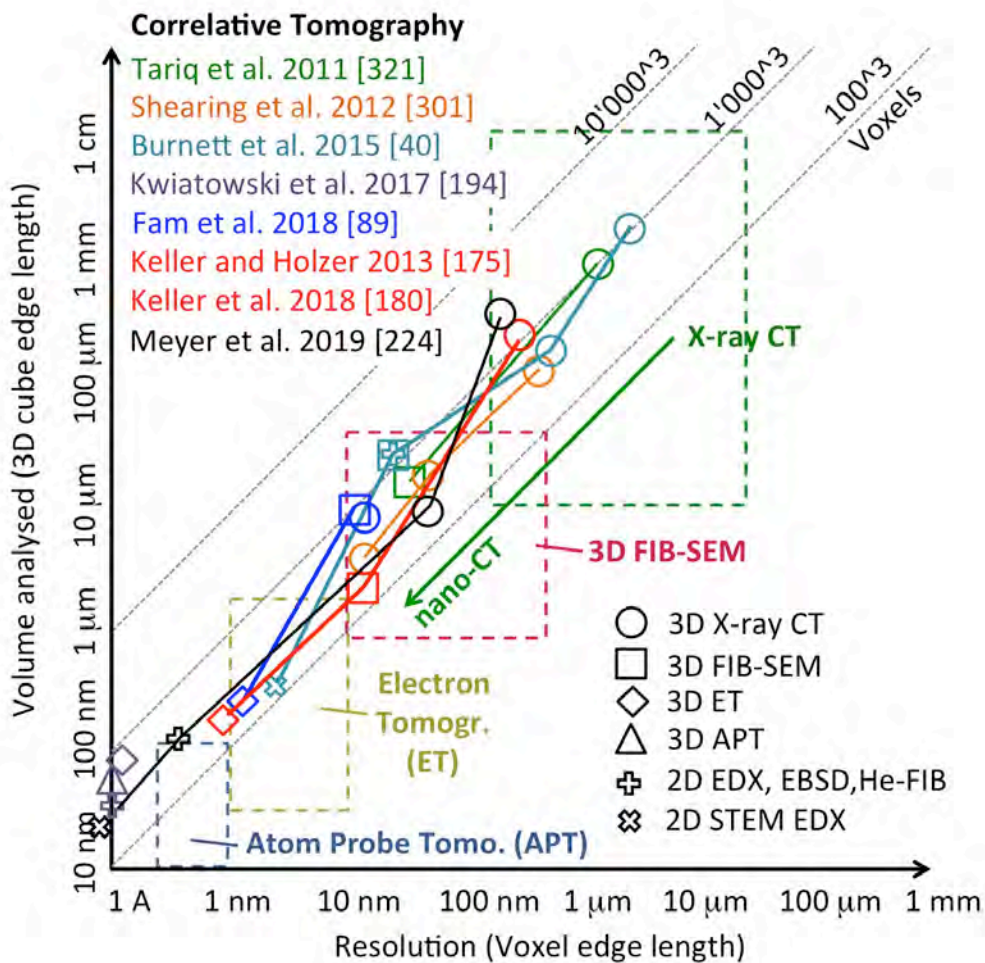


Fig. 20: Plot of datasets from correlative tomography studies (see table 'Correlative Tomography'). It illustrates that 3D datasets that were used so far for correlative tomography are usually smaller than  $1'000^3$  voxels, which is opposite to the trend in 'normal' tomography (XCT, PFIB-SEM etc.) where the limits are pushed towards larger image windows and larger data volumes (e.g.  $10'000^3$ )

## 4.2 Available software packages for 3D image processing and computation of tortuosity

Table 6 represents a list of software (SW) packages for 3D image processing and for pore scale modeling. The SW packages offer a wide range of applications and opportunities, which are typically structured in different modules. In the following section we will discuss the capabilities of the SW packages with their different modules.

### 4.2.1 Methodological modules

The different columns in Table 6 from left to right represent specific methodological modules, which are used in the workflows for the characterization of different tortuosity types (see the workflow in Fig. 14):

a) Image processing I: Modules for qualitative image processing (IP) provide solutions for 3D reconstruction, filtering of image defects, segmentation and 3D visualization. Some SW packages also provide an IP module for mesh generation, which is often used as a basis for numerical simulations.

b) Stochastic modeling: Such SW modules enable the generation of virtual 3D microstructures with stochastic modeling or with discrete element modeling (DEM), which is an important option for data drive, statistical investigations of micro-macro relationships (see Chapter 5).

c) Image processing II: Modules for quantitative image processing are used for the determination of morphological microstructure characteristics. In particular, dedicated SW modules are used for characterization of direct geometric tortuosities ( $\tau_{dir\_geodesic}$ ,  $\tau_{dir\_median\_axis}$ ,  $\tau_{dir\_skeleton}$ ,  $\tau_{dir\_PTM}$ ,  $\tau_{dir\_percolation}$ ,  $\tau_{dir\_FMM}$ ,  $\tau_{dir\_pore\_centroid}$ ) and also for mixed tortuosities.

It must be emphasized that the determination of indirect-tortuosities ( $\tau_{indir\_phys\_sim}$ ) and mixed tortuosities ( $\tau_{mixed\_phys}$ ) cannot be performed with geometric image analysis alone, because the determination of these tortuosities requires modules for 3D numerical simulation of the underlying transport process.

In addition to tortuosity, several other morphological characteristics are important in the context with effective transport properties, which are the following: solid and pore volume fractions ( $\phi$ ,  $\epsilon$ ), continuous size distributions (*cPSD*) and mean radius of pore bulges ( $r_{max} = r_{50\_cPSD}$ ), simulated mercury intrusion porosimetry (*MIP-PSD*) and mean bottleneck radius ( $r_{min} = r_{50\_MIP-PSD}$ ), constrictivity ( $\beta$ ), hydraulic radius ( $r_h$ ), specific surface and interface areas (*SSA*, *SIA*). Further morphological microstructure descriptors for microstructure characterization can be found in [53,248,295].

### d) Numerical simulation of transport / pore scale modeling

We distinguish two main groups of SW packages with modules for 3D-simulation of physical and/or chemical (transport) processes:

d1) SW packages that are powerful in micro-scale simulations use voxels to capture structural input and they typically solve one specific transport equation at a time (e.g. Navier-Stokes solver for viscous flow).

d2) SW-packages that are strong in solving coupled processes (e.g. coupling of transport with electrochemistry, thermal behavior and/or mechanics) typically use a mesh-based representation of the structural input. The mesh-based representation reduces the data volume significantly. But this benefit comes at the cost of lesser morphological details

and precision. SW packages for multi-physics simulations operating with mesh-based input are thus rather suitable for macro-homogeneous modeling, whereas SW packages operating with voxel-based input are better suited for microstructure simulations.

The SW tools for pore scale modeling are of particular importance for the computation of the two following tortuosity categories:

- Indirect-tortuosities ( $\tau_{indir\_phys}$  with variations  $\tau_{indir\_ele}$ ,  $\tau_{indir\_therm}$ ,  $\tau_{indir\_diff}$ ,  $\tau_{Kn\_indir}$ ,  $\tau_{indir\_hydr}$ ) are computed from effective transport properties (conductivity  $\sigma_{ele}$ ,  $\sigma_{therm}$ , diffusivity  $D_{eff}$ ,  $D_{Kn}$  or permeability  $\kappa$ ), which can be obtained from numerical transport simulations.
- Mixed tortuosities ( $\tau_{mixed\_phys\_streamline/V_{av}}$ ) are computed by image analysis from 3D vector fields, which represent the local flux within the pore structure. SW packages that enable to calculate the mixed tortuosities must be capable of performing both, numerical transport simulations (preferably voxel-based) and quantitative image analysis of 3D vector fields.

Table 6: Compilation of available SW packages with various modules for 3D image processing, modeling and simulation. An extended version with the corresponding web-links and further details can be downloaded from the electronic appendix ('Appendix\_electronic\_2-Table\_6.xls').

Legend: IP = image processing, DEM = discrete element method, FEM/FVM/FDM = finite element/volume/difference method, RWM = random walk method, LBM = lattice boltzmann model, CFD = computational fluid dynamics, VOF = volume of fluid, DIC/DVC = digital image/volume correlation



#### 4.2.2 Different types of SW packages

The available SW packages can be grouped according to the modules that they include. The following six groups are distinguished in Table 6 (from top to bottom):

a) Multi-modular SW packages for 3D microstructure analysis and microstructure modeling: These SW packages provide combined solutions for image processing, quantitative microstructure analysis and numerical simulation. An important characteristic is the capability to perform transport simulations with voxel-based structural input. This option is available, for example, in the SW packages GeoDict (Math2Market), PuMa (NASA), Avizo/Amira (ThermoScientific), PerGeos (ThermoScientific) and Pore3D (Elettra Scientific). Voxel-based simulations are capable to capture the microstructure input from tomography with higher precision and accuracy (compared to meshed-based simulations). Another important characteristic is the ability to determine and compare different types of tortuosities based on quantitative image processing and numerical modeling. In this context, GeoDict is currently the only SW package that enables characterizing all three tortuosity categories (direct geometric, indirect physics-based and mixed tortuosities) via the included Compute Tortuosity App. The third important characteristic refers to the option of stochastic modeling, which is used to generate virtual 3D microstructures, so-called digital twins. This option is provided e.g. by GeoDict, Digimat (eXtreme engineering), PuMA and Micress (RWTH-Aachen). These multi-modular SW packages also provide the exciting opportunities to perform digital materials design (DMD). Thereby large numbers of 3D microstructures can be created and their performances can be characterized by virtual testing (using voxel-based numerical simulations). Based on the combination of stochastic microstructure modeling, virtual testing and quantitative image analysis, these SW packages also provide outstanding opportunities for statistical investigations of microstructure-property relationships (see Chapter 5).

b) SW packages for tortuosity analysis (quantitative image processing and numerical simulation)

Some SW packages are specifically developed for tortuosity analysis (IP II). A prominent example is TauFactor from Imperial College London (Cooper et al. [59]), which is a Matlab code for voxel-based simulations of diffusive transport using the finite difference method. It provides physics-based indirect tortuosity ( $\tau_{indir\_diff}$ ) and the associated tortuosity factor ( $\tau^2$ ), respectively. Furthermore, TauFactor is also capable to compute various other microstructure characteristics such as porosity, surface area and three phase boundary (TPB) length.

The Bruggemann estimator is a Mathematica code developed at ETH Zurich (Ebner and Wood [77]), which uses the Bruggemann relation ( $\tau = \varepsilon^\alpha$ ) for estimation of indirect tortuosity in granular materials. It is primarily designed for the characterization of battery electrodes. Two orthogonal 2D images are used as input for the statistical analysis of particle shapes and particle orientations. Differential effective medium theory is then applied as a tool to predict the Bruggeman exponent ( $\alpha$ ) and the associated indirect tortuosity.

Fiji plugins for skeletonization (imagej.net/Fiji: skeletonize3D, AnalyzeSkeleton) can be used for the determination of geometric tortuosity ( $\tau_{dir\_skeleton}$ ). Moreover, various other microstructure characteristics such as *cPSD*, *MIP-PSD* and constrictivity can be determined with the XLib plugin in Fiji (imagej.net/Fiji: XLib [232,233]).

The SW package MIST [15] for image processing also provides tools for the computation of the geometric tortuosity defined in [16].

Dedicated SW for the computation of mixed tortuosities is rare. Matyka and Koza [220] describe how to implement an in-house code for analysis of volume-averaged tortuosity ( $\tau_{mixed\_phys\_Vav}$ ).

#### c) SW packages for qualitative 3D image processing and visualization

Numerous SW packages are available for qualitative image processing (IP I) and visualization. They provide various options for raw data import from tomography, 3D reconstruction and visualization, filtering of noise and correction of image defects (e.g. background correction), segmentation and mesh generation. Some of these image-processing modules are embedded within a larger commercial SW package (e.g. image-processing toolkit in Matlab and in Mathematica). ImageJ/Fiji [291] is an important freeware for image processing. Moreover, numerous SW packages for image processing are developed for medical and life science applications (e.g. ITK, VTK, TTK etc.). However, in many cases, the life science oriented SW packages do not consider morphological characteristics that are frequently used in physical and engineering sciences (tortuosity, constrictivity, pore size distributions).

#### d) SW packages for specific tomography data

Some SW packages provide dedicated image-processing solutions such as 3D reconstruction, which are specially designed for a certain type of tomography. For example, the ASTRA toolbox [1] is designed for processing of raw data from synchrotron Xray CT. TomViz is dedicated to data processing from electron tomography (TEM, STEM) and Dream3D for EBSD data from FIB-SEM tomography.

#### e) SW packages for numerical (multi-physics) modeling

Numerous SW packages are available for so-called multi-physics simulations. They are usually based either on finite element (FEM), finite difference (FDM), finite volume (FVM) or lattice Boltzmann methods (LBM). The SW packages for numerical modeling are particularly strong in simulating coupled processes (i.e. combinations of CFD, transport, electrochemistry, structural mechanics etc.) at different lengths-scales. Well-known commercial SW packages of this type are for example Comsol, Simcenter Star CCM+ (Siemens), Ansys/Fluent and Abacus (Dassault). There are also powerful freeware packages and libraries available like OpenFOAM, FreeFEM, FEniCS or SESES.

In most cases the multi-physics modeling approach makes use of a mesh-based structural input. However, as mentioned above, precise descriptions of complex 3D microstructure information from tomography are difficult to achieve with mesh-based representations. Therefore, most SW-packages for multi-physics simulation are better suited for simulations at macro-homogeneous scales and/or scenarios with relatively simple morphologies. Mesh-based simulations are thus not recommended for tortuosity analysis of complex microstructures. Note that GeoDict offers packages for voxel-based multi-physics simulation on the microstructure scale for specific applications (i.e. electrochemistry, structural mechanics, digital rock physics and filtration).

#### f) SW packages for 3D microstructure modeling

Besides the examples mentioned in part a), only a few further SW packages are available, which can be used for the generation of virtual 3D microstructures. Freeware

packages like ESyS, GenGeo, Yade and Mote3D are based on purely geometric packing of particles using the discrete element method (DEM).

The particle flow code (PFC, Itasca Consulting Group) enables virtual particle packing based on physical interactions (i.e., simulating mechanical densification and/or particle growth and crystallization). As mentioned above, also some multi-modular SW packages (e.g. GeoDict and PuMa) offer the option to generate virtual 3D microstructures. In particular, GeoDict offers specific modules for virtual design of granular and fibrous 3D microstructures. A short review of methods and models from stochastic geometry for the creation of virtual 3D microstructures is given in Section 4.6.

In the following sections (4.3-4.6), the workflow from 3D image acquisition to quantitative analysis of tortuosity is discussed in more detail.

#### 4.3 From raw tomography data to segmented 3D microstructures: step by step example of qualitative image processing

After image acquisition with a suitable tomography method, it is necessary to transform the raw data into a segmented 3D microstructure (see Fig. 14). This transformation typically includes the following steps of qualitative image processing (IP I): corrections of image defects (noise filtering, background removal and contrast leveling), 3D reconstruction (e.g. alignment of FIB-stack or filtered back projection of CT scans) and finally segmentation (i.e. phase identification, object recognition, labeling). Image processing procedures for all these steps are well established and suitable algorithms are implemented either in freeware or in commercial software packages (see Table 6, column 'Image Processing I'). Details on qualitative image processing can also be found in textbooks and review articles (e.g. Russ [278], Schlüter et al. [292]). Note that the use of machine learning leads to significant advances in the field of image processing. For machine learning algorithms, which are powerful for image segmentation, we refer, e.g., to [9,23]. Examples of hybrid approaches combining classical image analysis with machine learning are presented in [99,101], while a deep neural network is trained in [91] which allows for a reliable segmentation of FIB-SEM image data even if shine-through artifacts are present.

Nevertheless, it must be emphasized that it is very difficult to establish standardized procedures for 3D reconstruction and segmentation that allow user independent automation, because each raw data set is somehow unique due to the specific underlying settings associated with the tomography method, the used imaging parameters and the specific sample and materials properties. For each dataset, a careful adaptation of the image processing procedure for 3D reconstruction and segmentation is thus very important in order to achieve reliable quantitative results.

It is beyond the scope of this article to describe the various 3D reconstruction and segmentation procedures for different tomography methods and different materials. Instead, for illustration, we discuss the basic principles of 'qualitative image processing' (IP I) for a selected example. Thereby we consider a dataset from Pecho et al. [254,255], which was acquired with FIB-SEM tomography from a fine grained Ni-YSZ anode for solid oxide fuel cells (SOFC). Fig. 21a shows three orthogonal cross-sections of the original 3D raw data cube, before and after alignment. The raw data cube consists of 678 gray scale images with 2048 x 1768 pixels (i.e.  $2.45 \cdot 10^9$  voxels in total). The initial voxel

resolution was  $19.5 \times 19.5 \times 20$  nm. The size of the initial 3D image window (i.e. raw data volume) is thus  $40 \times 34.5 \times 13.6$   $\mu\text{m}$  ( $1.87 \times 10^4$   $\mu\text{m}^3$  in total). The raw data contains the following imperfections that need to be corrected before segmentation: a) noise caused by relatively fast acquisition rates, b) gray scale gradients typical for FIB-SEM images that are acquired under an angle of  $52^\circ$ , c) vertical stripes in y-direction (so called curtaining) caused by materials inhomogeneity and associated variation of the local ion milling rates, d) distortions in the image stack due to drift that could not be fully compensated during serial sectioning, e) brightness-flickering from image to image due to detector instabilities and/or charging.

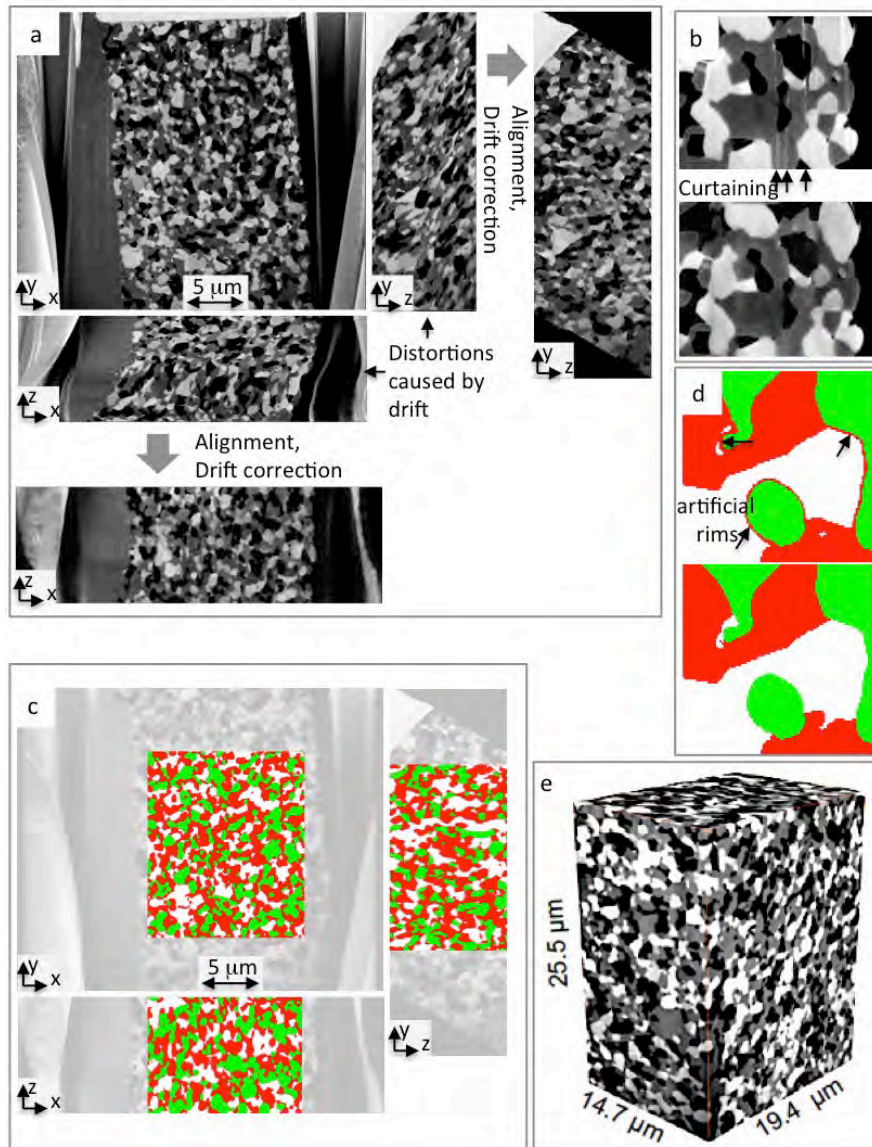


Fig. 21: Illustration of the workflow for qualitative image processing (IP I) for a FIB-SEM image stack. The processing includes filtering, 3D reconstruction and segmentation. The images represent the microstructure of a porous Ni-YSZ anode for SOFC [254,255]. a) 3D reconstruction of FIB-SEM raw data stack, before and after correction of drift in x, y- and z-directions, b) correction of curtaining, c) cropping region of interest (ROI) and segmentation into 3 phases, d) removal of artificial rims at pore-nickel interface after threshold segmentation, e) visualization of the final 3D microstructure model: pores=black (white in c, d), nickel=white (green in c, d), YSZ=gray (red in c, d).

For filtering, 3D-reconstruction and segmentation standard procedures were used, which are implemented in the commercial software GeoDict. Similar options are also available in other SW packages (see Table 6: e.g. Avizo, ImageJ, Fiji). In a first step, curtaining and flickering filters are applied for each 2D image of the stack (Fig. 21b). Then the 2D images are realigned so that the distortions caused by drift in x, y and z directions are corrected (as shown in Fig. 21a). After that, the reconstructed 3D volume is then resampled in order to obtain cubic voxels with edge lengths of 20 nm. Additional 3D image filters are applied in a careful and conservative manner using a so-called non-local means (NLM) algorithm [33]. A suitable region of interest is then cropped (see the colored regions in Fig. 21c with 3D image window size of  $17.28 \times 20.48 \times 12.96 \mu\text{m} = \text{total } 0.46 \cdot 10^4 \mu\text{m}^3$ , consisting of  $864 \times 1024 \times 648 \text{ voxels} = \text{total } 0.73 \cdot 10^9 \text{ voxels}$ ). Finally, the gray scale volume is then segmented into the three major phases (nickel, YSZ and pores) by means of suitable threshold values obtained from histogram-analysis. Note that there exists a gray-scale gradient at the solid-pore interface due to the limited spatial resolution, which results from the non-finite beam-sample interaction volume (so-called excitation volume). Upon threshold segmentation, the intermediate gray levels at the interface between pores (black) and nickel (white) lead to artificial rims (gray) that are erroneously attributed to the gray YSZ phase (red in c, d). Such erroneous rims represent a typical segmentation-artifact in three-phase materials, also described in [292]. They can be removed with a morphological opening operation, which is a combination of erosion and dilation steps (Fig. 21 d). The final, segmented 3D microstructure is visualized in Fig. 21e). It represents a suitable input for quantitative image analysis and numerical modeling.

#### 4.4 Calculation approaches for tortuosity

This section describes methods for the computation of different tortuosity types. More specific reviews on tortuosity calculation approaches were recently given by Tjaden et al. [329] and Fu et al. [98].

##### 4.4.1 Calculation approaches and SW for direct geometric tortuosities ( $\tau_{\text{dir\_geom}}$ )

In principle, almost all geometric tortuosities are based on the analysis of shortest pathways across the 3D microstructure in a predefined direction from inlet- to outlet-planes (i.e.  $\tau_{\text{dir\_geom}} = L_{\text{eff}}/L_0$ ). Since, typically, there exist numerous shortest pathways connecting numerous couples of inlet- and outlet-points, the analysis of geometric tortuosity generally results in a histogram of paths lengths, from which a mean (effective) length with the corresponding mean tortuosity value can be determined. The crux is that the length of shortest pathways can be defined and measured in many different ways. Consequently, there exist various geometric tortuosities. The underlying principles and definitions for direct geometric tortuosities have already been discussed in section 2.4. Here we only present a short summary of the corresponding calculation approaches

a) The calculation approach for geodesic tortuosity ( $\tau_{\text{dir\_geodesic}}$ ) is very simple and fast. The shortest pathways are defined in terms of the geodesic distance within the voxel space that represents the transporting phase [312]. Sometimes, this approach is also

called the direct shortest path searching method (DSPSM) [98]. In the past, most authors dealing with geodesic tortuosity worked with in-house SW. Recently, an option for the computation of geodesic tortuosity was implemented in the commercial GeoDict software. The particular type of geodesic tortuosity introduced in [16] is implemented in the software package MIST [15]. Geodesic tortuosity currently takes a special role among the different geometric tortuosity types, because it is used as a basis for empirical relationships between microstructure characteristics (porosity, tortuosity, constrictivity, hydraulic radius) and effective transport properties (see e.g. Stenzel et al. [312], Neumann et al. [243], and the discussion in Chapter 5). It was found in [312] that the geodesic tortuosity has a higher prediction power for estimating effective transport properties compared to medial axis tortuosity ( $\tau_{dir\_medial\_axis}$ ).

b) The computation of the medial axis tortuosity ( $\tau_{dir\_medial\_axis}$ ) is more complicated. It first requires the extraction of a medial axis skeleton [206]. Tortuosity is then computed from the shortest pathways along the medial axis skeleton [178,179]. Note that there exist many different skeletonization algorithms, which are for example implemented in dedicated modules of the software packages from Avizo/Amira (XPore Network) and/or Fiji (Skeletonize3D). Thereby, the resulting skeletons do not necessarily represent the medial axes. In this case, skeleton tortuosity ( $\tau_{dir\_skeleton}$ ) is used as a more general term. Hence, to some degree, the resulting values depend on the algorithm used for skeletonization, which leads to an additional complexity and uncertainty. For example, empirical data shows that  $\tau_{dir\_medial\_axis}$  and  $\tau_{dir\_skeleton}$  are usually not too different from each other, but they are consistently higher than  $\tau_{dir\_geodesic}$  and  $\tau_{dir\_FMM}$ . The different geometries of pathways for medial axis/skeleton tortuosity and geodesic tortuosity are illustrated and compared in Fig. 2.

c) The fast marching method tortuosity ( $\tau_{dir\_FMM}$ ) is based on the simulation of a propagating front, which reveals the shortest geodesic pathways within the transporting phase [121,166,338]. This relatively simple calculation approach is thus very similar to the one used for the computation of geodesic tortuosity. Usually, in-house SW is used in order to determine  $\tau_{dir\_FMM}$ .

d) The path tracking method tortuosity ( $\tau_{dir\_PTM}$ ) can be considered as a fast and simple skeletonization approach, which however is only applicable for structures consisting of packed spheres. The algorithm identifies tetragons consisting of neighboring spheres. The pathways through the interstitial pores are found by connecting the gravity centers of adjacent tetragons in a predefined transport direction [307–309].

e) The percolation path tortuosity ( $\tau_{dir\_percolation}$ ) is determined with an algorithm that allows the largest possible sphere(s) to travel along the shortest possible path from inlet- to outlet-plane. It should be noted that for a hypothetical case with very small 'spheres' (i.e. 1 pixel) the results for  $\tau_{dir\_percolation}$  are identical to those for  $\tau_{dir\_geodesic}$ . However, when the largest possible sphere is considered, the narrow bottlenecks in the pore network hinder the direct passage of the sphere, which leads to longer pathways and higher tortuosity values compared to geodesic tortuosity. These different pathway-geometries are illustrated and compared in Fig. 2. The percolation path method is implemented for example in GeoDict, which allows the user to vary the range of sphere radii as well as the number of shortest pathways to be analyzed (as optional input parameters).

f) The pore-centroid tortuosity ( $\tau_{dir\_pore\_centroid}$ ) is a quantity, which can be computed by a quick and simple method that is based on determining the center of mass of the transporting phase in single 2D slices. The tortuous pathway is then tracked by connecting the centers of adjacent 2D slices in transport direction. This method is for example implemented in Avizo. It turns out that the obtained values decrease towards 1 when the volume fraction of the transporting phase increases but also when the image window size increases (i.e. the center of gravity tends to be identical with the image center). Therefore the relevance of the pore-centroid tortuosity is questionable.

#### 4.4.2 Calculation approaches and SW for indirect physics-based tortuosities ( $\tau_{indir\_phys}$ )

Indirect, physics-based tortuosities (sometimes also called 'flux-based') are determined from effective transport properties, which are measured through specific transport experiments. These transport experiments can be performed either as a real physical experiment in the laboratory or as a virtual experiment by numerical simulation. A detailed discussion of literature dealing with laboratory experiments for electrochemical cells and for diffusion cells can be found in Tjaden et al. [329]. In the present section, however we focus on the simulation-based approaches, which use 3D microstructure models from tomography as geometric input.

Table 7: Summary of material properties and physical laws relevant for different transport experiments and associated simulation approaches

Experiment	el. conduction	bulk diffusion	thermal conduction	viscous flow
Type of $\tau$	$\tau_{indir\_ele\_sim}$	$\tau_{indir\_diff\_sim}$	$\tau_{indir\_therm\_sim}$	$\tau_{indir\_hydr\_sim}$
Transported species	electrons (or ions)	chem. species	heat	viscous media
Transporting phase	electrolyte in pore or conductive solid	gas or liq. in pore or solid	gas or liq. in pore or solid	gas or liq. in pore
Intrinsic property	intr. el./ionic cond. ( $\sigma_0$ )	intr. diffusivity ( $D_0$ )	intr. therm. cond. ( $K_0$ )	viscosity ( $\mu$ )
effective property	eff. conductivity ( $\sigma_{eff}$ )	eff. diffusivity ( $D_{eff}$ )	eff. conductivity ( $K_{eff}$ )	permeability ( $\kappa$ )
Driving force	voltage gradient ( $\Delta U/L$ )	conc. gradient ( $\Delta C/L$ )	temp. gradient ( $\Delta T/L$ )	pressure grad. ( $\Delta P/L$ )
Transport law	Ohm's law $J_{ele} = \sigma_{eff} (\Delta U/L)$ Eq. 21	Fick's law $J_{diff} = D_{eff} (\Delta C/L)$ Eq. 29	Fourier's law $J_{therm} = K_{eff} (\Delta T/L)$	Darcy's law (simple case) $J_{hydr} = (\kappa/\mu) (\Delta P/L)$ Navier-Stokes (general)
micro-macro rel.	$\sigma_{eff} = \sigma_0 \varepsilon / \tau_{ele}^2$ Eq. 24b	$D_{eff} = D_0 \varepsilon / \tau_{diff}^2$ Eq. 31	$K_{eff} = K_0 \varepsilon / \tau_{therm}^2$	$\kappa = r_{hydr}^2 \varepsilon / \tau_{hydr}^2$ Eq. 9
resolving $\tau$	$\tau_{ele} = \sqrt{(\sigma_0 \varepsilon / \sigma_{eff})}$ Eq. 25	$\tau_{diff} = \sqrt{(D_0 \varepsilon / D_{eff})}$ Eq. 32	$\tau_{therm} = \sqrt{(K_0 \varepsilon / K_{eff})}$	$\tau_{hydr} = \sqrt{(r_{hydr}^2 \varepsilon / \kappa)}$ Eq. 16

It is often mentioned that the mathematical treatment for different transport processes in numerical simulations is very similar and that the corresponding physics-based tortuosities can therefore be used interchangeably (i.e. it is assumed that  $\tau_{indir\_ele} = \tau_{indir\_diff} = \tau_{indir\_therm}$ ). This hypothesis needs to be reevaluated critically. The aim is to understand which indirect tortuosities can or cannot be used interchangeably.

#### a) Comparison of indirect electrical, diffusive and thermal tortuosities

Materials characteristics and physical laws that are relevant for the simulation of different transport experiments are summarized in Table 7. We first consider the case of an electrical conduction experiment and its simulation, respectively. The liquid electrolyte in the pores acts as the transporting phase. The relevant intrinsic property is

the electrical conductivity of the electrolyte ( $\sigma_0$ ). In the simulation experiment a voltage difference between inlet and outlet planes is applied as driving force ( $\Delta U/L$ ). The Laplace equation is solved under the assumption of charge conservation. At steady state conditions, the simulation reveals a constant electrical flux ( $J_{ele}$ ). The effective conductivity ( $\sigma_{eff}$ ) can then be calculated by substituting the simulated flux ( $J_{ele}$ ) and associated voltage drop divided by the length of the simulation domain ( $\Delta U/L$ ) in Ohm's law (Eq. 21). The resulting effective conductivity ( $\sigma_{eff}$ ) is always smaller than the intrinsic conductivity ( $\sigma_0$ ) due to the retarding effects from the underlying microstructure. These retarding effects are generally attributed to the reduced pore volume fraction ( $\varepsilon < 1$ ) and to the indirect electrical tortuosity ( $\tau_{indir\_ele}$ ). Then, Eq. 24b ( $\sigma_{eff} = \sigma_0 \varepsilon / \tau_{ele}^2$ ) is usually taken as a quantitative description of the involved micro-macro relationship. Hence, knowing the porosity ( $\varepsilon$ ) from image analysis and the effective conductivity ( $\sigma_{eff}$ ) from simulation, the electrical tortuosity can be computed indirectly according to Eq. 25 ( $\tau_{indir\_ele} = \sqrt{(\sigma_0 \varepsilon / \sigma_{eff})}$ ).

As shown in Table 7, the material laws and the physical laws for thermal conduction and for bulk diffusion are very similar to those for the electrical conduction. Therefore the simulation of these transport processes can be performed in a very similar way. From a mathematical point of view, Ohm's law, Fick's law and Fourier's law reveal exactly the same relationship between the steady state fluxes (electric, diffusive or thermal fluxes), the effective properties (electric conductivity, diffusivity, thermal conductivity) and the applied driving forces (gradients of electric potential, concentration, temperature). Several authors [98,156,201,323,329,334] performed comparative modeling studies using identical 3D microstructures as input for simulations of different transport processes (i.e. bulk diffusion as well as electrical and thermal conduction). These studies document that the three simulation approaches reveal exactly the same results for the relative properties (i.e.  $X_{rel} = \sigma_{eff\_ele} / \sigma_{0\_ele}$  or  $D_{eff} / D_0$  or  $K_{eff\_thermal} / K_{0\_thermal}$ ) and consequently also for the corresponding indirect tortuosities ( $\tau_{indir\_ele} = \tau_{indir\_diff} = \tau_{indir\_thermal}$ ). In these studies, the consistency of results could be demonstrated even for cases where different numerical methods were used (i.e. FVM, FDM, FVM, LBM and random walk). These findings indicate that, in principle, different numerical simulation approaches for diffusion and conduction are highly reproducible and thus, the corresponding indirect tortuosities for electric and thermal conduction as well as Fick's diffusion can be used interchangeably.

As an exception, it must be emphasized that diffusion in nano-porous media requires a different treatment of the microstructure effects. The so-called Knudsen diffusion, which was discussed earlier (see Eq. 34), is then often simulated with a random walk approach.

In the context of indirect tortuosity, a critical point and a source of uncertainty is the underlying assumption of a known quantitative micro-macro relationship. It is often postulated that the micro-macro relationship in porous media can be described with simple expressions such as Eq. 24b for electrical conduction ( $\sigma_{eff} = \sigma_0 \varepsilon / \tau_{indir\_ele}^2$ ) and with analogous relationships for diffusivity and thermal conduction (Eq. 31:  $D_{eff} = D_0 \varepsilon / \tau_{indir\_ele}^2$ ). This is, however, a very simplified assumption, whereby all resistive effects induced by the morphology of the microstructure are lumped together in the indirect tortuosity, with the exception of the volume effect that is represented by  $\varepsilon$  (see Eq. 25:  $\tau_{indir\_phys} = \sqrt{(\varepsilon / \sigma_{rel})}$ ). For the same 3D microstructures, this calculation approach

typically results in indirect tortuosities that are much higher than the direct geometric tortuosities (see Chapter 3, comparison of empirical data). However, in the past, various authors came up with alternative descriptions for the underlying micro-macro relationships. Some authors postulate a more exclusive approach, whereby the bottleneck effect is removed from indirect tortuosity [20,21,30,141,142]. This exclusion is achieved by adding a distinct constrictivity parameter ( $\beta$ ) into the micro-macro relationships (i.e.  $\tau_{indir\_phys} = \sqrt{(\varepsilon \beta / \sigma_{rel})}$ , see also Eqs. 26, 27 and 33). As discussed in [142], the exclusive approach with separate treatment of constrictivity results in significantly lower values for the indirect tortuosity compared to the standard definition via Eqs 24b and 25. The values obtained in this way for indirect tortuosity are then more similar to the values obtained for direct geometric tortuosity.

In contrast to this, in an even more inclusive approach, some authors added the pore volume effect to the indirect tortuosity by removing  $\varepsilon$  from the equation (i.e.  $\tau_{indir\_phys} = \sqrt{(1 / \sigma_{rel})}$ ). Then, the corresponding property is sometimes called diffusibility instead of indirect tortuosity [144]. This inclusive approach leads to even higher values for the indirect tortuosity compared to the standard definition.

In summary, this discussion illustrates that the indirect tortuosity heavily depends on the specification of the underlying micro-macro relationships. Regardless which definition one chooses, in any case the indirect tortuosity does not capture the true geometric paths lengths. The indirect tortuosity describes some kind of a microstructure resistance, which always requires a clear definition of the underlying micro-macro relationship.

#### b) Indirect hydraulic tortuosity

A 3D numerical framework can be established for pore-scale simulation of viscous flow in a similar way as discussed above for electrical conductivity. In this framework, a pressure gradient ( $\Delta P/L$ ) is externally applied as driving force (instead of a potential gradient). The transporting phase is the viscous medium in the pores. The hydraulic flux ( $J_{hydr}$ ) can be computed at steady-state conditions by solving the (Navier-) Stokes equation using different numerical approaches (e.g. FVM, FEM, LBM). Permeability ( $\kappa$ ) can then be calculated by substituting the simulated hydraulic flux and the corresponding pressure gradient into Darcy's equation (see Table 7).

Despite the obvious analogies with conduction and diffusion (Ohm's law, Fourier's law, Fick's law), there also exist some fundamental differences in the physical and mathematical description of viscous flow (Navier Stokes equations). An important difference concerns the nature of the effective properties (i.e. permeability versus conductivity and diffusivity). Actually, permeability itself is a pure microstructure property. In contrast to conduction and diffusion, there is no analogy for 'intrinsic permeability'. The intrinsic flow property can be ascribed to viscosity. In principle, permeability ( $\kappa$ ) is comparable with the relative properties of conduction and diffusion (i.e.  $\kappa \approx (\sigma_{eff\_ele} / \sigma_{0\_ele}) \approx (D_{eff} / D_0)$ ). These relative properties are entirely dependent on the microstructure. Thereby, small values for the relative properties represent high transport resistances. Nevertheless, whereas relative conductivity and relative diffusivity are dimensionless properties, permeability has units of  $m^2$ . This indicates that the microstructure imposes different limitations to viscous flow compared to conduction and diffusion (which is also obvious from the different differential equations that are used to describe these transport processes). For conduction and diffusion, the microstructure limitations associated with volume fraction, paths lengths and bottlenecks are described by the dimensionless characteristics of porosity ( $\varepsilon$ ), tortuosity

( $\tau$ ) and constrictivity ( $\beta$ ) (see e.g. Eqs 24b, 26, 27, 31 and 33). For flow and permeability, there exists an additional microstructure effect, which is caused by viscous drag at the pore walls. As discussed in Chapter 2, this flow specific effect at the pore walls can be expressed with the squared hydraulic radius ( $r_h^2$ ). Permeability is thus described by a combination of dimensionless characteristics ( $\varepsilon$ ,  $\tau$ ) and a length-dependent characteristic ( $r_h$ ) according to Eq. 9 ( $\kappa = r_h^2 \varepsilon / \tau_{hydr}^2$ ). In principle, the hydraulic tortuosity can now be computed indirectly from Eq. 9 ( $\tau_{indir\_hydr} = \sqrt{r_h^2 \varepsilon / \kappa}$ ). However, to do so it is necessary to also assess the hydraulic radius ( $r_h$ ), in addition to permeability and porosity. Unfortunately, until recently, suitable 3D image analysis methods for the measurement of hydraulic radius were lacking for complex microstructures. As discussed in Chapter 2, the Carman-Kozeny equations provide solutions that are valid only for simplified microstructures (packed spheres, parallel tubes). Novel methods of 3D image analysis to determine the hydraulic radius, which can be reliably computed for complex, disordered microstructures, will be discussed in Chapter 5. The lack of suitable methods for characterization of the hydraulic radius may be the main reason why indirect hydraulic tortuosity ( $\tau_{indir\_hydr}$ ) has not been considered in previous studies of pore-scale flow. As an alternative approach, it is possible to measure hydraulic tortuosity from simulated 3D velocity fields (and associated streamlines). These types of hydraulic tortuosity (i.e.  $\tau_{mixed\_hydr\_streamline}$ ,  $\tau_{mixed\_hydr\_Vav}$ ) however belong to the class of mixed tortuosities and they contain completely different information than the indirect tortuosities (see Section 4.4.3).

For indirect tortuosities, it can be summarized that the microstructure resistance is different for viscous flow compared to conduction and diffusion. The computation of indirect hydraulic tortuosity related to flow is more complex and therefore it is hardly used. The physics-based indirect tortuosities for electrical and thermal conduction and for bulk diffusion can be used interchangeably (but not for Knudsen diffusion). In several comparative studies [59,156,201,323,329,334] it was shown that different simulation approaches (FVM, FDM, random walk) and different voxel-based SW packages (TauFactor, Avizo, GeoDict, PyTrax) provide almost identical results for the indirect tortuosities of conduction and diffusion ( $\tau_{indir\_ele}$ ,  $\tau_{indir\_diff}$ ,  $\tau_{indir\_thermal}$ ). Tjaden et al. [329] concluded that uncertainties and errors from segmentation and meshing are much more important than those from different simulation approaches.

Commercial and open source SW packages for 3D numerical simulation of different kinds of transport (conduction, diffusion, flow) and for computation of associated indirect tortuosities are summarized in Table 6. For the characterization of complex microstructures it is recommended to use SW packages that enable transport simulations with a precise geometric representation of the microstructure (e.g. voxel-based), because this approach is usually more precise than mesh-based approaches with a reduced number of elements. The voxel-based option is available for example in the SW packages GeoDict, PuMA, Avizo, Amira, PerGeos, Pore3D, TauFactor, Pytrax, OpenLB and Palabos.

#### 4.4.3 Calculation approaches for mixed tortuosities

Hydraulic tortuosity can not easily be determined indirectly from effective properties as this is the case for electric or diffusive tortuosities (e.g.  $\tau_{indir\_ele}$ ). An alternative approach to characterize hydraulic tortuosity focuses on streamlines representing the flow paths.

This approach was discussed already in 1937 by Carman [47]. According to Eq. 17, the effective length of the hydraulic flow path is defined as weighted average of streamline lengths ( $L_{eff\_weighted}$ ), from which the hydraulic tortuosity can then be deduced as follows

$$\text{Eq. 47} \quad \tau_{mixed\_hydr\_streamline} = \frac{L_{eff\_weighted}}{L} = \frac{1}{L} \frac{\sum_i L_i w_i}{\sum_i w_i}.$$

As discussed by various authors [185–187,189,219,238], the definition and computation of suitable weighting factors ( $w_i$ ) is a major challenge, which puts strong limitations to the practical use of streamline tortuosities.

As an alternative approach, it was shown by Matyka and Koza [220] and Duda et al. [73] that hydraulic tortuosity can be computed in a much simpler way, based on the integration of local vector components from a simulated 3D velocity field. This so-called volume-averaged tortuosity was described in Chapter 2, Eq. 13 ( $\tau_{mixed\_hydr\_Vav} = \langle v_c \rangle / \langle v_x \rangle$ ) and Eq. 18.

Hence, both, volume-averaged as well as streamline tortuosities, require a 3D vector field from numerical flow simulation as a basis for the computation of mixed hydraulic tortuosity. The underlying flow simulations can be performed with different numerical methods (FVM, FDM, FEM, LBM). Furthermore, these mixed tortuosities can be determined not only for viscous flow but also for other types of transport (i.e. conduction and diffusion), for which a 3D vector field can be computed. Hence, the streamline and volume-averaged tortuosities also are physics- or flux-based tortuosities. However, in contrast to the indirect physics-based tortuosities, streamline and volume-averaged tortuosities are calculated by a geometric analysis of 3D vector fields (and not from the effective property itself). The mixed tortuosities thus bear a higher level of information since they combine physical and geometric information. The mixed tortuosities are thus of major importance if one wants to understand the true path length effects. As discussed in Chapter 3 (compilation of empirical data), the values obtained from mixed tortuosities are in the same range as those from geometric tortuosities, but consistently lower than indirect tortuosities. This finding supports the interpretation that indirect tortuosities overestimate the limiting effects from tortuous pathways.

In the literature, different modeling approaches are reported in order to obtain the required 3D vector fields for the calculation of mixed tortuosities. The numerical approach itself (FVM, LBM etc.) has a lower impact on the resulting tortuosity than e.g. meshing or segmentation. In most studies, in-house solutions are used for the analysis of the 3D vector fields. For a detailed description of volume-averaged tortuosity and its implementation see Matyka and Koza [220]. Recently, the option for characterizing volume-averaged tortuosities ( $\tau_{mixed\_hydr\_Vav}$ ,  $\tau_{mixed\_diff\_Vav}$ ,  $\tau_{mixed\_ele\_Vav}$ ,  $\tau_{mixed\_therm\_Vav}$ ) by combining numerical transport simulations with 3D image analysis of the flow fields was implemented in the SW package GeoDict.

#### 4.5 Pore scale modeling for tortuosity characterization: examples from literature

The analysis of mixed and indirect tortuosities is based on pore scale modeling. However, the pore scale modeling and associated analysis of tortuosity can be very

complex. Depending on the system under consideration, complexity can be introduced for example by coupling of a standard transport process (e.g. diffusion or flow) with additional processes such as electrochemical reactions, physical interactions at pore walls (Knudsen effect, adsorption etc.) and/or reactive transport (chemical interaction with solids). Also the simulation of transport phenomena at different length scales is often an important issue. It is beyond the scope of this review to discuss the impact of such complexities on tortuosity. Instead, we present some examples from literature with different modeling approaches:

#### a) Pore scale modeling in geoscience

Saxena et al. [288] define a benchmark with numerous 3D-microstructure models, which are used for comparison of different flow simulation codes (LBM; mesh-based FEM and openFoam; voxel-based FFT and stokes-LIR).

Su et al. [314] describe various methods for pore-scale simulation (2 phase flow), including the pore network model, LBM, Navier–Stokes equation-based interface tracking methods, and smoothed particle hydrodynamics.

Liu et al. [208] present a critical review on computational challenges in petro-physics using micro-CT and up-scaling.

He et al. [124] perform molecular dynamics (MD) simulations of gas diffusion in nanoporous shale in order to evaluate diffusive tortuosity.

Wang et al. [343] present a review of analytical and semi-analytical fluid flow models for ultra-tight hydrocarbon reservoir rocks (including fracking).

Müter et al. [234] simulate diffusion in nano-scale pore networks based on dissipative particle dynamics (DPD).

Tallarek et al. [319] present a multi-scale simulation approach for diffusion in porous media. It covers interfacial dynamics at molecular scale as well as hierarchical porosity at meso- and macro-scales.

Ghanbarian [108] discussed the problem of scale dependency in rocks and soils, which results in scattered plots of tortuosity and diffusion coefficient versus scales. By applying finite-size scaling analysis the data show a quasi-universal trend.

#### b) Pore scale modeling for energy and electrochemistry applications

Ryan and Muckerjee [279] give a critical overview on pore-scale modeling approaches for electrochemical devices (i.e. fuel cells and batteries). Particular focus is given to direct numerical simulation (DNS) techniques, which includes particle-based methods (smoothed particle hydrodynamics, dissipative particle dynamics, LBM) and fine-scale CFD methods (voxel-based vs. mesh-based).

Usseglio-Viretta et al. [336] demonstrated how to resolve the discrepancy in tortuosity factor estimation for Li-ion battery electrodes based on a combination of micro- and macro-modeling with experimental characterization.

Lu et al. [212] discuss the concept of digital microstructure design for lithium-ion battery electrodes based on a combination of nano-CT and multi-physics modeling.

Le Houx and Kramer [146] present a review on physics based modeling of porous lithium ion battery electrodes.

Zhang et al. [369] describe an experimentally validated pore-scale Lattice Boltzmann model to simulate the performance of redox flow batteries.

Recent publications dealing with the modeling of porous electrodes, the complex transport phenomena at pore scale (Chen et al. [52]), as well as multi-scale phenomena of ion transport (Tao et al. [320]) are addressed specifically.

Fundamental aspects of SOFC modeling such as coupled electrochemistry and transport at micro- to meso-scales as well as impedance analysis are reviewed by Grew and Chiu [118], Hanna et al. [123], Dierickx et al. [68] and Timurkutluk et al. [328]. Models for PEM fuel cells are discussed by Weber et al. [344] (review of transport models), Zenyuk et al. [368] (coupling of pore- and continuum-scales/up-scaling) and Liu et al. [209] (Liquid water transport in GDL).

#### 4.6 Stochastic microstructure modeling

Statistical analysis of microstructure effects (for example for establishing quantitative relationships between tortuosity, porosity and effective transport properties) is generally limited by the availability of suitable 3D image data. In a conventional approach using experimental materials fabrication followed by tomography and image analysis, the number of 3D analyses that can be performed with reasonable effort (in time and money) is usually quite limited. In this context, stochastic microstructure modeling is a powerful method that offers the possibility to increase the amount of 3D image data efficiently. Microstructure modeling is thus particularly important for data driven, statistical investigations of microstructure effects.

Stochastic geometry (also called mathematical morphology by some authors) represents the mathematical basis for stochastic microstructure modeling. Overviews related to the use of stochastic geometry for microstructure modeling are given by Chiu et al. [53], Matheron [218], Jeulin [160], Lantéjoul [199] and Schmidt [293]. In principle, stochastic geometry provides a mathematical toolbox for the generation of virtual, but realistic microstructures, which consists of many different approaches: random point processes, random closed sets, surface processes, random tessellations as well as random geometrical graphs representing spatial networks. The challenge of microstructure modeling is to use appropriate tools of stochastic geometry and mathematical morphology to develop stochastic 3D microstructure models, which allow for the generation of digital twins of a specific microstructure. In principle, two main quality criteria must be fulfilled:

- a) Prediction power: A suitably chosen stochastic model provides virtual 3D microstructures, based on which the structural properties (e.g. tortuosity) and performances (e.g. transport resistance) of real materials can be predicted with a high precision and reliability.
- b) Efficiency: The generation of virtual 3D microstructures with a stochastic model must be efficient in order to enable extensive parameter sweeps for data driven, statistical investigations.

An extensive literature review of microstructure modeling from a materials science perspective is given by Bargmann et al. [14]. In this review, different approaches for stochastic microstructure modelling are discussed in context with the type of microstructure for which these models are suitable (Table 8).

Table 8: Classification scheme for different types of microstructures, modified after Bargmann et al. [14].

1. Porous materials	Application examples:
1.1. Agglomerates (consolidated particles)	
1.1.1 Cellular structures	Lightweight materials
1.1.1.1 Open cells	Metallic and ceramic foams
1.1.1.2 Closed cells	Closed cell polyurethane (CCPU)
1.1.2 Granular materials with interstitial pore networks	
1.1.2.1 Two-phase materials	Sandstones, battery electrodes
1.1.2.2 Three-phase materials	Cermet anodes for SOFC
1.1.3 Dilute voids (porosity $\leq$ percolation threshold)	Low porosity rocks (clays), slag
1.2 Fabrics	
1.2.1 Woven fabrics	Textiles
1.2.2 Non-woven fabrics	Filter materials, PEM GDL
1.3 Aggregates (non-consolidated particles)	Sands, soils, powders
2. Non-porous materials	
2.1 Polycrystalline materials	Alloys, dense ceramics
2.1.1 Granular structures	e.g. Al-Sn alloy
2.1.2 Lamellar structures	Ti-aluminide with $\alpha + \gamma$ -phases
2.2 Bi-continuous composites (BC)	
2.2.1 Random BC	Cermets: ceramic-metal compos.
2.2.2 Regular BC	Block co-polymers
2.3 Matrix-inclusion composites (MIC)	Carbide particles in metal matrix
2.3.1 Particle reinforced MIC	Carbon black in rubber
2.3.2 Fiber reinforced MIC	Polymer matrix-fiber composites

In [14], two main approaches for microstructure modeling are distinguished:

a) Physics-based methods aiming at the simulation of physical processes liable for microstructure formation: For example, with the phase-field method, physical processes of grain growth or crystallization and associated microstructure formation are described with so-called transformation rules.

b) Geometrical methods aiming at mimicking the material's morphology disregarding the underlying physics of microstructure development: A prominent example for this approach is the random packing of particles (spheres, ellipsoids, polyhedron, cylinders, fibers etc.) by means of discrete element modeling (DEM), see e.g. Sheikh and Pak [303].

For almost any type of microstructure, descriptions of suitable models can be found in literature with both, geometrical as well as physics-based approaches. However, only a few SW packages are available for microstructure modeling by stochastic geometry, as shown in Table 6. ESyS, GenGeo, YADE and Mote3D represent a small group of dedicated SW packages for microstructure generation, which are based e.g. on discrete element modeling (DEM). Further SW packages with specific modules for microstructure generation are GeoDict (e.g. GrainGeo, FiberGeo), Digimat, and PuMa. The BruggemannEstimator provides a module for the generation of battery structures and

Dream3D for simulation of crystalline grain orientation patterns in the context with 3D EBSD.

In the following sections we present short reviews from two important application fields of stochastic microstructure modeling, which are digital materials design for electrochemical devices and digital rock physics (DRP). For stochastic microstructure modeling of cellular and foam materials, see e.g., [95,107,275,348].

#### 4.6.1 Stochastic modeling for Digital Materials Design (DMD) of electrochemical devices

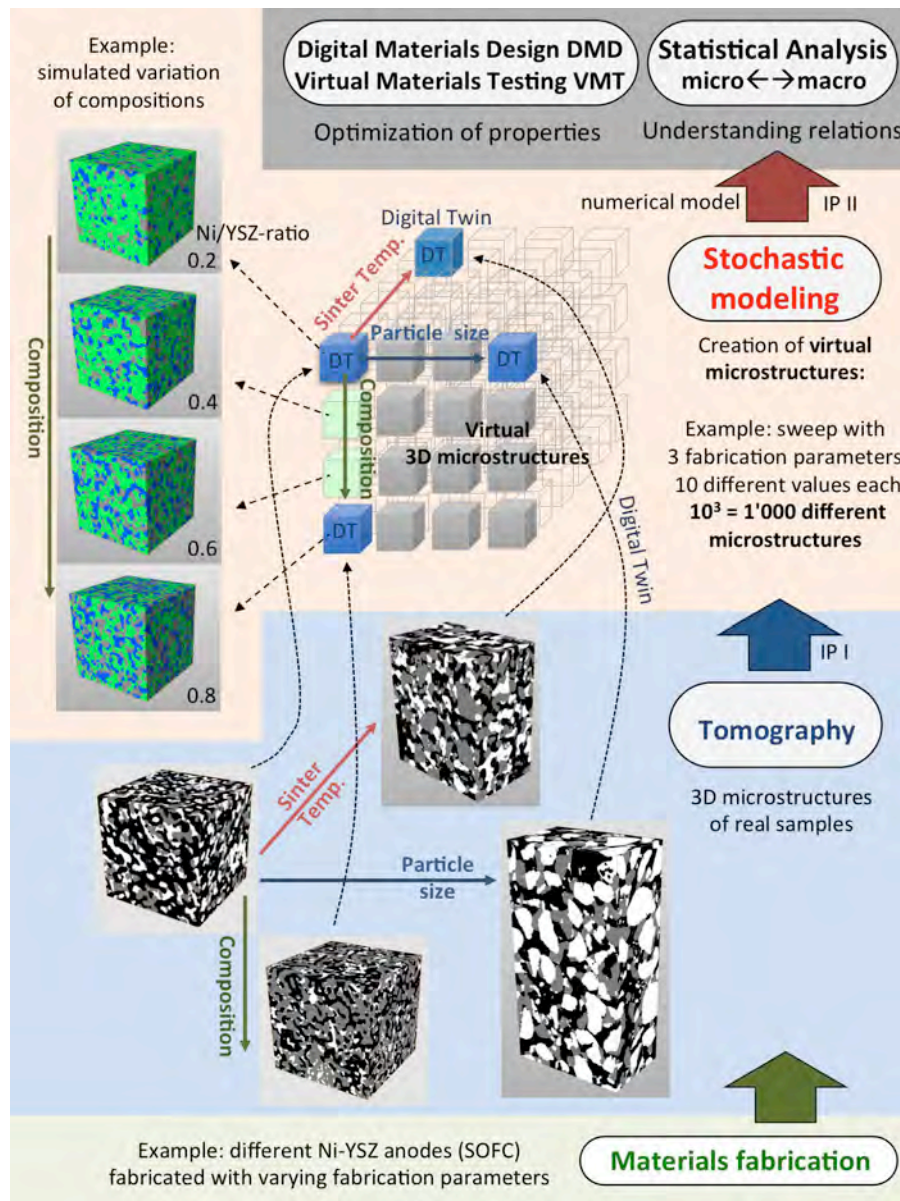


Fig. 22: Schematic illustration of the workflow for digital materials design (DMD) of SOFC anodes based on stochastic microstructure modeling. The stochastic model for the creation of numerous virtual anode microstructures is fitted to experimental tomography data (i.e. real anode microstructures), which is why the virtual microstructures have realistic properties (3D-data taken from Pecho et al. [254,255]).

An overview of microstructure modeling approaches for electrochemical devices can be found in Ryan and Mukherjee [279]. Thereby, different stochastic 3D reconstruction methods are presented, which include Monte Carlo modeling, dynamic particle packing, stochastic grids, simulated annealing and controlled random generation. These stochastic models enable the creation of various 3D microstructures that are important for batteries, PEM fuel cells and SOFCs.

Various stochastic models for electrochemical devices and energy materials have been presented in the literature, for example for the fibrous GDL in PEM fuel cells [324,325], for granular microstructures of battery electrodes [90,100,128,132,266,268,346,347,359], and for different types of SOFC electrodes [2,230,239,242,316]. Thereby, a particular challenge for the simulation of cermet anodes is the realistic description of connectivity in all three co-existing phases. This challenge can be solved with specific random geometric graphs, - so-called beta-skeletons [242].

In order to discuss stochastic modeling as a basis for digital materials design (DMD), we consider an example of cermet anodes for SOFC, which is illustrated in Fig. 22. The aim of this approach is to optimize the anode microstructure, which consists of three phases, namely nickel, YSZ (zirconium oxide) and pore phases. Tomography data of this example is taken from [254,255]. In an experimental approach, there are typically 3 to 5 main fabrication parameters, which can be used to vary the microstructure of cermet anodes. These parameters are related to composition (Ni/YSZ-ratio, pore former content), grain size of raw materials (powder fineness of Ni-oxide and YSZ) and sintering conditions (temperature, duration and  $pO_2$  of gas environment). In order to find an optimized microstructure, it is necessary to perform systematic parametric sweeps, which results in a rather large test matrix. With a conventional experimental approach, this test matrix cannot be covered with a reasonable amount of resources. Thus, in most studies, only a few samples can be investigated for example by means of FIB-SEM tomography and image analysis.

On the other hand, using a modern approach of digital materials design, the statistical basis is enlarged with the help of stochastic microstructure modeling. Thereby, the limited number of available 3D datasets from FIB-SEM tomography is used for model calibration. As shown in Fig. 22, the real 3D microstructures from tomography represent the corner stones of an extended virtual parameter space. For each tomography dataset a digital twin is created, whereby the parameters of an appropriately chosen stochastic 3D microstructure model are fitted to the microstructure resolved by 3D imaging. After a successful fitting procedure, the digital twins are statistically similar to the real microstructures observed by 3D imaging. This means that microstructure characteristics and effective properties coincide nicely. Given that the model type is fixed, the fitted parameters of the stochastic microstructure model can be understood as 'rules' by means of which 3D microstructures with predefined properties can be produced in a stochastic process, e.g. by randomly placing particles of a certain size, shape, orientation in a 3D image volume. Moreover, the complex information contained in the 3D image data of microstructures is reduced to a relatively small number of model parameters. The fitting of model parameters calibrates the stochastic model to real tomography data. Doing so, a link is established between experimental fabrication parameters, parameters of the stochastic microstructure model and microstructure properties. The stochastic model can then be used to perform extensive parameter sweeps, which mimic the generation of 3D microstructures in a real fabrication process.

Once relationships between fabrication parameters and parameters of the stochastic microstructure model are established, one could, e.g., perform a parametric sweep with three fabrication parameters (Ni-YSZ ratio, sintering temperature and particle size of YSZ) and for each of these fabrication parameters one can define 10 different values (e.g. 1100, 1120, 1140, ... 1280 °C for the sintering temperature). This sweep results in  $10^3$  different parameter combinations, for each of which the corresponding virtual 3D microstructure will then be created. This leads to a database of 1000 virtual microstructures mimicking the microstructure of differently manufactured electrodes. Such extensive parameter sweeps open new possibilities for data driven optimization of microstructures. Thereby, each virtual 3D microstructure must be analyzed by means of quantitative image analysis (i.e., determination of tortuosity, constrictivity, three phase boundary etc.) and numerical modeling (i.e., determination of effective properties). The invention of highly efficient computational solutions is thus becoming increasingly important. Massive simultaneous cloud computing (MSCC) and the use of artificial intelligence are promising techniques to solve the future challenges of big data analysis for digital materials design. Thus, novel concepts combining modern techniques for modeling and computing represent the methodological basis at the forefront of innovative materials research. Thereby, stochastic microstructure modeling is identified as a key technology for digital materials science.

#### 4.6.2 Stochastic modeling for digital rock physics and virtual materials testing of porous media

The progress of 3D imaging, analysis and modeling also opens new possibilities to establish quantitative relationships between morphological microstructure characteristics (e.g. tortuosity, constrictivity, porosity etc.) and effective properties (permeability, diffusivity, strength, elasticity etc.) by means of virtual materials testing (VMT). Thereby, stochastic microstructure modeling provides the statistical basis for such data-driven investigations of microstructure effects. In geoscience this approach is often called digital rocks physics (DRP [290]).

For example, Berg [20,21] applied DRP to investigate the impact of tortuosity and other microstructure effects on conductivity and permeability of porous rocks, where the investigations are based on 5 micro-CT scans from Bentheimer (1 scan) and Fontainebleau (4 scans) sandstones. A numerical rock model, called e-Core, was used to create additional virtual sandstone microstructures (12 for Bentheimer and 7 for Fontainebleau sandstone) with different porosities, but with realistic properties. In this way, the micro-macro relationships in those sandstones could be described based on a set of 24 microstructures from micro-CT scans and 3D-models with varying porosities.

In the meanwhile, a large number of 3D image data including CT scans from real samples as well as virtual microstructures from stochastic modeling is available for free download from the 'Digital Rocks Portal' [269]. The latter is a public repository focusing on 3D microstructure data of porous media in geoscience. Such data can be used to perform data-driven investigations of micro-macro relationships with a broader data-basis.

Saxena et al. [288] generated a reference dataset consisting of a large variety of 3D microstructures ranging from idealized pipes to realistic digital rocks. The 3D models are used as a benchmark for DRP and for the comparison of different numerical solvers that are used in pore scale simulations (LBM, CFD, voxel based FDM, mesh based FEM).

Nowadays, also commercial software for digital rocks physics has become available, such as e.g. PerGeos or GeoDict (see Table 6). These SW packages provide integrated solutions for the entire DRP-workflow, including 3D reconstruction, image analysis and numerical simulation. All these modern tools (including 3D data from repositories, stochastic models, SW packages for image analysis and numerical pore scale modeling) are increasingly used in different combinations for statistical analysis of microstructure effects (see e.g. Fu et al. [98]). The availability of the above mentioned SW packages and their application to 3D image data representing a vast range of different microstructures will significantly contribute to a better understanding of the different types of tortuosity and of their relationship with effective transport properties in porous media.

In this context, we also refer to the recent work of Prifling et al. [267], where relationships between descriptors of two-phase microstructures, consisting of solid and pores, and their mass transport properties, have been investigated. To that end, a vast database has been generated comprising 90,000 porous microstructures drawn from nine different stochastic models, and their effective diffusivity and permeability as well as various microstructural descriptors have been computed. To the best of our knowledge, this is the largest and most diverse dataset created so far for studying the influence of 3D microstructure on mass transport in porous materials. The microstructures, descriptors, and the code used to study microstructure-property relationships are available open access via the following Zenodo repository: <https://zenodo.org/record/4047774>.

## 5. Towards a quantitative understanding of microstructure-property relationships

In this chapter, empirical relationships between morphological characteristics (porosity, tortuosity, constrictivity, hydraulic radius) and macroscopic transport properties (effective conductivity, effective diffusivity and permeability) are described. Based on the rapid progress of analytical techniques (i.e. 3D imaging, image processing, stochastic simulation, numerical modeling, cloud computing) the prediction power of such equations has improved considerably over the last decade(s). The newest formulations are now capable to predict micro-macro relationships for many different types of materials and microstructures (e.g., granular, fibrous, cellular and platy microstructures) in a reliable way. Consequently, these empirical relationships do have some general meaning although they are not derived from a rigorous theoretical basis.

It must be emphasized that microstructure effects limiting the transport in porous media can be investigated in different ways and with different methodologies. In this context, transport simulations based on 3D microstructure models are particularly well suited to predict effective transport properties of porous media. However, the transport simulations themselves cannot replace the valuable information from micro-macro relationships. These empirical relationships provide a unique basis for controlled microstructure optimization and associated materials design, which cannot be replaced

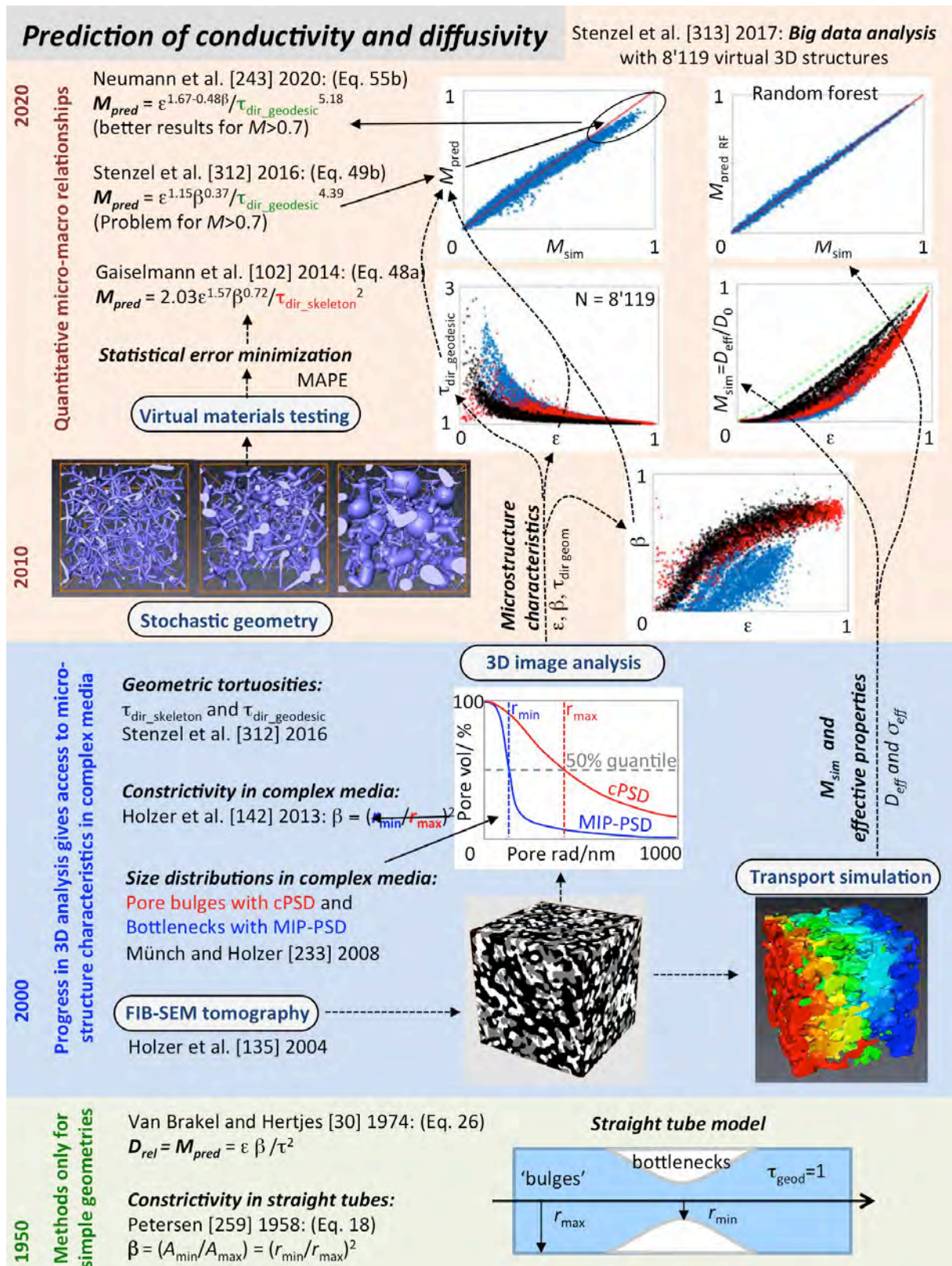
by transport simulations. In contrast, for settings with complex transport mechanisms, the concept of tortuosity typically comes to its limits and sophisticated transport simulations are better suited to study the properties of porous media. This is for example the case when diffusion and flow are coupled with physico-chemical reactions at the pore walls (e.g., with adsorption and/or chemical reactions). Hence, empirical micro-macro relationships and transport simulations represent different and complementary approaches for studying the properties of porous media, which do not replace each other.

As an introduction to this chapter, recall that the review of tortuosity, performed in this survey paper, basically reveals two main schools of thinking, where tortuosity is either determined indirectly or, alternatively, it is directly based on morphological descriptors of the underlying 3D microstructure.

a) In a traditional approach, tortuosity is interpreted as the predominant microstructure effect. Following this approach, tortuosity can be determined indirectly, assuming a relatively simple relationship with effective properties (see e.g. Eq. 31:  $D_{eff}/D_0 = D_{rel} = \varepsilon / \tau_{indir\_diff}^2$ ). However, the values obtained for indirect tortuosity are consistently higher than what would be expected from geometric considerations of e.g. streamlines. Hence, indirect tortuosity clearly overestimates the lengths of (shortest) transport pathways, which indicates that it includes other microstructure effects such as the limiting influence from narrow bottlenecks. Hence, the indirect tortuosity can be interpreted as bulk microstructure resistance, - normalized by the pore volume. Thus, this information is often used as valuable input for macro-homogeneous models, which intend to describe the bulk microstructure resistance.

b) An alternative 'geometric' school of thinking is focusing on geometric and mixed tortuosities, which provide reliable estimations of the lengths of transport paths. In order to establish quantitative relationships between microstructure and effective transport properties, it is necessary to capture all relevant microstructure characteristics - not only the geometric or mixed tortuosities. This approach thus requires an additional effort, e.g., for determining constrictivity and eventually also hydraulic radius. The quantitative micro-macro relationships obtained by this approach provide a deeper understanding of the relevant morphological effects, which represents the basis for a purposeful microstructure optimization and materials design.

It must be emphasized that the geometric school of thinking profits a lot from the recent progress in 3D analysis and virtual materials testing. These new options for 3D analysis are applied with the aim to establish quantitative micro-macro relationships for porous media. In the following sections selected results of such investigations are summarized first for conductivity and diffusivity, and subsequently also for flow and permeability.



## 5.1 Quantitative micro-macro relationships for the prediction of conductivity and diffusivity

In this section, micro-macro relationships describing the limiting effects of microstructure on conductivity and diffusivity are reviewed. Thereby, we typically consider transport in porous media like gas diffusion or liquid conduction. However, it must be emphasized that transport in solid phases of a composite material (e.g. ionic or electric conduction in a cermet electrode) is suspended, in principle, to the same microstructure limitations as the transport in porous media and can therefore be described with the same morphological characteristics and mathematical equations.

The progress made in the investigation of micro-macro relationships for conductivity and diffusivity is schematically illustrated in Fig. 23. Already a long time ago it was recognized that transport in porous media is limited not only by the lengths of tortuous pathways but also by narrow bottlenecks, see e.g. [250]. In 1974, van Brakel and Hertjes [30] thus postulated a micro-macro relationship for conductivity and diffusivity, which includes constrictivity ( $\beta$ ) as well as tortuosity (Eq. 33:  $D_{rel} = \varepsilon\beta/\tau^2$ ). Unfortunately, at that time, constrictivity as well as geometric or mixed tortuosity could not be determined for complex microstructures. Nevertheless, for the simple case of straight tubes ( $\tau_{dir\_geometric} = 1$ ) with varying cross-sections, it was shown by Petersen in 1958 [259] that the retarding impact of bottlenecks can be described by the ratio of the constricted cross-sectional area ( $A_{min}$ ) over the 'bulged' cross-sectional area ( $A_{max}$ ). This simple pipe-flow model, which is illustrated at the bottom of Fig. 23, led to the definition of constrictivity according to Eq. 18 ( $\beta = r_{min}^2/r_{max}^2$ ). However, in the last century the practical relevance of all theories dealing with resistive effects from bottlenecks (constrictivity) and/or path lengths (geometric tortuosity) was strongly limited, since there were no suitable 3D methods available for a quantitative morphological characterization.

With the introduction of FIB-tomography in 2004 [135], 3D imaging of porous media at sub- $\mu\text{m}$  scales became possible. As a next step, suitable tools for quantitative 3D image analysis were required. Two methods to quantify the size distributions of pore bulges and bottlenecks in complex disordered microstructures were introduced by Münch and Holzer [233]. Thereby the continuous pore size distribution (*cPSD*) was used in order to characterize the size distribution of pore bulges. Note that the *cPSD* uses the concept of granulometry functions, which were introduced in [218]. Going beyond granulometry functions, a method for a geometry-based 3D simulation of mercury intrusion porosimetry (MIP) was introduced in [233]. The *MIP-PSD* (sometimes also called 'porosimetry') reveals the size distribution of bottlenecks. Typical examples of *cPSD* and *MIP-PSD* curves are shown in Fig. 23.

It was then recognized by Holzer et al. [142] that the 50% quantiles (i.e.  $r_{50}$ ) of these two pore size distribution curves can be considered as mean effective sizes for bulges ( $r_{50\_cPSD} = r_{max}$ ) and for bottlenecks ( $r_{50\_MIP\_PSD} = r_{min}$ ), which can be substituted in Eq. 18 ( $\beta = r_{min}^2/r_{max}^2$ ). In this way, a quantitative method was found for the characterization of constrictivity, which also works for materials with complex microstructures. A formal definition of constrictivity in the framework of stochastic geometry is provided in [240].

Using experimental data for determining effective properties, as well as constrictivity and geometric tortuosity from 3D analysis, it was soon found that van Brakels equation

(Eq. 33:  $D_{rel} = \varepsilon\beta/\tau^2$ ) is not very precise in predicting the effective diffusivity. This finding led to the question, which type of equation has to be used in order to describe the relationship between microstructure characteristics and effective diffusivity ( $D_{eff}$ ) or effective conductivity ( $\sigma_{eff}$ ), respectively. In a series of studies [102,243,312,313], the following equations were considered as possible candidates:

Eq. 48	$\sigma_{rel}; D_{rel} = M = d\varepsilon^a\beta^b/\tau^c$	
Eq. 49	$\sigma_{rel}; D_{rel} = M = \varepsilon^a\beta^b/\tau^c$	
Eq. 50	$\sigma_{rel}; D_{rel} = M = d\varepsilon^a$	
Eq. 51	$\sigma_{rel}; D_{rel} = M = d\varepsilon^a/\tau^c$	
Eq. 52	$\sigma_{rel}; D_{rel} = M = d\varepsilon^a\beta^b$	
Eq. 53	$\sigma_{rel}; D_{rel} = M = d\varepsilon^a\beta^b/\tau^2$	
Eq. 54	$\sigma_{rel}; D_{rel} = M = \varepsilon^a\beta^b/\tau^2$	
Eq. 55	$\sigma_{rel}; D_{rel} = M = \varepsilon^{a1-a2\beta}/\tau^c$	
	$\sigma_{rel}; D_{rel} = M = \varepsilon^a$	(Eq. 23, Archie's law)
	$\sigma_{rel}; D_{rel} = M = \varepsilon/\tau^2$	(Eq. 31)
	$\sigma_{rel}; D_{rel} = M = \varepsilon\beta/\tau^2$	(Eq. 33)

According to the 'geometric' school of thinking, in all these equations  $\tau$  is thought as a direct geometric tortuosity ( $\tau_{dir\_geom}$ ). The prediction power of these equations was investigated thoroughly through a statistical approach of error minimization in [102,243,312,313]. For this purpose, models from stochastic geometry were used to generate a large number of 3D microstructures with varying characteristics and effective properties. 3D image analysis was used to compute the microstructure characteristics ( $\varepsilon, \beta, \tau_{dir\_geom}, r_{min}, r_{max}$ ). Numerical transport simulation was exploited to determine effective diffusivity and/or conductivity ( $D_{rel}, \sigma_{rel}$ ) for each virtual 3D microstructure generated by stochastic models. The unknown exponents ( $a, b, c, d$ ) in the above mentioned equations were then determined by means of error minimization. As a quality criterion for the predictive capabilities of the above mentioned equations, the mean absolute percentage error (MAPE) was used in [102], where

$$\text{Eq. 56} \quad MAPE (M_{sim}, M_{predict}) = \frac{1}{n} \sum_{i=1}^n \frac{|M_{sim,i} - M_{predict,i}|}{M_{sim,i}} 100\%$$

Thereby,  $M$  (microstructure-factor) stands for the relative properties (with respect to  $D_{rel}$  or  $\sigma_{rel}$ ), which were determined in two ways: a) either by numerical simulation (e.g.  $M_{sim} = D_{eff\_sim}/D_0$ ), or b) by substituting the values obtained from 3D image analysis for the microstructure characteristics ( $\varepsilon, \beta, \tau_{dir\_geom}$ ) into the equation under consideration (i.e.  $M_{pred}$ ). For example,  $M_{pred} = d\varepsilon^a\beta^b/\tau^c$  in Eq. 48. The exponents  $a, b, c, d$  were then fitted for each equation in order to minimize the corresponding MAPE (i.e. the absolute value of the difference  $M_{sim} - M_{pred}$ ). For the most relevant equations, the fitted pre-factor and exponents and the prediction errors (MAPE) are summarized in Table 9.

In a first publication of this series of investigations (Gaiselmann et al. [102]), it was shown that for the traditional equations (Eqs 31, 32, 33) the prediction power becomes significantly better when constrictivity is considered as a relevant microstructure effect, in addition to geometric tortuosity and porosity (cf. Eq. 31, where MAPE=625% vs. Eq. 33, where MAPE=37%). Note that the prediction power can be further improved when using equations with fitted pre-factor and exponents (Eqs 48-54). From all the equations

under consideration, Eq. 48 (and Eq. 49) revealed the best results with a MAPE of 25% (and 28%, respectively). Then Eq. 48 reads as

$$\text{Eq. 48a} \quad M_{pred} = 2.35 \varepsilon^{1.57} \beta^{0.71} / \tau_{dir\_skeleton}^{2.3} .$$

Again, equations including constrictivity in addition to geometric tortuosity reveal the best predictions. These findings underline the importance of the bottleneck effect. It must be emphasized that the skeleton tortuosity ( $\tau_{dir\_skeleton}$ ) was used throughout [102]. However, other types of geometric tortuosity should be tested as well.

Table 9: Summary of the most important micro-macro relationships (for conductivity and diffusivity) obtained by virtual materials testing, including fitted pre-factor ( $d$ ) and exponents ( $a$ ,  $b$ ,  $c$ ) for porosity ( $\varepsilon$ ), constrictivity ( $\beta$ ) and tortuosity ( $\tau_{dir\_geometric}$ ) and the corresponding mean absolute percentage error (MAPE) as quality criterion. The equations marked in blue represent the favorites with the highest prediction power. Note that quantitative image analysis is always performed only for the contiguous (connected) portion of the pore phase (i.e.  $\varepsilon_{eff}$ ). For example, trapped pores are excluded from the analysis of  $\varepsilon$ ,  $\beta$  and  $\tau$ .

Authors [Ref]	Nr of virtual 3D models	Eq. nr	Tortuosity type	$d$ (pre-factor)	$a$ ( $\varepsilon^a$ )	$b$ ( $\beta^b$ )	$c$ ( $\tau^c$ )	MAPE %	Comments
Gaiselmann et al [102]	105	31	$\tau_{dir\_skeleton}$	-	1	-	2	625	no constrictivity!
Gaiselmann et al [102]	105	33	$\tau_{dir\_skeleton}$	-	1	1	2	37	
Gaiselmann et al [102]	105	48 (a)	$\tau_{dir\_skeleton}$	2.346	1.569	0.709	2.298	25	
Gaiselmann et al [102]	105	49 (a)	$\tau_{dir\_skeleton}$	-	1.327	0.689	1.478	28	
Stenzel et al [312]	43	48 (b)	$\tau_{dir\_geodesic}$	0.88	1.06	0.36	4.35	19	
Stenzel et al [312]	43	49 (b)	$\tau_{dir\_geodesic}$	-	1.15	0.37	4.39	19	
Stenzel et al [313]	8119	49 (b)	$\tau_{dir\_geodesic}$	-	1.15	0.37	4.39	13.6	Not precise for $M>0.7$
Stenzelet al [313]	8119	Neural network	$\tau_{dir\_geodesic}$	-	-	-	-	8.9	
Stenzelet al [313]	8119	Random forest	$\tau_{dir\_geodesic}$	-	-	-	-	8.5	
Neumann et al [243]	8119	55 (b)	$\tau_{dir\_geodesic}$	-	1.67-0.48 $\beta$	-	5.18	18.3	Precise for $M>0.7$ 10.3 for $M>0.05$ Large errors for $M<0.05$

The study presented by Stenzel et al. [312] is based on the same methodologies as in [102]. However, the results of [312] extend the investigations of [102] in the sense that the prediction power of these equations was compared for different types of geometric tortuosity. It turned out that the prediction power with geodesic tortuosity ( $\tau_{dir\_geodesic}$ ) is better than with skeleton tortuosity. For example, the prediction error (MAPE) for Eq. 49 improved from 28% with  $\tau_{dir\_skeleton}$  to 19% with  $\tau_{dir\_geodesic}$ . The prediction formula takes the form

$$\text{Eq. 49b} \quad M_{pred} = \varepsilon^{1.15} \beta^{0.37} / \tau_{dir\_geodesic}^{4.39} .$$

Moreover, modified definitions of constrictivity were investigated in [312]. They are based on considerations that the relevant sizes of bulges ( $r_{max}$ ) and bottlenecks ( $r_{min}$ ) do not necessarily correspond to the 50% quantiles ( $r_{50}$ ) of the  $cPSD$  and  $MIP-PSD$  curves, respectively. Other quantiles ( $r_0$ ,  $r_{10}$ ,  $r_{25}$ ,  $r_{50}$ ,  $r_{75}$ ,  $r_{90}$ ) from  $cPSD$  and  $MIP-PSD$  curves were thus taken into account as possible candidates for characteristic sizes of bottlenecks ( $r_{min}$ ) and bulges ( $r_{max}$ ). By varying the combination of these candidates, Stenzel et al.

[312] obtained 35 different  $r_{\min}/r_{\max}$ -ratios as possible definitions for constrictivity (e.g.  $\beta = r_{25\_MIP-PSD^2}/r_{75\_CPSD^2}$ ). The impact of these different definitions on the prediction power was then tested for five equations (Eqs. 31, 33, 48, 49, 54) using the MAPE as a quality criterion. In short, it turned out that the initial definition of constrictivity (i.e.  $\beta = r_{50\_MIP-PSD^2}/r_{50\_CPSD^2}$ ) from Holzer et al. [142] gives the most reliable and most precise predictions for all equations. It is thus proposed to maintain the initial definition of constrictivity.

Up to this stage, the statistical analyses included only a moderate number of 105 [102] and 43 [312] different 3D microstructure models, respectively. In an extensive simulation study by Stenzel et al. [313] the number of virtual 3D models was increased to 8119. With this big data approach it was confirmed that effective diffusivity and conductivity are well predicted by Eq. 49b. The corresponding MAPE decreased further to 13.6% due to the better statistical data basis. However, it also became clear that  $M_{\text{pred}}$  and associated effective properties are underestimated by Eq. 49b for highly porous materials (i.e. for microstructures with  $M > 0.7$ ). Better predictions, in particular for  $M > 0.7$ , could be achieved with methods from machine learning, namely random forests and neural networks, which reveal MAPEs of 8.5 % and 8.9 %, respectively. However, these tools from machine learning often do not provide a clear physical interpretation of the microstructure influence on effective transport properties. Therefore, random forests and neural networks could not be used as a basis for microstructure optimization.

In a recent paper by Neumann et al. [243], it was recognized that the problem of Eq. 49b for microstructures with  $M > 0.7$  originates from an overestimation of the bottleneck-effect at high porosities (particularly in the limit when  $\varepsilon$  tends to 1). A modified equation (Eq. 55) was thus proposed, where constrictivity appears in the exponent of porosity. In this way, constrictivity acts as a correction factor for the effective pore volume, but the effect of  $\beta$  becomes negligible when porosity is close to 1. The 8119 virtual 3D microstructures from [313] were then used as a basis for testing the prediction power of Eq. 55b in [243]. Overall, this resulted in a MAPE of 18.3 %, which is - when taking all structures into account - not better than the MAPE of Eq. 49b obtained in [313]. The prediction formula derived in [243] reads as follows:

$$\text{Eq. 55b} \quad M_{\text{pred}} = \varepsilon^{1.67-0.48\beta} / \tau_{\text{dir\_geodesic}}^{5.18} .$$

However, Eq. 55b has the advantage that - in contrast to Eq. 49b - it is consistent with theoretical results in the dilute limit, i.e., in the case when the obstacles of the transport process vanish. For materials exhibiting high porosities with  $M > 0.7$ , the predictions obtained by means of Eq. 55b are much better than those obtained by Eq. 49b. Nevertheless, for low porosity materials with  $M < 0.05$ , the predictions by Eq. 55b are even worse. Therefore, when considering only structures with  $M > 0.05$ , the MAPE for Eq. 55b improves significantly to 10.3%. Hence, the higher the  $M$ -value, the better the prediction power of Eq. 55b.

From the numerous equations that were evaluated statistically, the following three favorite equations remain (marked with blue color in Table 9):

- Eq. 48a from [102] gives the best predictions when skeleton tortuosity is used.
- Eq. 49b from [312] gives the best results with geodesic tortuosity, but only for microstructures with  $M < 0.7$ .

- Eq. 55b from [243] also gives good results with geodesic tortuosity. In particular this equation should be used for highly porous materials with  $M > 0.7$  (but not for low porosity materials with  $M < 0.05$ ).

The prediction power of these equations was also validated experimentally for different porous materials by means of tomography (FIB-SEM and  $\mu$ CT). The validation was done by comparing the predicted properties ( $M_{\text{pred}}$ ) from 3D image analysis either with results from experimental characterization ( $M_{\text{exp}}$ ) or from simulations ( $M_{\text{sim}}$ ) or both. In this way, it has been shown in [102,243,312] that the equations considered in these papers give good results for SOFC cermet electrodes, including gas diffusivity in the pores as well as electrical conductivities of the solid phases.

Furthermore, Eq. 49b was experimentally validated for very different types of microstructures, such as sintered ceramic membranes [141], fibrous GDL in PEM fuel cells [140] and even for open cellular materials (unpublished data). These results confirm that the established micro-macro relationships are rather general in the sense that they are capable to predict effective properties for a wide spectrum of microstructures, the morphologies of which differ significantly from those used for deriving the microstructure-property relationships. This generality may be surprising, considering the fact that the predictions are based on three volume-averaged parameters ( $\varepsilon$ ,  $\beta$ ,  $\tau_{\text{dir\_geometric}}$ ) only. However, these findings also indicate that these three parameters indeed capture most microstructure effects, which are relevant for conduction and diffusion, to a large extent. Exceptions are discussed in [28].

Due to the progress in microstructure characterization as well as in mathematical and numerical 3D modeling, many researchers are now considering the distinct morphological limitations that can be described with geometric tortuosity, constrictivity and phase volume fractions. Hence, the geometric school of thinking is permanently expanding. For example, quantitative relationships between  $\varepsilon$ - $\beta$ - $\tau_{\text{dir\_geometric}}$  and effective transport properties are the basis for recent investigations of Li-ion batteries [121], polymer films [16], tight gas reservoirs [376], sandstones [20,21], packed beds in oil combustion [360], biomaterials/bone tissue [26] and general packings of slightly overlapping spheres [28], see also [267] where large-scale statistical learning has been performed for the prediction of effective diffusivity in porous materials using 90,000 artificially generated microstructures.

## 5.2 Quantitative micro-macro relationships for the prediction of permeability

The evolution of quantitative micro-macro relationships for the prediction of permeability is schematically illustrated in Fig. 24. Basically, this evolution can be subdivided into an early period, when methods for 3D-analysis were not yet available, and a recent period after the year. 2000, when micro- and nano-tomography, 3D-image processing as well as stochastic 3D modeling became available.

The basic principles describing the limiting effects, which arise from the underlying microstructure, were introduced by Kozeny in 1927 [190] and Carman in 1937 [47] (see also the discussion of hydraulic tortuosity in Chapter 2 of the present paper). The theories of Carman and Kozeny [47,190] are based on simplified geometrical models, which serve as analogues for realistic pore structures. The bundle-of-tubes model

[190,289] and the sphere-packing model [47] are of particular importance. However, the morphological descriptors determined for such simplified models can not easily be transferred to more complex microstructures. A large amount of literature that has been published since the work of Kozeny and Carman thus intends to improve the prediction power of Carman-Kozeny-type equations and to make them applicable for more realistic materials models with complex microstructures. Early examples are given by Panda and Lake (1994) [251] for poly-disperse granular media, and by Costa (2006) [62] for fractal pore geometries.

Over the last two decades, the progress in 3D imaging and image processing opened new possibilities to quantify the relevant microstructure characteristics (geometric and mixed tortuosity, bottleneck radius, constrictivity). The availability of new morphological descriptors also led to new expressions for the micro-macro relationships that were presented in literature. Basically, all equations (the classical and new ones) can be reduced to a representation of permeability  $\kappa$  by the simple product of characteristic length and  $M$ -factor, i.e.,

$$\text{Eq. 57} \quad \kappa = L_{char} M .$$

Thereby, the term of characteristic length ( $L_{char}$ ) accounts for wall friction effects, which are captured by the squared hydraulic radius ( $r_{hc}^2$ ). Note that the characteristic length term has a major impact on permeability. For example, when the hydraulic radius ( $r_{hc}$ ) of a porous material changes from 10  $\mu\text{m}$  to 0.1  $\mu\text{m}$  due to pore clogging, the corresponding permeabilities ( $\kappa$ ) decrease by 4 orders of magnitudes, e.g. from 5  $10^{-11}$  to 5  $10^{-15}$   $\text{m}^2$  (assuming a constant  $M$ -factor of 0.5). Hence, the precise determination of the characteristic length and hydraulic radius ( $L_{char}$ ,  $r_{hc}$ ) is of major importance for a reliable prediction of permeability.

The second term in Eq. 57 is the microstructure  $M$ -factor for flow. It accounts for all the other transport limitations, except for wall friction. Thereby, the effects of varying pore-volume fractions, transport path lengths and bottlenecks can be described by dimensionless characteristics ( $\varepsilon$ ,  $\tau$ ,  $\beta$ ). The resulting  $M$ -factor then takes values between 0 to 1.

In the following sections, important expressions that were proposed for prediction of permeability are briefly reviewed in chronological order. The evolution of these expressions is also visualized in Fig. 24. For better comparison, all expressions are reformulated such that the two terms for characteristic length and  $M$ -factor are clearly distinguished.

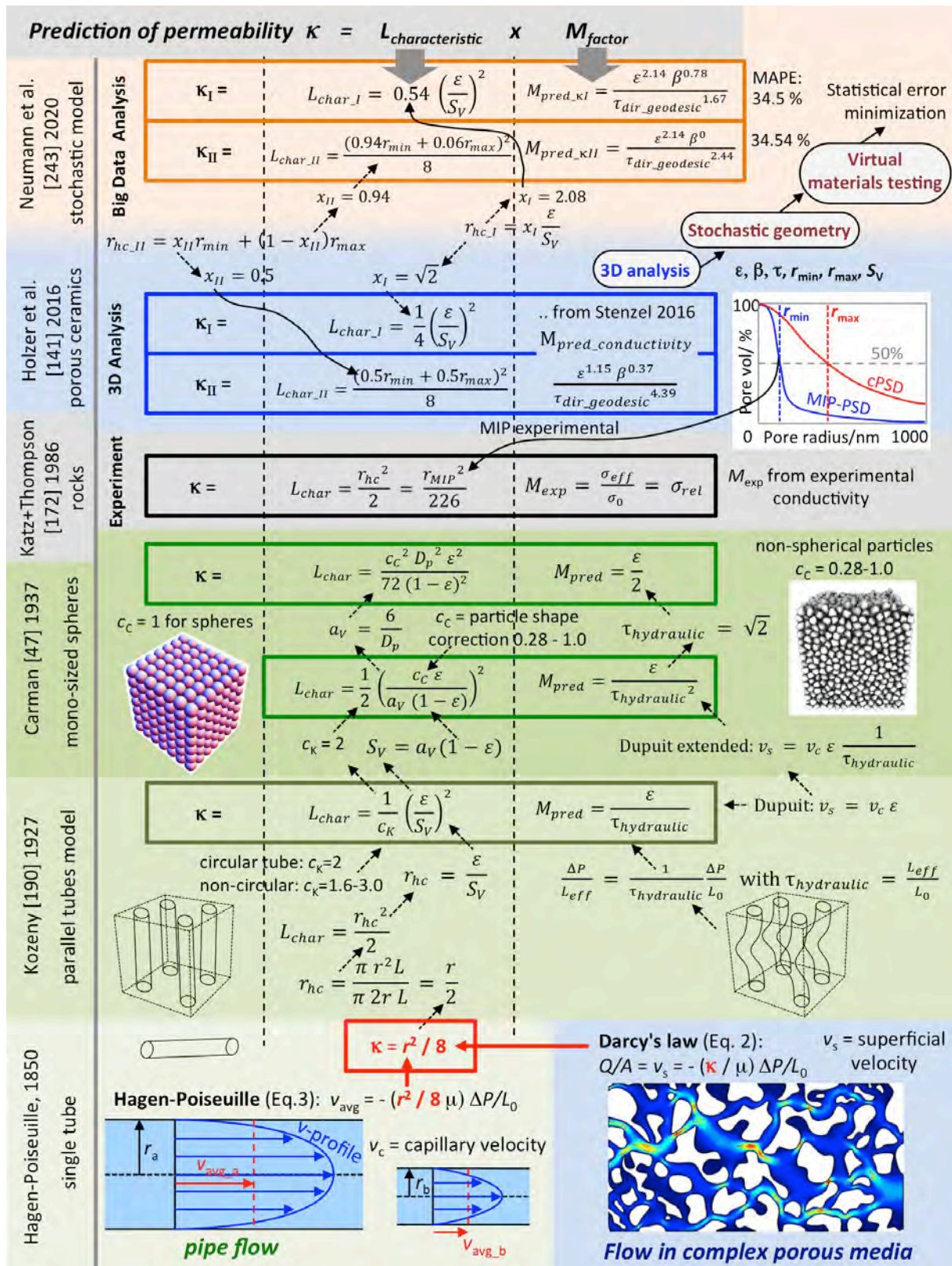


Fig. 24: Evolution of quantitative micro-macro relationships for prediction of permeability in porous media.

### 5.2.1 Bundle of tubes model

Kozeny's description of flow [190] from 1927 is based on the consideration of a bundle of tubes. Flow in a single, straight tube can be described by the Hagen-Poiseuille law (Eq. 3). From comparison with Darcy's law (Eq. 2) for porous media, it follows that 'permeability' of a single pipe depends only on the radius, i.e.,

$$\text{Eq. 58} \quad \kappa_{\text{pipe\_flow}} = L_{\text{char}} = r^2 / 8 .$$

Kozeny [190] then introduced a general definition for the hydraulic radius by

$$\text{Eq. 59} \quad r_{hc} = \frac{\text{Vol open to flow}}{\text{wetted surface}} = \frac{\pi r^2 L}{\pi 2r L} = \frac{r}{2} ,$$

which is the ratio of the tube volume open to flow over the surface area that is wetted by the fluid. The combination of Eqs. 58 and 59 leads to the following 'pipe-flow permeability' given by

$$\text{Eq. 60} \quad \kappa_{\text{pipe\_flow}} = L_{\text{char}} = r_{hc}^2 / 2 .$$

For porous media consisting of bundles of tubes, the hydraulic radius and associated volume-to-surface ratio from Eq. 59 can also be written in terms of porosity over specific surface area per volume ( $S_v$ , with units  $\text{m}^2/\text{m}^3$ ), i.e.

$$\text{Eq. 61} \quad r_{hc} = \frac{\varepsilon}{S_v}$$

The characteristic length term for a bundle of tubes thus becomes

$$\text{Eq. 62} \quad L_{\text{char}} = \frac{1}{2} \left( \frac{\varepsilon}{S_v} \right)^2 = \frac{1}{c_K} \left( \frac{\varepsilon}{S_v} \right)^2 .$$

Thereby, the Kozeny factor ( $c_K$ ) for circular tubes is equal to 2, in accordance with Eq. 60. For non-circular tubes the  $c_K$ -values vary in the range from 1.6 (for triangular tubes) to 3 (for rectangular tubes with a high aspect ratio).

Furthermore, Kozeny pointed out in [190] that the superficial velocity ( $v_s$ ) in Darcy's macroscopic description of porous media flow (and thus also for a bundle of tubes) is different from the capillary velocity ( $v_c$ ) in Poiseuille's microscopic description of flow in a single pipe. According to Dupuit's relation the two velocities are linked by porosity, i.e.,

$$\text{Eq. 63} \quad v_s = v_c \varepsilon .$$

Kozeny [190] thus introduced porosity as part of the M-factor for flow. In addition, from the comparison of the models for sinusoidal and straight tubes model, it follows that the lengths of the pathways increase from  $L_0$  to  $L_{\text{eff}}$ . Consequently, the pressure gradient (in Hagen-Poiseuille's and Darcy's law) needs to be corrected accordingly from  $\Delta P/L_0$  to  $\Delta P/L_{\text{eff}}$ . In this context, Kozeny [190] introduced the tortuosity concept with the definition of tortuosity ( $\tau = L_{\text{eff}}/L_0$ ) in order to describe the path length effect on the pressure gradient. This reads as

$$\text{Eq. 64} \quad \frac{\Delta P}{L_{eff}} = \frac{1}{\tau_{hydraulic}} \frac{\Delta P}{L_0}.$$

Note that Kozeny's formulation of the M-factor thus includes corrections for porosity and path lengths (tortuosity), which leads to

$$\text{Eq. 65} \quad M_{pred} = \frac{\varepsilon}{\tau_{hydraulic}}.$$

Combining the M-factor (Eq. 65) and the characteristic length term (Eq. 62) gives the full Kozeny equation, which describes permeability for a bundle of tubes-model by

$$\text{Eq. 66:} \quad \kappa_{Kozeny} = \frac{1}{c_K} \left( \frac{\varepsilon}{S_V} \right)^2 \frac{\varepsilon}{\tau_{hydraulic}},$$

with Kozeny's shape factor  $c_K = 2$  for circular tubes.

### 5.2.2 Sphere packing model

In Carman's work [47] from 1937, the Kozeny equation (Eq. 66) was modified such that it describes flow in a packed bed of spheres. For a simplified model with mono-sized spheres, it is straightforward to determine the specific surface area of the spheres ( $S_P$ ) per solid volume ( $V_P$ ) of the spheres ( $a_V = S_P / V_P$ ). In order to obtain the specific surface area per total volume of the porous material ( $S_V = S_P / V_{tot}$ ), a correction for the solid volume fraction ( $1 - \varepsilon$ ) is required, i.e.,

$$\text{Eq. 67} \quad S_V = a_V (1 - \varepsilon).$$

In geometrical models for non-spherical particles, an additional shape correction factor ( $c_C$ , the so-called Carman factor) was introduced by Carman [47]. At the same time, Kozeny's correction factor (Eq. 62) for tube shape becomes redundant, and thus  $c_K$  is replaced with the constant 2. This leads to the characteristic length term

$$\text{Eq. 68} \quad L_{char} = \frac{1}{2} \left( \frac{c_C \varepsilon}{a_V (1 - \varepsilon)} \right)^2$$

for granular media consisting of mono-sized objects. According to Carman [47], the shape factor ( $c_C$ ) takes values in the range from 1 (for spheres) down to 0.28 (for platy minerals, mica). The surface-to-volume ratio ( $a_V$ ) for packing of mono-sized objects (spheres, particles) is often written in terms of the particle diameter ( $a_V = 6/D_p$ ), which then leads to

$$\text{Eq. 69} \quad L_{char} = \frac{c_C^2 D_p^2 \varepsilon^2}{72(1 - \varepsilon)^2}.$$

Kozeny [190] correctly recognized that the pressure gradient in granular media must be corrected for the effect of path length and, therefore, tortuosity was introduced for this correction (see Eq. 64). However, it was Carman [47] who realized that the increase of path lengths also has an effect on the computed (superficial) flow velocity and he

therefore extended Dupuits relationship (cf. Eq. 63) for the influence of tortuosity, which leads to

$$\text{Eq. 62b} \quad v_s = v_c \varepsilon \frac{1}{\tau_{hydraulic}}.$$

In this way, tortuosity was introduced a second time in the M-factor by Carman [47], which leads to

$$\text{Eq. 70} \quad M_{pred} = \frac{\varepsilon}{\tau_{hydraulic}^2}.$$

Thereby,  $\tau^2$  is also called tortuosity factor ( $T$ ).

Combining the M-factor (Eq. 70) with the characteristic length term (Eq. 68) gives the full Carman-Kozeny equation

$$\text{Eq. 71:} \quad \kappa_{C-K} = \frac{1}{2} \left( \frac{c_C \varepsilon}{a_V(1-\varepsilon)} \right)^2 \frac{\varepsilon}{\tau_{hydraulic}^2} = \frac{c_C^2 D_p^2 \varepsilon^2}{72(1-\varepsilon)^2} \frac{\varepsilon}{\tau_{hydraulic}^2},$$

which describes permeability for a packed bed of mono-sized particles. In the appendix of [47], a geometrical model for packed spheres is presented, which enables one to estimate the length of flow streamlines. Based on these geometric considerations, Carman argued in [47] that the streamline tortuosity in most granular media must be close to  $\sqrt{2}$ . Following this argumentation, the value for tortuosity is thus often fixed at  $\tau = \sqrt{2}$ . The M-factor for flow then simplifies to  $\varepsilon/2$ . In the simplest form for mono-sized spheres ( $c_C = 1$ ) the Carman-Kozeny equation reduces to

$$\text{Eq. 72} \quad \kappa_{C-K} = \frac{1}{2} \left( \frac{\varepsilon}{S_V} \right)^2 \frac{\varepsilon}{2} = \frac{D_p^2 \varepsilon^2}{72(1-\varepsilon)^2} \frac{\varepsilon}{2}.$$

Note that the Carman-Kozeny equation was developed at a time when methods for 3D imaging and image analysis were not yet available and therefore morphological descriptors were used, which are relatively easy to access ( $\varepsilon$ ,  $S_V$ ,  $D_p$ ,  $\tau = \sqrt{2}$ ). Still nowadays, this equation is widely used by the research community. However, it must be emphasized that the applicability of the Kozeny (Eq. 66) and the Carman-Kozeny (Eq. 72) equations are limited to simple microstructures such as the bundle-of-tubes model and the (mono-sized) packed-spheres model. Already for relatively small deviations from these idealized geometries (e.g. non-circular tubes or non-spherical grains) specific correction factors ( $c_K$ ,  $c_C$ ) must be fitted, which introduce considerable uncertainties.

Despite these drawbacks, the Carman-Kozeny equation (Eq. 72) is often applied also for the study of more complex microstructures such as dispersed granular materials and even foams and fibrous materials. However, it was shown by many authors that the predictions obtained by the Carman-Kozeny equation are highly uncertain for such complex microstructures [150,153,244,246]. Big efforts were undertaken to modify the Carman-Kozeny equation in order to improve the prediction power also for more realistic (complex) microstructures, e.g. in [62,251]. In principle, most of these modifications still use the same relatively simple morphological descriptors ( $\varepsilon$ ,  $S_V$ ,  $D_p$ ,  $\tau = \sqrt{2}$ ). In this context, it is worth to critically consider, which microstructure effects are

reliably captured with the Carman-Kozeny equation and which are not. From the above description, it can easily be recognized that the M-factor in the Carman-Kozeny equation is rather simple. Important microstructure effects resulting from the variation of path-lengths (constant tortuosity,  $\tau = \sqrt{2}$ ) and bottlenecks (no constrictivity included) are not captured accurately. However, the strength of the Carman-Kozeny equation is clearly the description of characteristic length and hydraulic radius, respectively, which enables to capture the wall friction effects in (mono-sized) granular media quite well.

### 5.2.3 Determination of characteristic length and M-factor by laboratory experiments

Katz and Thompson (1986) [172] presented an experimental solution for measuring characteristic length and M-factor ( $M_{exp}$ ), which enables to predict permeability of complex porous media. In order to measure the characteristic length, it was proposed to use mercury intrusion porosimetry (MIP). The pore size distribution curve (MIP-PSD) typically shows a steep rise, the corresponding radius of which can be interpreted as 'break-through radius' ( $r_{MIP}$ ). When the pressure is raised to the break-through range, a large portion of the pore space is filled almost instantaneously with liquid mercury. The domain, which is filled with mercury, thus represents a contiguous pore network. Katz and Thompson [172] defined the inflection point of the MIP-PSD curve (convex-concave transition) as break-through radius ( $r_{MIP}$ ). They argued that  $r_{MIP}$  is a characteristic quantity of the pore network, which has a significant influence on flow and permeability, and which can thus be interpreted as an equivalent of the hydraulic radius ( $r_{hc}$ ). Based on experimental evidence, a constant of  $1/226$  was determined in [172] as part of the characteristic length, i.e.,

$$\text{Eq. 73} \quad L_{char} = \frac{r_{hc}^2}{2} = \frac{r_{MIP}^2}{226}.$$

Moreover, it was argued in [172] that there are additional effects from pore morphology and connectivity, which may have the same limiting influence on flow as they have on electrical conductivity (i.e. non-viscous/non-frictional effects). Consequently, it has been proposed in [172] that the M-factor for flow could be determined based on experimental measurements of effective electrical conductivity (i.e. using porous media saturated with an electrolyte, whereby  $\sigma_0$  denotes the intrinsic conductivity of the electrolyte). Doing so, an experimental M-factor was obtained with is defined by

$$\text{Eq. 74} \quad M_{exp} = \frac{\sigma_{eff}}{\sigma_0} = \sigma_{rel}.$$

Katz and Thompson [172] thus proposed to predict permeability from  $L_{char}$  and  $M_{exp}$ , using the relationship

$$\text{Eq. 75} \quad \kappa_{Katz-Thompson} = L_{char} \frac{\sigma_{eff}}{\sigma_0} = \frac{(r_{MIP})^2}{226} \frac{\sigma_{eff}}{\sigma_0}.$$

Note that both characteristics,  $L_{char}$  and  $M_{exp}$ , are easily accessible with standard experimental methods.

### 5.2.4 Determination of characteristic length and M-factor by 3D image analysis

With the advent of 3D imaging at sub- $\mu\text{m}$  resolution (e.g. by FIB-SEM tomography in 2004 [135]), it became possible to quantify specific morphological characteristics in complex microstructures. Hence, direct geometric and mixed tortuosities are nowadays accessible from 3D image analysis and can be used to describe the effects resulting from variations of path lengths. Similarly, constrictivity ( $\beta$ ) is accessible and can be used to describe the bottleneck effect. Based on these characteristics ( $\varepsilon$ ,  $\beta$ ,  $\tau$ ), new expressions for the relationship between microstructure characteristics and conductivity/diffusivity could be established. As described in Chapter 5.1,  $M_{pred\_conductivity}$  was determined by Stenzel et al. [312,313] by using modern methods of stochastic geometry, virtual materials testing and statistical error minimization (compare Eq. 49b:  $M_{pred} = \varepsilon^a \beta^b / \tau_{geodesic}^c$ , with  $a=1.15$ ,  $b=0.37$ ,  $c=4.39$ ).

In analogy to the paper of Katz and Thompson [172] reviewed in Section 5.2.3, Holzer, et al. (2016) [141] argued that the M-factor of conductivity from Stenzel et al. [312] (Eq. 49b) can be used as a first approximation for the M-factor of flow. In addition, for the effective lengths term, two different definitions for hydraulic radius ( $r_{hc\_I}$ ,  $r_{hc\_II}$ ) were proposed in [141]. Note that the two different definitions for hydraulic radius lead to two different equations for the prediction of permeability ( $\kappa_{pred\_I}$ ,  $\kappa_{pred\_II}$ ).

The first approach presented in [141] uses the classical definition of the hydraulic radius (i.e. the ratio of porosity over specific surface area per volume). However, in contrast to the initial Carman-Kozeny approach, specific surface area ( $S_V$ ) is not determined from the characteristic sphere diameter ( $D_p$ ), but it is determined directly from the complex microstructures using 3D image analysis, i.e.,

$$\text{Eq. 76} \quad r_{hc\_I} = X_I \frac{\varepsilon}{S_V},$$

where  $X_I$  is a fitting parameter. Based on detailed investigations of sintered porous ceramics in [141], the effective properties ( $\kappa$ ,  $\sigma_{eff}$ ) were determined by experiments ( $\kappa_{exp}$ ), pore scale simulation ( $\kappa_{sim}$ ) as well as 3D imaging/image analysis ( $\kappa_{pred\_I}$ ,  $S_V$ ,  $\beta$ ,  $\varepsilon$ ,  $\tau_{dir\_geodesic}$ ). By error minimization ( $\kappa_{pred\_I} - \kappa_{sim}$  and  $\kappa_{pred\_I} - \kappa_{exp}$ ) a value of  $X_I = \sqrt{2}$  was estimated. This leads to

$$\text{Eq. 77} \quad L_{char\_I} = \frac{r_{hc}^2}{8} = \frac{1}{4} \left( \frac{\varepsilon}{S_V} \right)^2$$

as a description of the characteristic length. Permeability ( $\kappa_{pred\_I}$ ) can thus be obtained from the combination of  $L_{char\_I}$  (Eq.77) with the M-factor for conductivity from Stenzel et al. [312] (Eq. 49b) by

$$\text{Eq. 78} \quad \kappa_{pred\_I} = \frac{1}{4} \left( \frac{\varepsilon}{S_V} \right)^2 \frac{\varepsilon^{1.15} \beta^{0.37}}{\tau_{dir\_geodesic}^{4.39}}.$$

For the second approach considered in [141], it was argued that the hydraulic radius can also be defined as convex combination of the mean size of bottlenecks ( $r_{min}$ ) and the mean size of pore bulges ( $r_{max}$ ), i.e.,

$$\text{Eq. 79} \quad r_{hc\_II} = x_{II} r_{min} + (1 - x_{II}) r_{max}$$

(We refer to [233] for the determination of  $r_{min}$  and  $r_{max}$ , respectively). Using results from 3D image analysis ( $\kappa_{pred\_II}, r_{min}, r_{max}, \beta, \tau_{dir\_geod}$ ), numerical simulation ( $\kappa_{sim}$ ) and experimental characterization ( $\kappa_{exp}$ ) as well as applying error minimization, a value of 0.5 was obtained  $x_{II}$ , which leads to

$$\text{Eq. 80} \quad L_{char\_II} = \frac{r_{hc}^2}{8} = \frac{(0.5 r_{min} + 0.5 r_{max})^2}{8}.$$

Permeability ( $\kappa_{pred\_II}$ ) is thus predicted by a combination of  $L_{char\_II}$  (Eq.80) with the M-factor for conductivity (see Eq. 49b). More precisely,

$$\text{Eq. 81} \quad \kappa_{pred\_II} = \frac{(0.5 r_{min} + 0.5 r_{max})^2}{8} \frac{\varepsilon^{1.15} \beta^{0.37}}{\tau_{dir\_geodesic}^{4.39}}.$$

Both approaches ( $\kappa_{pred\_I}, \kappa_{pred\_II}$ ) were tested with fibrous materials of a gas diffusion layer (GDL) in PEM fuel cells [140]. In-situ time-lapse tomography ( $\mu$ -CT) was used to capture the changing 3D water-distribution upon ongoing imbibition. A good agreement was obtained between the predicted permeabilities ( $\kappa_{pred\_I}, \kappa_{pred\_II}$ ) based on 3D characterization with simulated permeabilities ( $\kappa_{sim}$ ) based on a numerical 3D flow model. Thereby, the predictions obtained by  $\kappa_{pred\_II}$  (Eq. 81) resulted in smaller differences to  $\kappa_{sim}$ , compared to the predictions by  $\kappa_{pred\_I}$  (Eq. 78).

Note that the prediction formula for permeability  $\kappa_{pred\_II}$  (Eq. 81) presented [141] is similar to the prediction proposed by Katz and Thompson [172], in the sense that both approaches use MIP-PSDs ( $r_{min}$  and  $r_{MIP}$ , respectively) for determining the hydraulic radius (cf. Eqs. 73 and 79). Furthermore, in both approaches, the M-factor is determined from effective/relative conductivity (cf Eqs. 49b and 74). The difference is that physical experiments are used in [172], while the approach in [141] is based on 3D image analysis.

### 5.2.5 Determination of characteristic length and M-factor by virtual materials testing (Neumann et al., 2020 [243])

Using the same expressions as in Holzer et al [141] for  $r_{hc\_I}$  ( $= x_I \varepsilon / S_V$ ),  $r_{hc\_II}$  ( $= x_{II} r_{min} + (1 - x_{II}) r_{max}$ ) and  $M_{pred}$  ( $= \varepsilon^a \beta^b / \tau^c$ ), the corresponding constants and exponents ( $x_I, x_{II}, a, b, c$ ) were determined recently by means of stochastic geometry and virtual materials testing (see Neumann et al., 2020 [243]). Thereby, the 8119 different 3D microstructures from Stenzel et al. [313] served as a basis for big data analysis. It must be emphasized that in this approach the results obtained with respect of the fitting of constants used in  $r_{hc}$  ( $x_I$  or  $x_{II}$ ) and of the exponents used in  $M_{pred}$  ( $a, b, c$ ) are not independent of each other, since the fitting is performed with one simultaneous error minimization procedure. The resulting M-factor is thus specifically fitted for flow and permeability, respectively (i.e.  $M_{pred\_K}$ ). This approach is thus more specific than the permeability predictions of Holzer et al. [141] and Katz and Thompson [172] (see previous sections), where the M-factors are derived from electrical conductivity (i.e.  $M_{pred\_conductivity}$ ).

Using virtual materials testing and error minimization, Neumann et al. [243] obtained a constant of  $x_I = 2.08$  for the classical definition of the hydraulic radius ( $r_{hc,I} = x_I \varepsilon / S_V$ ). The resulting description of the characteristic length ( $L_{char}$ ) is thus very similar to the one from Kozeny [190] for circular pipes with  $c_K = 2$ , i.e.,

$$\text{Eq. 82} \quad L_{char\_I} = \frac{r_{hc}^2}{8} = \frac{1}{8} \left( 2.08 \frac{\varepsilon}{S_V} \right)^2 = 0.54 \left( \frac{\varepsilon}{S_V} \right)^2 = \frac{1}{c_K} \left( \frac{\varepsilon}{S_V} \right)^2$$

Furthermore, for the prediction of permeability considered in [243], the exponents of  $M_{pred\_KI}$  are significantly different from those in  $M_{pred\_cond}$  for conductivity (see Eq. 49b, proposed in Stenzel et al. [313]). The fitting revealed a higher exponent for porosity and lower exponent for tortuosity, which leads to

$$\text{Eq. 83} \quad M_{pred\_KI} = \frac{\varepsilon^{3.56} \beta^{0.78}}{\tau_{dir\_geodesic}^{1.67}}$$

The full equation for the prediction of permeability ( $\kappa_{pred\_I}$ ) is then given by

$$\text{Eq. 84} \quad \kappa_{pred\_I} = 0.54 \left( \frac{\varepsilon}{S_V} \right)^2 \frac{\varepsilon^{3.56} \beta^{0.78}}{\tau_{dir\_geodesic}^{1.67}}$$

For the second case, where the hydraulic radius is determined based on pore size analysis (i.e.  $r_{hc,II} = x_{II} r_{min} + (1 - x_{II}) r_{max}$ ), the virtual materials testing revealed a relatively high value of 0.94 for  $X_{II}$  (compared to 0.5 that was estimated in [141]). The corresponding characteristic length is then given by

$$\text{Eq. 85} \quad L_{char\_II} = \frac{r_{hc}^2}{8} = \frac{(0.94r_{min} + 0.06r_{max})^2}{8}$$

This result indicates that the hydraulic radius is almost identical with the mean radius of bottlenecks ( $r_{min}$  from MIP-PSD), which is similar to the definition of the hydraulic radius proposed by Katz and Thomson [172], where  $r_{hc} \approx r_{MIP}$ .

The M-factor ( $M_{pred\_KII}$ ) for permeability that is obtained from the fitting procedure for  $\kappa_{pred\_II}$  is quite different to the M-factors for  $\kappa_{pred\_I}$  (see Eq. 83) and for conductivity (see Eq. 49b), i.e.,

$$\text{Eq. 86} \quad M_{pred\_KII} = \frac{\varepsilon^{2.14} \beta^{-0.05}}{\tau_{dir\_geodesic}^{2.44}} \approx \frac{\varepsilon^{2.14}}{\tau_{dir\_geodesic}^{2.44}}$$

For  $\kappa_{pred\_KII}$  the exponent for constrictivity ( $\beta^b$ ) is slightly below 0, which is counterintuitive from a physical point of view. In [243], it was shown that the statistical error (MAPE) for  $\kappa_{pred\_KII}$  is almost identical when comparing Eq. 86 with  $\beta^{0.05}$  and Eq. 86 without constrictivity (i.e. the case  $\beta^0$ ). Hence, constrictivity drops out from Eq. 86. This can be explained by the fact that in  $\kappa_{pred\_KII}$ , the bottleneck effect is already contained (as  $r_{min}$ ) in the characteristic length term ( $L_{char\_II}$ ). The equation for  $\kappa_{pred\_KII}$  thus becomes

$$\text{Eq. 87} \quad \kappa_{II} = \frac{(0.94r_{min} + 0.06r_{max})^2}{8} \frac{\varepsilon^{2.14}}{\tau_{dir\_geodesic}^{2.44}}$$

The statistical analysis performed by Neumann et al. [243] shows that the prediction powers of  $\kappa_{pred\_KI}$  and  $\kappa_{pred\_KII}$  are almost identical. The MAPE is 34.5 % for both permeability approaches.

In summary, the approach considered in [243] is based on a statistical analysis of more than 8'000 different 3D scenarios, which cover a wide range of microstructures and effective properties. Due to this large data basis, the proposed equations have a rather general character, since they are capable to predict permeability for various kinds of realistic materials even with very complex microstructures. For example,  $\mu$ CT-data from cellular, foam like-structures was used in [243] to demonstrate the prediction power of Eqs. 84 and 87 for image data from materials, which have not been used to fit the parameters in these prediction formulas. For comparison, the Kozeny and Carman-Kozeny equations were derived from parallel-tube and packed-spheres models with idealized geometries. Consequently, the prediction powers of these traditional equations are strongly limited and not really applicable to more complex microstructures. An important difference of recently proposed expressions compared to the traditional Carman-Kozeny approach is the introduction of constrictivity in the  $M$ -factor. More precisely, it is one of the main shortcomings of the Carman-Kozeny approach, that the effect resulting from narrow bottlenecks is not properly addressed. The equations for the prediction of permeability (and conductivity) have also improved due to a better description of path length effects. Carman [47] proposed to use a constant value of  $\sqrt{2}$  for  $\tau_{hydraulic}$ . In the approach proposed by Neumann et al. [243], geodesic tortuosity is used. For the 8'000 3D microstructures, geodesic tortuosity varies between 1.05 and 2.4 (see Figs 13b and 13c). The variation of  $\tau_{dir\_geodesic}$  is particularly large (1.2 to 2.4) for structures with low porosity ( $\epsilon < 0.25$ ). Hence, neither can tortuosity be considered as a constant ( $\sqrt{2}$ ), as proposed by Carman [47], nor is tortuosity a simple function of porosity, as proposed in widely used tortuosity-porosity relationships (e.g. the Bruggemann relationship). For complex microstructures the permeability can only be predicted in a reliable way with suitable descriptions of geometric or mixed tortuosity and other relevant characteristics (effective porosity, constrictivity, hydraulic radius) gained from 3D analysis, see also [267], where large-scale statistical learning has been performed for the prediction of permeability in porous materials using 90,000 artificially generated microstructures.

## 6. Summary and conclusions

Classical theories of transport in porous media (e.g. the Carman-Kozeny equations for flow; Archie's law for conduction) and associated tortuosity concepts are reviewed in Chapter 2. These theories were derived a long time ago, when suitable methods for tomography and 3D image analysis were not yet available. The inherent micro-macro relationships are thus based on the consideration of simplified geometry models such as packed beds of mono-sized spheres or parallel tubes. In this way, many aspects of the microstructure could be captured by means of simple morphological descriptors. For example, the wall friction effect and the associated hydraulic radius are described with diameters of spheres or tubes, which are building blocks of simplified microstructure models. Unfortunately, these classical micro-macro relationships with their simplified descriptors cannot easily be transferred to realistic materials with more complex microstructures.

The effect of varying path lengths has also been recognized a long time ago as a major microstructure limitation for transport in porous media. Therefore, tortuosity was included as a relevant parameter in the classical theories. However, for practical applications, path lengths and tortuosity are rather complex descriptors, which could not be measured directly from the microstructure until recently. This is one of the reasons why many different definitions, methods and names were introduced in the literature dealing with tortuosity. This multitude of approaches created much confusion, which still nowadays leads to controversial discussions of the topic.

As a countermeasure to this unsatisfactory situation, we propose a new tortuosity classification scheme. The classification is based on the selected method, which is used to determine tortuosity (direct vs. indirect determination of tortuosities) and on the type of definition (geometric vs. physics-based definition of tortuosities). This classification scheme leads to three main tortuosity categories:

- a) direct geometric tortuosities
- b) mixed tortuosities
- c) indirect physics-based tortuosities

Based on this classification scheme, we also propose a systematic tortuosity nomenclature, which includes relevant information about the underlying method of determination and details on the geometric or physical definition. The proposed classification scheme and the associated nomenclature are illustrated in Fig. 3.

Chapter 3 contains an extensive collection of empirical data (tortuosity-porosity couples) from 69 different studies that investigate tortuosity for different materials (appearing in batteries, fuel cells, rocks, packed spheres, fibrous textures, etc.). This collection includes many cases, where different tortuosity types were measured for the same materials. Furthermore, these datasets allow a direct comparison of different tortuosity types, which reveals a surprisingly clear picture in the sense that certain tortuosity types give consistently higher values than others, irrespective of the material under investigation. With respect to the three main categories of tortuosity, it can be concluded that the measured values for indirect tortuosities are consistently larger (often  $\gg 2$ ) than those for the mixed and direct tortuosities (often around  $\sqrt{2}$  and below). The observed, systematic order among the various tortuosity types is illustrated in Fig. 12.

The empirical data furthermore indicates that the measured values for tortuosity are more strongly dependent on the type of tortuosity than on the material itself. These findings underline the importance of carefully selecting a suitable method and to precisely declare the corresponding type of tortuosity with the help of the proposed classification scheme and nomenclature.

The empirical data also shows that tortuosity-porosity couples do not follow a certain trend in general, but they are scattering within certain limits. In the dilute limit where porosity approaches the value of 1, tortuosity values asymptotically go to 1 as well, which lowers the upper bound of the scattering field. With decreasing porosity, however, the scattering of tortuosity becomes more pronounced as the upper bound increases. For indirect tortuosities, the upper bound is much higher (up to 20 and more) compared to direct and mixed tortuosities. Therefore, the scattering of indirect tortuosity is stronger. Based on this observation, it must be concluded that mathematical expressions for tortuosity-porosity relationships (e.g. the Bruggemann relation) cannot have any universal meaning. Mathematical tortuosity-porosity formulas

can thus only be meaningful when they are derived for a specific tortuosity type and for special microstructure variations, which are discussed in the present paper. Hence, from a generalized point of view, there is much evidence that microstructure characteristics, such as tortuosity, porosity, constrictivity and pore size, can vary independently of each other. In order to describe microstructure effects properly it is therefore necessary to find suitable characterization techniques for all relevant microstructure characteristics.

In Chapter 4, an extensive overview of methodologies is given for microstructure characterization in general and for tortuosity analysis in particular. The workflow for a thorough 3D characterization (see Fig. 14) includes several methodologies that are still rapidly evolving. Each of these methodologies is reviewed specifically: Tomography, qualitative image processing (3D reconstruction, filtering and segmentation), quantitative image analysis (specific algorithms for each tortuosity type), numerical simulation of transport (conduction, diffusion, flow), stochastic microstructure modeling, machine learning and virtual materials testing.

In particular, the different calculation approaches for the three main tortuosity categories are discussed separately: The computation of direct geometric tortuosities is based on quantitative 3D image analysis. The indirect physics-based tortuosities are computed from effective properties, which are determined by numerical transport simulations (or by real laboratory experiments). For mixed tortuosities, volume fields obtained by numerical transport simulation are used. The mixed tortuosities are then computed by geometric analysis of these volume fields (i.e. 3D image analysis of streamlines or velocity vectors). Hence, the mixed tortuosities contain information that covers physics-based as well as geometric aspects. In this sense, the mixed tortuosities can be considered as the most advanced and most relevant descriptors for the path length effect. For practical help, an extensive list with available SW packages and codes for microstructure analysis and modeling is presented (see Table 6), with a special emphasize on tortuosity characterization.

Based on the methodological progress in tomography, 3D image analysis, stochastic microstructure modeling, artificial intelligence and virtual materials testing, new possibilities become available, which allow a thorough characterization of microstructures at different length scales and with different complexities. Investigations using combinations of these modern methodologies provide a better understanding of the underlying micro-macro relationships. A prerequisite for these improvements are better descriptors for the path length effect by means of direct geometric and mixed tortuosities. But also for the bottleneck effect and for the wall friction effect, improved descriptors could be found, such as constrictivity and hydraulic radius based on MIP-PSD and cPSD. In Chapter 5, it is summarized how these new descriptors were used to establish new quantitative micro-macro relationships. Typically, recent approaches are data-driven and, for this purpose, they involve methods of stochastic geometry, machine learning, virtual materials testing and error minimization. In particular, we refer to a series of studies [102,141,243,267,312,313], where the microstructure influence on effective transport properties is quantified by means of virtual materials testing.

For conduction and diffusion, the evolution of micro-macro formulas is summarized in Fig. 22. From the numerous equations that were evaluated, Eq. 49b, i.e.,

$$\text{Eq. 49b} \quad M_{pred} = \varepsilon^{1.15} \beta^{0.37} / \tau_{dir\_geodesic}^{4.39}, \quad \text{MAPE: 19.06\%}$$

has the highest overall prediction power with a MAPE of 19.06%. Thereby,  $M_{pred}$  is equivalent to the relative conductivity ( $\sigma_{ele,rel}$ ) and/or relative diffusivity ( $D_{rel}$ ). It must be emphasized that for microstructures with a high porosity, more precise predictions are obtained by Eq. 55b, i.e.,

$$M_{pred} = \varepsilon^{1.67-0.48\beta} / \tau_{dir\_geodesic}^{5.18},$$

with a MAPE<sub>total</sub> of 18.3 % (and a MAPE of 10.3 % for microstructures with  $M > 0.05$ ).

For viscous flow in porous media, the evolution of micro-macro formulas is summarized in Fig. 23. Two different expressions for permeability ( $\kappa_I, \kappa_{II}$ ) are derived, namely Eq. 84, i.e.,

$$\kappa_I = 0.54 \left( \frac{\varepsilon}{S_V} \right)^2 \frac{\varepsilon^{3.56} \beta^{0.78}}{\tau_{dir\_geodesic}^{1.67}},$$

with a MAPE of 34.5 %, and Eq. 87, i.e.,

$$\kappa_{II} = \frac{(0.94r_{min}+0.06r_{max})^2}{8} \frac{\varepsilon^{2.14}}{\tau_{dir\_geodesic}^{2.44}},$$

with a MAPE of 34.54 %. Thus, both formulas have almost the same prediction powers. Moreover, compared to classical theories such as the Carman-Kozeny equation for flow and Archie's law for conduction, these new micro-macro relationships have a much higher prediction power. In particular, they can also be used for complex disordered microstructures, where the classical theories mentioned above are not applicable. These improvements are mainly due to the progress of recent 3D methodologies, which provide better morphological descriptors.

Nowadays many different possibilities are available for the characterization of tortuosity. In this context the findings from the review of empirical data (Chapter 4) must be kept in mind. Thereby a consistent pattern is observed, which indicates that the measured values of tortuosity are more strongly dependent on the tortuosity type (and on the associated method) than on the material itself. It is thus important to understand the differences between specific tortuosity types. Which type of tortuosity and which calculation approach one should choose, depends on the information that is required for a specific purpose. The basic arguments for different tortuosity classes can be summarized as follows:

a) Indirect physics-based tortuosities describe bulk resistances of the microstructure against specific transport processes. They do not contain strict geometric information and therefore they do not really contribute to a fundamental understanding of the path length effect. Indirect tortuosities are lumped parameters, which include not only the limiting effect of paths lengths variations but also other microstructure limitations such as the bottleneck effects. Indirect tortuosities are often used as input for macro-homogeneous models. For this purpose they are well suited, since they describe the bulk resistive influence of the microstructure.

b) Direct geometric tortuosities are based on measurements of path lengths through the 3D microstructure. For materials engineers, the geometric tortuosity reveals morphological information that is relevant for purposeful microstructure optimization. However, microstructure limitations on transport can not be fully described by the geometric tortuosity alone. In order to understand the relationship between microstructure and effective transport properties, it is necessary to consider additional microstructure characteristics, such as constrictivity, porosity and hydraulic radius. In context with new micro-macro formulas (e.g. Eq. 49b), the geodesic tortuosity turns out to be a suitable geometric descriptor for path-length effects. However, since the geometric tortuosities are not physics-based, this leaves some room for further improvement of micro-macro formulas and their prediction power.

c) Mixed tortuosities include the advantages of both calculation approaches, in the sense that they contain true information of the path lengths (i.e. geometric) and at the same time, they are specific for the underlying transport process (i.e. physics-based). Mixed tortuosities thus bear key information that is necessary to understand path length effects of specific transport mechanisms on a fundamental level. It is thus probable that the prediction power of modern micro-macro relationships (such as Eq. 49b and Eq. 84) can be further improved by using mixed tortuosities as descriptors for the paths length effect.

## Electronic Appendix

Extended versions of Tables 2 and 6 are provided as excel files.

- Appendix\_electronic\_1-Table\_2.xlsx
- Appendix\_electronic\_2-Table\_6.xlsx

## References:

- [1] Van Aarle, W., Palenstijn, W.J., De Beenhouwer, J., Altantzis, T., Bals, S., Batenburg, K.J., Sijbers, J. (2015) The ASTRA toolbox: A platform for advanced algorithm development in electron tomography. *Ultramicroscopy* 157(35–47), 157.
- [2] Abdallah, B., Willot, F., Jeulin, D. (2016) Morphological modelling of three-phase microstructures of anode layers using SEM images. *J. Microsc.* 263(1), 51–63, Doi: 10.1111/jmi.12374.
- [3] Adler, P.M. (2013) *Porous Media: Geometry and Transports*, Series in Chemical Engineering. Butterworth-Heinemann, Boston.
- [4] Ahmadi, M.M., Mohammadi, S., Hayati, A.N. (2011) Analytical derivation of tortuosity and permeability of monosized spheres: A volume averaging approach. *Phys. Rev. E* 83(2), 026312, Doi: 10.1103/PhysRevE.83.026312.
- [5] Al-Raoush, R.I., Madhoun, I.T. (2017) TORT3D: A MATLAB code to compute geometric tortuosity from 3D images of unconsolidated porous media. *Powder Technol.* 320, 99–107, Doi: 10.1016/j.powtec.2017.06.066.
- [6] Almar, L., Joos, J., Weber, A., Ivers-Tiffée, E. (2019) Microstructural feature analysis of commercial Li-ion battery cathodes by focused ion beam tomography. *J. Power Sources* 427(January), 1–14, Doi: 10.1016/j.jpowsour.2019.04.019.
- [7] Almar, L., Szasz, J., Weber, A., Ivers-Tiffée, E. (2017) Oxygen Transport Kinetics of Mixed Ionic-Electronic Conductors by Coupling Focused Ion Beam tomography and Electrochemical Impedance Spectroscopy.pdf. *J. Electrochem. Soc.* 164(4), F289–97, Doi: 10.1149/2.0851704jes.
- [8] Archie G.E. (1942) The Electrical Resistivity Log as an Aid in Determining Some Reservoir Characteristics. *Trans AIME*, 146–54.
- [9] Arganda-Carreras, I., Kaynig, V., Rueden, C., Eliceiri, K.W., Schindelin, J., Cardona, A., Sebastian Seung, H. (2017) Trainable Weka Segmentation: a machine learning tool for microscopy pixel classification. *Bioinformatics* 33(15), 2424–6, Doi: 10.1093/bioinformatics/btx180.
- [10] Arora, P., Doyle, M., Gozdz, A.S., White, R.E., Newman, J. (2000) Comparison between computer simulations and experimental data for high-rate discharges of plastic lithium-ion batteries. *J. Power Sources* 88(2), 219–31, Doi: 10.1016/S0378-7753(99)00527-3.
- [11] Aslannejad, H., Hassanizadeh, S.M., Raoof, A., de Winter, D.A.M., Tomozeiu, N., van Genuchten, M.T. (2017) Characterizing the hydraulic properties of paper coating layer using FIB-SEM tomography and 3D pore-scale modeling. *Chem. Eng. Sci.* 160(November 2016), 275–80, Doi: 10.1016/j.ces.2016.11.021.
- [12] Babovsky, H. (1986) On Knudsen flows within thin tubes. *J. Stat. Phys.* 44(5–6), 865–78, Doi: 10.1007/BF01011911.
- [13] Bae, K., Kim, J.W., Son, J. won., Lee, T., Kang, S., Prinz, F.B., Shim, J.H. (2018) 3D Evaluation of Porous Zeolite Absorbents Using FIB-SEM Tomography. *Int. J. Precis. Eng. Manuf. - Green Technol.* 5(2), 195–9, Doi: 10.1007/s40684-018-0019-4.
- [14] Bargmann, S., Klusemann, B., Markmann, J., Schnabel, J.E., Schneider, K., Soyarslan, C., Wilmers, J. (2018) Generation of 3D representative volume elements for heterogeneous materials: A review. *Prog. Mater. Sci.* 96, 322–84, Doi: 10.1016/j.pmatsci.2018.02.003.
- [15] Barman, S., Bolin, D., Fager, C., Gebäck, T., Lorén, N., Olaaon, E., Rootzén, H., Särkkä, A. (2019) Mist - A program package for visualization and characterization of 3D geometries.
- [16] Barman, S., Rootzén, H., Bolin, D. (2019) Prediction of diffusive transport through

- polymer films from characteristics of the pore geometry. *AIChE J.* 65(1), 446–57, Doi: 10.1002/aic.16391.
- [17] Bassim, N., Scott, K., Giannuzzi, L.A. (2014) Recent advances in focused ion beam technology and applications. *MRS Bull.* 39(4), 317–25, Doi: 10.1557/mrs.2014.52.
- [18] Bear, J. (1972) *Dynamics of fluid in porous media*. New York.
- [19] Beeckman, J.W. (1990) Mathematical description of heterogeneous materials. *Chem. Eng. Sci.* 45(8), 2603–10, Doi: 10.1016/0009-2509(90)80148-8.
- [20] Berg, C.F. (2014) Permeability Description by Characteristic Length, Tortuosity, Constriction and Porosity. *Transp. Porous Media* 103(3), 381–400, Doi: 10.1007/s11242-014-0307-6.
- [21] Berg, C.F. (2012) Re-examining Archie’s law: Conductance description by tortuosity and constriction. *Phys. Rev. E* 86(4), 046314, Doi: 10.1103/PhysRevE.86.046314.
- [22] Berg, C.F., Kennedy, W.D., Herrick, D.C. (2022) Conductivity in partially saturated porous media described by porosity, electrolyte saturation and saturation-dependent tortuosity and constriction factor. *Geophys. Prospect.* 70(2), 400–20, Doi: 10.1111/1365-2478.13166.
- [23] Berg, S., Kutra, D., Kroeger, T., Straehle, C.N., Kausler, B.X., Haubold, C., Schiegg, M., Ales, J., Beier, T., Rudy, M., Eren, K., Cervantes, J.I., Xu, B., Beuttenmueller, F., Wolny, A., Zhang, C., Koethe, U., Hamprecht, F.A., Kreshuk, A. (2019) ilastik: interactive machine learning for (bio)image analysis. *Nat. Methods* 16(12), 1226–32, Doi: 10.1038/s41592-019-0582-9.
- [24] Bertei, A., Ruiz-Trejo, E., Tariq, F., Yufit, V., Atkinson, A., Brandon, N.P. (2016) Validation of a physically-based solid oxide fuel cell anode model combining 3D tomography and impedance spectroscopy. *Int. J. Hydrogen Energy* 41(47), 22381–93, Doi: 10.1016/j.ijhydene.2016.09.100.
- [25] Bhatia, S. (1985) Directional autocorrelation and the diffusional tortuosity of capillary porous media. *J. Catal.* 93(1), 192–6, Doi: 10.1016/0021-9517(85)90163-0.
- [26] Bini, F., Pica, A., Marinozzi, A., Marinozzi, F. (2019) A 3D Model of the Effect of Tortuosity and Constrictivity on the Diffusion in Mineralized Collagen Fibril. *Sci. Rep.* 9(1), 1–14, Doi: 10.1038/s41598-019-39297-w.
- [27] Bird, R.B., Stewart, W.E., Lightfoot, E.N. (2007) *Transport Phenomena*. Second Edi, John Wiley & Sons, New York.
- [28] Birkholz, O., Neumann, M., Schmidt, V., Kamlah, M. (2021) Statistical investigation of structural and transport properties of densely-packed assemblies of overlapping spheres using the resistor network method. *Powder Technol.* 378, 659–66, Doi: 10.1016/j.powtec.2020.09.056.
- [29] Bradley, R.S., Withers, P.J. (2016) Correlative multiscale tomography of biological materials. *MRS Bull.* 41(07), 549–56, Doi: 10.1557/mrs.2016.137.
- [30] Van Brakel, J., Heertjes, P.M. (1974) Analysis of diffusion in macroporous media in terms of a porosity, a tortuosity and a constrictivity factor. *Int. J. Heat Mass Transf.* 17, 1093–103.
- [31] Brisard, S., Serdar, M., Monteiro, P.J.M. (2020) Multiscale X-ray tomography of cementitious materials: A review. *Cem. Concr. Res.* 128(November 2019), 105824, Doi: 10.1016/j.cemconres.2019.105824.
- [32] Bruggeman, D.A.G. (1935) Berechnung verschiedener physikalischer Konstanten von heterogenen Substanzen. I. Dielektrizitätskonstanten und Leitfähigkeiten der Mischkörper aus isotropen Substanzen. *Ann. Phys.* 416(7), 636–64, Doi:

- 10.1002/andp.19354160705.
- [33] Buades, A., Coll, B., Morel, J.-M. (2005) A Non-Local Algorithm for Image Denoising. *IEEE Computer Society Conference on Computer Vision and Pattern Recognition (CVPR'05)*, vol. 2, IEEE, pp. 60–5.
  - [34] Bugelnig, K., Barriobero-Vila, P., Requena, G. (2018) Synchrotron computer tomography as a characterization method for engineering materials. *Prakt. Metallogr. Metallogr.* 55(8), 556–68, Doi: 10.3139/147.110534.
  - [35] Bühner, M., Stampanoni, M., Rochet, X., Büchi, F., Eller, J., Marone, F. (2019) High-numerical-aperture microscope optics for time-resolved experiments. *J. Synchrotron Radiat.* 26, 1161–72, Doi: 10.1107/S1600577519004119.
  - [36] Buljac, A., Jailin, C., Mendoza, A., Neggers, J., Taillandier-Thomas, T., Bouterf, A., Smaniotto, B., Hild, F., Roux, S. (2018) Digital Volume Correlation: Review of Progress and Challenges. *Exp. Mech.* 58(5), 661–708, Doi: 10.1007/s11340-018-0390-7.
  - [37] Bultreys, T., De Boever, W., Cnudde, V. (2016) Imaging and image-based fluid transport modeling at the pore scale in geological materials: A practical introduction to the current state-of-the-art. *Earth-Science Rev.* 155, 93–128, Doi: 10.1016/j.earscirev.2016.02.001.
  - [38] Bultreys, T., Boone, M.A., Boone, M.N., De Schryver, T., Masschaele, B., Van Hoorebeke, L., Cnudde, V. (2016) Fast laboratory-based micro-computed tomography for pore-scale research: Illustrative experiments and perspectives on the future. *Adv. Water Resour.* 95, 341–51, Doi: 10.1016/j.advwatres.2015.05.012.
  - [39] Burnett, T.L., Kelley, R., Winiarski, B., Contreras, L., Daly, M., Gholinia, A., Burke, M.G., Withers, P.J. (2016) Large volume serial section tomography by Xe Plasma FIB dual beam microscopy. *Ultramicroscopy* 161, 119–29, Doi: 10.1016/j.ultramic.2015.11.001.
  - [40] Burnett, T.L., McDonald, S.A., Gholinia, A., Geurts, R., Janus, M., Slater, T., Haigh, S.J., Ornek, C., Almuaili, F., Engelberg, D.L., Thompson, G.E., Withers, P.J. (2015) Correlative Tomography. *Sci. Rep.* 4(1), 4711, Doi: 10.1038/srep04711.
  - [41] Burnett, T.L., Withers, P.J. (2019) Completing the picture through correlative characterization. *Nat. Mater.* 18(10), 1041–9, Doi: 10.1038/s41563-019-0402-8.
  - [42] Cannarella, J., Arnold, C.B. (2013) Ion transport restriction in mechanically strained separator membranes. *J. Power Sources* 226, 149–55, Doi: 10.1016/j.jpowsour.2012.10.093.
  - [43] Cantoni, M., Holzer, L. (2014) Advances in 3D focused ion beam tomography. *MRS Bull.* 39(04), 354–60, Doi: 10.1557/mrs.2014.54.
  - [44] Cao, C., Toney, M.F., Sham, T.-K., Harder, R., Shearing, P.R., Xiao, X., Wang, J. (2020) Emerging X-ray imaging technologies for energy materials. *Mater. Today* 34(xx), 132–47, Doi: 10.1016/j.mattod.2019.08.011.
  - [45] Caplan, J., Niethammer, M., Taylor, R.M., Czymmek, K.J. (2011) The power of correlative microscopy: Multi-modal, multi-scale, multi-dimensional. *Curr. Opin. Struct. Biol.* 21(5), 686–93, Doi: 10.1016/j.sbi.2011.06.010.
  - [46] De Carlo, F., Gürsoy, D., Ching, D.J., Batenburg, K.J., Ludwig, W., Mancini, L., Marone, F., Mokso, R., Pelt, D.M., Sijbers, J., Rivers, M. (2018) TomoBank: A tomographic data repository for computational x-ray science. *Meas. Sci. Technol.* 29(3), Doi: 10.1088/1361-6501/aa9c19.
  - [47] Carman, P.C. (1997) Fluid flow through granular beds. *Chem. Eng. Res. Des.* 75, S32–48, Doi: 10.1016/S0263-8762(97)80003-2.
  - [48] Carman, P.C. (1956) *Flow of gases through porous media*. Butterworth, London.

- [49] Çeçen, A., Wargo, E.A., Hanna, A.C., Turner, D.M., Kalidindi, S.R., Kumbur, E.C. (2012) 3-D Microstructure Analysis of Fuel Cell Materials: Spatial Distributions of Tortuosity, Void Size and Diffusivity. *J. Electrochem. Soc.* 159(3), B299–307, Doi: 10.1149/2.068203jes.
- [50] Ceguerra, A. V., Marceau, R.K.W. (2019) Atom probe tomography of aluminium alloys: A systematic meta-analysis review of 2018. *Metals (Basel)*. 9(10), 1–16, Doi: 10.3390/met9101071.
- [51] Chen-Wiegart, Y.C.K., Demike, R., Erdonmez, C., Thornton, K., Barnett, S.A., Wang, J. (2014) Tortuosity characterization of 3D microstructure at nano-scale for energy storage and conversion materials. *J. Power Sources* 249, 349–56, Doi: 10.1016/j.jpowsour.2013.10.026.
- [52] Chen, L., He, A., Zhao, J., Kang, Q., Li, Z.-Y., Carmeliet, J., Shikazono, N., Tao, W.-Q. (2022) Pore-scale modeling of complex transport phenomena in porous media. *Prog. Energy Combust. Sci.* 88, 100968, Doi: 10.1016/j.pecs.2021.100968.
- [53] Chiu, S.N., Stoyan, D., Kendall, W., Mecke, J. (2013) *Stochastic Geometry and its Applications*. 3rd ed., John Wiley & Sons, Chichester, UK.
- [54] Chung, D.W., Ebner, M., Ely, D.R., Wood, V., Edwin García, R. (2013) Validity of the Bruggeman relation for porous electrodes. *Model. Simul. Mater. Sci. Eng.* 21(7), Doi: 10.1088/0965-0393/21/7/074009.
- [55] Clennell, M.B. (1997) Tortuosity: a guide through the maze. In: Lovell, M.A., Harvey, P.K., (Eds.), *Developments in Petrophysics*, Geol. Soc. Spec. Publ. No. 122, pp. 299–344.
- [56] Cnudde, V., Boone, M.N. (2013) High-resolution X-ray computed tomography in geosciences: A review of the current technology and applications. *Earth-Science Rev.* 123, 1–17, Doi: 10.1016/j.earscirev.2013.04.003.
- [57] Cocco, A.P., Nelson, G.J., Harris, W.M., Nakajo, A., Myles, T.D., Kiss, A.M., Lombardo, J.J., Chiu, W.K.S. (2013) Three-dimensional microstructural imaging methods for energy materials. *Phys. Chem. Chem. Phys.* 15(39), 16377, Doi: 10.1039/c3cp52356j.
- [58] Comiti, J., Renaud, M. (1989) A new model for determining mean structure parameters of fixed beds from pressure drop measurements: application to beds packed with parallelepipedal particles. *Chem. Eng. Sci.* 44(7), 1539–45, Doi: 10.1016/0009-2509(89)80031-4.
- [59] Cooper, S.J., Bertei, A., Shearing, P.R., Kilner, J.A., Brandon, N.P. (2016) TauFactor: An open-source application for calculating tortuosity factors from tomographic data. *SoftwareX* 5, 203–10, Doi: 10.1016/j.softx.2016.09.002.
- [60] Cooper, S.J., Eastwood, D.S., Gelb, J., Damblanc, G., Brett, D.J.L., Bradley, R.S., Withers, P.J., Lee, P.D., Marquis, A.J., Brandon, N.P., Shearing, P.R. (2014) Image based modelling of microstructural heterogeneity in LiFePO<sub>4</sub> electrodes for Li-ion batteries. *J. Power Sources* 247, 1033–9, Doi: 10.1016/j.jpowsour.2013.04.156.
- [61] Cooper, S.J., Kishimoto, M., Tariq, F., Bradley, R.S., Marquis, A.J., Brandon, N.P., Kilner, J.A., Shearing, P.R. (2013) Microstructural Analysis of an LSCF Cathode Using In Situ Tomography and Simulation. *ECS Trans.* 57(1), 2671–8, Doi: 10.1149/05701.2671ecst.
- [62] Costa, A. (2006) Permeability-porosity relationship: A reexamination of the Kozeny-Carman equation based on a fractal pore-space geometry assumption. *Geophys. Res. Lett.* 33(2), L02318, Doi: 10.1029/2005GL025134.
- [63] Currie, J.A. (1960) Gaseous diffusion in porous media. Part 2. - Dry granular

- materials. *Br. J. Appl. Phys.* 11(8), 318–24, Doi: 10.1088/0508-3443/11/8/303.
- [64] Daemi, S.R., Lu, X., Sykes, D., Behnsen, J., Tan, C., Palacios-Padros, A., Cookson, J., Petrucco, E., Withers, P.J., Brett, D.J.L., Shearing, P.R. (2019) 4D visualisation of in situ nano-compression of Li-ion cathode materials to mimic early stage calendaring. *Mater. Horizons* 6(3), 612–7, Doi: 10.1039/C8MH01533C.
- [65] Darcy, H. (1856) *Les fontaines publiques de la ville de Dijon*. Paris.
- [66] Delgado, J.M.P.Q. (2008) A Simple Experimental Technique to Measure Tortuosity in Packed Beds. *Can. J. Chem. Eng.* 84(6), 651–5, Doi: 10.1002/cjce.5450840603.
- [67] Denk, W., Horstmann, H. (2004) Serial Block-Face Scanning Electron Microscopy to Reconstruct Three-Dimensional Tissue Nanostructure. *PLoS Biol.* 2(11), e329, Doi: 10.1371/journal.pbio.0020329.
- [68] Dierickx, S., Joos, J., Weber, A., Ivers-Tiffée, E. (2018) Advanced impedance modelling of Ni/8YSZ cermet anodes. *Electrochim. Acta* 265, 736–50, Doi: 10.1016/j.electacta.2017.12.029.
- [69] Dijkstra, W. (1959) A note on two problems in connection with graphs. *Numer. Math.* 1, 269–71.
- [70] Dirrenberger, J., Forest, S., Jeulin, D. (2014) Towards gigantic RVE sizes for 3D stochastic fibrous networks. *Int. J. Solids Struct.* 51(2), 359–76, Doi: 10.1016/j.ijsolstr.2013.10.011.
- [71] Ditscherlein, R., Furat, O., Löwer, E., Mehnert, R., Trunk, R., Leißner, T., Krause, M.J., Schmidt, V., Peuker, U.A. (2022) PARROT: A Pilot Study on the Open Access Provision of Particle-Discrete Tomographic Datasets. *Microsc. Microanal.*, 1–11, Doi: 10.1017/S143192762101391X.
- [72] Doyle, M. (1996) Comparison of Modeling Predictions with Experimental Data from Plastic Lithium Ion Cells. *J. Electrochem. Soc.* 143(6), 1890, Doi: 10.1149/1.1836921.
- [73] Duda, A., Koza, Z., Matyka, M. (2011) Hydraulic tortuosity in arbitrary porous media flow. *Phys. Rev. E - Stat. Nonlinear, Soft Matter Phys.* 84(3), Doi: 10.1103/PhysRevE.84.036319.
- [74] Dullien, F.A.L. (2012) *Porous Media: Fluid Transport and Pore Structure*. Academic Press Ltd, London.
- [75] Dumitraschkewitz, P., Gerstl, S.S.A., Uggowitzer, P.J., Löffler, J.F., Pogatscher, S. (2017) Atom Probe Tomography Study of As-Quenched Al–Mg–Si Alloys. *Adv. Eng. Mater.* 19(4), 1–5, Doi: 10.1002/adem.201600668.
- [76] Ebner, M., Chung, D.W., García, R.E., Wood, V. (2014) Tortuosity anisotropy in lithium-ion battery electrodes. *Adv. Energy Mater.* 4(5), 1–6, Doi: 10.1002/aenm.201301278.
- [77] Ebner, M., Wood, V. (2015) Tool for Tortuosity Estimation in Lithium Ion Battery Porous Electrodes. *J. Electrochem. Soc.* 162(2), A3064–70, Doi: 10.1149/2.0111502jes.
- [78] Echlin, M.P., Burnett, T.L., Polonsky, A.T., Pollock, T.M., Withers, P.J. (2020) Serial sectioning in the SEM for three dimensional materials science. *Curr. Opin. Solid State Mater. Sci.* 24(2), 100817, Doi: 10.1016/j.cossms.2020.100817.
- [79] Echlin, M.P., Straw, M., Randolph, S., Filevich, J., Pollock, T.M. (2015) The TriBeam system: Femtosecond laser ablation in situ SEM. *Mater. Charact.* 100, 1–12, Doi: 10.1016/j.matchar.2014.10.023.
- [80] Eder, K., McCarroll, I., La Fontaine, A., Cairney, J.M. (2018) Nanoscale Analysis of Corrosion Products: A Review of the Application of Atom Probe and Complementary Microscopy Techniques. *Jom* 70(9), 1744–51, Doi:

- 10.1007/s11837-018-2967-0.
- [81] Eller, J., Roth, J., Marone, F., Stampanoni, M., Büchi, F.N. (2017) Operando Properties of Gas Diffusion Layers: Saturation and Liquid Permeability. *J. Electrochem. Soc.* 164(2), F115–26, Doi: 10.1149/2.0881702jes.
- [82] Elwinger, F., Pourmand, P., Furó, I. (2017) Diffusive Transport in Pores. Tortuosity and Molecular Interaction with the Pore Wall. *J. Phys. Chem. C* 121(25), 13757–64, Doi: 10.1021/acs.jpcc.7b03885.
- [83] Endler-Schuck, C., Joos, J., Niedrig, C., Weber, A., Ivers-Tiffée, E. (2015) The chemical oxygen surface exchange and bulk diffusion coefficient determined by impedance spectroscopy of porous  $\text{La}_{0.58}\text{Sr}_{0.4}\text{Co}_{0.2}\text{Fe}_{0.8}\text{O}_{3-\delta}$  (LSCF) cathodes. *Solid State Ionics* 269, 67–79, Doi: 10.1016/j.ssi.2014.11.018.
- [84] Epstein, N. (1989) On tortuosity and the tortuosity factor in flow and diffusion through porous media. *Chem. Eng. Sci.* 44(3), 777–9.
- [85] Ercius, P., Alaidi, O., Rames, M.J., Ren, G. (2015) Electron Tomography: A Three-Dimensional Analytic Tool for Hard and Soft Materials Research. *Adv. Mater.* 27(38), 5638–63, Doi: 10.1002/adma.201501015.
- [86] Erni, R., Rossell, M.D., Kisielowski, C., Dahmen, U. (2009) Atomic-Resolution Imaging with a Sub-50-pm Electron Probe. *Phys. Rev. Lett.* 102(9), 096101, Doi: 10.1103/PhysRevLett.102.096101.
- [87] Etiemble, A., Tranchot, A., Douillard, T., Idrissi, H., Maire, E., Roué, L. (2016) Evolution of the 3D Microstructure of a Si-Based Electrode for Li-Ion Batteries Investigated by FIB/SEM Tomography. *J. Electrochem. Soc.* 163(8), A1550–9, Doi: 10.1149/2.0421608jes.
- [88] Faas, F.G.A., Avramut, M.C., M. van den Berg, B., Mommaas, A.M., Koster, A.J., Ravelli, R.B.G. (2012) Virtual nanoscopy: Generation of ultra-large high resolution electron microscopy maps. *J. Cell Biol.* 198(3), 457–69, Doi: 10.1083/jcb.201201140.
- [89] Fam, Y., Sheppard, T.L., Diaz, A., Scherer, T., Holler, M., Wang, W., Wang, D., Brenner, P., Wittstock, A., Grunwaldt, J.-D. (2018) Correlative Multiscale 3D Imaging of a Hierarchical Nanoporous Gold Catalyst by Electron, Ion and X-ray Nanotomography. *ChemCatChem* 10(13), 2858–67, Doi: 10.1002/cctc.201800230.
- [90] Feinauer, J., Brereton, T., Spetl, A., Weber, M., Manke, I., Schmidt, V. (2015) Stochastic 3D modeling of the microstructure of lithium-ion battery anodes via Gaussian random fields on the sphere. *Comput. Mater. Sci.* 109, 137–46, Doi: 10.1016/j.commatsci.2015.06.025.
- [91] Fend, C., Moghiseh, A., Redenbach, C., Schladitz, K. (2021) Reconstruction of highly porous structures from FIB-SEM using a deep neural network trained on synthetic images. *J. Microsc.* 281(1), 16–27, Doi: 10.1111/jmi.12944.
- [92] Ferguson, J.C., Borner, A., Panerai, F., Close, S., Mansour, N.N. (2022) Continuum to rarefied diffusive tortuosity factors in porous media from X-ray microtomography. *Comput. Mater. Sci.* 203, 111030, Doi: 10.1016/j.commatsci.2021.111030.
- [93] Finegan, D.P., Scheel, M., Robinson, J.B., Tjaden, B., Hunt, I., Mason, T.J., Millichamp, J., Di Michiel, M., Offer, G.J., Hinds, G., Brett, D.J.L., Shearing, P.R. (2015) In-operando high-speed tomography of lithium-ion batteries during thermal runaway. *Nat. Commun.* 6, 1–10, Doi: 10.1038/ncomms7924.
- [94] Flückiger, R., Freunberger, S.A., Kramer, D., Wokaun, A., Scherer, G.G., Büchi, F.N. (2008) Anisotropic, effective diffusivity of porous gas diffusion layer materials for PEFC. *Electrochim. Acta* 54(2), 551–9, Doi: 10.1016/j.electacta.2008.07.034.

- [95] Föhst, S., Osterroth, S., Arnold, F., Redenbach, C. (2022) Influence of geometry modifications on the permeability of open-cell foams. *AIChE J.* 68(2), Doi: 10.1002/aic.17446.
- [96] Froning, D., Brinkmann, J., Reimer, U., Schmidt, V., Lehnert, W., Stolten, D. (2013) 3D analysis, modeling and simulation of transport processes in compressed fibrous microstructures, using the Lattice Boltzmann method. *Electrochim. Acta* 110, 325–34, Doi: 10.1016/j.electacta.2013.04.071.
- [97] Froning, D., Yu, J., Gaiselmann, G., Reimer, U., Manke, I., Schmidt, V., Lehnert, W. (2016) Impact of compression on gas transport in non-woven gas diffusion layers of high temperature polymer electrolyte fuel cells. *J. Power Sources* 318, 26–34, Doi: 10.1016/j.jpowsour.2016.03.102.
- [98] Fu, J., Thomas, H.R., Li, C. (2020) Tortuosity of porous media: Image analysis and physical simulation. *Earth-Science Rev.*, 1–52.
- [99] Furat, O., Finegan, D.P., Diercks, D., Usseglio-Viretta, F., Smith, K., Schmidt, V. (2021) Mapping the architecture of single lithium ion electrode particles in 3D, using electron backscatter diffraction and machine learning segmentation. *J. Power Sources* 483, 229148, Doi: 10.1016/j.jpowsour.2020.229148.
- [100] Furat, O., Petrich, L., Finegan, D.P., Diercks, D., Usseglio-Viretta, F., Smith, K., Schmidt, V. (2021) Artificial generation of representative single Li-ion electrode particle architectures from microscopy data. *Npj Comput. Mater.* 7(1), 105, Doi: 10.1038/s41524-021-00567-9.
- [101] Furat, O., Wang, M., Neumann, M., Petrich, L., Weber, M., Krill, C.E., Schmidt, V. (2019) Machine Learning Techniques for the Segmentation of Tomographic Image Data of Functional Materials. *Front. Mater.* 6, Doi: 10.3389/fmats.2019.00145.
- [102] Gaiselmann, G., Neumann, M., Schmidt, V., Pecho, O., Hocker, T., Holzer, L. (2014) Quantitative relationships between microstructure and effective transport properties based on virtual materials testing. *AIChE J.* 60(6), 1983–99, Doi: 10.1002/aic.14416.
- [103] Gao, X., Diniz da Costa, J.C., Bhatia, S.K. (2014) Understanding the diffusional tortuosity of porous materials: An effective medium theory perspective. *Chem. Eng. Sci.* 110, 55–71, Doi: 10.1016/j.ces.2013.09.050.
- [104] Garcea, S.C., Wang, Y., Withers, P.J. (2018) X-ray computed tomography of polymer composites. *Compos. Sci. Technol.* 156, 305–19, Doi: 10.1016/j.compscitech.2017.10.023.
- [105] García-Salaberri, P.A., Gostick, J.T., Hwang, G., Weber, A.Z., Vera, M. (2015) Effective diffusivity in partially-saturated carbon-fiber gas diffusion layers: Effect of local saturation and application to macroscopic continuum models. *J. Power Sources* 296, 440–53, Doi: 10.1016/j.jpowsour.2015.07.034.
- [106] Garrouch, A.A., Ali, L., Qasem, F. (2001) Using Diffusion and Electrical Measurements to Assess Tortuosity of Porous Media. *Ind. Eng. Chem. Res.* 40(20), 4363–9, Doi: 10.1021/ie010070u.
- [107] Geißendörfer, M., Liebscher, A., Proppe, C., Redenbach, C., Schwarzer, D. (2014) Stochastic multiscale modeling of metal foams. *Probabilistic Eng. Mech.* 37, 132–7, Doi: 10.1016/j.probengmech.2014.06.006.
- [108] Ghanbarian, B. (2022) Scale dependence of tortuosity and diffusion: Finite-size scaling analysis. *J. Contam. Hydrol.* 245, 103953, Doi: 10.1016/j.jconhyd.2022.103953.
- [109] Ghanbarian, B., Hunt, A.G., Ewing, R.P., Sahimi, M. (2013) Tortuosity in Porous Media: A Critical Review. *Soil Sci. Soc. Am. J.* 77(5), 1461–77, Doi:

- 10.2136/sssaj2012.0435.
- [110] Ghassemi, A., Pak, A. (2011) Pore scale study of permeability and tortuosity for flow through particulate media using Lattice Boltzmann method. *Int. J. Numer. Anal. Methods Geomech.* 35(8), 886–901, Doi: 10.1002/nag.932.
- [111] Gholinia, A., Curd, M.E., Bousser, E., Taylor, K., Hosman, T., Coyle, S., Shearer, M.H., Hunt, J., Withers, P.J. (2020) Coupled Broad Ion Beam–Scanning Electron Microscopy (BIB–SEM) for polishing and three dimensional (3D) serial section tomography (SST). *Ultramicroscopy* 214(March), 112989, Doi: 10.1016/j.ultramic.2020.112989.
- [112] Glenn, D.R., Zhang, H., Kasthuri, N., Schalek, R., Lo, P.K., Trifonov, A.S., Park, H., Lichtman, J.W., Walsworth, R.L. (2012) Correlative light and electron microscopy using cathodoluminescence from nanoparticles with distinguishable colours. *Sci. Rep.* 2(1), 865, Doi: 10.1038/srep00865.
- [113] Golin, Y.L., Karyarin, V.E., Postelov, B.S., Sevedkin, V.I. (1992) Tortuosity estimates in porous media. *Sov. Electrochem.* 28, 87–91.
- [114] Gommès, C.J., Bons, A.-J., Blacher, S., Dunsmuir, J.H., Tsou, A.H. (2009) Practical methods for measuring the tortuosity of porous materials from binary or gray-tone tomographic reconstructions. *AIChE J.* 55(8), 2000–12, Doi: 10.1002/aic.11812.
- [115] Gondzio, J., Lassas, M., Latva-Äijö, S.-M., Siltanen, S., Zanetti, F. (2022) Material-separating regularizer for multi-energy x-ray tomography. *Inverse Probl.* 38(2), 025013, Doi: 10.1088/1361-6420/ac4427.
- [116] Gonzalez, J.F., Antartis, D.A., Chasiotis, I., Dillon, S.J., Lambros, J. (2018) In situ X-ray micro-CT characterization of chemo-mechanical relaxations during Sn lithiation. *J. Power Sources* 381(October 2017), 181–9, Doi: 10.1016/j.jpowsour.2018.01.056.
- [117] Grew, K., Peracchio, A.A., Izzo, J.R., Chiu, W. (2009) Nondestructive Imaging and Analysis of Transport Processes in the Solid Oxide Fuel Cell Anode. *ECS Transactions*, vol. 25, ECS, pp. 1861–70.
- [118] Grew, K.N., Chiu, W.K.S. (2012) A review of modeling and simulation techniques across the length scales for the solid oxide fuel cell. *J. Power Sources* 199, 1–13, Doi: 10.1016/j.jpowsour.2011.10.010.
- [119] Grew, K.N., Peracchio, A. a., Joshi, A.S., Izzo Jr., J.R., Chiu, W.K.S. (2010) Characterization and analysis methods for the examination of the heterogeneous solid oxide fuel cell electrode microstructure. Part 1: Volumetric measurements of the heterogeneous structure. *J. Power Sources* 195(24), 7930–42, Doi: 10.1016/j.jpowsour.2010.07.005.
- [120] Haj Ibrahim, S., Neumann, M., Klingner, F., Schmidt, V., Wejrzanowski, T. (2017) Analysis of the 3D microstructure of tape-cast open-porous materials via a combination of experiments and modeling. *Mater. Des.* 133, 216–23, Doi: 10.1016/j.matdes.2017.07.058.
- [121] Hamann, T., Zhang, L., Gong, Y., Godbey, G., Gritton, J., McOwen, D., Hitz, G., Wachsman, E. (2020) The Effects of Constriction Factor and Geometric Tortuosity on Li-Ion Transport in Porous Solid-State Li-Ion Electrolytes. *Adv. Funct. Mater.* 30(14), Doi: 10.1002/adfm.201910362.
- [122] Handschuh, S., Baeumler, N., Schwaha, T., Ruthensteiner, B. (2013) A correlative approach for combining microCT, light and transmission electron microscopy in a single 3D scenario. *Front. Zool.* 10(1), 44, Doi: 10.1186/1742-9994-10-44.
- [123] Hanna, J., Lee, W.Y., Shi, Y., Ghoniem, A.F. (2014) Fundamentals of electro- and

- thermochemistry in the anode of solid-oxide fuel cells with hydrocarbon and syngas fuels. *Prog. Energy Combust. Sci.* 40, 74–111, Doi: 10.1016/j.pecs.2013.10.001.
- [124] He, J., Ju, Y., Lammers, L., Kulasinski, K., Zheng, L. (2020) Tortuosity of kerogen pore structure to gas diffusion at molecular- and nano-scales: A molecular dynamics simulation. *Chem. Eng. Sci.* 215, 115460, Doi: 10.1016/j.ces.2019.115460.
- [125] Heenan, T.M.M., Finegan, D.P., Tjaden, B., Lu, X., Iacoviello, F., Millichamp, J., Brett, D.J.L., Shearing, P.R. (2018) 4D nano-tomography of electrochemical energy devices using lab-based X-ray imaging. *Nano Energy* 47(February), 556–65, Doi: 10.1016/j.nanoen.2018.03.001.
- [126] Heenan, T.M.M., Tan, C., Hack, J., Brett, D.J.L., Shearing, P.R. (2019) Developments in X-ray tomography characterization for electrochemical devices. *Mater. Today* (June), Doi: 10.1016/j.mattod.2019.05.019.
- [127] Heenan, T.M.M., Tan, C., Wade, A.J., Jervis, R., Brett, D.J.L., Shearing, P.R. (2020) Theoretical transmissions for X-ray computed tomography studies of lithium-ion battery cathodes. *Mater. Des.* 191, Doi: 10.1016/j.matdes.2020.108585.
- [128] Hein, S., Feinauer, J., Westhoff, D., Manke, I., Schmidt, V., Latz, A. (2016) Stochastic microstructure modeling and electrochemical simulation of lithium-ion cell anodes in 3D. *J. Power Sources* 336, 161–71, Doi: 10.1016/j.jpowsour.2016.10.057.
- [129] Hidayetoglu, M., Bicer, T., de Gonzalo, S.G., Ren, B., Gursoy, D., Kettimuthu, R., Foster, I.T., Hwu, W.-M.W. (2022) MemXCT: Design, Optimization, Scaling, and Reproducibility of X-Ray Tomography Imaging. *IEEE Trans. Parallel Distrib. Syst.* 33(9), 2014–31, Doi: 10.1109/TPDS.2021.3128032.
- [130] Hilfier, R. (1992) Local-porosity theory for flow in porous media. *Phys. Rev. B* B45, 7115–21.
- [131] Hilfier, R. (1991) Geometric and dielectric characterization of porous media. *Phys. Rev. B* 44, 60–75.
- [132] Hofmann, T., Westhoff, D., Feinauer, J., Andrä, H., Zausch, J., Schmidt, V., Müller, R. (2020) Electro-chemo-mechanical simulation for lithium ion batteries across the scales. *Int. J. Solids Struct.* 184, 24–39, Doi: 10.1016/j.ijsolstr.2019.05.002.
- [133] Holzer, L., Cantoni, M. (2011) Review of FIB-Tomography. In: Utke, I., Moshkalev, S., Russell, P., (Eds.), *Nanofabrication Using Focused Ion and Electron Beams: Principles and Applications*, Oxford University Press, New York, pp. 410–35.
- [134] Holzer, L., Gasser, P., Kaech, A., Wegmann, M., Zingg, A., Wepf, R., Muench, B. (2007) Cryo-FIB-nanotomography for quantitative analysis of particle structures in cement suspensions. *J. Microsc.* 227(3), 216–28, Doi: 10.1111/j.1365-2818.2007.01804.x.
- [135] Holzer, L., Indutnyi, F., Gasser, P., Münch, B., Wegmann, M. (2004) Three-dimensional analysis of porous BaTiO<sub>3</sub> ceramics using FIB nanotomography. *J. Microsc.* 216(1), 84–95.
- [136] Holzer, L., Iwanschitz, B., Hocker, T., Keller, L., Pecho, O., Sartoris, G., Gasser, P., Muench, B. (2013) Redox cycling of Ni-YSZ anodes for solid oxide fuel cells: Influence of tortuosity, constriction and percolation factors on the effective transport properties. *J. Power Sources* 242, 179–94, Doi: 10.1016/j.jpowsour.2013.05.047.
- [137] Holzer, L., Münch, B. (2009) Toward reproducible three-dimensional microstructure analysis of granular materials and complex suspensions. *Microsc.*

- Microanal. 15, 130–46, Doi: 10.1017/S1431927609090163.
- [138] Holzer, L., Münch, B., Rizzi, M., Wepf, R., Marschall, P., Graule, T. (2010) 3D-microstructure analysis of hydrated bentonite with cryo-stabilized pore water. *Appl. Clay Sci.* 47(3–4), 330–42, Doi: 10.1016/j.clay.2009.11.045.
- [139] Holzer, L., Pecho, O., Schumacher, J., Marmet, P., Büchi, F.N., Lamibrac, A., Münch, B. (2017) Microstructure-property relationships in a gas diffusion layer (GDL) for Polymer Electrolyte Fuel Cells, Part II: pressure-induced water injection and liquid permeability. *Electrochim. Acta* 241, 414–32, Doi: 10.1016/j.electacta.2017.04.141.
- [140] Holzer, L., Pecho, O., Schumacher, J., Marmet, P., Stenzel, O., Büchi, F.N., Lamibrac, A., Münch, B. (2017) Microstructure-property relationships in a gas diffusion layer (GDL) for Polymer Electrolyte Fuel Cells, Part I: effect of compression and anisotropy of dry GDL. *Electrochim. Acta* 227, 419–34, Doi: 10.1016/j.electacta.2017.01.030.
- [141] Holzer, L., Stenzel, O., Pecho, O., Ott, T., Boiger, G., Gorbar, M., de Hazan, Y., Penner, D., Schneider, I., Cervera, R., Gasser, P. (2016) Fundamental relationships between 3D pore topology, electrolyte conduction and flow properties: Towards knowledge-based design of ceramic diaphragms for sensor applications. *Mater. Des.* 99, 314–27, Doi: 10.1016/j.matdes.2016.03.034.
- [142] Holzer, L., Wiedenmann, D., Münch, B., Keller, L., Prestat, M., Gasser, P., Robertson, I., Grobéty, B. (2013) The influence of constrictivity on the effective transport properties of porous layers in electrolysis and fuel cells. *J. Mater. Sci.* 48(7), 2934–52, Doi: 10.1007/s10853-012-6968-z.
- [143] Holzinger, A., Neusser, G., Austen, B.J.J., Gamero-Quijano, A., Herzog, G., Arrigan, D.W.M., Ziegler, A., Walther, P., Kranz, C. (2018) Investigation of modified nanopore arrays using FIB/SEM tomography. *Faraday Discuss.* 210, 113–30, Doi: 10.1039/C8FD00019K.
- [144] Hoogschagen, J. (1955) Diffusion in porous catalysts and adsorbents. *Ind Eng Chem* 47(5), 906–912.
- [145] Hormann, K., Baranau, V., Hlushkou, D., Höltzel, A., Tallarek, U. (2016) Topological analysis of non-granular, disordered porous media: Determination of pore connectivity, pore coordination, and geometric tortuosity in physically reconstructed silica monoliths. *New J. Chem.* 40(5), 4187–99, Doi: 10.1039/c5nj02814k.
- [146] Le Houx, J., Kramer, D. (2020) Physics based modelling of porous lithium ion battery electrodes—A review. *Energy Reports* 6, 1–9, Doi: 10.1016/j.egyr.2020.02.021.
- [147] Hovden, R., Muller, D. (2020) Electron tomography for functional nanomaterials. *ArXiv*, 1–16.
- [148] Huang, X., Wang, Q., Zhou, W., Deng, D., Zhao, Y., Wen, D., Li, J. (2015) Morphology and transport properties of fibrous porous media. *Powder Technol.* 283, 618–26, Doi: 10.1016/j.powtec.2015.06.015.
- [149] Hunt, A., Ewing, R., Ghanbarian, B. (2014) *Percolation Theory for Flow in Porous Media*. vol. 880, 2nd Editio, Springer International Publishing, Cham.
- [150] Hunt, A.G., Ewing, R.P. (2003) ON THE VANISHING OF SOLUTE DIFFUSION IN POROUS MEDIA AT A THRESHOLD MOISTURE CONTENT. *Soil Sci. Soc. Am. J.* 67(6), 1701–2, Doi: 10.2136/sssaj2003.1701.
- [151] Hutzenlaub, T., Asthana, A., Becker, J., Wheeler, D.R., Zengerle, R., Thiele, S. (2013) FIB/SEM-based calculation of tortuosity in a porous LiCoO<sub>2</sub> cathode for a Li-ion

- battery. *Electrochem. Commun.* 27, 77–80, Doi: 10.1016/j.elecom.2012.11.006.
- [152] Iacoviello, F., Lu, X., Mitchell, T.M., Brett, D.J.L., Shearing, P.R. (2019) The Imaging Resolution and Knudsen Effect on the Mass Transport of Shale Gas Assisted by Multi-length Scale X-Ray Computed Tomography. *Sci. Rep.* 9(1), 1–10, Doi: 10.1038/s41598-019-55999-7.
- [153] Ichikawa, Y., Selvadurai, A.P.S. (2012) *Transport Phenomena in Porous Media*. Springer Berlin Heidelberg, Berlin, Heidelberg.
- [154] Idris, A., Muntean, A., Mesic, B. (2022) A review on predictive tortuosity models for composite films in gas barrier applications. *J. Coatings Technol. Res.*, Doi: 10.1007/s11998-021-00579-6.
- [155] Iversen, N., Jørgensen, B.B. (1993) Diffusion coefficients of sulfate and methane in marine sediments: Influence of porosity. *Geochim. Cosmochim. Acta* 57(3), 571–8, Doi: 10.1016/0016-7037(93)90368-7.
- [156] Iwai, H., Shikazono, N., Matsui, T., Teshima, H., Kishimoto, M., Kishida, R., Hayashi, D., Matsuzaki, K., Kanno, D., Saito, M., Muroyama, H., Eguchi, K., Kasagi, N., Yoshida, H. (2010) Quantification of SOFC anode microstructure based on dual beam FIB-SEM technique. *J. Power Sources* 195(4), 955–61, Doi: 10.1016/j.jpowsour.2009.09.005.
- [157] Jahns, K., Krupp, U., Sundell, G., Geers, C. (2020) Formation of corrosion pockets in FeNiCrAl at high temperatures investigated by 3D FIB-SEM tomography. *Mater. Corros.* 71(11), 1774–82, Doi: 10.1002/maco.201911386.
- [158] Jailin, C., Roux, S. (2018) Dynamic tomographic reconstruction of deforming volumes. *Materials (Basel)*. 11(8), Doi: 10.3390/ma11081395.
- [159] Jennings, S. (1988) The mean free path in air. *J. Aerosol Sci.* 19(2), 159–66, Doi: 10.1016/0021-8502(88)90219-4.
- [160] Jeulin, D. (2021) *Morphological Models of Random Structures*. Springer, Cham.
- [161] Jeulin, D., Vincent, L., Serpe, G. (1992) Propagation algorithms on graphs for physical applications. *J. Vis. Commun. Image Represent.* 3(2), 161–81, Doi: 10.1016/1047-3203(92)90013-J.
- [162] Jin, Y., Dong, J.B., Li, X., Wu, Y. (2015) Kinematical measurement of hydraulic tortuosity of fluid flow in porous media. *Int. J. Mod. Phys. C* 26(2), Doi: 10.1142/S0129183115500175.
- [163] Johnson, T.F., Iacoviello, F., Hayden, D.J., Welsh, J.H., Levison, P.R., Shearing, P.R., Bracewell, D.G. (2020) Packed bed compression visualisation and flow simulation using an erosion-dilation approach. *J. Chromatogr. A* 1611, 1–9, Doi: 10.1016/j.chroma.2019.460601.
- [164] Joos, J., Ender, M., Carraro, T., Weber, A., Ivers-Tiffée, E. (2012) Representative volume element size for accurate solid oxide fuel cell cathode reconstructions from focused ion beam tomography data. *Electrochim. Acta* 82, 268–76, Doi: 10.1016/j.electacta.2012.04.133.
- [165] Jørgensen, P.S., Ebbenhøj, S.L., Hauch, A. (2015) Triple phase boundary specific pathway analysis for quantitative characterization of solid oxide cell electrode microstructure. *J. Power Sources* 279, 686–93, Doi: 10.1016/j.jpowsour.2015.01.054.
- [166] Jørgensen, P.S., Hansen, K. V., Larsen, R., Bowen, J.R. (2011) Geometrical characterization of interconnected phase networks in three dimensions. *J. Microsc.* 244(1), 45–58, Doi: 10.1111/j.1365-2818.2011.03504.x.
- [167] Juliust, H., Amien, M.N., Pantouw, G.T., Eljabbar Latief, F.D. (2019) Complexity analysis of interconnected pore using hydraulic tortuosity. *IOP Conf. Ser. Earth*

- Environ. Sci. 311, 012034, Doi: 10.1088/1755-1315/311/1/012034.
- [168] Jungnickel, D. (1999) *Graphs, Network and Algorithm*. Springer, Berlin.
- [169] Kanit, T., Forest, S., Galliet, I., Mounoury, V., Jeulin, D. (2003) Determination of the size of the representative volume element for random composites: statistical and numerical approach. *Int. J. Solids Struct.* 40(13–14), 3647–79, Doi: 10.1016/S0020-7683(03)00143-4.
- [170] Kanno, D., Shikazono, N., Takagi, N., Matsuzaki, K., Kasagi, N. (2011) Evaluation of SOFC anode polarization simulation using three-dimensional microstructures reconstructed by FIB tomography. *Electrochim. Acta* 56(11), 4015–21, Doi: 10.1016/j.electacta.2011.02.010.
- [171] Katsube, T.J., Mudford, B.S., Best, M.E. (1991) Petrophysical characteristics of shales from the Scotian shelf. *GEOPHYSICS* 56(10), 1681–9, Doi: 10.1190/1.1442980.
- [172] Katz, A.J., Thompson, A.H. (1986) Quantitative prediction of permeability in porous rock. *Phys. Rev. B* 34(11), 8179–81.
- [173] Kazantsev, D., Guo, E., Phillion, A.B., Withers, P.J., Lee, P.D. (2017) Model-based iterative reconstruction using higher-order regularization of dynamic synchrotron data. *Meas. Sci. Technol.* 28(9), Doi: 10.1088/1361-6501/aa7fa8.
- [174] Kehrwald, D., Shearing, P.R., Brandon, N.P., Sinha, P.K., Harris, S.J. (2011) Local Tortuosity Inhomogeneities in a Lithium Battery Composite Electrode. *J. Electrochem. Soc.* 158(12), A1393, Doi: 10.1149/2.079112jes.
- [175] Keller, L.M., Holzer, L. (2018) Image-Based Upscaling of Permeability in Opalinus Clay. *J. Geophys. Res. Solid Earth* 123(1), 285–95, Doi: 10.1002/2017JB014717.
- [176] Keller, L.M., Holzer, L., Gasser, P., Erni, R., Rossell, M.D. (2015) Intergranular pore space evolution in MX80 bentonite during a long-term experiment. *Appl. Clay Sci.* 104, Doi: 10.1016/j.clay.2014.11.024.
- [177] Keller, L.M., Holzer, L., Schuetz, P., Gasser, P. (2013) Pore space relevant for gas permeability in Opalinus clay: Statistical analysis of homogeneity, percolation, and representative volume element. *J. Geophys. Res. Solid Earth* 118(6), Doi: 10.1002/jgrb.50228.
- [178] Keller, L.M., Holzer, L., Wepf, R., Gasser, P. (2011) 3D geometry and topology of pore pathways in Opalinus clay: Implications for mass transport. *Appl. Clay Sci.* 52(1–2), 85–95.
- [179] Keller, L.M., Holzer, L., Wepf, R., Gasser, P., Münch, B., Marschall, P. (2011) On the application of focused ion beam nanotomography in characterizing the 3D pore space geometry of Opalinus clay. *Phys. Chem. Earth* 36(17–18), Doi: 10.1016/j.pce.2011.07.010.
- [180] Keller, L.M., Schuetz, P., Erni, R., Rossell, M.D., Lucas, F., Gasser, P., Holzer, L. (2013) Characterization of multi-scale microstructural features in Opalinus Clay. *Microporous Mesoporous Mater.* 170, 83–94, Doi: 10.1016/j.micromeso.2012.11.029.
- [181] Kishimoto, M., Iwai, H., Saito, M., Yoshida, H. (2011) Quantitative evaluation of solid oxide fuel cell porous anode microstructure based on focused ion beam and scanning electron microscope technique and prediction of anode overpotentials. *J. Power Sources* 196(10), 4555–63, Doi: 10.1016/j.jpowsour.2010.12.100.
- [182] Kishimoto, M., Lomberg, M., Ruiz-Trejo, E., Brandon, N.P. (2016) Numerical modeling of nickel-infiltrated gadolinium-doped ceria electrodes reconstructed with focused ion beam tomography. *Electrochim. Acta* 190, 178–85, Doi: 10.1016/j.electacta.2015.12.044.

- [183] Klinkenberg, L.J. (1951) Analogy between diffusion and electrical conductivity in porous rocks. *GSA Bull.* 62(6), 559–564, Doi: [https://doi.org/10.1130/0016-7606\(1951\)62\[559:ABDAEC\]2.0.CO;2](https://doi.org/10.1130/0016-7606(1951)62[559:ABDAEC]2.0.CO;2).
- [184] Knackstedt, M.A., Arns, C.H., Saadatfar, M., Senden, T.J., Sakellariou, A., Sheppard, A.P., Sok, R.M., Schrof, W., Steininger, H. (2005) Virtual Materials Design: Properties of Cellular Solids Derived from 3D Tomographic Images. *Adv. Eng. Mater.* 7(4), 238–43, Doi: 10.1002/adem.200400212.
- [185] Knackstedt, M.A., Zhang, X. (1994) Direct evaluation of length scales and structural parameters associated with flow in porous media. *Phys. Rev. E* 50(3), 2134–8, Doi: 10.1103/PhysRevE.50.2134.
- [186] Koponen, A., Kataja, M., Timonen, J. (1997) Permeability and effective porosity of porous media. *Phys. Rev. E* 56(3), 3319–25, Doi: 10.1103/PhysRevE.56.3319.
- [187] Koponen, A., Kataja, M., Timonen, J. (1996) Tortuous flow in porous media. *Phys. Rev. E* 54(1), 406–10, Doi: 10.1103/PhysRevE.54.406.
- [188] Kotula, P.G., Rohrer, G.S., Marsh, M.P. (2014) Focused ion beam and scanning electron microscopy for 3D materials characterization. *MRS Bull.* 39(4), 361–5, Doi: 10.1557/mrs.2014.55.
- [189] Koza, Z., Matyka, M., Khalili, A. (2009) Finite-size anisotropy in statistically uniform porous media. *Phys. Rev. E* 79(6), 066306, Doi: 10.1103/PhysRevE.79.066306.
- [190] Kozeny, J. (1927) Über kapillare Leitung des Wassers im Boden. *Sitzungsbericht Der Akad. Der Wissenschaften Wien* 136(2a), 271–306.
- [191] Kristensen, A.H., Thorbjørn, A., Jensen, M.P., Pedersen, M., Moldrup, P. (2010) Gas-phase diffusivity and tortuosity of structured soils. *J. Contam. Hydrol.* 115(1–4), 26–33, Doi: 10.1016/j.jconhyd.2010.03.003.
- [192] Kruk, A., Cempura, G., Lech, S., Czyska -Filemonowicz, A. (2016) Stem-EDX and FIB-SEM Tomography of ALLVAC 718Plus Superalloy. *Arch. Metall. Mater.* 61(2), 535–42, Doi: 10.1515/amm-2016-0093.
- [193] Kulkarni, N., Kok, M.D.R., Jervis, R., Iacoviello, F., Meyer, Q., Shearing, P.R., Brett, D.J.L. (2019) The effect of non-uniform compression and flow-field arrangements on membrane electrode assemblies - X-ray computed tomography characterisation and effective parameter determination. *J. Power Sources* 426(February), 97–110, Doi: 10.1016/j.jpowsour.2019.04.018.
- [194] Kwiatkowski da Silva, A., Leyson, G., Kuzmina, M., Ponge, D., Herbig, M., Sandlöbes, S., Gault, B., Neugebauer, J., Raabe, D. (2017) Confined chemical and structural states at dislocations in Fe-9wt%Mn steels: A correlative TEM-atom probe study combined with multiscale modelling. *Acta Mater.* 124, 305–15, Doi: 10.1016/j.actamat.2016.11.013.
- [195] Landesfeind, J., Ebner, M., Eldiven, A., Wood, V., Gasteiger, H.A. (2018) Tortuosity of Battery Electrodes: Validation of Impedance-Derived Values and Critical Comparison with 3D Tomography. *J. Electrochem. Soc.* 165(3), A469–76, Doi: 10.1149/2.0231803jes.
- [196] Landesfeind, J., Eldiven, A., Gasteiger, H.A. (2018) Influence of the Binder on Lithium Ion Battery Electrode Tortuosity and Performance. *J. Electrochem. Soc.* 165(5), A1122–8, Doi: 10.1149/2.0971805jes.
- [197] Landesfeind, J., Hattendorff, J., Ehrl, A., Wall, W.A., Gasteiger, H.A. (2016) Tortuosity Determination of Battery Electrodes and Separators by Impedance Spectroscopy. *J. Electrochem. Soc.* 163(7), A1373–87, Doi: 10.1149/2.1141607jes.
- [198] Lanfrey, P.-Y., Kuzeljevic, Z.V., Dudukovic, M.P. (2010) Tortuosity model for fixed

- beds randomly packed with identical particles. *Chem. Eng. Sci.* 65(5), 1891–6, Doi: 10.1016/j.ces.2009.11.011.
- [199] Lantuéjoul, C. (2013) *Geostatistical Simulation: Models and Algorithms*. Springer, Berlin.
- [200] Lantuéjoul, C., Beucher, S. (1981) On the use of the geodesic metric in image analysis. *J. Microsc.* 121(1), 39–49, Doi: 10.1111/j.1365-2818.1981.tb01197.x.
- [201] Latt, J., Malaspinas, O., Kontaxakis, D., Parmigiani, A., Lagrava, D., Brogi, F., Belgacem, M. Ben., Thorimbert, Y., Leclaire, S., Li, S., Marson, F., Lemus, J., Kotsalos, C., Conradin, R., Coreixas, C., Petkantchin, R., Raynaud, F., Beny, J., Chopard, B. (2021) Palabos: Parallel Lattice Boltzmann Solver. *Comput. Math. with Appl.* 81, 334–50, Doi: 10.1016/j.camwa.2020.03.022.
- [202] Laurencin, J., Quey, R., Delette, G., Suhonen, H., Cloetens, P., Bleuet, P. (2012) Characterisation of Solid Oxide Fuel Cell Ni–8YSZ substrate by synchrotron X-ray nano-tomography: from 3D reconstruction to microstructure quantification. *J. Power Sources* 198, 182–9, Doi: 10.1016/j.jpowsour.2011.09.105.
- [203] Li, J.-H., Yu, B.-M. (2011) Tortuosity of Flow Paths through a Sierpinski Carpet. *Chinese Phys. Lett.* 28(3), 034701, Doi: 10.1088/0256-307X/28/3/034701.
- [204] Li, Z., Liu, D., Cai, Y., Ranjith, P.G., Yao, Y. (2017) Multi-scale quantitative characterization of 3-D pore-fracture networks in bituminous and anthracite coals using FIB-SEM tomography and X-ray  $\mu$ -CT. *Fuel* 209, 43–53, Doi: 10.1016/j.fuel.2017.07.088.
- [205] Lichtner, A.Z., Jauffrès, D., Roussel, D., Charlot, F., Martin, C.L., Bordia, R.K. (2015) Dispersion, connectivity and tortuosity of hierarchical porosity composite SOFC cathodes prepared by freeze-casting. *J. Eur. Ceram. Soc.* 35(2), 585–95, Doi: 10.1016/j.jeurceramsoc.2014.09.030.
- [206] Lindquist, W.B., Lee, S.-M., Coker, D.A., Jones, K.W., Spanne, P. (1996) Medial axis analysis of void structure in three-dimensional tomographic images of porous media. *J. Geophys. Res. Solid Earth* 101(B4), 8297–310, Doi: 10.1029/95jb03039.
- [207] Liu, H., Foster, J.M., Gully, A., Krachkovskiy, S., Jiang, M., Wu, Y., Yang, X., Protas, B., Goward, G.R., Botton, G.A. (2016) Three-dimensional investigation of cycling-induced microstructural changes in lithium-ion battery cathodes using focused ion beam/scanning electron microscopy. *J. Power Sources* 306, 300–8, Doi: 10.1016/j.jpowsour.2015.11.108.
- [208] Liu, J., Pereira, G.G., Liu, Q., Regenauer-Lieb, K. (2016) Computational challenges in the analyses of petrophysics using microtomography and upscaling: A review. *Comput. Geosci.* 89, 107–17, Doi: 10.1016/j.cageo.2016.01.014.
- [209] Liu, X., Peng, F., Lou, G., Wen, Z. (2015) Liquid water transport characteristics of porous diffusion media in polymer electrolyte membrane fuel cells: A review. *J. Power Sources* 299, 85–96, Doi: 10.1016/j.jpowsour.2015.08.092.
- [210] Liu, Z., Chen-Wiegart, Y.K., Wang, J., Barnett, S.A., Faber, K.T. (2016) Three-Phase 3D Reconstruction of a LiCoO<sub>2</sub> Cathode via FIB-SEM Tomography. *Microsc. Microanal.* 22(1), 140–8, Doi: 10.1017/S1431927615015640.
- [211] Lo, C., Sano, T., Hogan, J.D. (2019) Microstructural and mechanical characterization of variability in porous advanced ceramics using X-ray computed tomography and digital image correlation. *Mater. Charact.* 158(May), 109929, Doi: 10.1016/j.matchar.2019.109929.
- [212] Lu, X., Bertei, A., Finegan, D.P., Tan, C., Daemi, S.R., Weaving, J.S., O'Regan, K.B., Heenan, T.M.M., Hinds, G., Kendrick, E., Brett, D.J.L., Shearing, P.R. (2020) 3D microstructure design of lithium-ion battery electrodes assisted by X-ray nano-

- computed tomography and modelling. *Nat. Commun.* 11(1), 1–13, Doi: 10.1038/s41467-020-15811-x.
- [213] Machado Charry, E., Neumann, M., Lahti, J., Schennach, R., Schmidt, V., Zojer, K. (2018) Pore space extraction and characterization of sack paper using  $\mu$ -CT. *J. Microsc.* 272(1), 35–46, Doi: 10.1111/jmi.12730.
- [214] Mackie, J.S., Meares, P. (1955) The diffusion of electrolytes in a cation- exchange resin membrane. *Proc. R. Soc. A* 232, 498–509.
- [215] Mahbub, R., Hsu, T., Epting, W.K., Nuhfer, N.T., Hackett, G.A., Abernathy, H., Rollett, A.D., De Graef, M., Litster, S., Salvador, P.A. (2017) A Method for Quantitative 3D Mesoscale Analysis of Solid Oxide Fuel Cell Microstructures Using Xe-plasma Focused Ion Beam (PFIB) Coupled with SEM. *ECS Trans.* 78(1), 2159–70, Doi: 10.1149/07801.2159ecst.
- [216] Maire, E., Le Bourlot, C., Adrien, J., Mortensen, A., Mokso, R. (2016) 20 Hz X-ray tomography during an in situ tensile test. *Int. J. Fract.* 200(1–2), 3–12, Doi: 10.1007/s10704-016-0077-y.
- [217] Maire, E., Withers, P.J. (2014) Quantitative X-ray tomography. *Int. Mater. Rev.* 59(1), 1–43, Doi: 10.1179/1743280413Y.0000000023.
- [218] Matheron, G. (1975) *Random Sets and Integral Geometry*. J. Wiley & Sons, New York.
- [219] Matyka, M., Khalili, A., Koza, Z. (2008) Tortuosity-porosity relation in porous media flow. *Phys. Rev. E* 78(2), 026306, Doi: 10.1103/PhysRevE.78.026306.
- [220] Matyka, M., Koza, Z. (2012) How to Calculate Tortuosity Easily? *AIP Conf. Proc.* 1453(1), 17–22, Doi: 10.1063/1.4711147.
- [221] Maxwell, J.C. (1873) *A treatise on electricity and magnetism*. Vol. I. Clarendon Press, London.
- [222] McCarroll, I.E., Bagot, P.A.J., Devaraj, A., Perea, D.E., Cairney, J.M. (2020) New frontiers in atom probe tomography: a review of research enabled by cryo and/or vacuum transfer systems. *Mater. Today Adv.* 7, 100090, Doi: 10.1016/j.mtadv.2020.100090.
- [223] Meffert, M., Wankmüller, F., Störmer, H., Weber, A., Lupetin, P., Ivers-Tiffée, E., Gerthsen, D. (2020) Optimization of Material Contrast for Efficient FIB-SEM Tomography of Solid Oxide Fuel Cells. *Fuel Cells* 20(5), 580–91, Doi: 10.1002/fuce.202000080.
- [224] Meyer, Q., Hack, J., Mansor, N., Iacoviello, F., Bailey, J.J., Shearing, P.R., Brett, D.J.L. (2019) Multi-Scale Imaging of Polymer Electrolyte Fuel Cells using X-ray Micro- and Nano-Computed Tomography, Transmission Electron Microscopy and Helium-Ion Microscopy. *Fuel Cells* 19(1), 35–42, Doi: 10.1002/fuce.201800047.
- [225] Miyaki, T., Kawasaki, Y., Hosoyamada, Y., Amari, T., Kinoshita, M., Matsuda, H., Kakuta, S., Sakai, T., Ichimura, K. (2020) Three-dimensional imaging of podocyte ultrastructure using FE-SEM and FIB-SEM tomography. *Cell Tissue Res.* 379(2), 245–54, Doi: 10.1007/s00441-019-03118-3.
- [226] Mokso, R., Schlepütz, C.M., Theidel, G., Billich, H., Schmid, E., Celcer, T., Mikuljan, G., Sala, L., Marone, F., Schlumpf, N., Stampanoni, M. (2017) GigaFRoST: The gigabit fast readout system for tomography. *J. Synchrotron Radiat.* 24(6), 1250–9, Doi: 10.1107/S1600577517013522.
- [227] Monteiro, S.N., Paciornik, S. (2017) From Historical Backgrounds to Recent Advances in 3D Characterization of Materials: An Overview. *JOM* 69(1), 84–92, Doi: 10.1007/s11837-016-2203-8.
- [228] Morelly, S.L., Gelb, J., Iacoviello, F., Shearing, P.R., Harris, S.J., Alvarez, N.J., Tang,

- M.H. (2018) Three-Dimensional Visualization of Conductive Domains in Battery Electrodes with Contrast-Enhancing Nanoparticles. *ACS Appl. Energy Mater.* 1(9), 4479–84, Doi: 10.1021/acsaem.8b01184.
- [229] Mota, M., Teixeira, J.A., Yelshin, A. (2001) Binary spherical particle mixed beds porosity and permeability relationship measurement. *Trans. Filtr. Soc.* 1, 101–6.
- [230] Moussaoui, H., Laurencin, J., Gavet, Y., Delette, G., Hubert, M., Cloetens, P., Le Bihan, T., Debayle, J. (2018) Stochastic geometrical modeling of solid oxide cells electrodes validated on 3D reconstructions. *Comput. Mater. Sci.* 143, 262–76, Doi: 10.1016/j.commatsci.2017.11.015.
- [231] Mularczyk, A., Lin, Q., Blunt, M.J., Lamibrac, A., Marone, F., Schmidt, T.J., Buchi, F.N., Eller, J. (2020) Droplet and percolation network interactions in a fuel cell gas diffusion layer. *J. Electrochem. Soc.*, Doi: 10.1149/1945-7111/ab8c85.
- [232] Münch, B. (2014) Empa Bundle of ImageJ Plugins for Image Analysis (EBIPIA), <http://wiki.imagej.net/Xlib>.
- [233] Münch, B., Holzer, L. (2008) Contradicting Geometrical Concepts in Pore Size Analysis Attained with Electron Microscopy and Mercury Intrusion. *J. Am. Ceram. Soc.* 91(12), 4059–67, Doi: 10.1111/j.1551-2916.2008.02736.x.
- [234] Müter, D., Sørensen, H.O., Bock, H., Stipp, S.L.S. (2015) Particle diffusion in complex nanoscale pore networks. *J. Phys. Chem. C* 119(19), 10329–35, Doi: 10.1021/jp5117867.
- [235] Nabovati, A., Sousa, A.C.M. (2007) Fluid flow simulation in random porous media at pore level using the lattice boltzmann method. *Sci. Technol.* 2(3), 226–37.
- [236] Nagai, Y., Eller, J., Hatanaka, T., Yamaguchi, S., Kato, S., Kato, A., Marone, F., Xu, H., Büchi, F.N. (2019) Improving water management in fuel cells through microporous layer modifications: Fast operando tomographic imaging of liquid water. *J. Power Sources* 435(June), 226809, Doi: 10.1016/j.jpowsour.2019.226809.
- [237] Nan, N., Wang, J. (2019) FIB-SEM Three-Dimensional Tomography for Characterization of Carbon-Based Materials. *Adv. Mater. Sci. Eng.* 2019(Figure 1), 1–8, Doi: 10.1155/2019/8680715.
- [238] Nemati, R., Rahbar Shahrouzi, J., Alizadeh, R. (2020) A stochastic approach for predicting tortuosity in porous media via pore network modeling. *Comput. Geotech.* 120(July 2019), 103406, Doi: 10.1016/j.compgeo.2019.103406.
- [239] Neumann, M., Abdallah, B., Holzer, L., Willot, F., Schmidt, V. (2019) Stochastic 3D Modeling of Three-Phase Microstructures for Predicting Transport Properties: A Case Study. *Transp. Porous Media* 128(1), Doi: 10.1007/s11242-019-01240-y.
- [240] Neumann, M., Hirsch, C., Staněk, J., Beneš, V., Schmidt, V. (2019) Estimation of geodesic tortuosity and constrictivity in stationary random closed sets. *Scand. J. Stat.* 46(3), 848–84, Doi: 10.1111/sjos.12375.
- [241] Neumann, M., Machado Charry, E., Zojer, K., Schmidt, V. (2021) On Variability and Interdependence of Local Porosity and Local Tortuosity in Porous Materials: a Case Study for Sack Paper. *Methodol. Comput. Appl. Probab.* 23(2), 613–27, Doi: 10.1007/s11009-019-09761-1.
- [242] Neumann, M., Staněk, J., Pecho, O.M., Holzer, L., Beneš, V., Schmidt, V. (2016) Stochastic 3D modeling of complex three-phase microstructures in SOFC-electrodes with completely connected phases. *Comput. Mater. Sci.* 118, 353–64, Doi: 10.1016/j.commatsci.2016.03.013.
- [243] Neumann, M., Stenzel, O., Willot, F., Holzer, L., Schmidt, V. (2020) Quantifying the influence of microstructure on effective conductivity and permeability: Virtual

- materials testing. *Int. J. Solids Struct.* 184, 211–20, Doi: 10.1016/j.ijsolstr.2019.03.028.
- [244] Nield, D.A., Bejan, A. (2013) *Convection in Porous Media*. Springer New York, New York, NY.
- [245] Nikitin, V. V., Dugarov, G.A., Duchkov, A.A., Fokin, M.I., Drobchik, A.N., Shevchenko, P.D., De Carlo, F., Mokso, R. (2020) Dynamic in-situ imaging of methane hydrate formation and self-preservation in porous media. *Mar. Pet. Geol.* 115(January), 104234, Doi: 10.1016/j.marpetgeo.2020.104234.
- [246] Niya, S.M.R., Selvadurai, A.P.S. (2018) A Statistical Correlation Between Permeability, Porosity, Tortuosity and Conductance. *Transp. Porous Media* 121(3), 741–52, Doi: 10.1007/s11242-017-0983-0.
- [247] Ohser, J., Dobrovolskij, D., Blankenburg, C., Rack, A. (2020) Time-resolved phase-contrast microtomographic imaging of two-phase solid-liquid flow through porous media. *Int. J. Mater. Res.* 111(1), 86–95, Doi: 10.3139/146.111850.
- [248] Ohser, J., Schladitz, K. (2009) *3D Images of Materials Structures: Processing and Analysis*. J. Wiley & Sons, Weinheim, Germany.
- [249] Ott, T., Roldán, D., Redenbach, C., Schladitz, K., Godehardt, M., Höhn, S. (2019) Three-dimensional structural comparison of tantalum glancing angle deposition thin films by FIB-SEM. *J. Sensors Sens. Syst.* 8(2), 305–15, Doi: 10.5194/jsss-8-305-2019.
- [250] Owen, J.E. (1952) The Resistivity of a Fluid-Filled Porous Body. *J. Pet. Technol.* 4(07), 169–74, Doi: 10.2118/952169-G.
- [251] Panda, M.N., Lake, L.W. (1994) Estimation of Single-Phase Permeability from Parameters of Particle-Size Distribution. *Am. Assoc. Pet. Geol. Bull.* 78(7), 1028–39.
- [252] Paul-Gilloteaux, P., Heiligenstein, X., Belle, M., Domart, M.-C., Larijani, B., Collinson, L., Raposo, G., Salamero, J. (2017) eC-CLEM: flexible multidimensional registration software for correlative microscopies. *Nat. Methods* 14(2), 102–3, Doi: 10.1038/nmeth.4170.
- [253] Pawlowski, S., Nayak, N., Meireles, M., Portugal, C.A.M., Velizarov, S., Crespo, J.G. (2018) CFD modelling of flow patterns, tortuosity and residence time distribution in monolithic porous columns reconstructed from X-ray tomography data. *Chem. Eng. J.* 350(February), 757–66, Doi: 10.1016/j.cej.2018.06.017.
- [254] Pecho, O., Mai, A., Münch, B., Hocker, T., Flatt, R., Holzer, L. (2015) 3D Microstructure Effects in Ni-YSZ Anodes: Influence of TPB Lengths on the Electrochemical Performance. *Materials (Basel)*. 8(10), 7129–44, Doi: 10.3390/ma8105370.
- [255] Pecho, O., Stenzel, O., Iwanschitz, B., Gasser, P., Neumann, M., Schmidt, V., Prestat, M., Hocker, T., Flatt, R., Holzer, L. (2015) 3D Microstructure Effects in Ni-YSZ Anodes: Prediction of Effective Transport Properties and Optimization of Redox Stability. *Materials (Basel)*. 8(9), 5554–85, Doi: 10.3390/ma8095265.
- [256] Peng, S., Marone, F., Dultz, S. (2014) Resolution effect in X-ray microcomputed tomography imaging and small pore's contribution to permeability for a Berea sandstone. *J. Hydrol.* 510, 403–11, Doi: 10.1016/j.jhydrol.2013.12.028.
- [257] Perea, D.E., Schreiber, D.K., Ryan, J. V., Wirth, M.G., Deng, L., Lu, X., Du, J., Vienna, J.D. (2020) Tomographic mapping of the nanoscale water-filled pore structure in corroded borosilicate glass. *Npj Mater. Degrad.* 4(1), 1–7, Doi: 10.1038/s41529-020-0110-5.
- [258] Perré, P., Nguyen, D.M., Almeida, G. (2022) A macroscopic Washburn approach of

- liquid imbibition in wood derived from X-ray tomography observations. *Sci. Rep.* 12(1), 1750, Doi: 10.1038/s41598-022-05508-0.
- [259] Petersen, E.E. (1958) Diffusion in a pore of varying cross section. *AIChE J.* 4(3), 343–5, Doi: 10.1002/aic.690040322.
- [260] Pietsch, P., Wood, V. (2017) X-Ray Tomography for Lithium Ion Battery Research: A Practical Guide. *Annu. Rev. Mater. Res.* 47(1), 451–79, Doi: 10.1146/annurev-matsci-070616-123957.
- [261] Pisani, L. (2011) Simple Expression for the Tortuosity of Porous Media. *Transp. Porous Media* 88(2), 193–203, Doi: 10.1007/s11242-011-9734-9.
- [262] du Plessis, A., Boshoff, W.P. (2019) A review of X-ray computed tomography of concrete and asphalt construction materials. *Constr. Build. Mater.* 199, 637–51, Doi: 10.1016/j.conbuildmat.2018.12.049.
- [263] Du Plessis, A., Yadroitsev, I., Yadroitsava, I., Le Roux, S.G. (2018) X-Ray Microcomputed Tomography in Additive Manufacturing: A Review of the Current Technology and Applications. *3D Print. Addit. Manuf.* 5(3), 227–47, Doi: 10.1089/3dp.2018.0060.
- [264] Du Plessis, J.P., Masliyah, J.H. (1991) Flow through isotropic granular porous media. *Transp. Porous Media* 6(3), 207–21, Doi: 10.1007/BF00208950.
- [265] Pollard, W.G., Present, R.D. (1948) On Gaseous Self-Diffusion in Long Capillary Tubes. *Phys. Rev.* 73(7), 762–74, Doi: 10.1103/PhysRev.73.762.
- [266] Prifling, B., Ademmer, M., Single, F., Benevolenski, O., Hilger, A., Osenberg, M., Manke, I., Schmidt, V. (2021) Stochastic 3D microstructure modeling of anodes in lithium-ion batteries with a particular focus on local heterogeneity. *Comput. Mater. Sci.* 192, 110354, Doi: 10.1016/j.commatsci.2021.110354.
- [267] Prifling, B., Röding, M., Townsend, P., Neumann, M., Schmidt, V. (2022) Large-scale statistical learning for mass transport prediction in porous materials using 90,000 artificially generated microstructures. Submitted.
- [268] Prifling, B., Westhoff, D., Schmidt, D., Markötter, H., Manke, I., Knoblauch, V., Schmidt, V. (2019) Parametric microstructure modeling of compressed cathode materials for Li-ion batteries. *Comput. Mater. Sci.* 169, 109083, Doi: 10.1016/j.commatsci.2019.109083.
- [269] Prodanovic, M., Esteva, M., Hanlon, M., Nanda, G., Agarwal, P. (2015) Digital Rocks Portal: a repository for porous media images, Doi: <http://dx.doi.org/10.17612/P7CC7K>.
- [270] Provis, J.L., Myers, R.J., White, C.E., Rose, V., Van Deventer, J.S.J. (2012) X-ray microtomography shows pore structure and tortuosity in alkali-activated binders. *Cem. Concr. Res.* 42(6), 855–64, Doi: 10.1016/j.cemconres.2012.03.004.
- [271] Quinn, A., Moutinho, H., Usseglio-Viretta, F., Verma, A., Smith, K., Keyser, M., Finegan, D.P. (2020) Electron Backscatter Diffraction for Investigating Lithium-Ion Electrode Particle Architectures. *Cell Reports Phys. Sci.* 1(8), 100137, Doi: 10.1016/j.xcrp.2020.100137.
- [272] Randolph, S., Geurts, R., Wang, J., Winiarski, B., Rue, C. (2019) Femtosecond Laser-Enabled TriBeam as a Platform for Analysis of Thermally- and Charge-Sensitive Materials. *Microsc. Microanal.* 25(S2), 352–3, Doi: 10.1017/S1431927619002496.
- [273] Randolph, S.J., Filevich, J., Botman, A., Gannon, R., Rue, C., Straw, M. (2018) In situ femtosecond pulse laser ablation for large volume 3D analysis in scanning electron microscope systems. *J. Vac. Sci. Technol. B* 36(6), 06JB01, Doi: 10.1116/1.5047806.
- [274] Rawson, S.D., Maksimcuka, J., Withers, P.J., Cartmell, S.H. (2020) X-ray computed

- tomography in life sciences. *BMC Biol.* 18(1), 1–15, Doi: 10.1186/s12915-020-0753-2.
- [275] Redenbach, C. (2009) Microstructure models for cellular materials. *Comput. Mater. Sci.* 44(4), 1397–407, Doi: 10.1016/j.commatsci.2008.09.018.
- [276] Rohatgi, A. (2019) Webplotdigitizer. <https://automeris.io/WebPlotDigitizer/>. [accessed March 1, 2020].
- [277] Rowenhorst, D.J., Nguyen, L., Murphy-Leonard, A.D., Fonda, R.W. (2020) Characterization of Microstructure in Additively Manufactured 316L using Automated Serial Sectioning. *Curr. Opin. Solid State Mater. Sci.* 24(3), 100819, Doi: 10.1016/j.cossms.2020.100819.
- [278] Russ, J.C. (2011) *The Image Processing Handbook, Sixth Edition* - CRC Press Book. CRC Press, Boca Raton, USA.
- [279] Ryan, E.M., Mukherjee, P.P. (2019) Mesoscale modeling in electrochemical devices—A critical perspective. *Prog. Energy Combust. Sci.* 71, 118–42, Doi: 10.1016/j.pecs.2018.11.002.
- [280] Saif, T., Lin, Q., Butcher, A.R., Bijeljic, B., Blunt, M.J. (2017) Multi-scale multi-dimensional microstructure imaging of oil shale pyrolysis using X-ray microtomography, automated ultra-high resolution SEM, MAPS Mineralogy and FIB-SEM. *Appl. Energy* 202, 628–47, Doi: 10.1016/j.apenergy.2017.05.039.
- [281] Saomoto, H., Katagiri, J. (2015) Direct comparison of hydraulic tortuosity and electric tortuosity based on finite element analysis. *Theor. Appl. Mech. Lett.* 5(5), 177–80, Doi: 10.1016/j.taml.2015.07.001.
- [282] Saomoto, H., Katagiri, J. (2015) Particle Shape Effects on Hydraulic and Electric Tortuosities: A Novel Empirical Tortuosity Model Based on van Genuchten-Type Function. *Transp. Porous Media* 107(3), 781–98, Doi: 10.1007/s11242-015-0467-z.
- [283] Sarkar, J., Bhattacharyya, S. (2012) Application of graphene and graphene-based materials in clean energy-related devices Minghui. *Arch. Thermodyn.* 33(4), 23–40, Doi: 10.1002/er.
- [284] Sato, M., Bitter, I., Bender, M.A., Kaufman, A.E., Nakajima, M. (2000) TEASAR: Tree-structure Extraction Algorithm for Accurate and Robust Skeletons. *Eighth Pacific Conference on Computer Graphics and Applications (PG'00)*, p. 281.
- [285] Satterfield, C.N., Cadle, P.J. (1968) Gaseous Diffusion and Flow in Commercial Catalysts at Pressure Levels above Atmospheric. *Ind. Eng. Chem. Fundam.* 7(2), 202–10, Doi: 10.1021/i160026a005.
- [286] Satterfield, C.N., Cadle, P.J. (1968) Diffusion in Commercially Manufactured Pelleted Catalysts. *Ind. Eng. Chem. Process Des. Dev.* 7(2), 256–60, Doi: 10.1021/i260026a017.
- [287] Satterfield, C.N., Sherwood, T.K. (1963) *The role of diffusion in catalysis*. Addison-Wesley Pub. Co.
- [288] Saxena, N., Hofmann, R., Alpak, F.O., Berg, S., Dietderich, J., Agarwal, U., Tandon, K., Hunter, S., Freeman, J., Wilson, O.B. (2017) References and benchmarks for pore-scale flow simulated using micro-CT images of porous media and digital rocks. *Adv. Water Resour.* 109, 211–35, Doi: 10.1016/j.advwatres.2017.09.007.
- [289] Scheidegger, A.E. (1974) *The physics of flow through porous media*. 3rd Ed., Univ. of Toronto Press, Toronto.
- [290] Schepp, L.L., Ahrens, B., Balcewicz, M., Duda, M., Nehler, M., Osorno, M., Uribe, D., Steeb, H., Nigon, B., Stöckhert, F., Swanson, D.A., Siegert, M., Gurriss, M., Saenger, E.H. (2020) Digital rock physics and laboratory considerations on a high-porosity

- volcanic rock. *Sci. Rep.* 10(1), 1–16, Doi: 10.1038/s41598-020-62741-1.
- [291] Schindelin, J., Arganda-Carreras, I., Frise, E., Kaynig, V., Longair, M., Pietzsch, T., Preibisch, S., Rueden, C., Saalfeld, S., Schmid, B., Tinevez, J.-Y., White, D.J., Hartenstein, V., Eliceiri, K., Tomancak, P., Cardona, A. (2012) Fiji: an open-source platform for biological-image analysis. *Nat. Methods* 9(7), 676–82, Doi: 10.1038/nmeth.2019.
- [292] Schlüter, S., Sheppard, A., Brown, K., Wildenschild, D. (2014) Image processing of multiphase images obtained via X-ray microtomography: a review. *Water Resour. Res.* 50(4), 3615–3639.
- [293] Schmidt, V. (2014) *Stochastic Geometry, Spatial Statistics and Random Fields*. Springer, Cham.
- [294] Schröder, D., Bender, C.L., Arlt, T., Osenberg, M., Hilger, A., Risse, S., Ballauff, M., Manke, I., Janek, J. (2016) In operando x-ray tomography for next-generation batteries: a systematic approach to monitor reaction product distribution and transport processes. *J. Phys. D. Appl. Phys.* 49(40), 404001, Doi: 10.1088/0022-3727/49/40/404001.
- [295] Serra, J. (1982) *Image Analysis and Mathematical Morphology*. Academic Press Ltd, London.
- [296] Sethian, J.A. (1996) A fast marching level set method for monotonically advancing fronts. *Proc. Natl. Acad. Sci. U. S. A.* 93(4), 1591–5, Doi: 10.1073/pnas.93.4.1591.
- [297] Sethian, J.A. (1999) Fast Marching Methods. *SIAM Rev.* 41(2), 199–235, Doi: 10.1137/S0036144598347059.
- [298] Sethian, J.A. (2001) Evolution, Implementation, and Application of Level Set and Fast Marching Methods for Advancing Fronts. *J. Comput. Phys.* 169(2), 503–55, Doi: 10.1006/jcph.2000.6657.
- [299] Sethian, J.A., Popovici, A.M. (2002) 3-D imaging using higher order fast marching traveltimes. *Geophysics* 64(2), 516–23.
- [300] Shanti, N.O., Chan, V.W.L., Stock, S.R., De Carlo, F., Thornton, K., Faber, K.T. (2014) X-ray micro-computed tomography and tortuosity calculations of percolating pore networks. *Acta Mater.* 71, 126–35, Doi: 10.1016/j.actamat.2014.03.003.
- [301] Shearing, P.R., Brandon, N.P., Gelb, J., Bradley, R., Withers, P.J., Marquis, A.J., Cooper, S., Harris, S.J. (2012) Multi Length Scale Microstructural Investigations of a Commercially Available Li-Ion Battery Electrode. *J. Electrochem. Soc.* 159(7), A1023–7, Doi: 10.1149/2.053207jes.
- [302] Shearing, P.R., Howard, L.E., Jørgensen, P.S., Brandon, N.P., Harris, S.J. (2010) Characterization of the 3-dimensional microstructure of a graphite negative electrode from a Li-ion battery. *Electrochem. Commun.* 12(3), 374–7, Doi: 10.1016/j.elecom.2009.12.038.
- [303] Sheikh, B., Pak, A. (2015) Numerical investigation of the effects of porosity and tortuosity on soil permeability using coupled three-dimensional discrete-element method and lattice Boltzmann method. *Phys. Rev. E - Stat. Nonlinear, Soft Matter Phys.* 91(5), 1–14, Doi: 10.1103/PhysRevE.91.053301.
- [304] Shen, L., Chen, Z. (2007) Critical review of the impact of tortuosity on diffusion. *Chem. Eng. Sci.* 62(14), 3748–55, Doi: 10.1016/j.ces.2007.03.041.
- [305] Shikazono, N., Kanno, D., Matsuzaki, K., Teshima, H., Sumino, S., Kasagi, N. (2010) Numerical Assessment of SOFC Anode Polarization Based on Three-Dimensional Model Microstructure Reconstructed from FIB-SEM Images. *J. Electrochem. Soc.* 157(5), B665, Doi: 10.1149/1.3330568.
- [306] Singh, S.S., Loza, J.J., Merkle, A.P., Chawla, N. (2016) Three dimensional

- microstructural characterization of nanoscale precipitates in AA7075-T651 by focused ion beam (FIB) tomography. *Mater. Charact.* 118, 102–11, Doi: 10.1016/j.matchar.2016.05.009.
- [307] Sobieski, W. (2016) The use of Path Tracking Method for determining the tortuosity field in a porous bed. *Granul. Matter* 18(3), 1–9, Doi: 10.1007/s10035-016-0668-3.
- [308] Sobieski, W. (2019) Numerical investigations of tortuosity in randomly generated pore structures. *Math. Comput. Simul.* 166, 1–20, Doi: 10.1016/j.matcom.2019.04.005.
- [309] Sobieski, W., Matyka, M., Gołembiewski, J., Lipiński, S. (2018) The Path Tracking Method as an alternative for tortuosity determination in granular beds. *Granul. Matter* 20(4), Doi: 10.1007/s10035-018-0842-x.
- [310] Soille, P. (2004) *Morphological Image Analysis*. Springer Berlin Heidelberg, Berlin, Heidelberg.
- [311] Song, H., Yang, Y., Geng, J., Gu, Z., Zou, J., Yu, C. (2019) Electron Tomography: A Unique Tool Solving Intricate Hollow Nanostructures. *Adv. Mater.* 31(38), 1–22, Doi: 10.1002/adma.201801564.
- [312] Stenzel, O., Pecho, O., Holzer, L., Neumann, M., Schmidt, V. (2016) Predicting effective conductivities based on geometric microstructure characteristics. *AIChE J.* 62(5), 1834–43, Doi: 10.1002/aic.15160.
- [313] Stenzel, O., Pecho, O., Holzer, L., Neumann, M., Schmidt, V. (2017) Big data for microstructure-property relationships: A case study of predicting effective conductivities. *AIChE J.* 63(9), 4224–32, Doi: 10.1002/aic.15757.
- [314] Su, J., Wang, L., Gu, Z., Zhang, Y., Chen, C. (2018) Advances in pore-scale simulation of oil reservoirs. *Energies* 11(5), Doi: 10.3390/en11051132.
- [315] Sun, Z., Tang, X., Cheng, G. (2013) Numerical simulation for tortuosity of porous media. *Microporous Mesoporous Mater.* 173, 37–42, Doi: 10.1016/j.micromeso.2013.01.035.
- [316] Suzue, Y., Shikazono, N., Kasagi, N. (2008) Micro modeling of solid oxide fuel cell anode based on stochastic reconstruction. *J. Power Sources* 184(1), 52–9, Doi: 10.1016/j.jpowsour.2008.06.029.
- [317] Taiwo, O.O., Finegan, D.P., Eastwood, D.S., Fife, J.L., Brown, L.D., Darr, J.A., Lee, P.D., Brett, D.J.L., Shearing, P.R. (2016) Comparison of three-dimensional analysis and stereological techniques for quantifying lithium-ion battery electrode microstructures. *J. Microsc.* 263(3), 280–92, Doi: 10.1111/jmi.12389.
- [318] Taiwo, O.O., Loveridge, M., Beattie, S.D., Finegan, D.P., Bhagat, R., Brett, D.J.L., Shearing, P.R. (2017) Investigation of cycling-induced microstructural degradation in silicon-based electrodes in lithium-ion batteries using X-ray nanotomography. *Electrochim. Acta* 253, 85–92, Doi: 10.1016/j.electacta.2017.08.161.
- [319] Tallarek, U., Hlushkou, D., Rybka, J., Höltzel, A. (2019) Multiscale Simulation of Diffusion in Porous Media: From Interfacial Dynamics to Hierarchical Porosity. *J. Phys. Chem. C* 123(24), 15099–112, Doi: 10.1021/acs.jpcc.9b03250.
- [320] Tao, H., Chen, G., Lian, C., Liu, H., Coppens, M. (2022) Multiscale modeling of ion transport in porous electrodes. *AIChE J.* 68(4), Doi: 10.1002/aic.17571.
- [321] Tariq, F., Haswell, R., Lee, P.D., McComb, D.W. (2011) Characterization of hierarchical pore structures in ceramics using multiscale tomography. *Acta Mater.* 59(5), 2109–20, Doi: 10.1016/j.actamat.2010.12.012.
- [322] Tariq, F., Shearing, P.R., Bradley, R.S., Gelb, J., Withers, P.J., Brandon, N.P. (n.d.) 4D

- Tomography : Imaging of Microstructural Evolution in Fuel Cells using high resolution x-ray tomography, 1–12.
- [323] Tariq, F., Yufit, V., Kishimoto, M., Shearing, P.R., Menkin, S., Golodnitsky, D., Gelb, J., Peled, E., Brandon, N.P. (2014) Three-dimensional high resolution X-ray imaging and quantification of lithium ion battery mesocarbon microbead anodes. *J. Power Sources* 248, 1014–20, Doi: 10.1016/j.jpowsour.2013.08.147.
- [324] Tayarani-Yoosefabadi, Z., Harvey, D., Bellerive, J., Kjeang, E. (2016) Stochastic microstructural modeling of fuel cell gas diffusion layers and numerical determination of transport properties in different liquid water saturation levels. *J. Power Sources* 303, 208–21, Doi: 10.1016/j.jpowsour.2015.11.005.
- [325] Thiedmann, R., Hartnig, C., Manke, I., Schmidt, V., Lehnert, W. (2009) Local Structural Characteristics of Pore Space in GDLs of PEM Fuel Cells Based on Geometric 3D Graphs. *J. Electrochem. Soc.* 156(11), B1339, Doi: 10.1149/1.3222737.
- [326] Thorat, I. V., Stephenson, D.E., Zacharias, N.A., Zaghbi, K., Harb, J.N., Wheeler, D.R. (2009) Quantifying tortuosity in porous Li-ion battery materials. *J. Power Sources* 188(2), 592–600, Doi: 10.1016/j.jpowsour.2008.12.032.
- [327] Thulasiraman, K., Swamy, M.N.S. (1992) *Graphs, Theory and Algorithms*. John Wiley & Sons, New York.
- [328] Timurkutluk, B., Mat, M.D. (2016) A review on micro-level modeling of solid oxide fuel cells. *Int. J. Hydrogen Energy* 41(23), 9968–81, Doi: 10.1016/j.ijhydene.2016.02.089.
- [329] Tjaden, B., Brett, D.J.L., Shearing, P.R. (2018) Tortuosity in electrochemical devices: a review of calculation approaches. *Int. Mater. Rev.* 63(2), 47–67, Doi: 10.1080/09506608.2016.1249995.
- [330] Tjaden, B., Cooper, S.J., Brett, D.J., Kramer, D., Shearing, P.R. (2016) On the origin and application of the Bruggeman correlation for analysing transport phenomena in electrochemical systems. *Curr. Opin. Chem. Eng.* 12, 44–51, Doi: 10.1016/j.coche.2016.02.006.
- [331] Tjaden, B., Lane, J., Withers, P.J., Bradley, R.S., Brett, D.J.L., Shearing, P.R. (2016) The application of 3D imaging techniques, simulation and diffusion experiments to explore transport properties in porous oxygen transport membrane support materials. *Solid State Ionics* 288, 315–21, Doi: 10.1016/j.ssi.2016.01.030.
- [332] Tomadakis, M.M., Sotirchos, S. V. (1996) Transport through random arrays of conductive cylinders dispersed in a conductive matrix. *J. Chem. Phys.* 104(17), 6893, Doi: 10.1063/1.471356.
- [333] Torquato, S. (2002) *Random Heterogeneous Materials: Microstructure and Macroscopic Properties*. Springer, New York.
- [334] Tranter, T.G., Kok, M.D.R., Lam, M., Gostick, J.T. (2019) pytrax: A simple and efficient random walk implementation for calculating the directional tortuosity of images. *SoftwareX* 10, 100277, Doi: 10.1016/j.softx.2019.100277.
- [335] Uchic, M.D., Holzer, L., Inkson, B.J., Principe, E.L., Munroe, P. (2007) Three-Dimensional Microstructural Characterization Using Focused Ion Beam Tomography. *MRS Bull.* 32(5), 408–16, Doi: 10.1557/mrs2007.64.
- [336] Usseglio-Viretta, F.L.E., Colclasure, A., Mistry, A.N., Claver, K.P.Y., Pouraghajan, F., Finegan, D.P., Heenan, T.M.M., Abraham, D., Mukherjee, P.P., Wheeler, D., Shearing, P., Cooper, S.J., Smith, K. (2018) Resolving the Discrepancy in Tortuosity Factor Estimation for Li-Ion Battery Electrodes through Micro-Macro Modeling and Experiment. *J. Electrochem. Soc.* 165(14), A3403–26, Doi: 10.1149/2.0731814jes.

- [337] Veldsink, J.W., van Damme, R.M.J., Versteeg, G.F., van Swaaij, W.P.M. (1995) The use of the dusty-gas model for the description of mass transport with chemical reaction in porous media. *Chem. Eng. J. Biochem. Eng. J.* 57(2), 115–25, Doi: 10.1016/0923-0467(94)02929-6.
- [338] Vicente, J., Topin, F., Daurelle, J.V. (2006) Open celled material structural properties measurement: From morphology to transport properties. *Mater. Trans.* 47(9), 2195–202, Doi: 10.2320/matertrans.47.2195.
- [339] Villanova, J., Daudin, R., Lhuissier, P., Jauffrès, D., Lou, S., Martin, C.L., Labouré, S., Tucoulou, R., Martínez-Criado, G., Salvo, L. (2017) Fast in situ 3D nanoimaging: a new tool for dynamic characterization in materials science. *Mater. Today* 20(7), 354–9, Doi: 10.1016/j.mattod.2017.06.001.
- [340] Vivet, N., Chupin, S., Estrade, E., Piquero, T., Pommier, P.L., Rochais, D., Bruneton, E. (2011) 3D Microstructural characterization of a solid oxide fuel cell anode reconstructed by focused ion beam tomography. *J. Power Sources* 196(18), 7541–9, Doi: 10.1016/j.jpowsour.2011.03.060.
- [341] Vivet, N., Chupin, S., Estrade, E., Richard, a., Bonnamy, S., Rochais, D., Bruneton, E. (2011) Effect of Ni content in SOFC Ni-YSZ cermets: A three-dimensional study by FIB-SEM tomography. *J. Power Sources* 196(23), 9989–97, Doi: 10.1016/j.jpowsour.2011.07.010.
- [342] Wagner, A.C., Bohn, N., Geßwein, H., Neumann, M., Osenberg, M., Hilger, A., Manke, I., Schmidt, V., Binder, J.R. (2020) Hierarchical Structuring of NMC111-Cathode Materials in Lithium-Ion Batteries: An In-Depth Study on the Influence of Primary and Secondary Particle Sizes on Electrochemical Performance. *ACS Appl. Energy Mater.* 3(12), 12565–74, Doi: 10.1021/acsaem.0c02494.
- [343] Wang, W., Fan, D., Sheng, G., Chen, Z., Su, Y. (2019) A review of analytical and semi-analytical fluid flow models for ultra-tight hydrocarbon reservoirs. *Fuel* 256(January), 115737, Doi: 10.1016/j.fuel.2019.115737.
- [344] Weber, a. Z., Borup, R.L., Darling, R.M., Das, P.K., Dursch, T.J., Gu, W., Harvey, D., Kusoglu, A., Litster, S., Mench, M.M., Mukundan, R., Owejan, J.P., Pharoah, J.G., Secanell, M., Zenyuk, I. V. (2014) A Critical Review of Modeling Transport Phenomena in Polymer-Electrolyte Fuel Cells. *J. Electrochem. Soc.* 161(12), F1254–99, Doi: 10.1149/2.0751412jes.
- [345] Weissberg, H.L. (1963) Effective Diffusion Coefficient in Porous Media. *J. Appl. Phys.* 34(9), 2636–9, Doi: 10.1063/1.1729783.
- [346] Westhoff, D., Feinauer, J., Kuchler, K., Mitsch, T., Manke, I., Hein, S., Latz, A., Schmidt, V. (2017) Parametric stochastic 3D model for the microstructure of anodes in lithium-ion power cells. *Comput. Mater. Sci.* 126, 453–67, Doi: 10.1016/j.commatsci.2016.09.006.
- [347] Westhoff, D., Manke, I., Schmidt, V. (2018) Generation of virtual lithium-ion battery electrode microstructures based on spatial stochastic modeling. *Comput. Mater. Sci.* 151, 53–64, Doi: 10.1016/j.commatsci.2018.04.060.
- [348] Westhoff, D., Skibinski, J., Šedivý, O., Wysocki, B., Wejrzanowski, T., Schmidt, V. (2018) Investigation of the relationship between morphology and permeability for open-cell foams using virtual materials testing. *Mater. Des.* 147, 1–10, Doi: 10.1016/j.matdes.2018.03.022.
- [349] Wiedenmann, D., Keller, L., Holzer, L., Stojadinović, J., Münch, B., Suarez, L., Fumey, B., Hagendorfer, H., Brönnimann, R., Modregger, P., Gorbar, M., Vogt, U.F., Züttel, A., Mantia, F. La., Wepf, R., Grobety, B. (2013) Three-dimensional pore structure and ion conductivity of porous ceramic diaphragms. *AIChE J.* 59(5), 1446–57, Doi:

- 10.1002/aic.14094.
- [350] Wiegmann, A., Zemitis, A. (2006) EJ-HEAT: A Fast Explicit Jump Harmonic Averaging Solver for the Effective Heat Conductivity of Composite Materials. vol. 94, Kaiserslautern.
- [351] Willot, F., Forest, S. (2018) Physics and Mechanics of Random Media: From Morphology to Material Properties. Presses des MINES, Paris.
- [352] Wilson, J.R., Kobsiriphat, W., Mendoza, R., Chen, H.-Y., Hiller, J.M., Miller, D.J., Thornton, K., Voorhees, P.W., Adler, S.B., Barnett, S. a. (2006) Three-dimensional reconstruction of a solid-oxide fuel-cell anode. *Nat. Mater.* 5(7), 541–4, Doi: 10.1038/nmat1668.
- [353] Winiarski, B., Gholinia, A., Mingard, K., Gee, M., Thompson, G.E., Withers, P.J. (2017) Broad ion beam serial section tomography. *Ultramicroscopy* 172, 52–64, Doi: 10.1016/j.ultramic.2016.10.014.
- [354] de Winter, D.A.M., Meirer, F., Weckhuysen, B.M. (2016) FIB-SEM Tomography Probes the Mesoscale Pore Space of an Individual Catalytic Cracking Particle. *ACS Catal.* 6(5), 3158–67, Doi: 10.1021/acscatal.6b00302.
- [355] Wolf, M., May, B.M., Cabana, J. (2017) Visualization of Electrochemical Reactions in Battery Materials with X-ray Microscopy and Mapping. *Chem. Mater.* 29(8), 3347–62, Doi: 10.1021/acs.chemmater.6b05114.
- [356] Wong, P. (1999) Conductivity, permeability and electrokinetics. In: Wong, P., (Ed.), *Methods in the physics of porous media*, Academic Press Ltd, London, pp. 115–159.
- [357] Wyllie, M.R.J., Rose, W.D. (1950) Some Theoretical Considerations Related To The Quantitative Evaluation Of The Physical Characteristics Of Reservoir Rock From Electrical Log Data. *J. Pet. Technol.* 2(04), 105–18, Doi: 10.2118/950105-G.
- [358] Xu, H., Marone, F., Nagashima, S., Nguyen, H., Kishita, K., Büchi, F.N., Eller, J. (2019) (Invited) Exploring Sub-Second and Sub-Micron X-Ray Tomographic Imaging of Liquid Water in PEFC Gas Diffusion Layers. *ECS Trans.* 92(8), 11–21, Doi: 10.1149/09208.0011ecst.
- [359] Xu, H., Zhu, J., Finegan, D.P., Zhao, H., Lu, X., Li, W., Hoffman, N., Bertei, A., Shearing, P., Bazant, M.Z. (2021) Guiding the Design of Heterogeneous Electrode Microstructures for Li-Ion Batteries: Microscopic Imaging, Predictive Modeling, and Machine Learning. *Adv. Energy Mater.* 11(19), 2003908, Doi: 10.1002/aenm.202003908.
- [360] Xu, Q., Long, W., Jiang, H., Ma, B., Zan, C., Ma, D., Shi, L. (2018) Quantification of the microstructure, effective hydraulic radius and effective transport properties changed by the coke deposition during the crude oil in-situ combustion. *Chem. Eng. J.* 331(September), 856–69, Doi: 10.1016/j.cej.2017.09.002.
- [361] Yan, H., Voorhees, P.W., Xin, H.L. (2020) Nanoscale x-ray and electron tomography. *MRS Bull.* 45(4), 264–71, Doi: 10.1557/mrs.2020.90.
- [362] Yu, B., Li, J. (2001) Some fractal characters of porous media. *Fractals* 9, 365–72.
- [363] Yu, Z., Carter, R.N., Zhang, J. (2012) Measurements of pore size distribution, porosity, effective oxygen diffusivity, and tortuosity of PEM fuel cell electrodes. *Fuel Cells* 12(4), 557–65, Doi: 10.1002/face.201200017.
- [364] Zacharias, N.A., Nevers, D.R., Skelton, C., Knackstedt, K., Stephenson, D.E., Wheeler, D.R. (2013) Direct Measurements of Effective Ionic Transport in Porous Li-Ion Electrodes. *J. Electrochem. Soc.* 160(2), A306–11, Doi: 10.1149/2.062302jes.
- [365] Zalc, J.M., Reyes, S.C., Iglesia, E. (2004) The effects of diffusion mechanism and void structure on transport rates and tortuosity factors in complex porous structures.

- Chem. Eng. Sci. 59(14), 2947–60, Doi: 10.1016/j.ces.2004.04.028.
- [366] Zeiss. (2020) An Overview of 3D X-ray Microscopy. *Essent. Knowl. Briefings* 1, 1–42.
- [367] Zekri, A., Knipper, M., Parisi, J., Plaggenborg, T. (2017) Microstructure degradation of Ni/CGO anodes for solid oxide fuel cells after long operation time using 3D reconstructions by FIB tomography. *Phys. Chem. Chem. Phys.* 19(21), 13767–77, Doi: 10.1039/C7CP02186K.
- [368] Zenyuk, I. V., Medici, E., Allen, J., Weber, A.Z. (2015) Coupling continuum and pore-network models for polymer-electrolyte fuel cells. *Int. J. Hydrogen Energy* 40(46), 16831–45, Doi: 10.1016/j.ijhydene.2015.08.009.
- [369] Zhang, D., Forner-Cuenca, A., Taiwo, O.O., Yufit, V., Brushett, F.R., Brandon, N.P., Gu, S., Cai, Q. (2020) Understanding the role of the porous electrode microstructure in redox flow battery performance using an experimentally validated 3D pore-scale lattice Boltzmann model. *J. Power Sources* 447(March 2019), 227249, Doi: 10.1016/j.jpowsour.2019.227249.
- [370] Zhang, L., Ge, K., Wang, J., Zhao, J., Song, Y. (2020) Pore-scale investigation of permeability evolution during hydrate formation using a pore network model based on X-ray CT. *Mar. Pet. Geol.* 113(July 2019), 104157, Doi: 10.1016/j.marpetgeo.2019.104157.
- [371] Zhang, P., Lee, Y. Il., Zhang, J. (2019) A review of high-resolution X-ray computed tomography applied to petroleum geology and a case study. *Micron* 124(June), 102702, Doi: 10.1016/j.micron.2019.102702.
- [372] Zhang, Y., Kong, C., Davidsen, R.S., Scardera, G., Duan, L., Khoo, K.T., Payne, D.N.R., Hoex, B., Abbott, M. (2020) 3D characterisation using plasma FIB-SEM: A large-area tomography technique for complex surfaces like black silicon. *Ultramicroscopy* 218, 113084, Doi: 10.1016/j.ultramic.2020.113084.
- [373] Zhang, Y., Kong, C., Scardera, G., Abbott, M., Payne, D.N.R., Hoex, B. (2022) Large volume tomography using plasma FIB-SEM: A comprehensive case study on black silicon. *Ultramicroscopy* 233, 113458, Doi: 10.1016/j.ultramic.2021.113458.
- [374] Zheng, K., Zhang, Y., Li, L., Ni, M. (2015) On the tortuosity factor of solid phase in solid oxide fuel cell electrodes. *Int. J. Hydrogen Energy* 40(1), 665–9, Doi: 10.1016/j.ijhydene.2014.10.111.
- [375] Zhu, Q., Wang, C., Qin, H., Chen, G., Zhang, P. (2019) Effect of the grain size on the microtensile deformation and fracture behaviors of a nickel-based superalloy via EBSD and in-situ synchrotron radiation X-ray tomography. *Mater. Charact.* 156(August), 109875, Doi: 10.1016/j.matchar.2019.109875.
- [376] Ziarani, A.S., Aguilera, R. (2012) Pore-throat radius and tortuosity estimation from formation resistivity data for tight-gas sandstone reservoirs. *J. Appl. Geophys.* 83, 65–73, Doi: 10.1016/j.jappgeo.2012.05.008.
- [377] Zielke, L., Hutzenlaub, T., Wheeler, D.R., Chao, C.-W., Manke, I., Hilger, A., Paust, N., Zengerle, R., Thiele, S. (2015) Three-Phase Multiscale Modeling of a LiCoO<sub>2</sub> Cathode: Combining the Advantages of FIB-SEM Imaging and X-Ray Tomography. *Adv. Energy Mater.* 5(5), 1401612, Doi: 10.1002/aenm.201401612.
- [378] Zingg, A., Holzer, L., Kaech, A., Winnefeld, F., Pakusch, J., Becker, S., Gauckler, L. (2008) The microstructure of dispersed and non-dispersed fresh cement pastes — New insight by cryo-microscopy. *Cem. Concr. Res.* 38(4), 522–9, Doi: 10.1016/j.cemconres.2007.11.007.
- [379] Zwanenburg, E.A., Williams, M.A., Warnett, J.M. (2022) Review of high-speed imaging with lab-based x-ray computed tomography. *Meas. Sci. Technol.* 33(1),

012003, Doi: 10.1088/1361-6501/ac354a.